Phosphonate Ligands in Extended Inorganic Hybrids and as Radical Units in Complexes

Dissertation

zur Erlangung des Grades
Doktor der Naturwissenschaften
im Promotionsfach Chemie

am Fachbereich Chemie, Pharmazie und Geowissenschaften
der Johannes Gutenberg–Universität in Mainz

Anna-Maria Pütz

geb. in Trier

Mainz, 2010

Dekan:

1. Berichterstatter:
2. Berichterstatter:

Tag der mündlichen Prüfung: 02.11.2010

Die vorliegende Dissertation wurde durch ein Promotionsstipendium im Rahmen des Programms MATCOR der Graduiertenschule MAINZ (*Materials Science in Mainz*) gefördert.

Contents

Abstract

Hybrid inorganic-organic framework materials are in general extremely versatile. Creating low-dimensional materials in a rational way with having control over the kind of connectivity, offers new possibilities in the field of molecular magnetism. Here, in case of metal phosphonate compounds as extended inorganic hybrids, the pH-value was adjusted during the reaction and the degree of protonation of the phosphonate ligand was controlled. Due to the fact that all obtained metal phosphonate compounds were neutral, the ligand to metal ratio could be predicted for the first time. Thus, several new metal-phosphonate compounds ranging from zero-dimensional (I^0O^0, co-crystallisation of $M(H_2O)_6$ with the deprotonated phosphonate ligand), over one-dimensional (I^1O^0, chain structures) to two-dimensional (I^2O^0, layered structures) were discussed in detail concerning their magnetic behaviour. In general, the exchange interactions expected in inorganic hybrid materials are strong, because often a superexchange through a single oxygen atom is possible. Here, often several competing exchange interactions were present, so that complicated magnetic behaviours were observed.

Furthermore, three new examples of nitronyl-nitroxide radicals were presented, where an additional acidic functionality was introduced. The consequences of the acidic character of the additionally introduced sulfonic acid or phosphonic acid group on the nitronyl-nitroxide radical unit was investigated in detail for the first time. With the phosphonic acid substituted nitronyl-nitroxide radicals, perfect samples for the investigation of the spin shift in nitronyl-nitroxide radicals by EPR spectroscopy in general are obtained, due to the phosphorus present. Also the protonation state of the additional phosphonic acid group was taken into account. In this work the first metal complexes of the new acidic substituted nitronyl-nitroxide radicals were presented. The coordination of nickel(II) metal ions to the acidic, second functional group of the nitronyl-nitroxide radical was described. The magnetic exchange interactions of the metal ions and the metal-radical exchange interactions were investigated.

In general interesting molecular magnetic materials can be designed due to the fact that the dimensionality of the metal phosphonate compounds as examples of extended inorganic hybrids can be controlled. With nitronyl-nitroxide radicals as organic linkers, in future even more spin carriers can be incorporated in the hybrid inorganic-organic framework materials and the magnetic behaviour can be enhanced.

1

Hybrid Inorganic-Organic Framework Materials - An Introduction

Around 1706, a Berliner colourmaker named Johann Jacob Diesbach made a mistake. Working for Johann Leonhard Frisch, Diesbach was attempting to create a red pigment known as cochineal red lake. The recipe was simple: Heating up cochineal lice in alum ($KAl(SO_4)_2$*12 H_2O) and iron sulfate, before the pigment was precipitated with potash (K_2CO_3). One day, the potash was empty and Diesbach borrowed some from Johann Konrad Dippel, which was contamined with animal oil made from ox blood. So instead of creating the red pigment, the precipitate turned blue. For the first time Prussian Blue was made, which was not only the first man-made coordination compound but also the first man-made coordination polymer [1]. Not later than 1708, Frisch began to promote and sell the pigment across Europe. In 1724, the recipe was finally published by Woodward [2]. Salpetre (KNO_3) and potassium tartrate were melted in equal parts to red heat. Dried animal blood was added and the mixture was heated up again. The resiue was washed with water and alum and iron sulfate were added. The green precipitate was washed with hydrochloric acid to obtain the Prussian Blue. However, it took around 270 years before the structure of Prussian Blue, $Fe_4[Fe(CN)_6]_3$*x H_2O, was determined [3].

Table 1.1: Classification of hybrid materials according to [6]; O^n is the metal-organic-metal connectivity (ranging from 0 to 3) and I^n is the dimensionality of the inorganic connectivity (also ranging from 0 to 3), the overall dimensionality of the compound is the sum of the exponents

O^nI^n	I^0O^n	I^1O^n	I^2O^n	I^3O^n
I^nO^0	Molecular complexes	Hybrid inorganic chains	Hybrid inorganic layers	3-D inorganic hybrids
I^nO^1	Chain coordination polymers	Mixed inorganic organic layers	Mixed inorganic organic frameworks	/
I^nO^2	Layered coordination polymers	mixed inorganic organic frameworks	/	/
I^nO^3	3-D coordination polymers	/	/	/

Today a whole family of Prussian blue-like phases with the general formula $C_nA_p[B(CN)_6]_q$*x H_2O (C is a univalent cation; A and B are six-coordinate transition metal ions which are high and low-spin ions, respectively) is known. These compounds exhibit a well known cubic structure, where A occupies all the corner and all the centres of the faces, $[B(CN)_6]$ fills the octahedral sites and C can be inserted in some of the tetrahedral holes. Due to the high symmetry of their structures, it is comparable easy to predict the nature of the magnetic exchange interaction, which only depends on the orbital geometry in the linear A-NC-B fragment. By applying simple orbital models which are based on the symmetry of the magnetic orbitals (singly occupied molecular orbitals, defined by Olivier Kahn [4]), Verdaguer et al. succesfully synthesized with $V^{II}_{0.42}V^{III}_{0.58}[Cr(CN)_6]_{0.86}$*2.8 H_2O the first molecule based magnet whose Curie temperature (T_c) is above room temperature (T_c = 315K) [5]. In comparison, the T_c value for Prussian blue itself is 5.6K.

Within the scope of hybrid inorganic-organic materials, one would classify Prussian blue and the Prussian blue-like phases as three-dimensional coordination polymer (I^0O^3) according to Cheetham et al. [6]. Here hybrid inorganic-organic framework material are defined as compounds that contain both inorganic and organic moieties as integral parts of a network with infinite bonding connectivity in at least one dimension. Furthermore hybrid inorganic-organic framework materials can be divided in two categories. The first one consists of the already mentioned coordination polymers which are also known as metal organic frame-

works (MOFs). These are defined as extended arrays composed of isolated metal atoms or clusters that are linked by polyfunctional organic ligands (in general L) resulting in extended M-L-M connectivities. The second category is made of systems that contain extended arrays of purely inorganic connectivity. Because most of the known materials in this area are based upon oxygen bridges with infinite metal-oxygen-metal (M-O-M) arrays, they are called hybrid metal oxides or (more general) extended inorganic hybrids. An overview of the different classes is given in table 1.1.

1.1 Coordination Polymers

As the knowledge of Prussian blue and its analogues became deeper, the interest in lower dimensionality cyanide-bridged compounds increased. So new strategies were developed to obtain coordination polymers of lower dimensionality (I^0O^1 and I^0O^2) and even to enter into the molecular regime (I^0O^0) [7]. In fact, the reaction of the hexacyanometallate unit $[B(CN)_6]^{(6-b)-}$ with the fully solvated species $[A(H_2O)_6]^{a+}$ affords the highly insoluble three-dimensional Prussian blue analogues. But by substitution of some water molecules in the fragment of A $[A(L)(H_2O)_x]^{(a-l)+}$ and reacting it with the hexacyanometallate unit $[B(CN)_6]^{(6-b)-}$ or as well by substitution of some cyanide molecules in B $[B(L)(CN)_x]^{(x+l-b)-}$, it is possible to design coordination polymers of lower dimensionality in a rational way.

But apart from the appropiate building blocks, another important factor in the design of coordination polymers has to be taken into account - the connectivity. Wells was the first one who described crystal structures in terms of networks in his book "Three dimensional nets and Polyhedra" [8] and Robson et al. outlined a net-based approach to design coordination polymers based on crystal structures [9, 10]. So structures with particular topologies can be designed by the use of metals and ligands with the appropiate coordination geometries. Even today, most of the coordination polymers are based on a few simple high-symmetry topologies like Diamond (as an example for a 4-connected net) [11]. One needs tetrahedral metal ions (Cu^I, Zn^{II} or Cd^{II}) as nodes and linear bridging ligands (like cyanide) as linkers for building up a diamond like network (one possible realisation). In general any coordination polymer can be described in terms of nodes and linkers, based on the network approach. Nevertheless, there are several notations used in literature, for simple uniform nets a labelling according to Wells [8] is appropiate:

(n,p) with n being the size of the shortest circuit and p being the connectivity of the nodes. Information of more detailled labelling like the Schläfli symbol can be found in the literature [1].

Cyanides are not the only used linkers in building up coordination polymers. As already explained, depending on the targed topology several other linkers have been used. Imidazole-based ligands e.g. are particular effective in mimicing Si-O-Si angles that are typically found in zeolithe structures, so that porous coordination polymers based on these purely inorganic framework materials were obtained [12]. But also carboxylates, especially aromatic carboxylates are widely used as linkers in coordination polymers. Again a zeolithe structure was build up from a chromium(III) trimeric building unit and 1,3,5-benzenetricarboxylate [13]. The most prominent example of a coordination polymer with rigid aromatic dicarboxylates, but also in general, is MOF-5 [14]. MOF-5 is a porous cubic zinc terephthalate which is topologically analogous to ReO_3. The nodes are ZnO_4 tetrahedra and the linker are terephthalate ions. By altering the length or other chemical details of the organic linker, more than 16 derivates with the same basic architecture have been made [15].

Two different strategies with metal carboxylate have been applied successfully in the literature [16]. A lot of secondary building units (SBU), another term for node when more as just one metal ion is used, are already known from coordination chemistry, small metal carboxylate clusters. The already mentioned chromium(III) trimeric building unit and the ZnO_4 tetrahedra as well as dimeric paddle-wheel complexes are prime examples for such secondary building units. One strategy is already introduced with MOF-5, by using rigid aromatic difunctional or in general multifunctional carboxylates one can link the secondary building units into coordination polymers. The same is true for a dimeric paddle-wheel copper complex, the carboxylates linking the copper dimer can be difunctional so that a coordination polymer can be obtained [17]. The second possibility is to take small metal carboxylate cluster and to link it via co-ligands [18]. Very often, there are co-ligands or solvent molecules needed to saturate the coordination sphere of the metal ions, like in the axial position of the Jahn-Teller distorted copper coordination sphere in a dimeric paddle-wheel complex. In that case small carboxylates like acetate are advantageous. A special case is with the smallest carboxylate-the formiate. Here chain or layered structures are reported as in the case of cupric formiate tetrahydrate, $Cu(HCOO)_2 *4H_20$ [19]. Also three-dimensional coordination polymers are accessible via solvothermal synthesis like anhydrous manganese(II) formiate [20]

or iron(II) formiate $[Fe(OOCH)_2]\cdot 1/3HCOOH$, an example of a mesoporous magnet [21]. A further three-dimensional coordination polymer of manganese(III) formiate is reported to trap carbon dioxide molecules [22].

1.2 Extended Inorganic Hybrids

Traditional inorganic oxides display a variety of useful properties e.g. as molecular sieves (zeolithes), catalysts (Cr_2O_3/Al_2O_3 for alkene polymerisation) and magnetic storage (CrO_2). Modifying inorganic materials by incorporating organic ligands is one way in which novel materials can be generated while hopefully retaining, or improving upon, some of the properties of the parent structures. Inorganic materials are normally associated with physical properties like ferromagnetism, luminescence, semiconducting behavior, whereas organic materials have typicial properties like mesomorphism, non-linear optics and plastic mechanical properties. So, extended inorganic hybrids provide an opportunity for tailoring new and functional materials for basic science and technological applications.

As for the coordination polymers, there were also early examples of hybrid materials with extended inorganic connectivity, the most notable being the zirconium phosphonates [23]. These layered materials have often structures which are very close to that of a purely inorganic phosphate. Especially the α-zirconium phosphate structure ($Zr(HPO_4)_2$) is often adopted by zirconium phosphonate compounds, because the layers of purely inorganic connections are retained, whereas the one remainaing hydroxyl-group of the phosphate is replaced by the organic residue of the phosphonate. As consequence, in metal phosphonate compounds the layers of purely inorganic connections are separated by regions of purely organic linkage. Alberti et al. was able to increase the interlayer distances by taking advantage of monophosphonates, which act as spacers between the layers without any additional bonding [24]. By taking diphosphonates it was possible to create connections between the inorganic layers and to build up a three-dimensional extended inorganic hybrid (I^2O^1). These materials are not porous, but porosity can be obtained by using a combination of diphosphonate linkers and shorter monophosphonate groups [23]. Additional functional groups can also be introduced in the extended inorganic hybrid by the careful choice of the diphosphonate derivate used in the synthesis [25]. Catalysis with organically pillared zirconium phosphate/phosphonate catalysts has been reviewed by Clearfield et al. [26].

But also divalent metal phosphonate compounds were in the focus, the first phenylphosphonate derivates of divalent magnesium, manganese, iron, cobalt, nickel, zinc and cadmium were reported in 1979 by Cunningham et al. [27]. A general problem of the metal phosphonate compounds was the crystallinity, so that diffraction data of powders were often poor and the structure solutions were not clear without ambiguity. By now, due to the possibility of solvothermal synthesis, single crystal data are available and the structure models of two-dimensional layered materials could be confirmed, quite similar to the already introduced zirconium phosphonate structures. As for the zirconium phosphonate structures with the α-zirconium phosphate structure, there exists also a purely inorganic analogue for the divalent metal phosphonates, the ternary metal phosphate structure M'M"PO_4*H_2O with M' being K^+ or NH_4^+ and M" being Mn^{2+}, Fe^{2+}, Co^{2+} or Ni^{2+} [28]. For monophosphonate compounds, independently of the organic residue and independently of the size and charge of the metal ion, such a two-dimensional layered structure seems to be favourable [29]. Due to the metal to ligand ratio of 1:1 and due to the fact, that the metal ions are six-coordinated, two of the phosphonate oxygens chelate the metal ions and, at the same time, bridge across adjacent metal ions in the same row. The third phosphonate oxygen bridges to an adjacent row, so creating a typical layer arrangement of edge-sharing metal-oxygen octahedra. The sixth position is occupied by the oxygen of a water molecule. The symmetry of the metal-oxygen octahedra is highly distorted and the resulting layers are kinked or crenellated. The organic layer is made by the organic residues of the phosphonate ligands, which extend through the C-P bond perpendicular to the inorganic planes. Typical examples are the phenylphosphonate derivates of $[M(RPO_3)(H_2O]$ with R=C_6H_5. The cobalt derivate with M=Co is shown in figure 2.16 on page 46 [30, 31], where also the magnetic behavior of $[Co(C_6H_5PO_3)(H_2O)]$ is explained. The manganese and nickel derivates $[M(C_6H_5PO_3)(H_2O)]$ (M=Mn, Ni) are known to posses canted antiferromagnetic interactions between the spin carriers resulting in a weak ferromagnetic behavior [32, 33]. Whereas the iron derivate $[Fe(C_6H_5PO_3)(H_2O)]$ exhibits long-range three-dimensional antiferromagnetic ordering, coupled with weak ferromagnetic behavior below its Neel temperature of 21.5K [34].

1.3 Applications of Hybrid Inorganic-Organic Framework Compounds

Hybrid Inorganic-Organic Framework Compounds have developed into an important class of materials due to their potential application in the field of catalysis, gas storage, nanoreactors or drug release [35]. The pores in a hybrid inorganic-organic framework material can be further functionalized, so that known catalysts e.g. for epoxidation reactions can be incooperated. An advantage is that now the catalytic reaction is carried out even size- and regio-selective [36, 37]. For gas storage or gas separation, hybrid inorganic-organic framework compounds can be used as well and are also tested by industry [38].

Another important field of interest is the investigation of the magnetic behaviour of hybrid inorganic-organic framework compounds. Creating low-dimensional materials (one-dimensional chain compounds or two-dimensional layered compounds) in a rational way with having control over the kind of connectivity, offers new possibilities in the field of molecular magnetism. Whereas a lot of theoretical work has been published already in the 1970 for interpreting the static and dynamic properties of one-dimensional and two-dimensional magnetic materials and, more generally, the critical phenomena appearing in such systems [39], the discovery of layered copper oxide compounds showing a high-T_c superconductivity as well as a 2D antiferromagnetic behavior has still accentuated the initial interest in the 1980s [40]. Up to the 90s, the key point for magnetic chain compounds was to control the stacking of the (ferromagnetic, ferrimagnetic or weak ferromagnetic) chains in such a way as to induce interchain ferromagnetic interactions at the lattice level and thus, magnetic ordering in the bulk.

A new strategy to create magnets with one-dimensional magnetic compounds arose from Glauber's theoretical work as early as 1963 [41]. He suggested that the conditions to be fullfilled to observe slow magnetic relaxation in a one-dimensional compound were that first it must behave as an Ising ferro- or ferrimagnetic chain and second the ratio J/J' has to be larger than 10000 (J and J' being the intrachain and interchain magnetic interactions, respectively). This prediction has opened exciting new perspectives to store information in low-dimensional materials. However, more than three decades were needed to observe this behaviour for the first time, because strong intrachain and very weak interchain magnetic interactions are required in addition to the Ising anisotropy. The first realisation of such a single-chain magnet (short:SCM) was with $[Co(hfac)_2(NITPhOMe)]_n$ made

by Caneschi et al. [42]. One of the spin carrier is a stable nitronyl-nitroxide radical and by now several more systems and strategies are known. One example is the combination of predefined monomeric building blocks of different metal ions resulting alternating bimetallic chains which can display a SCM behaviour like $[Mn_2(saltmen)_2Ni(pao)_2(py)_2](ClO_4)_2$ by Clerac et al. [43]. Apart from these examples with different spin carriers, also homometallic SCMs are known where the intrachain interaction is ferromagnetic in nature [44] or if a canted antiferromagnetic behaviour is observed [45].

Although the theoretical background for the investigation of the magnetic behaviour of low-dimensional hybrid inorganic-organic framework compounds is established for a long time since predicitons of the magnetic behaviour in low-dimensions can be calculated exactly in many cases, the experimental realisation, however, is more difficult to achieve. Interchain interactions or interlayer interactions have to be minimalised for a true low-dimensional magnetic behaviour. Therefore, it should be possible to build up a three-dimensional hybrid inorganic-organic framework compound, where magnetic exchange interactions in all three dimensions play an important role.

The advantage over "commercial" solid-state magnets is, that the magnetic behaviour of the resulting compound could be combined with other material properties which are characteristic of molecular materials like low specific density or optical transparency. Furthermore, in the case of hybrid inorganic-organic materials, the magnetic behaviour can be combined with the established properties of networks like catalytic reactivity or gas storage.

1.4 Nitronyl-Nitroxide Radicals

Organic molecules play an important role in building up molecular magnetic materials, they actually can also serve as spin carriers in case of radicals. Here the unpaired electron is not situated in a d- or f-orbital like in metal ions, but it is located in s- or p-orbitals of the organic molecule. Since the discovery of Gomberg's free triphenylmethyl or trityl radical in 1900, the research on free radicals was mainly focused on radicals as highly reactive intermediates in radical chain reactions like the ozone depletion [46, 47]. In contrast, stable radicals, per definition radicals that can be isolated and characterised in the presence of oxygen, are relatively rare.

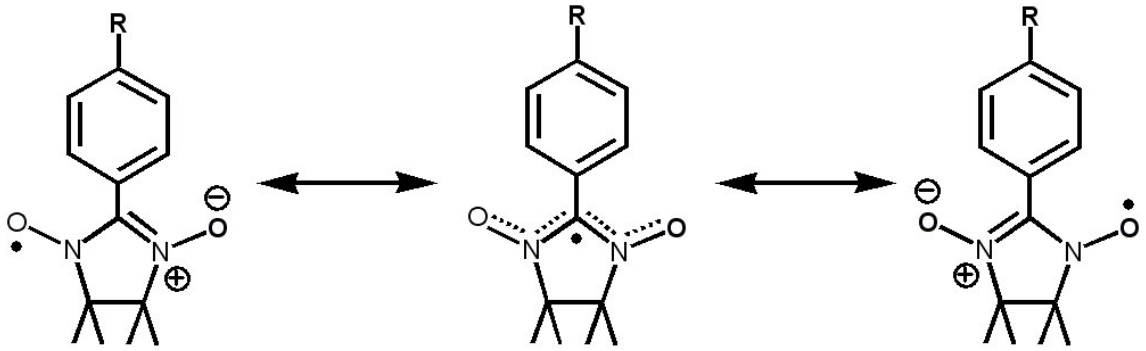

Figure 1.1: Stabilisation by mesomerism is schematically shown in the case of a substituted derivate of the 1-oxyl-3-oxide-4,4,5,5-tetramethyl-2-phenylimidazoline (short: Phenyl-NIT)

Several stable radicals are known like nitroxides, verdazyls and phenylhydrazyls, but the one discussed here is the class of nitronyl-nitroxide radicals (short: NIT radicals). Preserving the free radical character and preventing reactions of the unpaired electron is realised by delocalisation of the unpaired electron in a π^*-orbital of the nitrogen-oxygen bonds. Furthermore, it is sterically protected by four methylgroups that shields the radical to one side. Another stabilising mechanism is the mesomerism of the radical character, the unpaired electron is delocalised over both nitrogen-oxygen bonds as can be seen in figure 1.1. Delocalisation of the radical character is even further enhanced by integration in a larger aromatic system, e.g. the shown phenyl ring. This increases strongly the stability of the NIT radicals, since the bond of the substituted imidazoline ring to the choosen residue is in general electron poor. Another reason for the stability of the NIT radicals is that by a recombination of the NIT-radicals a quite labil peroxide bond has to be established, a reaction that is further permitted by the partly negative charged oxygen of the nitrogen oxygen bond.

Since the first description of the synthesis of a nitronyl-nitroxide radical by Ullman [48], the stability of the radical and its tolerance concerning other functional groups have led to a large family of nitronyl-nitroxides. Starting from the non-substituted 4,4,5,5-tetramethyl-imidazolin-3-oxide-1-oxyl radical over aliphatic substituted nitronyl-nitroxide radicals like 2,4,4,5,5-pentamethyl-2-imidazolin-3-oxide-1-oxyl [49] to Ullman's phenyl substituted 2-phenyl-4,4,5,5-tetramethyl-imidazolin-3-oxide-1-oxyl radical (short: Phenyl-NIT) [48], the varity of introduced residues is countless. The phenylring can be further substituted with hydroxyl [50], amine [51], nitro groups [52] or halids [49]. Even diradicals [53] or triradicals [54] with partly mixed classes of stable radicals are possible.

The idea of building up a bulk ferromagnet with only organic spin carriers was the main reason for the search of new nitronyl-nitroxide radicals. As a prerequisite for a bulk ferromagnet, ferromagnetic interactions in three dimensions are needed and so the three-dimensional packing of the nitronyl-nitroxide radicals in the solid state is responsible for the intermolecular interactions. The McConnell-I model [55], is probably the most employed model today, due to its simplicity. By short contacts between atoms with considerable atomic spin population of opposite sign of neighbouring molecules, the main spin population on the nitronyl-nitroxide units is oriented parallel, thus resulting ferromagnetic interactions. Otherwise, the interaction would be antiferromagnetic in nature or negligible. With residues introduced in the nitronyl-nitroxide unit, the packing should be influenced and ferromagnetic patterns or synthons should be identified [56]. Finally with R being a nitro-group NO_2 in figure 1.1, the first purely organic ferromagnet O is shown. At low temperatures (below 0.65 K), the β-phase of 2-(4-nitrophenyl)-4,4,5,5-tetramethyl-4,5-dihydro-1H-imidazol-1-oxyl-3-N-oxide (short: pNO_2-NIT) undergoes a phase transition to a ferromagnetic ordered state [52]. Although a lot of effort have been made to increase the ordering temperature, still today the record for the class of nitroxide radicals in general is at 1.48 K [57].

Another approach was carried out by Miller et al. [58], by the investigation of a class of charge-transfer molecular solids. They found that $[Fe^{III}(C_5Me_5)_2]^{\bullet+}[TCNE]^-$ exhibits bulk ferromagnetic behavior below 4.8 K. Charge-transfer compounds with nitroxide radicals are also known [59], but none of them shows a higher transition temperature than the record of 1.48 K of a pure nitroxide radical.

By combining stable radicals with metal ions in the so called "metal-radical approach" [60], the by far highest ordering temperatures have been obtained. As example the $V(TCNE)_x$ compound should be mentioned which has an ordering temperature of 400 K [61], although the final structure of the compound is still unknown today [62]. In the case of nitronyl-nitroxide radicals, successful attemps were carried out by coordination of the nitronyl-nitroxide group directly to a transition metal ion. This requires strong electron withdrawing co-ligands, because the nitrogen oxygen groups of a NIT radical in general are just weak Lewis bases. Such a co-ligand is 1,1,1,5,5,5-hexafluoroacetylacetonate (short: hfac), and some exemplary compounds with interesting magnetic properties are presented in the next paragraph.

With no further demand on the residue at the 2-position of the NIT radical, simple mononuclear compounds with the general formula [M(hfac)$_2$(NIT radical)$_2$]

can be obtained, as for M = Co and NITPhOMe as nitronyl-nitroxide radical published [63]. There is only one example of an unusual binding mode of an aliphatic substituted NIT radical in the literature [64], in the dinuclear complex $[M(hfac)_2NITEt]_2$, the metal ions (M = Co, Ni) are bridged by a κ^2 oxygen of the NIT radical, in all other higher nuclear compounds the NIT radical coordinates the metal ions with both oxygens of the nitronyl-nitroxide group or with an additional functional group of the residue attached in the 2-position. With structural more flexible residues at the 2-position of the NIT radical like a pyrazole ring in 4,4,5,5-Tetramethyl-2-(1-methyl-1H-pyrazol-4-yl)-imidazoline-3-oxide-1-oxyl, a whole range of structures are possible starting from binuclear molecules and trinuclear moleculs over hexanuclear ring structures to one-dimensional chain structures [65]. One-dimensional chain structures (I^0O^1) with the general formula $[M(hfac)_2(NIT\ radical)]_n$ display interesting magnetic properties, for M being Cu(II) ferromagnetic interaction between the different spin carriers are found, whereas for cobalt and manganese [66] antiferromagnetic ones are reported. In case of $[Co(hfac)_2(NITPhOMe)]_n$, the cobalt derivative, the resulting ferrimagnetic chain was the first example of a single chain magnet (short: SCM) [42]. Furthermore, by the appropiate choice of a second functional group in the residue in 2-position of the NIT radical, one-dimensional chain structures (I^0O^1) can be linked to two-dimensional layered structures (I^0O^2) [67]. As well lanthanides can be used as metal ions [68] or di-nitronyl-nitroxide radicals can be coordinated [69].

So far only the direct interaction of the nitronyl-nitroxide group with metal ions was discussed, but as already indicated in the last paragraph, the metal ions can as well be coordinated by functional groups of the attached residue in the 2-position. By now several compounds are known which are exclusively bound by the functional group in the residue of the nitronyl-nitroxide radical and not by the radical itself. So the weak interaction through the ligand molecule or through the space can be studied. In the case of a nitronyl-nitroxide radical with a hydroxyl-group in para-position of the phenyl ring attached to the 2-position, a second functional group in meta is needed to coordinate stable to the metal ions resulting in compounds with the general formula $[M(NIT\text{-}radical)_2]$*solvent with M = Ni and Cu [70]. By using a carboxylate substituted phenylring of the nitronyl-nitroxide (short: COOH-NIT) or a *tert*-butyl-nitroxide radical, a bridging of two metal ions by the second functional group is possible if the coordination spheres of the two metal ions is completed by a large co-ligand like N,N,N',N'-tetrakis-(N-propyl-2-benzimidazolyl)-2-hydroxy-1,3-diaminopropane (short: HPTB) [71]. In

both cases, a significant long distance exchange interaction between the peripheral radical unit and the copper metal ion dimer could be confirmed, for the COOH-NIT the interaction was antiferromagnetic in nature in contrast to the interaction to the *tert*-butyl-nitroxide radical unit, where it was ferromagnetic in nature. The difference can be explained by an effective spin-polarisation mechanism [72].

2

PART 1: Extended Phosphonate and Carboxylate Compounds

2.1 Extended Inorganic Hybrids build of Phosphonate Ligands

In general, metal phosphonate compounds are well-known in literature as two-dimensional inorganic hybrid materials [23, 29]. But here in this work it will be shown that with small changes in the organic residue of the phosphonate ligand, big effects on the structure and the magnetic behaviour of the metal-phosphonate compound can be obtained. In the following section, several derivates of the phenyl phosphonic acid will be introduced as partly new ligands in the synthesis of metal phosphonate compounds. Furthermore a new synthesis strategy is presented which offers the possibility to control the dimensionality of the resulting metal phosphonate compounds, so that for example also lower dimensional compounds like one-dimensional chain compounds can be obtained in a rational way. In general the derivates of the phenyl phosphonic acid are reacted with simple metal salts in a controlled pH region, so that by a self-assembly process the metal phosphonate compound with the desired dimensionality can be obtained. Due to the

fact that the magnetic properties of these compounds are also an important aspect of this work, paramagnetic transition metal ions are used, mainly the late 3d transition metal ions manganese(II), iron(II), cobalt(II), nickel(II) and copper(II). The next sections describe the new metal-phosphonate compounds ranging from zero-dimensional (I^0O^0, co-crystallisation of $M(H_2O)_6$ with the deprotonated phosphonate ligands), over one-dimensional (I^1O^0, chain structures) to two-dimensional (I^2O^0, layered structures).

2.1.1 Characterisation of Phosphonate Ligands

Three different approaches in the design of partly new phosphonate ligands are carried out. The first one is the use of rigid aromatic phosphonate ligands and to introduce some sterical hindrance in the form of a methyl group. The influence of the chain length of monoalkylphosphonate ligands on the resulting metal phosphonate compound is already well described in the literature for manganese [29] and nickel [33] phosphonate compounds, but using tolyl-phosphonic acid derivates as ligands in metal phosphonate compounds is surprisingly unexploited. The second approach is the introduction of a second functional group in the rigid aromatic phosphonate ligand. Various options are possible and here the carboxilic acid group was choosen. The last phosphonate ligand used in this work is 1H-benzimidazol-2-yl-methyl-phosphonic acid which is known from literature [73], but no metal phosphonate compound is reported so far.

In general, the method of choice for the synthesis of phosphonic acid derivates is the Michaelis-Arbuzov reaction. An alkylhalogenide is reacted with triethylphopshite and under loss of the appropiate ethylhalogenide the desired alkylphosphonicethylester can be made. Saponification with hydrochloric acid yields the free alkylphosphonic acid derivate. In case of aromatic halogenids catalytic amounts of a water free nickel salt are needed, in this work water free nickel chloride was used. The synthesis is well-established and pure products in high yields could be isolated. The reactions with appropiate 3d transition metal salts, mainly chloride and sulfonate salts, were carried out under solvothermal conditions. An important factor is the pH-value of the reaction media, because the phosphonic acid derivates R-PO_3H_2 can be classified as dibasic and weak acids with pK_A-values of 2.0 and 6.59 (for R = H) and 1.83 and 7.07 (for R = C_6H_5) [74].

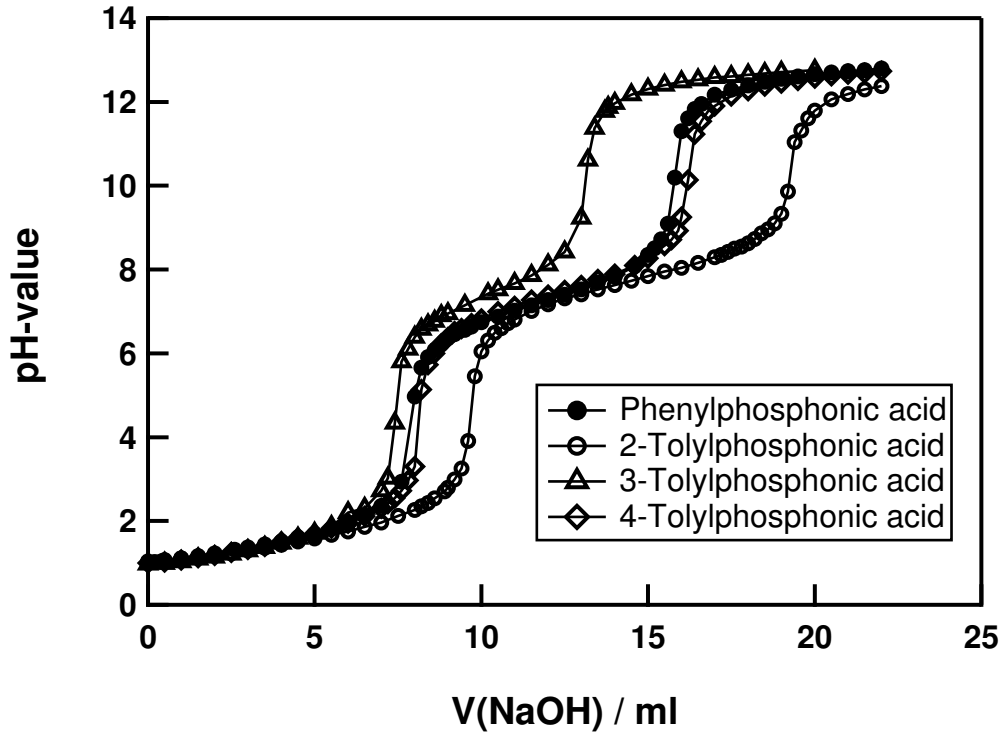

Figure 2.1: Titration curve of tolyl-phosphonic acid derivates (Volume of NaOH depends on the weighted sample, around 200 mg, probably some small impurities with NaCl salt); pK_A-value of R-PO_3H_2 is 1.8 and pK_A-value of R-PO_3H^- is 7.5

2.1.1.1 Tolyl-Phosphonic Acid Derivates

Although the synthesis procedure for the tolyl-phosphonic acids is known in the literature since 1970 [75] (a visualisation can be found in figure 5.1 on page 154), only one example can be found in the literature describing the meta-tolyl-phosphonate ligand coordinating a copper ion. Furthermore the coordination of the tolyl-phosphonate was not intended by the authors, because the effect of ring substituents on crystal packing and H-bonding in a series of halobis(phen)copper arylphosphonic acid co-crystals was investigated [76]. In contrast to the reported compound, here the phosphonate residue of the meta-tolyl-phosphonate ligand is intended to coordinate the transition metal ions used, resulting layered extended inorganic hybrid materials (I^2O^0) similar to the divalent metal phenylphosphonate compounds with the general formula $[M(C_6H_5PO_3)(H_2O)]_n$. As already pointed out, the pH-value of the reaction media can play an important role, but here no influence on the obtained metal phosphonate compounds with the general formula $[Co(H_3CC_6H_4PO_3)(H_2O)]_n$ (para **(11a)** , meta **(11b)**) could be found. These complexes will be discussed in detail in section 2.1.5.1. In this work, the obtained pK_A-values of the pure ligands seem to be higher compared to the literature values

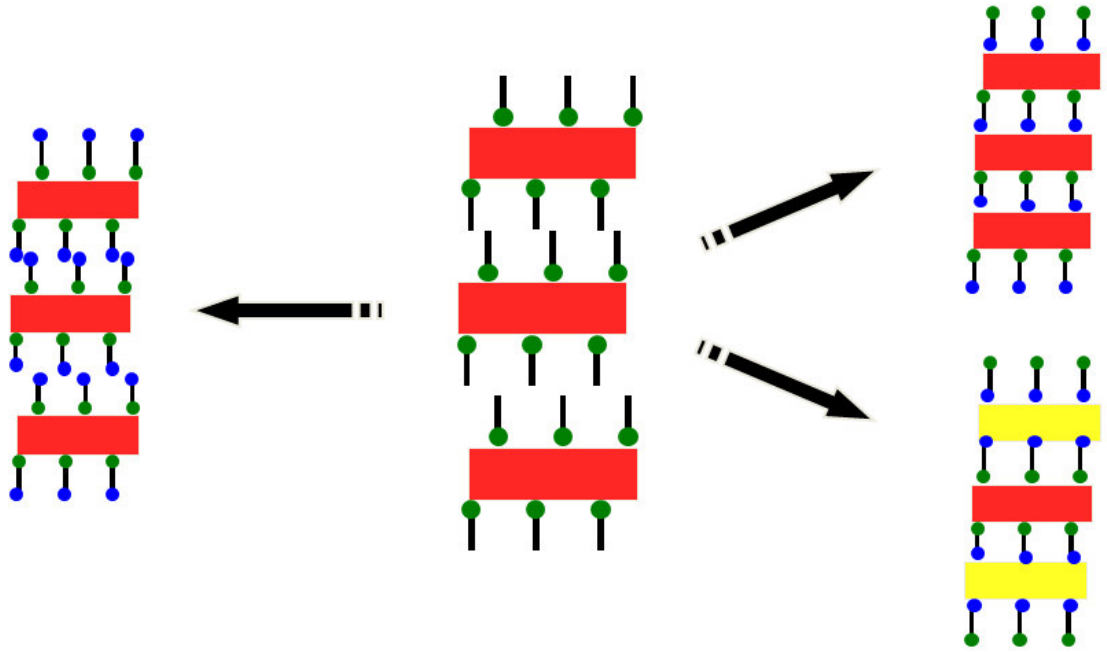

Figure 2.2: A strategy to built up new multi-functional and multi-dimensional materials is schematically shown; explanation can be found in the text

reported above as can be seen in figure 2.1. From the half-neutralisation point the pK_A-value of a weak acid can be calculated, the half-neutralization point is estimated from figure 2.1 and pK_A-values of 1.8 and 7.5 are obtained. In general no influence on the pK_A-values of the phosphonic acid group by the newly introduced methylgroup in the aromatic ring system can be found.

2.1.1.2 Phosphonbenzoic Acid Derivates

With the introduction of a second functional group in the rigid aromatic phosphonate linker, one has several new possibilities to build up hybrid inorganic-organic framework materials as can be seen in figure 2.2. It is schematically shown, how to build up a new multi-functional and multidimensional materials based on the layered extended inorganic hybrid materials (I^2O^0) of the divalent metal phenylphosphonate compounds with the general formula $[M(C_6H_5PO_3)(H_2O)]_n$. The red blocks are the extended inorganic layers and the small black blocks resemble the rigid aromatic backbones of the phenylphosphonate linker with the green head group for the phosphonate group. The blue head group stands for the newly introduced second functional group. Three possible different inorganic-organic framework materials are presented:

- Two-dimensional layered extended inorganic hybrid material with an additional functionality (I^2O^0)

  On the left side of figure 2.2, it is shown that the newly introduced functional group does not affect the binding between the phosphonate group and the metal ion, so that the layered extended inorganic hybrid material is retained. But an additional functionality is established in the overall known structure, generally an interesting approach to realise catalytic active materials or sensors. The inorganic part of the phosphonates determines the structure, the organic part determines the functionality. Concerning the magnetic properties of these layered extended inorganic hybrid materials, one expects them to be not very different to those already described for the divalent metal phenylphosphonate compounds with the general formula $[M(C_6H_5PO_3)(H_2O)]_n$.

- Three-dimensional homo-metallic mixed inorganic-organic framework materials (I^2O^1)

  On the right site of figure 2.2 (top), the homo-metallic case of a three-dimensional mixed inorganic-organic framework materials is shown (just red blocks), where both functional groups, the phosphonate and the other not yet defined one, coordinate to one kind of metal. In general it should be possible to link the layered extended inorganic hybrid materials (I^2O^0) of the divalent metal phenylphosphonate compounds to three-dimensional mixed inorganic-organic framework materials (I^2O^1). One approach is the use of diphosphonate compounds, another one is the substitution of the coordinating water molecule.

- Three-dimensional hetero-metallic mixed inorganic-organic framework materials (I^2O^1)

  On the right site of figure 2.2 (bottom), the hetero-metallic case of a three-dimensional mixed inorganic-organic framework materials is shown (red and yellow blocks). This can only be realised if one functional group coordinates preferably one kind of metal ions and the other functional group binds more likely another kind of metal ions.

The first requirement for the newly introduced group is, that it should have strong binding affinities to 3d transition metal ions, so donating atoms like nitrogen or oxygen are necessary. The binding ability should be controlled by the reaction conditions like the pH-value. Additional the group should have some other poten-

tial applications like promoting some possible catalytic activity or that it can be a reacting site in the hybrid material. The first residue to think of is a carboxylic acid group. Carboxylates are common in coordination chemistry and they are useful linkers in building up coordination polymers, as already pointed out in previous chapters. Furthermore, they play a significant role at the active sites of many metalloproteins and they are well-known for their flexible coordination behaviour. At the beginning of this work, a good synthesis strategy of the phosphonbenzoic acid derivates was not known, due to the incompatibility of the Michaelis-Arbuzov reation with acidic protons in general. I solved this problem by a two step synthesis procedure starting with the synthesis of the tolyl-phosphonic acids known from literature [75]. These are further oxidised with potassium permanganate in basic media to yield the desired phosphonbenzoic acid derivates in good yields as can be seen in figure 5.2 on page 157. By now due to the steadily increase in interest of phosphonate compounds, another synthesis strategy is reported by Rueff et al. [77].

Again, the titration curves of the phosphonbenzoic acids were determined as can be seen in figure 2.3. A comparison with the phenylphosphonic acid shows that the carboxilic proton is clearly adding another step in the titration curve. As expected by the reported pK_A-value of benzoic acid of 4.2, the first step in the titration curve is still the first deprotonation of the phosphonic acid group (pK_A-value of 1.5). The second step corresponds to the deprotonation of the carboxilic acid group (pK_A-value of 3.9). Both values are slightly smaller than the ones reported for benzoic acid and phenylphosphonic acid due to the electron withdrawing character of both substituents (what can be evaluated with Hammett's equation [74]). In the para and meta substituted case, the last deprotonation step, the second deprotonation of the phosphonate group is not affected by the substitution. The deprotonation scheme is also depicted in figure 2.3. The ortho derivate of the phosphonbenzoic acid displays a special behaviour due to the close proximity of both group. Here an intramolecular five-ring formation is possible after the second deprotonation step, which releases another equivalent of base resulting a dramatic increase in the pH-value and also the pK_A-value of the last step is changed to 10.0.

In the synthesis of the metal phosphonate compounds with the phosphonbenzoic acid derivates, the pH-value in the reaction media plays an crucial role. Depending on the pH-value of the reaction media and the choosen method, namely solvothermal or non-solvothermal, metal phosphonate compounds with different dimensionalities can be obtained by using the same starting compounds. Even the ratio

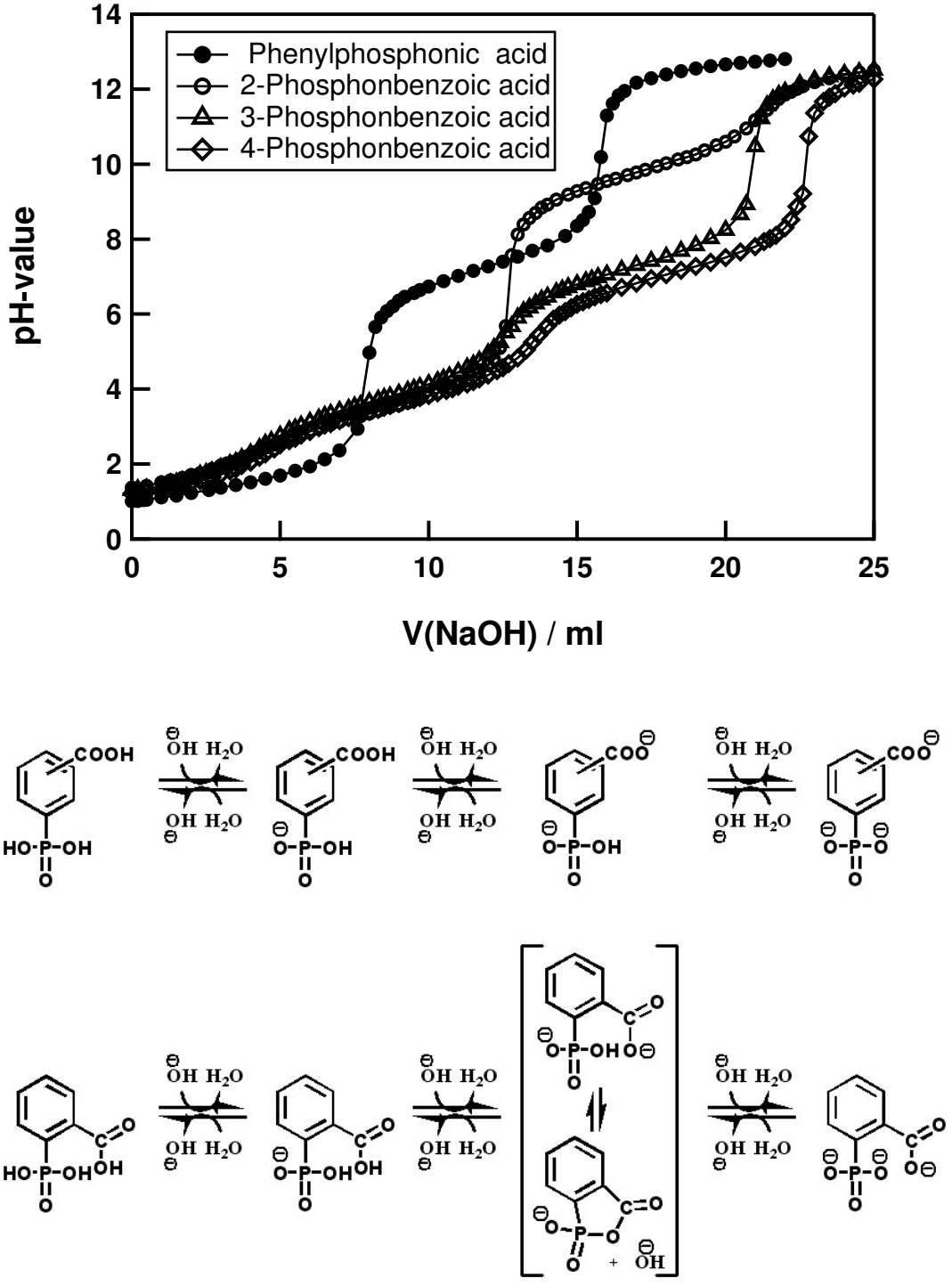

Figure 2.3: top: Titration curve of phosphonbenzoic acid derivates (Volume of NaOH depends on the weighted sample, around 200 mg, probably some small impurities with NaCl salt); bottom: deprotonation scheme of 3-/4-phosphonbenzoic acid and deprotonation scheme of 2-phosphonbenzoic acid explaining the higher pH-value after the second deprotonation step with an intramolecular five-ring formation

of the starting compounds seems not to be as important as the pH-value of the reaction media. Without addition of a base, the phosphonic acid group and the carboxilic acid group are completely protonated. Nevertheless, by using the solvothermal method it was possible to obtain single crystalline material after the reaction from the mother liquid with the general formula $[M(H_2O)_6(HOOCC_6H_4PO_3H)_2]$, where M can be nickel(II) or cobalt(II) and the phosphonbenzoic acid derivate can be para or meta (a detailed discussion can be found in section 2.1.3). Here, as expected from the titration curves, only the phosphonic acid group is deprotonated one time. But the phosphonbenzoic acid derivate is not coordinated to the metal ion, it just reacts as a counterion. In the case of the meta-phosphonbenzoic acid, even free meta-phosphonbenzoic acid is additionally co-crystallized. Furthermore in the case of the para-phosphonbenzoic acid, it was possible to characterise a one-dimensional hybrid inorganic chain (I^1O^0) with the formula $[Co(HOOCC_6H_4PO_3H)_2(H_2O)]_n$ from the reaction carried out under solvothermal conditions. The same compound could be obtained with the non-solvothermal method, but then an equivalent of base had to be added. Again just the phosphonic acid group is one time deprotonated, but this time the hydrogenphosphonate group is bridging in a μ_2-fashion two cobalt(II) ions resulting the one-dimensional chain. For the meta-phosphonbenzoic acid as well an one-dimensional hybrid inorganic chain could be characterized with the formula $[Mn(HOOCC_6H_4PO_3H)_2(H_2O)_2]_n$. Here the hydrogenphosphonate ligand adopts two different bridging modes, one is the K^2-bridging mode and the other again the μ_2-bridging mode. The one-dimensional chain compounds are further discussed in section 2.1.4. With one equivalent of base under solvothermal reaction conditions, two-dimensional hybrid inorganic layers (I^2O^0) are obtained. In the case of the ortho-phosphonbenzoic acid, the phosphonic acid is one time deprotonated and the carboxilic acid is deprotonated, as expected from the titration curve, but for the other two stereoisomers para and meta, only the phosphonic acid group is completely deprotonated in the obtained compounds. The reactions with the meta-phosphonbenzoic acid yields compounds with the general formula $[M(HOOCC_6H_4PO_3)(H_2O)]_n$, which resemble the metal phenylphosphonate compounds known from literature and the metal tolylphosphonate compounds already introduced, these compounds are discussed in section 2.1.5.1. In the case of the para-phosphonbenzoic acid, a new high-temperature modification with the formula $[M(HOOCC_6H_4PO_3)]_n$ is found with no coordinating water molecule (discussed in section 2.1.5.2). Both groups, as well the hydrogenphosphonate group as the carboxilic group coordinate to the metal ions in the case of the ortho-phosphonbenzoic acid resulting in a compound with the for-

mula $[Co(OOCC_6H_4PO_3H)(H_2O)]_n$ (discussion can be found in section 2.1.6). For all higher pH-values and independently of the used method, no single-crystalline material could be obtained.

Apart from these reactions of simple 3d divalent transition metal salts with phosphonbenzoic acid derivates in water, also experiments with co-ligands like 4,4'-bipyridine were carried out leading to the compound $[(HNC_5H_4C_5H_4NH)(HOOCC_6H_4PO_3H)_2]*2H_2O$ **(17)**. Furthermore, trivalent lanthanide ions were used like Pr(III) leading to the compound $[Pr_2(H_2O)_8(HOOCC_6H_4PO_3H)_6]$ **(18)**. A detailed describtion of the approaches for building up three-dimensional network structures can be found in section 2.1.7.

2.1.1.3 (1H-Benzimidazol-2-yl-methyl)Phosphonic Acid

The synthesis of the only aliphatic phosphonic acid derivate used as ligand in this work, namely (1H-benzimidazol-2-yl-methyl)phosphonic acid, is reported in literature [73]. The synthesis strategy is schematically shown in figure 5.3 on page 159. No metal phosphonate compound with this potential ligand is reported so far. This ligand was choosen, because it provides additionally to the phosphonic acid group a second functional group with a nitrogen donor atom, a benzimidazole residue. The benzimidazole residue is also sensitive to the pH-value of the reaction media, so that again the influence of the pH-value on the resulting metal phosphonate compound has to be taken into account. The titration behaviour can be found in the literature [73]. The aliphatic methylene bridge between the phosphonic acid group and the benzimidazole residue was choosen to provide the possibility for a stable six membered ring when coordinated to a metal ion. The solubility in all organic solvents and also in water is poor, so that the reactions with 3d transition metal salts were carried out under solvothermal conditions. Up to now, just one dimeric metal phosphonate compound with the formula $[Co_2(H_2O)_6(O_3PCH_2C_7H_5N_2)_2]*6H_2O$ **(16)** could be characterised, a detailed discussion can be found in section 2.1.6.

2.1.2 Overview: Metal Phosphonate Compounds

An overview of the obtained metal phosphonate compounds is given in table 2.1. In the case of the meta **(3b)** and para **(3c)** derivate of the phosphonbenzoic acid, the presented concept of how to influence the dimensionality of the resulting

compound works nicely. The pH value adjusted during the reaction mainly determines the dimensionality of the product. This can be explained by the fact that all obtained metal phosphonate compounds are neutral. In acidic conditions a hydrogenphosphonate ligand with a protonated carboxilic acid group is realised, so an one time negatively charged ligand is established. Although the hydrogenphosphonate ligand has three oxygen atoms which can coordinate in principle to metal ions, due to the fact that one of them is still protonated only the two other oxygen atoms are involved in coordination to metal ions. Therefore a μ_2-coordination mode is likely, which favours in this case the formation of one-dimensional chain compounds. In general for a neutral compound with a divalent transition metal ion two of these ligands are needed. For two-dimensional compounds, two protons of the phosphonbenzoic acid derivate have to be removed and although the carboxilic acid group is clearly more acidic than the second proton of the phosphonic acid, under the mentioned conditions only two-dimensional extended hybrid inorganic compounds (I^2O^0) are obtained, where the phosphonate group is completely deprotonated and the carboxilic acid group is still protonated (in the case of the meta/para-phosphonbenzoic acid). There are two reasons for this unusual behaviour, the first one is that the first proton of the phosphonic acid is the most acidic one, so that a coordination of the metal ion by the hydrogenphosphonate group is pronounced. Then due to a chelating effect, the second proton of the hydrogenphosphonate can be easier removed. The second reason is the stability of pairs of hydrogen bonded carboxilic acids, whenever such a structural motive or synthon is possible, it is realised as can be seen in all two-dimensional compounds with meta- or the para-phosphonbenzoic acid, so that probably this secondary interaction is necessary for the compound to crystallise. In consequence, all three oxygen of the phosphonate residue are involved in the coordination to metal ions, so that the organic residue of the phosphonate ligand is forced to orientate perpendicular to the resulting two-dimensional layered metal-oxygen structure out of sterical reasons of the tetrahedral surrounding of the sp^3 phosphorus atom. If the second functional group is in close proximity to the phosphonate group, this concept is no more applicable, so that new binding motives can be found. Again, the obtained metal phosphonate compounds are neutral, so one ligand compensates the charge of one divalent transition metal. For three-dimensional network compounds, one divalent transitions metal ion is not enough to fulfill the charge balance with a three times deprotonated phosphonbenzoic ligand, so that on the one side neutral co-ligands are used to further link the established two-dimensional layered compounds or on the other side threevalent metal ions have to be used.

Table 2.1: Overview of the presented metal phosphonate compounds; below the line approaches for the desired dimensionality are listed

	Section	Formula	Subsection	Page
0D	2.1.3	$[Ni(H_2O)_6(meta\text{-}HOOCC_6H_4PO_3H)_2]*(meta\text{-}HOOCC_6H_4PO_3H_2)_2$ **(7)**	2.1.3	26
0D	2.1.3	$[M(H_2O)_6(para\text{-}HOOCC_6H_4PO_3H)_2]*4(H_2O)$, M = Co **(8a)** and Ni **(8b)**	2.1.3	26
1D	2.1.4	$[Mn(meta\text{-}HOOCC_6H_4PO_3H)_2(H_2O)_2]_n$ **(9)**	2.1.4.1	27
1D	2.1.4	$[Co(para\text{-}HOOCC_6H_4PO_3H)_2(H_2O)]_n$ **(10)**	2.1.4.2	33
2D	2.1.5	$[Co(CH_3C_6H_4\ PO_3)(H_2O)]_n$, meta **(11b)** , para **(11a)**	2.1.5.1	45
2D	2.1.5	$[M(meta\text{-}HOOCC_6H_4PO_3)(H_2O)]_n$, M = Mn **(12a)** , Co **(12b)** and Ni **(12c)**	2.1.5.1	45
2D	2.1.5	$[M(para\text{-}HOOCC_6H_4PO_3)]_n$, M = Co **(13)** and Cu **(14)**	2.1.5.2	67
2D	2.1.6	$[Co(ortho\text{-}OOCC_6H_4PO_3H)(H_2O)]_n$ **(15)**	2.1.6.1	76
2D	2.1.6	$[Co_2(H_2O)_6(O_3PCH_2C_7H_5N_2)_2]*6H_2O$ **(16)**	2.1.6.2	79
3D	2.1.7	$[(HNC_5H_4C_5H_4NH)(HOOC\ C_6H_4PO_3H)_2]*2H_2O$ **(17)**	2.1.7.1	83
3D	2.1.7	$[Pr_2(H_2O)_8(HOOCC_6H_4PO_3H)_6]$ **(18)**	2.1.7.2	84

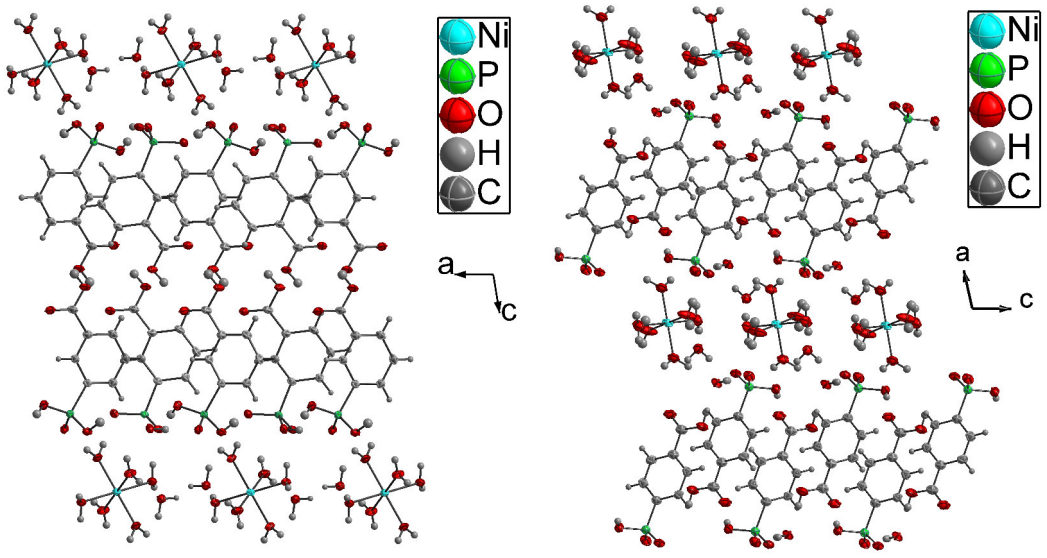

Figure 2.4: left: Part of the crystal structure of $[Ni(H_2O)_6$(meta-$HOOCC_6H_4PO_3H)_2]$*$2H_2O$*(meta-$HOOCC_6H_4PO_3H_2)_2$ **(7)**; right: Part of the crystal structure of $[M(H_2O)_6$ (para-$HOOCC_6H_4PO_3H)_2]$*$4(H_2O)$ for M = Ni **(8b)** shown, M = Co **(8a)** is not shown

2.1.3 Hydrated Metal Ions and Different Phosphonate Ligands as Counterions

In figure 2.4 the two different hydrogen bonded networks of hydrated metal ions and protonated phosphonbenzoic acid derivates are shown. These are in principle zero-dimensional compounds, because the metal-oxygen octahdra are not further linked by any covalent or coordinative bond. Nevertheless the metal-oxygen octahedra are incorporated in an extended network of hydrogen bonds. Depending on the used phosphonobenzoic acid derivate (meta or para), two different networks are obtained. Whereas in the crystal structure of $[Ni(H_2O)_6$(meta-$HOOCC_6H_4PO_3H)_2]$*$2H_2O$*(meta-$HOOCC_6H_4PO_3H_2)_2$ **(7)** even completely protonated meta-phosphonbenzoic acid can be found, forming with the one time deprotonated form a hydrogen-bonded phosphonbenzoic acid dimer anion, a very stable synthon in the field of supramolecular chemistry known for the phenylphosphonic acid [78], no such analoga can be found in the structure of the para-phosphonbenzoic acid derivate with the general formula $[M(H_2O)_6$(para-HOOC $C_6H_4PO_3H)_2]$*$4(H_2O)$, M = Co **(8a)** , Ni **(8b)** . Here, as expected from the titration behaviour, the phosphonate group is one time deprotonated and according to the sum formula two hydrogenphosphonate counterions are needed. Additionally some water molecules are incoporated so that also an extended hydrogen bonded

network is established. Although the ability of forming strong hydrogen bonds is known as well for the carboxilic acid group as for the phosphonic acid group, it is remarkable that it is stronger than the ability to coordinate a metal ion at least under this highly acidic conditions (without any addition of base).

2.1.4 1 D - Chain Compounds: Two Modifications depending on the used Ligand

The influence of the pH-value in the reaction media is crucial for the dimensionality of the resulting compound, is it too acidic (no addition of a base) only hydrogen-bonded networs can be synthesised, is it just acidic (pH≈2.5) enough to deprotonate the phosphonbenzoic acids one time, one-dimensional chain compounds can be obtained. As expetced from the titration behaviour, the most acidic proton is removed, so that always a hydrogenphosphonate ligand is found in the described compounds. The carboxilic acid group stays protonated and the one-dimensional chain compounds are stabilized by additional hydrogen bondings between the carboxilic acids groups of adjacent chains, forming a three-dimensional hydrogen bonded network again. Depending of the used phosphonbenzoic acid derivate, different linkages of the metal-oxygen octahedra are found.

2.1.4.1 A Manganese Chain build of meta-Phosphonbenzoic Acid and Water

The one-dimensional chain compound $[Mn(meta\text{-}HOOCC_6H_4PO_3H)_2(H_2O)_2]_n$ **(9)** was obtained by a non-solvothermal method. The manganese ions are coordinated in two different bridging modes by the hydrogenphosphonate ligand namely the K^2-bridging mode and the μ_2-bridging mode resulting a linear, but alternating chain. The manganese-manganese distance is in turn 3.43 Å (K^2-bridging mode) and 5.10 Å (μ_2-bridging mode). As shown in figure 2.5, dimers of edge-sharing manganese oxygen octahedra are linked by the μ_2-bridging phosphonate. The manganese coordination sphere is completed by two water molecules resulting distorted oxygen octahedra. The manganese water bond lengths are with 2.16 Å and 2.27 Å comparable to the manganese phosphonate bond lengths. Due to the two different bridging modes, the oxygen-manganese-oxygen angles differ from the ideal geometry with 98.61° for the μ_2-oxygens, 79.23° for the K^2-oxygens and 172.15° for the water molecules. For the magnetic behaviour the manganese-bridge-manganese angles are also important, with 100.7° for the K^2-oxygens and

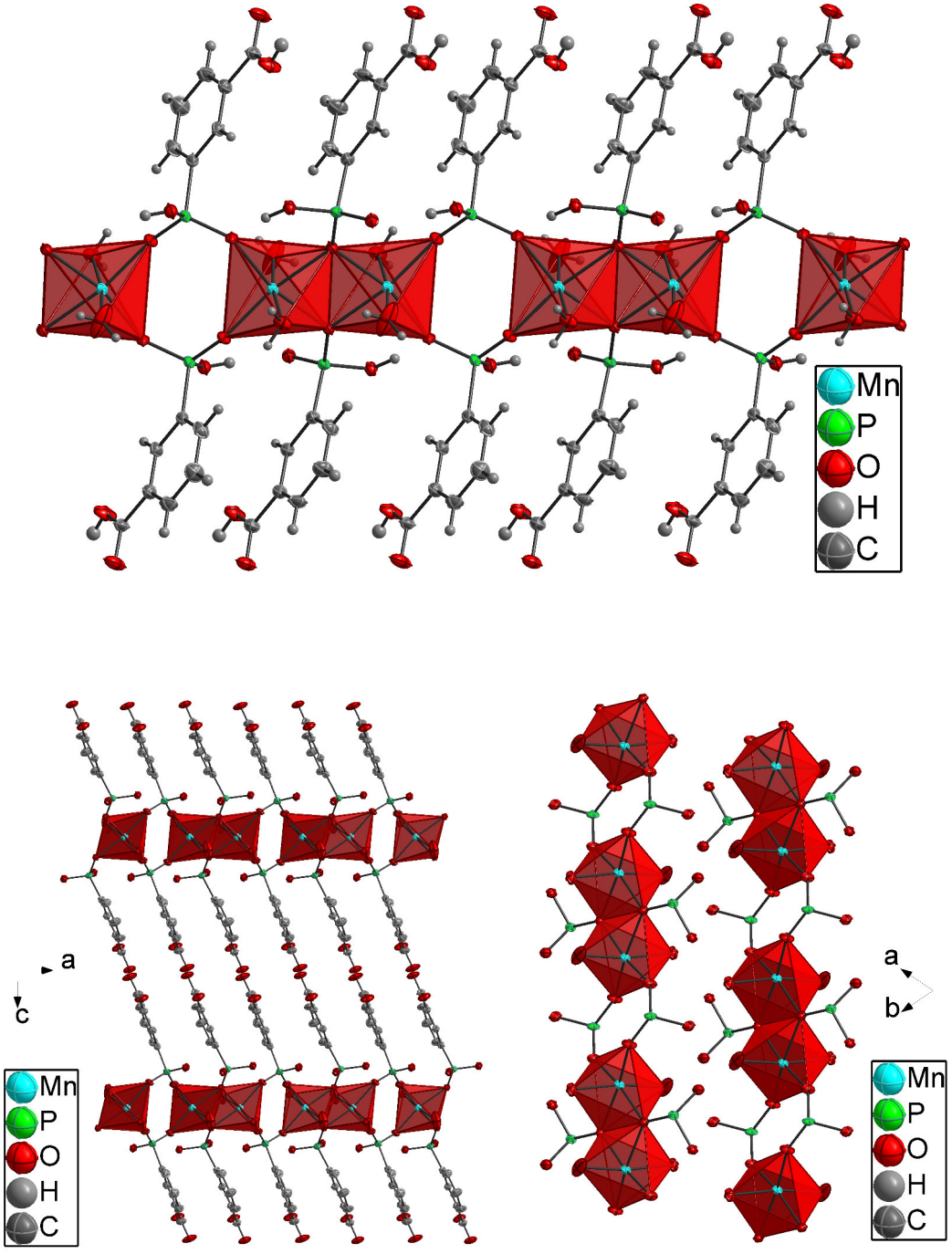

Figure 2.5: top: Part of the crystal structure of $[Mn(meta\text{-}HOOCC_6H_4PO_3H)_2(H_2O)_2]_n$ **(9)**, linear, but alternating chain motive with a K^2-bridging hydrogenphosphonate ligand and a μ_2-bridging hydrogenphosphonate ligand; bottom left: Packing of the chains along c by hydrogen bonding of the carboxilic acid groups; bottom right: Packing of the chains in the ab-crystal plane

94.4° for the "manganese-μ_2-phosphorus-manganese angle", mainly weak interactions should be expected. The separation of the chains in the solid-state is reasonably well as can be seen at the bottom of figure 2.5. The smallest manganese-manganese distance to the nearest chain is 6.18 Å in the ab-crystal plane, whereas the distance along c is much larger with 17.25 Å. The purity of the compound was further verified by powder diffraction as can be seen in figure 5.60 on page 246.

Very unusual is the combination of the K^2-bridging mode of one hydrogenphosphonate ligand with the μ_2-bridging mode of the second hydrogenphosphonate ligand, quite often a combined K^2- and μ_2-bridging mode of one phosphonic acid group linking three metal ions is found. But two examples were reported in the literature, the first one by Natarajan et al. [79] described an open network structure of $[Co(C_{10}H_8N_2)\ (H_2PO_3)_2]_n$. The cobalt ions were linked by dihydrogen phosphite acid ions in the same way as in $[Mn(meta\text{-}HOOCC_6H_4PO_3H)_2(H_2O)_2]_n$, but the one-dimensional chains were additionally connected by the 4,4'-bipyridine resulting a three-dimensional network. The second example of this unusual combination of bridging modes is $[Cu(NH(CH_2PO_3H)_2)]_n$ by Yang et al. [80]. Here, the ligand was imino-bis(methylphosphonic acid), where one phosphonic acid group coordinated two copper ions in the μ_2-bridging mode and the second phosphonic acid coordinated two copper ions in the K^2-bridging mode. Due to a coordinating deprotonated amine group, the copper ions were in a Jahn-Teller distored square-pyramidal surrounding. The resulting one-dimensional chain structure was linked by hydrogen bonding into a three-dimensional network. In both literature reported examples the magnetic behaviour was not investigated, so that comparison is not possible.

In general the Hamiltonian for a linear alternating chain can be derived from a linear uniform chain by adding a factor α for every second interaction [81]. The Hamiltonian is then defined as $\hat{H} = -2J\sum_i(S_{i-1}S_i + \alpha S_iS_{i+1})$ with -2J being the exchange interaction between a spin and one of its nearest neighbors and -2αJ being the exchange constant between the same spin and the other nearest neighbor in the chain. Per definition α is a number between zero and one (for antiferromagnetic/antiferromagnetic or ferromagnetic/ferromagnetic interactions, for antiferromagnetic/ferromagnetic interactions see [82]). The two limiting cases are for $\alpha = 1$ the uniform Bonner-Fischer chain and for $\alpha = 0$ an isolated dimer (Bleaney-Bowers equation). In figure 2.6 the measurement of the magnetic susceptibility of $[Mn(meta\text{-}HOOCC_6H_4PO_3H)_2(H_2O)_2]_n$ **(9)** is shown, especially the χ_m^{-1} vs. T plot makes clear that there are not any strong exchange

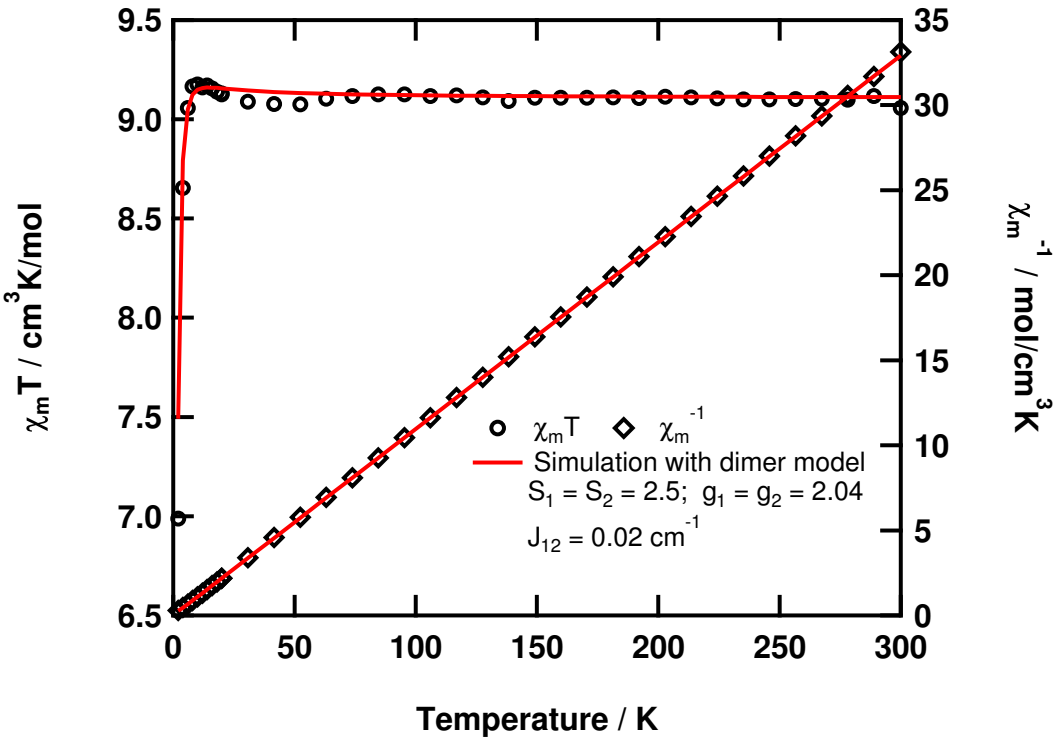

Figure 2.6: Measurement of the magnetic susceptibility of [Mn(meta-$HOOCC_6H_4PO_3H)_2(H_2O)_2]_n$ **(9)** with a field of 1 T, χ_mT vs. T and χ_m^{-1} vs. T plots are shown normalized to two metal ions; simulation with a dimer model

interactions, nearly a perfect Curie-Weiss behaviour is observed. The χ_m vs. T plot does not show a maximum whereas a maximum is expected for linear chain compounds. The χ_mT vs. T plot clearifies the nature of the exchange interaction and also the simulation based on a simple dimer model results a weak ferromagnetic interaction of $J_{12} = 0.02$ cm^{-1}. This value is consistent with a weak ferromagnetic interaction reported by Cao et al. [83] for the dimeric complex $[Mn_2(((C_7H_5N_2)CH_2)_2NCH_2PO_3)_2(H_2O)_2]$ where also a double bridge of K^2-coordinated phosphonate ligands is responsible for the magnetic exchange interaction. The manganese-oxygen-manganese angle is quite similar with 102.8° and the manganese-manganese distance is with 3.358Å a bit longer compared to the edge-sharing dimer present in $[Mn(meta\text{-}HOOCC_6H_4PO_3H)_2(H_2O)_2]_n$.

Overall true alternating linear chain systems are not very common in the literature, mainly bimetallic chains or metal ions coordinated to stable radicals are discussed [84]. In general linear alternating chains have been extensively studied especially in a theoretical way in the last decades due to their similarity with one-dimensional materials that undergo a spin-Peierls transition [85].

During the internship in the group of Prof. A. in Nagoya (Japan) this compound $[Mn(HOOCC_6H_4PO_3H)_2(H_2O)_2]_n$ **(9)** as well as the later presented two-dimensional layered compound $[Mn(HOOCC_6H_4PO_3)(H_2O)]_n$ **(12a)** were tested as cathode materials for rechargeable molecular cluster batteries [86]. The advantage of using molecular materials as cathode materials is the easier and faster charging process. Disadvantages are in general the lower stability and the lower capacity. Some of the metal-phosphonate compounds were tested as cathode materials, because they are quite stable compared with other molecular materials due to the normally needed solvothermal syntheses process where high pressures and high temperatures were present. The two manganese containing compounds were choosen because of the diversity of different stable oxidation states, that can be realised with a oxygen-rich enviroment of the manganese ions (starting with Mn^{2+}, but also possible Mn^{3+} and Mn^{4+}) as well as the good experience with the single molecular magnet $[Mn_{12}O_{12}(CH_3COO)_{16}(H_2O)_4]$ as cathode material. The difference between the two choosen manganese phosphonate compounds is the metal to phosphonate ratio. In the first example, the already introduced one-dimensional chain compound with the general formula $[Mn(HOOCC_6H_4PO_3H)_2(H_2O)_2]_n$, the ratio is one manganese(II) ion to two meta-$HOOCC_6H_4PO_3H$ ligands, because the ligand is a hydrogenphosphonate ligand and just one time deprotonated. In the second example, the two-dimensional layered compound with the general formula $[Mn(HOOCC_6H_4PO_3)(H_2O)]_n$, the phosphonate group of meta-$HOOCC_6H_4PO_3$ is completely deprotonated, so that the ratio is one manganese(II) ion to one phosphonate ligand.

First of all, cyclovoltameric measurement were carried out in a 0.1 molar KCl solution. All redox-waves of the manganese phosphonate compounds could be assigned as ligand centred by comparison with the cyclovoltameric measurement of the pure ligand as shown in figure 9. The battery was assembled in inert atmosphere, the cathode material was a mixture of black carbon, PVF (poly(vinylidenefluoride)) as binder and the manganese phosphonate compound as active material (ratio 7:2:1). The anode was a thin plate of lithium and the electrolyte was 1-Methyl-2-pyrrolidinone. Five charging/discharging cycles were measured to get an impression of the stability of the compound. During the assembly process the battery is already partly charged, which explains the higher starting potential. The theoretical capacity can be calculated according to following formula for one transferred electron $C_{theo} = (N_A * e)/(3600 * M_{Mol}/1000)$ with N_A the Avogadro constant, "e" the elementary charge and M_{mol} the molecular weight of the sample. The values calculated with 54 Ah/kg for the one-dimensional chain compound

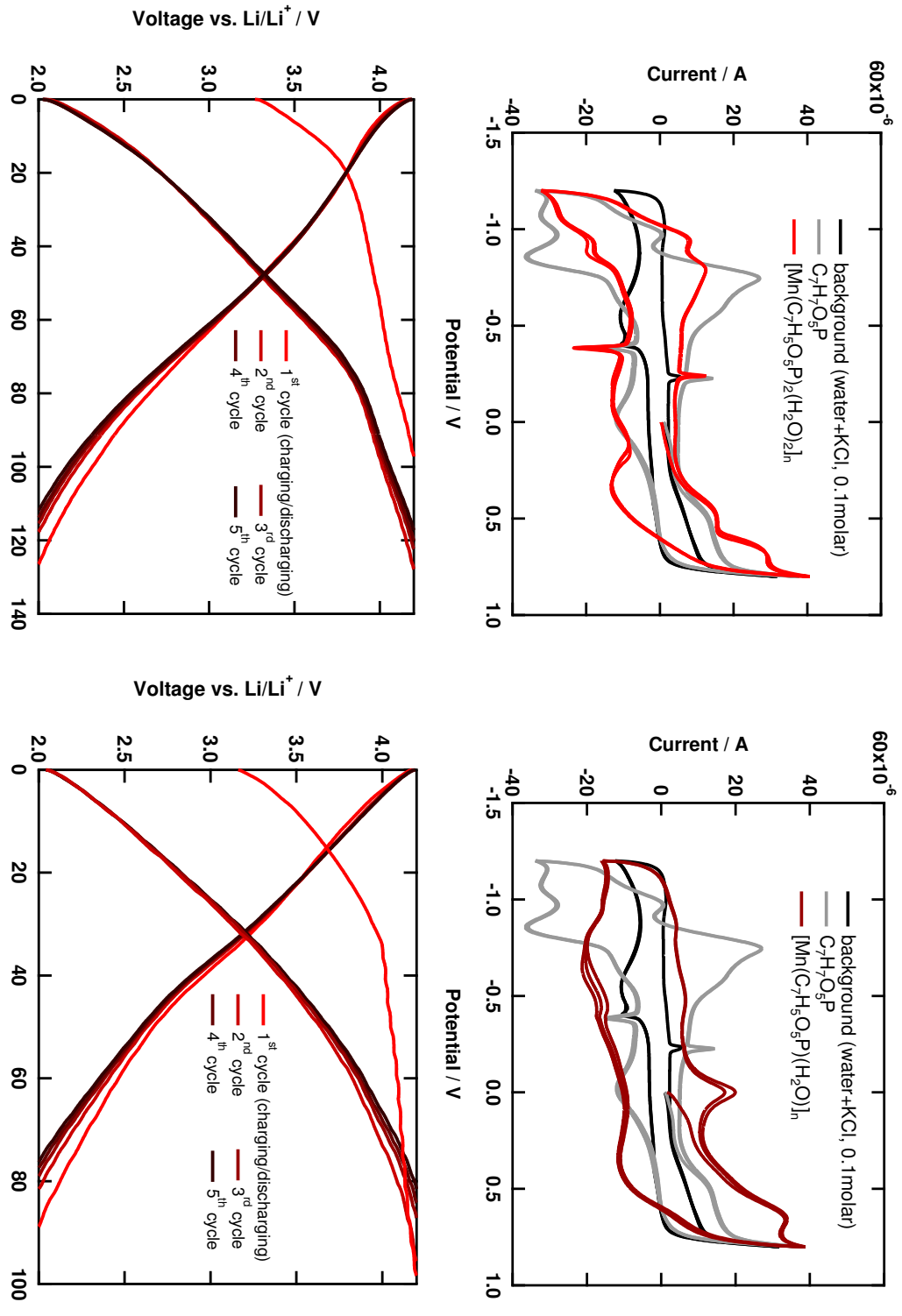

Figure 2.7: top: cyclovoltametry in water/KCl solution of $[Mn(HOOCC_6H_4PO_3H)_2(H_2O)_2]_n$ (left) and $[Mn(HOOCC_6H_4PO_3)(H_2O)]_n$ (right); bottom: battery measurement (five charging/discharging cycles of $[Mn(HOOCC_6H_4PO_3H)_2(H_2O)_2]_n$ (left) and $[Mn(HOOCC_6H_4PO_3)(H_2O)]_n$ (right)

$[Mn(HOOCC_6H_4PO_3H)_2(H_2O)_2]_n$ and 98 Ah/kg for the two-dimensional layered compound $[Mn(HOOCC_6H_4PO_3)(H_2O)]_n$ are in a good agreement with the experimental values 110 Ah/kg for $[Mn(HOOCC_6H_4PO_3H)_2(H_2O)_2]_n$ (clearly a two electron process) and 80 Ah/kg for $[Mn(HOOCC_6H_4PO_3)(H_2O)]_n$ (just a one electron process). Obviously the whole redox-process takes place at the ligand, the applied voltage is not high enough to oxidize/reduce the manganese(II) ions in these compounds. Nevertheless, the cycle reproducibility is good. However, the capacity is too low to be of any industrial interest.

2.1.4.2 A Cobalt Chain build of para-Phosphonbenzoic Acid and Water displaying a Spin-Flop behaviour

In figure 2.8, a part of the crystal structure of the one-dimensional chain compound $[Co(para\text{-}HOOCC_6H_4PO_3H)_2(H_2O)]_n$ **(10)** is shown. The metal to ligand ratio in this compound is one to two and again, as in the one-dimensional manganese chain compound presented before, the ligand, in this case the para-phosphonbenzoic acid, is not fully deprotonated and a hydrogenphosphonate is obtained. One water molecule is additionally bridging two cobalt(II) ions. Compared to the one-dimensional manganese chain compound with the meta phosphonbenzoic acid as ligand, the linkage of the metal-oxygen octahedra is completely different. Here a uniform linear chain is obtained with just μ_2-bridging hydrogenphosphonate ligands and the water molecules are not only completing the coordination sphere, they also link the cobalt(II) ions, so that a triple-bridge is established. The resulting chains of $[Co(para\text{-}HOOCC_6H_4PO_3H)_2(H_2O)]_n$ run in the c-direction, the cobalt-cobalt distances between two chains along the a-direction are 19.6 Å, the ones along the b-direction are 6.0 Å as can be seen at the bottom of figure 2.8. The one-dimensional chain structure is further stabilised by hydrogen bonding of the carboxilic acid groups of adjacent chains (in the a direction) and hydrogen bonding of the one time protonated hydrogenphosphonate groups of adjacent chains (in the b direction) into a three-dimensional network.

With the discovery of homometallic canted antiferromagnetic chains that can display single chain magnetic (SCM) behaviour [87], the interest in uniform chains build of phosphonate ligands increases. The requirements needed to observe a SCM behaviour consist generally in a strong easy axis anisotropy and strong intra-chain interactions with negligible interchain ones. This results in a slow dynamics of the magnetisation out of the thermal equilibrium of pure one-dimensional char-

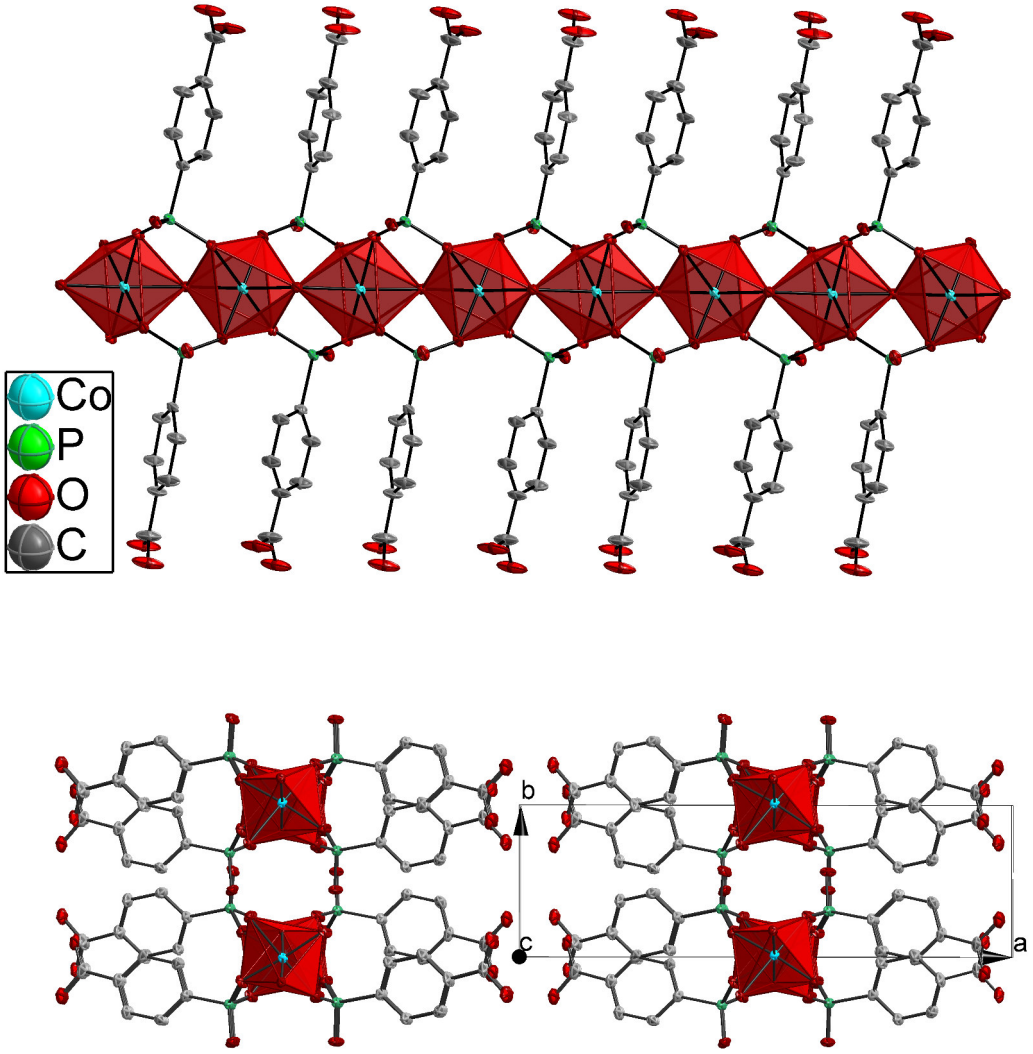

Figure 2.8: top: Part of the crystal structure of $[Co(para\text{-}HOOCC_6H_4PO_3H)_2(H_2O)]_n$ **(10)**, linear and uniform chain motive with just μ_2-bridging hydrogenphosphonate ligands; bottom: Packing of the chains in the ab-crystal plane by hydrogen bonding of the carboxilic acid groups

acter with no evidence of a three-dimensional magnetic order. The spin dynamics is driven by thermal activated jumps of the spin orientations, described in first approximation by the model developed in the sixties by Glauber [41]. The kind of interaction does not play a significant role as long as a ground state unequal zero is realised. So ferromagnetic interactions, relying on the orthogonality of the magnetic orbitals of the interacting building blocks, are in general significantly weaker and less common than antiferromagnetic ones [4]. The latter have been exploited in the case of interactions between different spins to yield ferrimagnetic

SCM, like the first example of a SCM a cobalt(II) nitronyl-nitroxide radical chain with the formula [Co(hfac)$_2$(NITPhOMe)] [42]. Antiferromagnetic interactions between the same spin carriers in principle can also be exploited to give SCM, provided that magnetic anisotropy is present and the easy axes are not collinear. Two structural quite similar examples to the here presented cobalt(II) chain compound [Co(para-HOOCC$_6$H$_4$PO$_3$H)$_2$(H$_2$O)]$_n$ can be found in the literature, which both exhibit SCM behaviour. The first one is a homometallic manganese(III) uniform chain, where manganese(III) tetraphenylporphyrin units are connected by phenylphosphinic acid (which is structural quite similar to a hydrogenphosphonate ligand) [45]. The second example is a cobalt(II) diphosphonate compound which has a one-dimensional zigzag-structure [88].

[Co(para-HOOCC$_6$H$_4$PO$_3$H)$_2$(H$_2$O)]$_n$ is a homometallic canted antiferromagnetic chain compound consisting of highly anisotropic cobalt(II) ions. However, it does not fulfill all requirements for a SCM as can be seen in the different measurements shown in figures 2.9 and 2.10. Whereas the temperature dependence of the magnetic susceptibility measured at different fields looks quite promising in the χ_mT vs. T and the χ_m^{-1} vs. T plot, showing clearly some canted antiferromagnetic behaviour, already the heat capacity measurement shown in the inset reveals that a three-dimensional ordering occurs at low temperatures. The phase transition is confirmed by the field dependent measurements of the magnetisation, also shown in figure 2.9. A non-zero ground state is established below the phase transition temperature due to the canting of the spins. Even a hysteresis with a small coercive field of 10 Oe and a remanence of 0.13 μ_B could be found at 1.8 K. In consequence the dynamic magnetic susceptibilities shown in figure 2.10 also don't show the typical large shift in temperature depending on the applied wave frequency of the maxima of the in-phase signal χ' and the out-of-phase signal χ''. Especially clear is the Argand-plot shown in the inset, where the absence of one relaxation process is visualised. A possible explanation for the small shift in temperature depending on the applied wave frequency of both maxima can be fluctuations of the boundaries of the Weiss regions present in weak ferromagnets in general.

To clearify the magnetic behaviour of the compound [Co(para-HOOCC$_6$H$_4$PO$_3$H)$_2$(H$_2$O)]$_n$ in detail, single crystal magnetic measurements were carried out during the internship in the group of Prof. A. in Nagoya (Japan). One indexed single crystal was mounted in two different orientations during the measurements as can be seen in figure 2.11. For reasons of practical realisation the monoclinic crystal system with an angle β of 93.2° was assumed to be an orthorhombic one with three

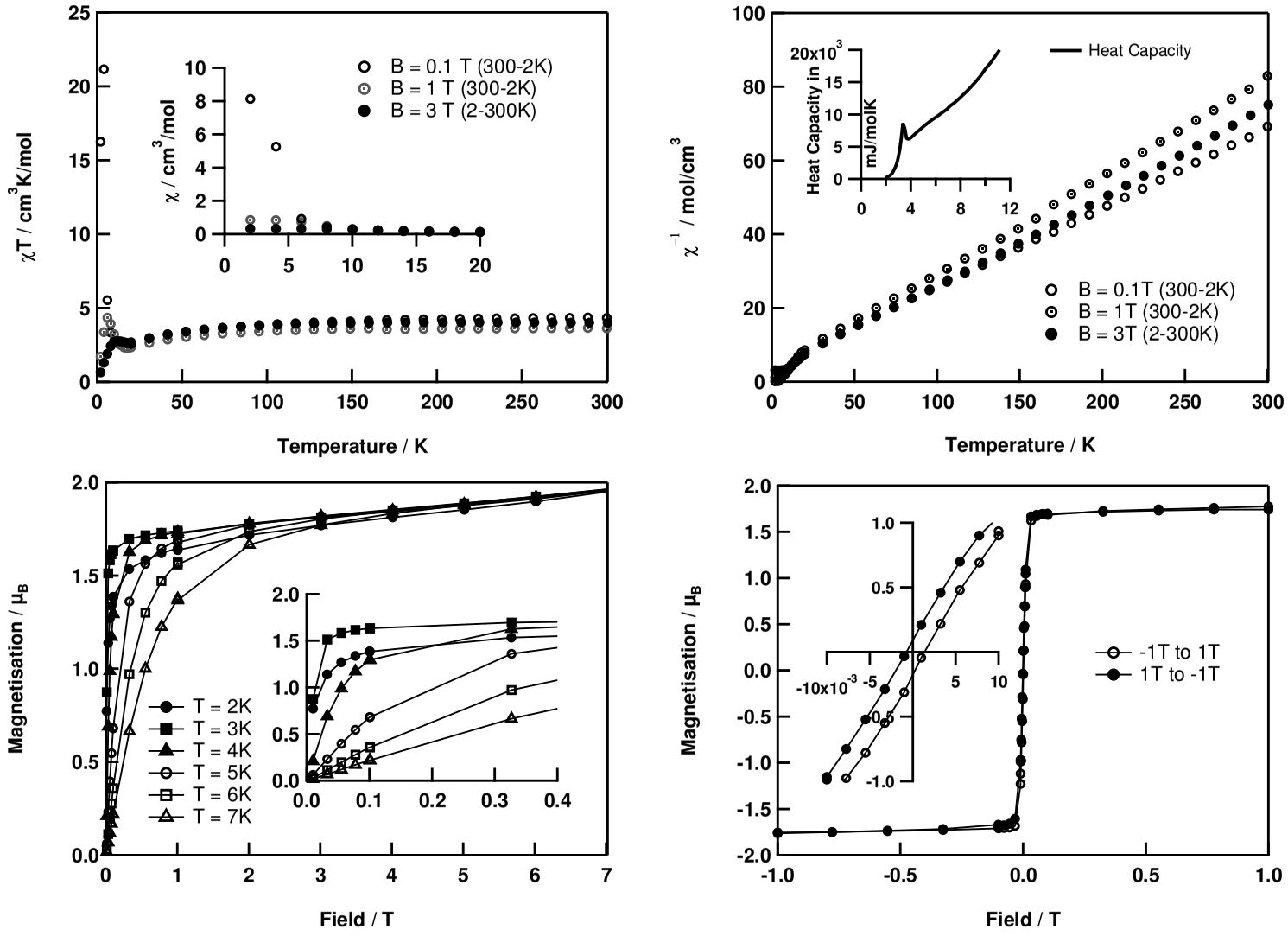

Figure 2.9: Temperature dependence of the magnetic susceptibility of $[Co(para\text{-}HOOCC_6H_4PO_3H)_2(H_2O)]_n$ **(10)** measured at different fields normalized to one cobalt ion is shown as χ_mT vs. T and χ_m vs. T plots (top left) as well as χ_m^{-1} vs. T (top right), inset shows heat capacity; field dependence of the magnetisation is shown at the bottom left and a small hystereses is obtained at T = 1.8 K as can be seen at the bottom right

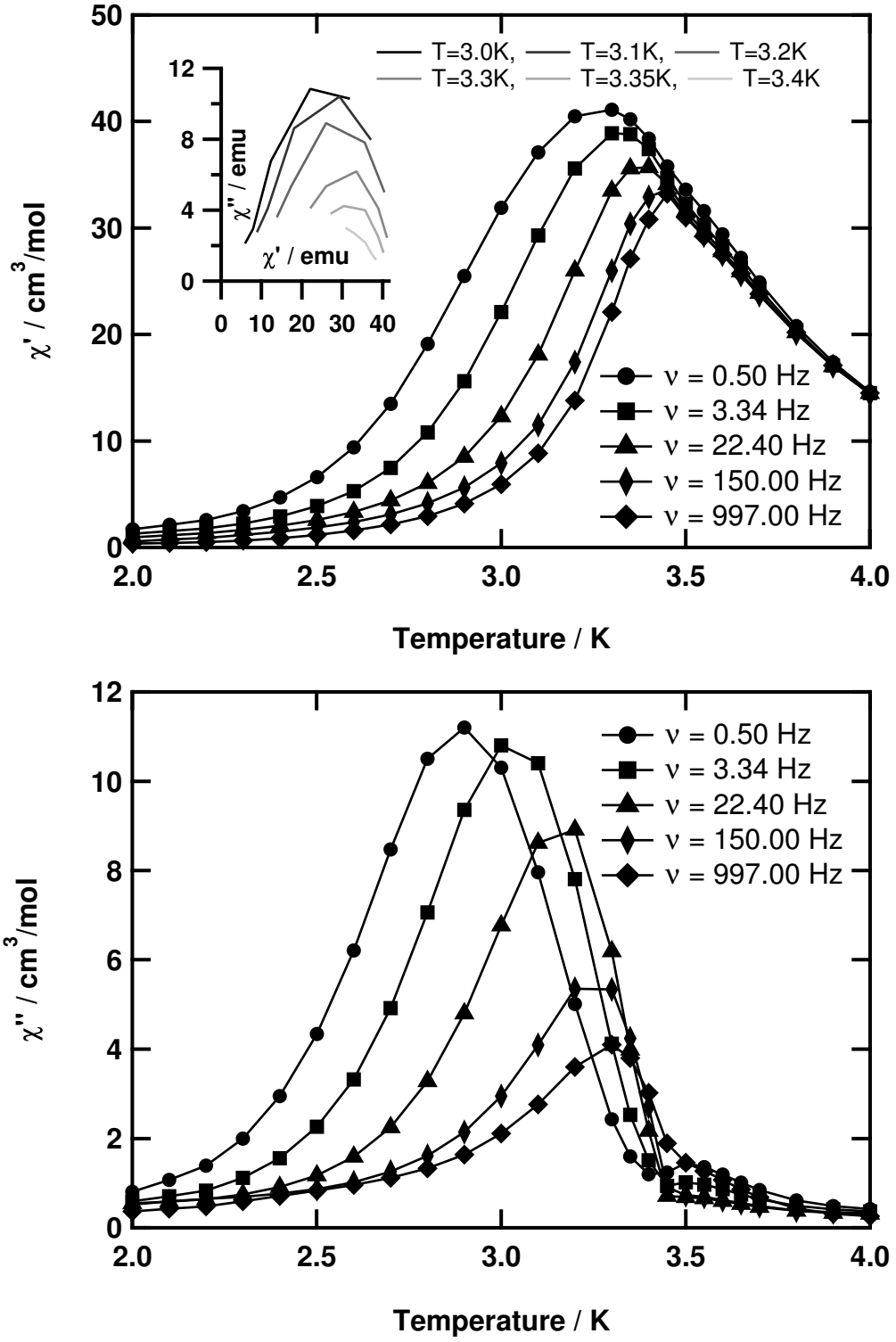

Figure 2.10: Temperature dependence of the dynamic magnetic susceptibility of $[Co(para\text{-}HOOCC_6H_4PO_3H)_2(H_2O)]_n$ **(10)** measured with a static field of 3Oe; top: in-phase signal, inset shows Argand-plot; bottom: out-of-phase signal

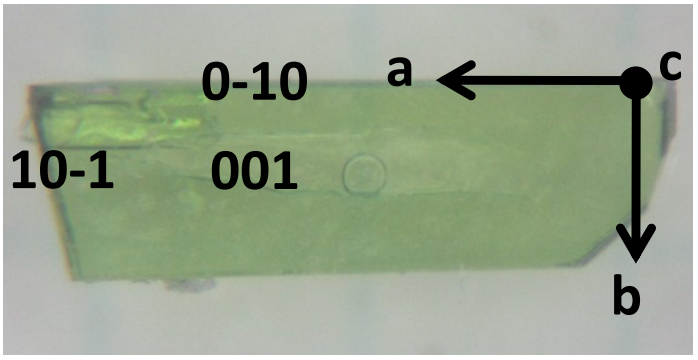

Figure 2.11: Indexed single crystal of [Co(para-$HOOCC_6H_4PO_3H)_2$ $(H_2O)]_n$ which was investigated in the single crystal magentic measurement; for the magnetic measurement the monoclinic crystal system with an angle β of 93.2° was assumed to be orthorhombic for reasons of simplification; two orientations were realised, the first one was a turn around the crystallographic axis a, the second one was a turn around the crystallographic axis b

90° angles. The same temperature dependence for χ_m can be found in the powder measurement shown in the inset of figure 2.9, χ_m is decreasing with increasing temperature. Also the values obtained for χ_m in the single crystal measurements matches the powder measurement which should be the average value of all orientations, what shows that the measurements of the SQUID is precise even when the mass of the sample is quite low (below 0.1 mg).

The first orientation was a turn around the crystallographic axis a, the result of the rotation dependent measurements is shown at the top of figure 2.12. Cleary the anisotropy of the system at low temperatures can be seen with the appearance of a hard axis (maxima occuring at 156° and 336°) and an easy axis (minima occuring at 66° and 246°), for an isotropic system no rotation dependence of χ_m would be expected. A rotation symmetry is retained, that means that values of the rotation angles and the rotation angles + 180° are the same. As a prerequiste an orthorhombic crystal system was assumed due to the fact that the β angle of the monoclinic crystal system is quite close to 90°, this assumption can be approved by the fact that the magnetic axis are also perpendicular to each other. The second orientation was a turn around the crystallographic axis b, the result of the rotation dependent measurements is shown at the bottom of figure 2.12. Again the anisotropy of the system can be seen, although it is by far less compared to the first orientation. This can be understood by the fact that the measurement was carried out perpendicular to the hard axis, so that just the difference between the intermediate axis (maxima at 138° and 318°) and the easy axis again is depicted.

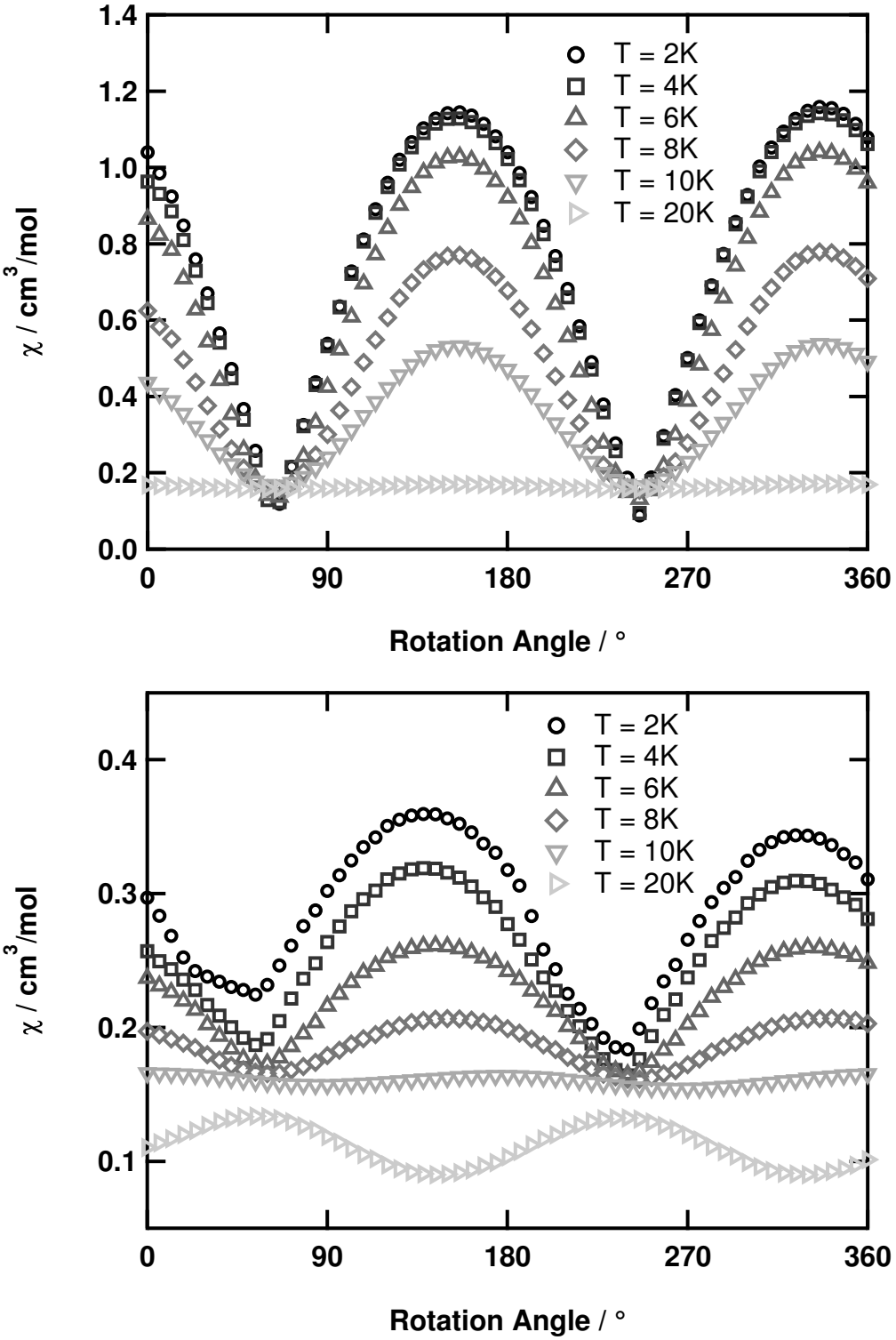

Figure 2.12: Rotation dependence of the magnetic susceptibility of [Co(para-$HOOCC_6H_4PO_3H)_2(H_2O)]_n$ **(10)** measured with a static field of 1T; top: single crystal was so oriented that the turn is around the crystal axis a; bottom: single crystal was so oriented that the turn is around the crystal axis b

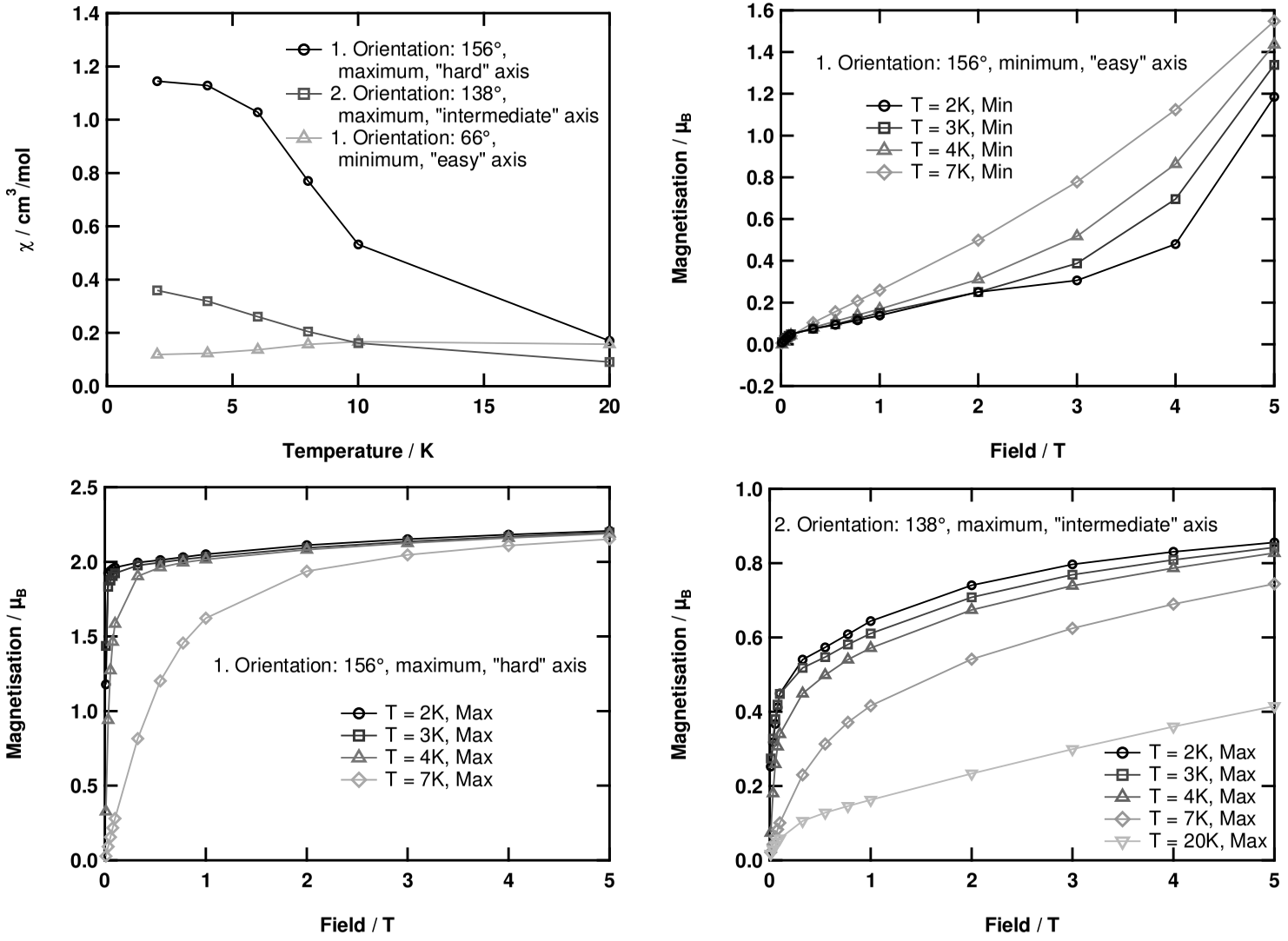

Figure 2.13: top left: Temperature dependence of the magnetic susceptibility of $[Co(para\text{-}HOOCC_6H_4PO_3H)_2(H_2O)]_n$ **(10)** at specified orientations of the rotation dependent measurements shown in figure 2.12 is shown; furthermore field dependence of the magnetisation is measured at different temperatures; top right: measurements of the first orientation (turn around a) at the easy axis (mimimum in χ_m); bottom left: hard axis (maximum in χ_m); bottom right: measurement of the second orientation (turn around b) at the intermediate axis (maximum in χ_m); lines are only guidance for the eyes

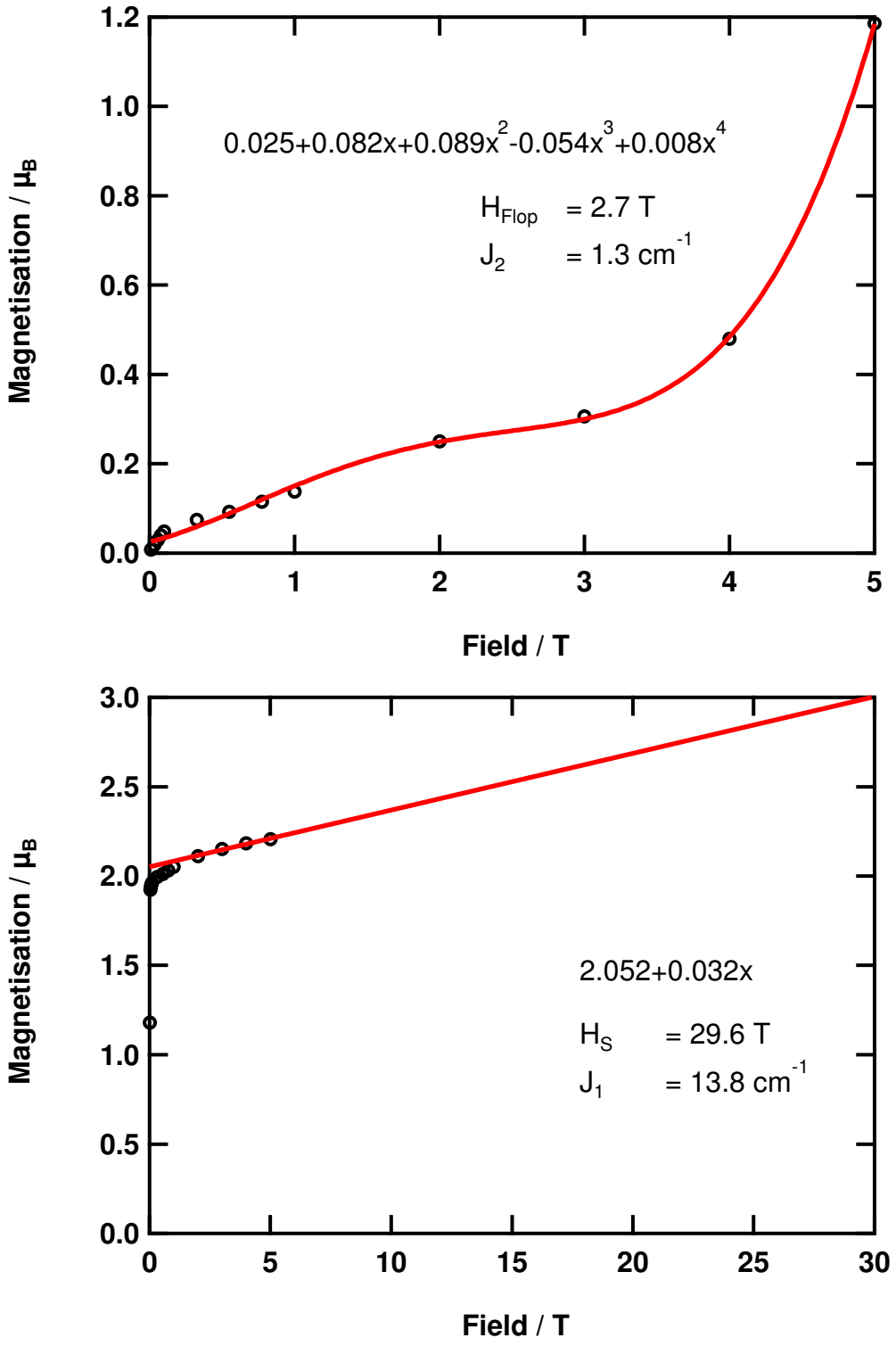

Figure 2.14: Field dependence of the magnetisation of [Co(para-$HOOCC_6H_4PO_3H)_2(H_2O)]_n$ **(10)** is measured at 2K, top: measurement of the easy axis, spin-flop field is determined out of the inflexion point of the polynom used to simulate the measured data points, assumption for the interchain interaction possible; bottom: measurement of the hard axis, saturation value of the magnetisation is extrapolated, assumption for the intrachain interaction and the canting angle possible

In figure 2.13, the temperature dependence of the magnetic susceptibility of [Co(para-$HOOCC_6H_4PO_3H)_2(H_2O)]_n$ **(10)** at specified orientations of the rotation dependent measurements is shown. A typicial behaviour of an antiferromagnet is obtained, where below the Neel temperature the magnetic susceptibilities of the different orientations show different temperature dependences. The termed "hard" axis is oriented perpendicular to the preferred antiferromagnetic ordering, therefore the magnetic susceptibility has the largest value. In contrast the termed "easy" axis is oriented parallel to the preferred antiferromagnetic ordering, therefore the magnetic susceptibility has the lowest value. The experimentally determined magnetic axes are perpendicular to each other (in the scope of the experiment), but do not coincide with the crystallographic axes, what is expected for the monoclinic crystal system [89].

Field dependent measurements of the magnetisation taken at the position specified before (maximum and minimum first orientation, maximum second orientation) reveal the nature of the magnetic behaviour at low temperatures, as can be seen in figure 2.13. The magnetisation measured at low temperatures in the easy axis is not linear with the field, even a discontinuity is observed. This is a clear sign for a spin-flop behaviour which is typical for three-dimensional ordered canted antiferromagnets with some anisotropy. A spin-flop can occur when the system is in the antiferromagnetic state, i.e. at $T < T_N$, and the external field is applied parallel to the preferred easy axis. When the external field reaches a critical value, the moments flop perpendicular to the applied field remaining in the canted state. This is then the thermodynamically favoured state, and the transition is first order. The discontinuity seen in the magnetisation (net alignment of spins) is the crossing of the antiferromagnet-spin-flop phase boundary [81]. As a prerequiste the canting angle α, defined as $\alpha = M_W/M_S$ [4] with M_W being the magnetisation value in weak field and M_S being the saturation value of magnetisation, has to be larger than 45° for a spin-flop behaviour. The saturation value of magnetisation M_S can be calculated, one formula unit of [Co(para-$HOOCC_6H_4PO_3H)_2(H_2O)]_n$ comprises one cobalt(II) ion in the high-spin state with three unpaired electrons, so with an assumed g-value of 2.0 the saturation value of magnetisation is predicted to be $M_S = 3.0\ \mu_B$. The extrapolation of the field dependence of the magnetisation measured at the hard axis of [Co(para-$HOOCC_6H_4PO_3H)_2(H_2O)]_n$ at T = 2 K shown at the bottom of figure 2.14, gives $M_W = 2.05\ \mu_B$ and $M_S = 3.0\ \mu_B$ (due to theory for one cobalt) and a value of $\alpha = 43°$. Taking into account that the determined magnetic axis do not coincide with the crystallographic axis and that the values of the measured axis are still projections on the ac-/bc-crystal plane, the

value of α is still in a good agreement with the theory for a spin-flop behaviour. Furthermore, also the value of the intrachain interaction $|J_1| = 13.8$ cm^{-1} can be estimated of the saturation field of the magnetisation, $H_S = 29.6$ T. Also a value of the interchain interaction $|J_2| = 1.3$ cm^{-1} can be estimated of the magnetisation measurement of the hard axis shown at the top of figure 2.14, where the flop field is determined $H_F = 2.7$ T. The quite low ratio of $|J_1|/|J_2| \approx 10$, compared to single chain magnets where this ratio is larger than 1000, can be explained by the fact that the separation of the chains in the solid-state is not perfect as already shown in figure 2.8 on page 34. Probably by increasing the interchain distances the phase transition to a three-dimensional order can be suppressed and a single chain magnet can be obtained quite similar to the reported manganese(III) phosphite chain [45].

In cooperation with T. G. and V. K. of the group of Prof. F., also University of Mainz, the pressure dependent behaviour of the magnetic susceptibility of [Co(para-$HOOCC_6H_4PO_3H)_2$ was investigated. A homemade pressure cell, using silicon oil as pressure-transmitting medium, was used. The cell has the following characteristics: weight: 8 g, range of pressure 0-1.3 GPa, accuracy ≈0.025 GPa, and nonhydrostaticity less than 0.05 GPa. Cylindrically shaped sample dimensions are 1 mm in diameter and 5-7 mm in length. Here, the applied pressure was not calibrated using the transition temperature of superconducting tin of purity 0.9999, because the transition temperature is too close to the phase transition temperature of 3.5 K observed in [Co(para-$HOOCC_6H_4PO_3H)_2(H_2O)]_n$.

The overall magnetic behaviour seems not to be strongly influenced by the applied pressure as shown in figure 2.15. Still the canted antiferromagnetic chain compound orders at low temperatures as can be seen in the magnetisation measurements with a non-zero ground state realised at low temperatures and low fields. In contrast to the magnetisation measurements of the powdered sample without any pressure applied (shown in figure 2.9 on page 36), here the magnetisation measurements also show the influence of the spin-flop transition by the occurence of a discontinuity at low temperatures in figure 2.15. Due to the preparation procedure in the pressure cell, the powdered sample does not have the possibility to reorientate when an external field is applied, so that in contrast to the magnetisation measurement shown before, here the real isotropic behaviour is measured (average value of all orientation). Again, as in the single crystal measurements, the spin-flop field can be determined out of the inflexion point of a polynominal fit of the measured data at T = 2 K and thus an assumption of the interchain in-

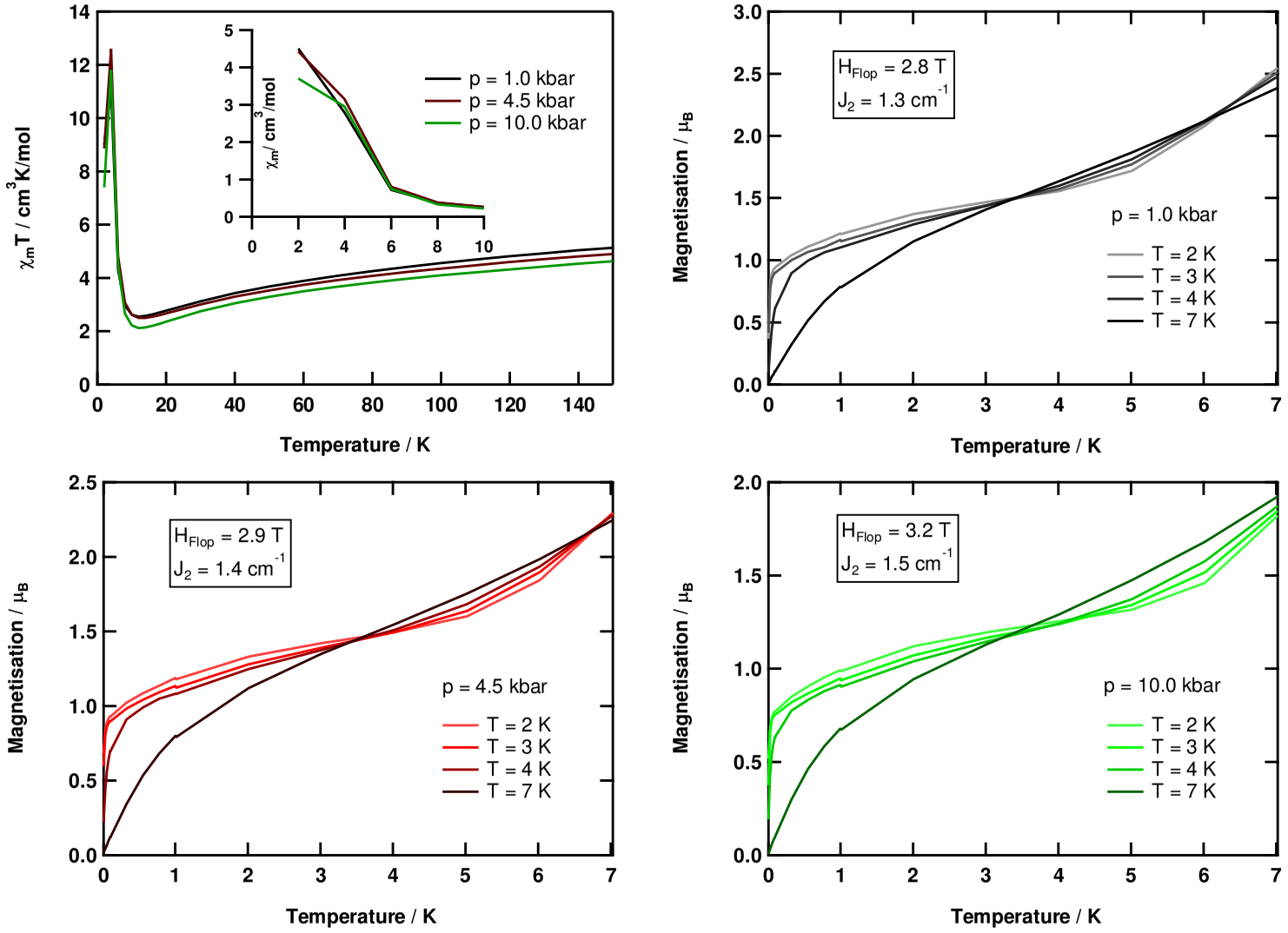

Figure 2.15: Temperature dependence of the magnetic susceptibility of $[Co(para\text{-}HOOCC_6H_4PO_3H)_2(H_2O)]_n$ **(10)** measured at B = 0.1 T and different applied pressures normalized to one cobalt ion is shown as $\chi_m T$ vs. T and χ_m vs. T plots (top left); field dependence of the magnetisation measured at different applied pressures; top right: p = 1 kbar, bottom left: p = 4.5 kbar, bottom right: p = 10 kbar; spin-flop field is determined out of the inflexion point of a polynom used to simulate the measured data points at T = 2 K, assumption for the interchain interaction possible

teraction $|J_2|$ can be made. By increasing the pressure in the cell, the interchain interaction increases as well as expected by the simple picture that the shorter the distances, the larger the magnetic interactions are. But overall the observed effect is small.

Summing up the two presented one-dimensional chain compounds [Mn(meta-$HOOCC_6H_4PO_3H)_2(H_2O)_2]_n$ **(9)** and [Co(para-$HOOCC_6H_4PO_3H)_2(H_2O)]_n$ **(10)**: It is remarkable that although the two compounds are built of quite similar single deprotonated phosphonbenzoic acid ligands, the linkage of the metal-oxygen octahedra is so different. The difference in the substitution pattern of the phosphonbenzoic acid determines the overall packing in the crystal structure and in consequence the magnetic behaviour, whereas the control of the pH-value in the reaction media ensures that the obtained compound is in all cases one-dimensional.

2.1.5 2 D - Layered Structures: Two Modifications depending on the used Ligand

2.1.5.1 First Modification: Corner-Sharing Metal-Oxygen Octahedra

In figure 2.16 a typicial example of a divalent metal phosphonate compound with the general formula $[M(RPO_3)(H_2O)]_n$ is shown. With M being cobalt and R being a simple phenylring, $[Co(C_6H_5PO_3)(H_2O)]_n$ displays a layered crystal structure similar to the purely inorganic ternary metal phosphates M'M"PO_4*H_2O with M' being K^+ or NH_4^+ and M" being Mn^{2+}, Fe^{2+}, Co^{2+} or Ni^{2+}. For monophosphonate compounds, especially with a rigid aromatic backbone like the phenylring, such a two-dimensional layered structure seems to be favourable [29]. The crystal structure of $[Co(C_6H_5PO_3)(H_2O)]_n$ (taken from references [30, 31]) consists of inorganic layers of CoO_6 octahedra,which corner-share via oxygens into a continuous sheet as can be seen at the bottom of figure 2.16. Each of these in-plane oxygens (four for each octahedron) also bound to one phosphorus, and are therefore triply-bridging. Since each CoO_6 octahedron connects to four octahedra and four phosphonates, the metal to ligand ratio is 1:1 as reflected in the formula of the compound. The fifth and sixth vertices of the CoO_6 octahedra are occupied by two out-of-plane oxygens. One is a terminal water molecule involved in an intralayer hydrogen bond, while the other is a doubly-bridging oxygen that also connects to a phosphorus centre. Overall the symmetry of the CoO_6 octahedra is highly distorted and the resulting layers are kinked or crenellated. The phospho-

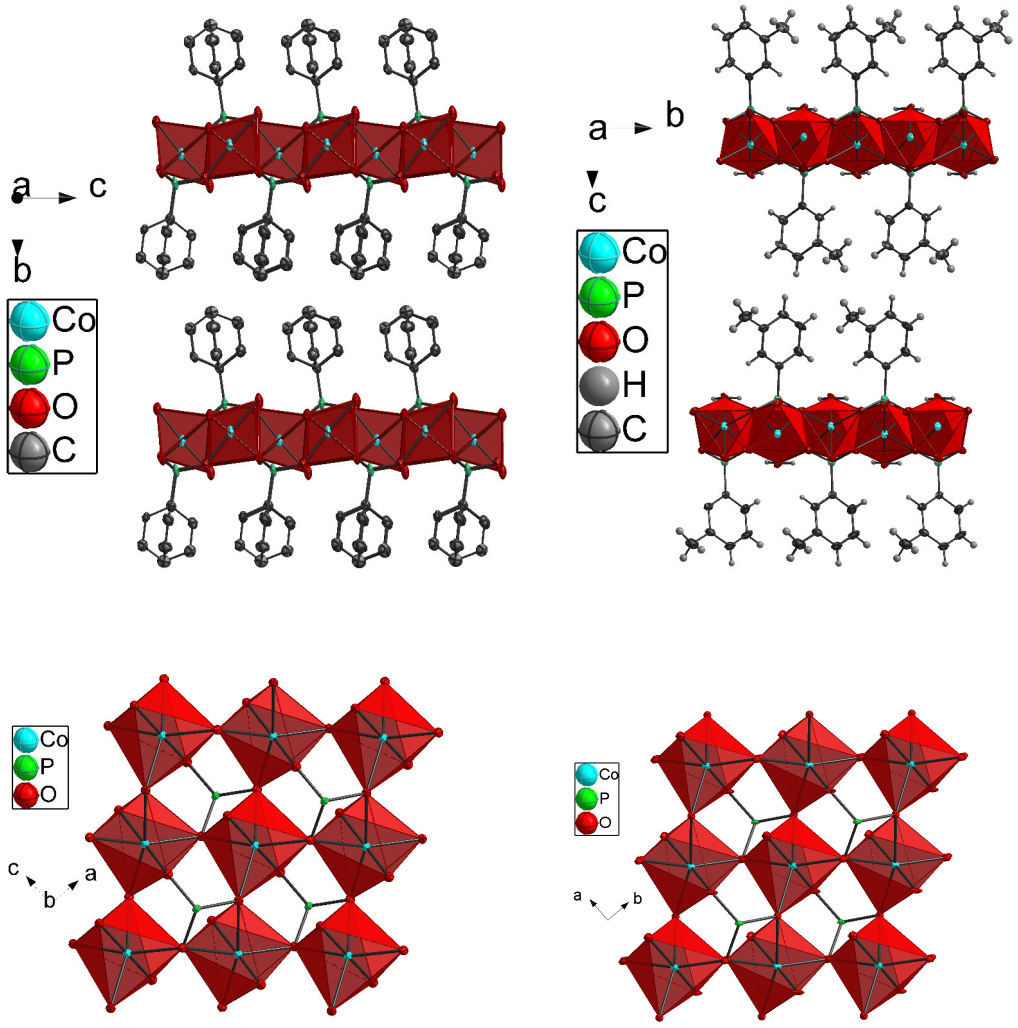

Figure 2.16: top: Part of the crystal structure of $[Co(C_6H_5PO_3)(H_2O)]_n$ (left, taken from references [30, 31]) and $[Co(H_3CC_6H_4PO_3)(H_2O)]_n$ (right); bottom: Cut-out of the inorganic metal-oxygen part of $[Co(C_6H_5PO_3)(H_2O)]_n$ (left) and $[Co(H_3CC_6H_4PO_3)(H_2O)]_n$ (right), a layer of corner-sharing octahedra is decorated above and below the plane with phosphonate groups

nates cap the layers alternately above and below the plane of the layer as can be seen at the top of figure 2.16. As for other metal phenylphosphonates, the phenyl rings point into the interlayer space, defining a hydrophobic bilayer region. Furthermore, it has been found that the phenyl rings are disordered between two orientations. The compound crystallizes in the orthorhombic space group $Pmn2_1$, which is also typical for divalent metal phenylphosphonate compounds as can be seen in table 2.2. As two-dimensional inorganic hybrid materials, divalent metal phenylphosphonate compounds contain interesting examples of magnetic materials. They are paramagnetic at room temperature and on cooling, they show long-range magnetic ordering. In some members of the isostructural series of

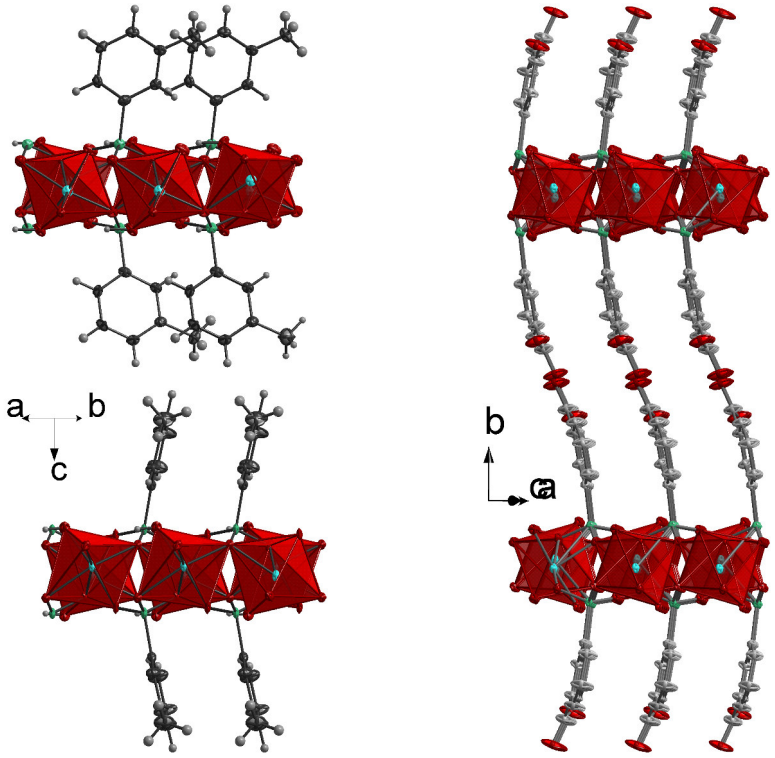

Figure 2.17: Comparison of the orientation of the π-π-stacking; left: $[Co(CH_3C_6H_4PO_3)(H_2O)]_n$, although two orientations of the π-π-stacking are observed, the distance between adjacent phenyl rings is the same with 4.802(5) Å; right: $[Co(HOOCC_6H_4PO_3)(H_2O)]_n$, just one orientation of the π-π-stacking is observed, the distance between adjacent phenyl rings is 5.672(3) Å

$[M(C_6H_5PO_3)(H_2O)]_n$ (M = Mn [28], Fe [34], Co [31], Ni [33]) the phenomenon of canted antiferromagnetism or weak ferromagnetism is observed.

As shown with the later introduced iron-formiate sheet structure $[Fe^{II}_2Fe^{III}_2(HCOO)_{10}(\gamma\text{-}C_6H_7N)_6]_n$, the orientation in a π-π-stacked system can be crucial for the magnetic behaviour of a compound. In the latter case, the π-systems of the γ-picoline residues of two adjacent layers overlapped with distances between 3.8 and 4.9 Å as can be seen in figure 2.41 on page 92. In $[Co(C_6H_5PO_3)(H_2O)]_n$ the phenyl rings are disordered between two orientations with a distance of 4.84 Å in the one orientation (π-π-stacking along c) and 5.61 Å in the other direction (π-π-stacking along a). Both π-π-stackings are within a layer, no overlapp between two adjacent layers can be observed. Due to the newly introduced methyl group in the tolylphosphonic acid, the rotation of the phenyl rings in the $[Co(CH_3C_6H_4PO_3)(H_2O)]_n$ compounds **(11a)** and **(11b)** should be hindered. Unfortunately no single crystal

structure of $[Co(para\text{-}CH_3C_6H_4PO_3)(H_2O)]_n$ could be obtained, but the simulation of the powder diffraction data suggest that the compound also crystallizes in the space group $Pmn2_1$, which is typical for all divalent phenylphosphonate compounds, with a significant longer b-axes due to the newly introduced methylgroup causing a larger interlayer distance. The quality of the powder data is not good, so that just hints for this structural model could be obtained (figure 5.64, page 250).

In the crystal structure of $[Co(meta\text{-}CH_3C_6H_4PO_3)(H_2O)]_n$ shown in figure 2.16, the rotation of the phenyl rings is no longer possible due to the sterical hindrance of the methyl group. A π-π-stacking is still possible in $[Co(meta\text{-}CH_3C_6H_4PO_3)(H_2O)]_n$ and as well as in the phenylphosphonate compound two directions of π-π-stacking are observed. But in one layer the π-π-stacking is only in one direction, which also seems responsible for the changed space group (comparison in table 2.2). The result is that adjacent layers have their π-π-systems oriented perpendicular to each other, so that still no π-π-stacking between two layers is possible as shown in figure 2.17 on the left side. The distance between the phenyl rings of one layer is independently of the orientation 4.802(5) Å. The right side of figure 2.17 displays a similar view on the cobalt phosphonate compound with the meta-phosphonbenzoic acid derivate with the formula $[Co(meta\text{-}HOOCC_6H_4PO_3)(H_2O)]_n$. Due to the carboxilic group in meta-position, which is still protonated, the phenylrings are also not able to rotate, because they are fixed by hydrogen-bridges between carboxilic groups of adjacent layers. Again no overlapp of two adjacent layers is possible. Here just one orientation of the π-π-stacking is observed, with a distance of 5.672(3) Å between the phenyl rings of one layer. By taking a closer look on the distances between the phenyl rings of one layer in all three cobalt phenylphosphonate derivates, it is remarkable that the two distances observed in the phenylphosphonate compound (4.84 and 5.61 Å) can be found again in the two derivates of the cobalt phenylphosphonate compounds (4.802 Å in $[Co(meta\text{-}CH_3C_6H_4PO_3)(H_2O)]_n$ and 5.672(3) in $[Co(meta\text{-}HOOCC_6H_4PO_3)(H_2O)]_n$). The size of the substituent seems to be critical for the orientation of the π-π-stacking. Furthermore the crystallisation of metal phenylphosphonate derivate compounds with the right size for one or the other π-π-stacking seems to be favourable. Compared to the iron-formiate sheet structure $[Fe^{II}_2Fe^{III}_2(HCOO)_{10}(\gamma\text{-}C_6H_7N)_6]_n$, where two distances between the γ-picoline rings in one layer are observed, here in the phenylphosphonate derivate compounds just one distance is realized, probably they are too rigid to allow a rotation.

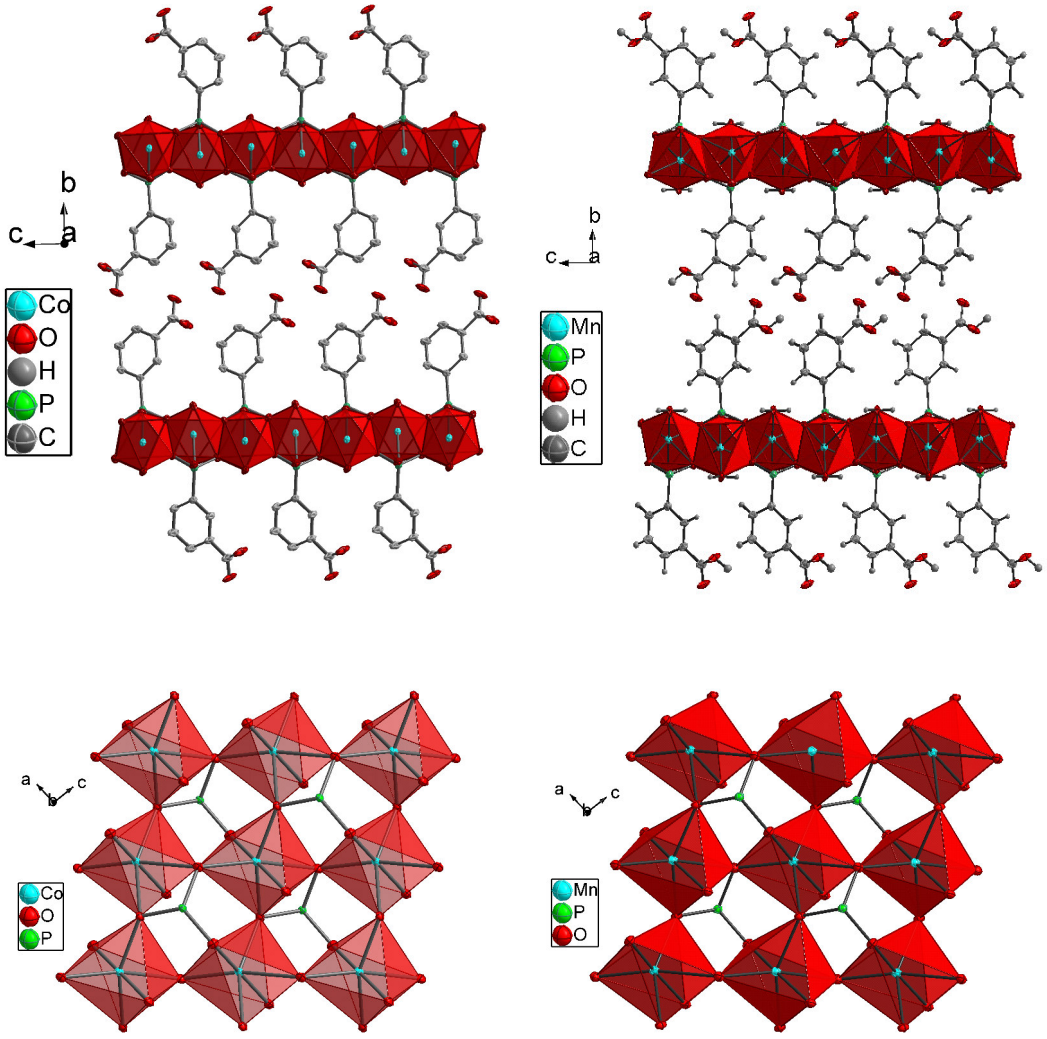

Figure 2.18: top: Part of the crystal structure of $[M(HOOCC_6H_4PO_3)(H_2O)]_n$ with M=Co (left) and M=Mn (right); bottom: Cut-out of the inorganic metal-oxygen part of $[M(HOOCC_6H_4PO_3)(H_2O)]_n$ with M=Co (left) and M=Mn (right), a layer of corner-sharing octahedra is decorated above and below the plane with phosphonate groups

In figure 2.18 again a part of the crystal structure of $[M(meta\text{-}HOOCC_6H_4PO_3)(H_2O)]_n$ is shown with M = Co on the left site and M = Mn on the right site. For M being nickel, no single crystal structure was obtained, but the prove of an isostructural compound was done by powder diffraction data (LeBay-Fit with the starting parameters of the cobalt compound, Figure 5.69 on page 256). A summary of the cell parameters can be found in table 2.3. The similarity of the inorganic metal-oxygen part shown at the bottom of figure 2.18 to the already introduced metal phenylphosphonate structures is obvious. That is why also the magnetic behaviour of these compounds namely $[Co(CH_3C_6H_4PO_3)(H_2O)]_n$ (meta and para

derivate) and [Co(meta-$HOOCC_6H_4PO_3$)$(H_2O)]_n$ are expected to be quite similar to [Co($C_6H_5PO_3$)$(H_2O)]_n$, whereas [Mn(meta-$HOOCC_6H_4PO_3$)$(H_2O)]_n$ is expected to be similar to [Mn($C_6H_5PO_3$)$(H_2O)]_n$ and [Ni(meta-$HOOCC_6H_4PO_3$) $(H_2O)]_n$ is expected to be similar to [Ni($C_6H_5PO_3$)$(H_2O)]_n$. In figures 2.19 and 2.20, the magnetic susceptibility measurements of all five compounds are shown as χ^{-1} vs. T plot (measured with a field of B = 1 T) and the Curie-law is applied. In figure 2.19, the three cobalt compounds are shown, in figure 2.20 the [M(meta-$HOOCC_6H_4PO_3$)$(H_2O)]_n$ derivates with M = Mn, Co, Ni are displayed. The simulation results are listed again in tables 2.2 and 2.3. As known from literature, the phenomenon of canted antiferromagnetism or weak ferromagnetism is observed in some members of the isostructural series of [M($C_6H_5PO_3$)$(H_2O)]_n$ (M = Mn [28], Fe [34], Co [31], Ni [33]). The five compounds were also investigated in zero-field cooled (ZFC) and field cooled (FC) measurements with an applied field of B = 0.01 T, the results are also displayed in figure 2.19 for the two [Co($CH_3C_6H_4PO_3$)$(H_2O)]_n$ compounds and in figure 2.20 for the [M(meta-$HOOCC_6H_4PO_3$)$(H_2O)]_n$ derivates with M = Mn, Co, Ni.

As shown in table 2.3, the temperatures where the canted antiferromagnetic behaviour occurs depends mainly on the used metal ion. For the cobalt compounds, shown in table 2.3, the temperature is quite low with 4 K, whereas it is not clear in the literature if the cobalt phenylphosphonate compounds shows a long-range ordering or not [31, 33], but the reported value for the temperature is 4K. In figure 2.19 the differences of the field cooled (FC) measurements and the zero-field cooled (ZFC) measurements are shown for the [Co($CH_3C_6H_4PO_3$)$(H_2O)]_n$ compounds and in the case of the para-derivate it is questionable if a long-range ordering occurs. The meta-derivate shows a clear difference of the FC and ZFC measurements of χ, but the difference is still small. For the [M(meta-$HOOCC_6H_4PO_3$) $(H_2O)]_n$ derivates with M = Mn, Co, Ni, shown in figure 2.20, the differences of the FC and ZFC measurements of χ are more pronounced and all three compounds clearly are canted antiferromagnets at low temperatures.

One can conclude that, so far, independently of the substituent on the phenylphosphonate ligand, the inorganic metal-oxygen part is retained which is responsible for the overall magnetic behaviour of the compound. No influence was found for the difference in π-π-stacking of the compounds or of the hybrid organic part in general, which has e.g. different interlayer distances as consequence as can be seen in tables 2.2 and 2.3. Only in the cobalt compounds a dependence of the substituent can be found concerning the strength of the canted antiferromagnetic

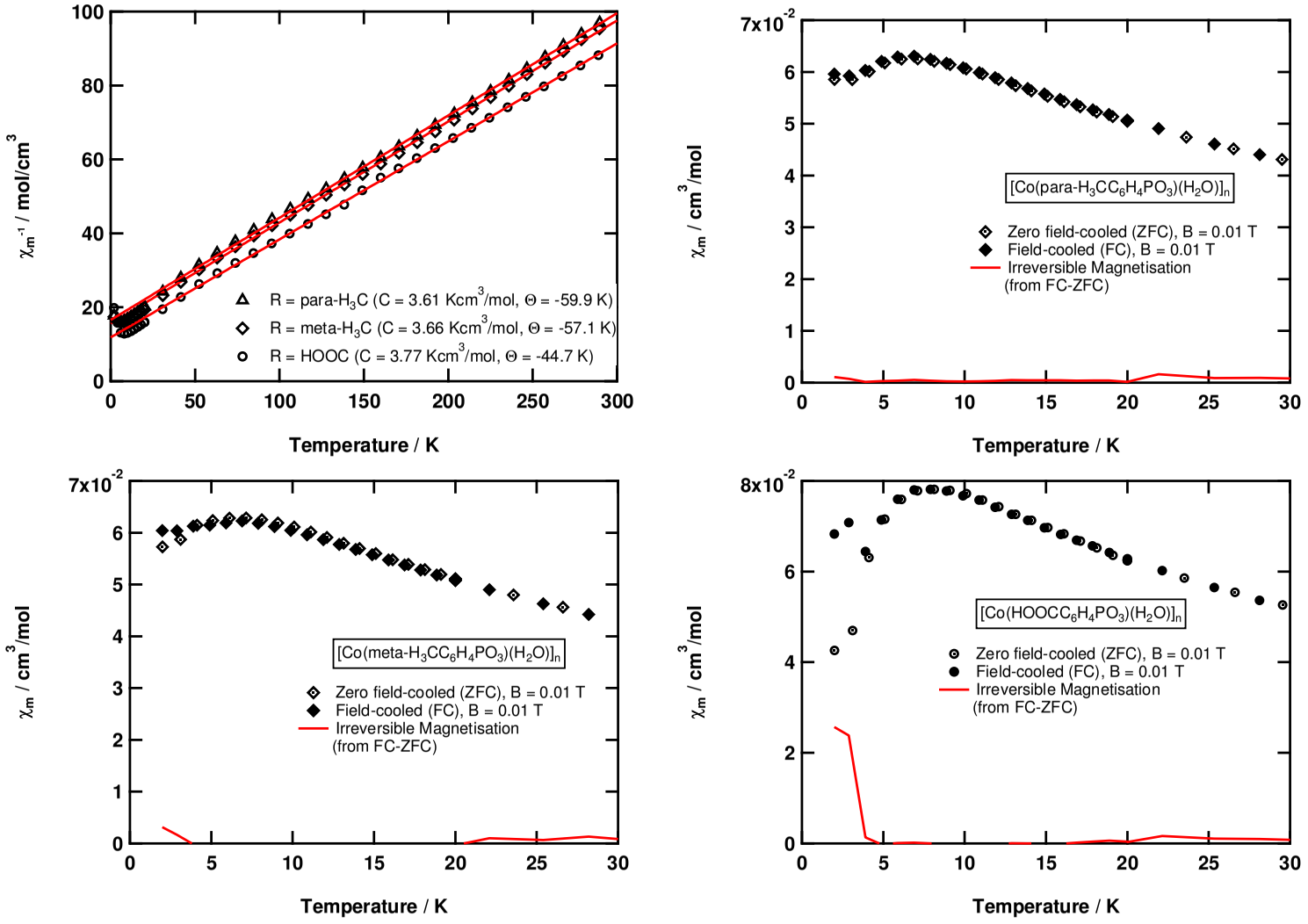

Figure 2.19: Measurement of the magnetic susceptibility of $[Co(R\text{-}C_6H_4PO_3)(H_2O)]_n$, R = para-$H_3C$, meta-$H_3C$, HOOC with a field of 1 T, χ^{-1} vs. T plot is shown normalized to one metal ion, simulation according to the Curie-Law for T > 20K (top left); Temperature dependence of the ZFC (filled) and the FC (open) susceptibility of $[Co(para\text{-}H_3CC_6H_4PO_3)(H_2O)]_n$ (top right), $[Co(meta\text{-}H_3CC_6H_4PO_3)(H_2O)]_n$ (bottom left) and $[Co(HOOCC_6H_4PO_3)(H_2O)]_n$ (bottom right) are shown; the full line represents the difference of FC and ZFC measurements

Table 2.2: top: Comparison of the cell parameters of different obtained metal phosphonate compounds with the same inorganic metal-oxygen part shown in figure 2.16 and figure 2.18; the parameters for the phenylphosphonate derivates are taken from literature [30, 31]; the cell parameters of $[Co(para\text{-}H_3CC_6H_4PO_3)(H_2O)]_n$ are obtained with a LeBay-Fit of powder diffraction data; bottom: Summary of magnetic parameters, the intraplanar superexchange can be estimated through molecular-field theory with J/k = -3Θ/2zS(S+1) with z=4; Neel temperature is taken from zero-field/field-cooled measurements shown in figure 2.19 and 2.20

Formula	$[M(C_6H_5PO_3)(H_2O)]_n$	$[Co(H_3CC_6H_4PO_3)(H_2O)]_n$		$[Co(meta\text{-}HOOCC_6H_4PO_3)(H_2O)]_n$
Compound	M=Co [31]	para **(11a)**	meta **(11b)**	M=Co **(12b)**
Sum formula	$C_6H_7CoO_4P$	$C_7H_9CoO_4P$		$C_7H_7CoO_6P$
crystal system	orthorhombic	orthorhombic		monoclinic
space group	$Pmn2_1$	$Pmn2_1$	$P2_1cn$	$P2_1/n$
a / Å	5.6097(6)	5.6194(2)	4.8020(4)	4.8556(1)
b / Å	14.305(2)	16.678(1)	5.6700(4)	31.8632(9)
c / Å	4.8397(6)	4.8356(2)	30.803(2)	5.6722(2)
α / °	90	90	90	90
β / °	90	90	90	94.012(2)
γ / °	90	90	90	90
distance / Å	14.31	16.68	15.25, 16.05	15.55, 16.34
C / Kcm^3/mol		3.61	3.66	3.77
Θ / K		-59.9	-57.1	-44.7
$\lvert J\rvert$/k / K (MF)		5.99	5.71	4.47
T_N / K	(4)	(3)	4	4

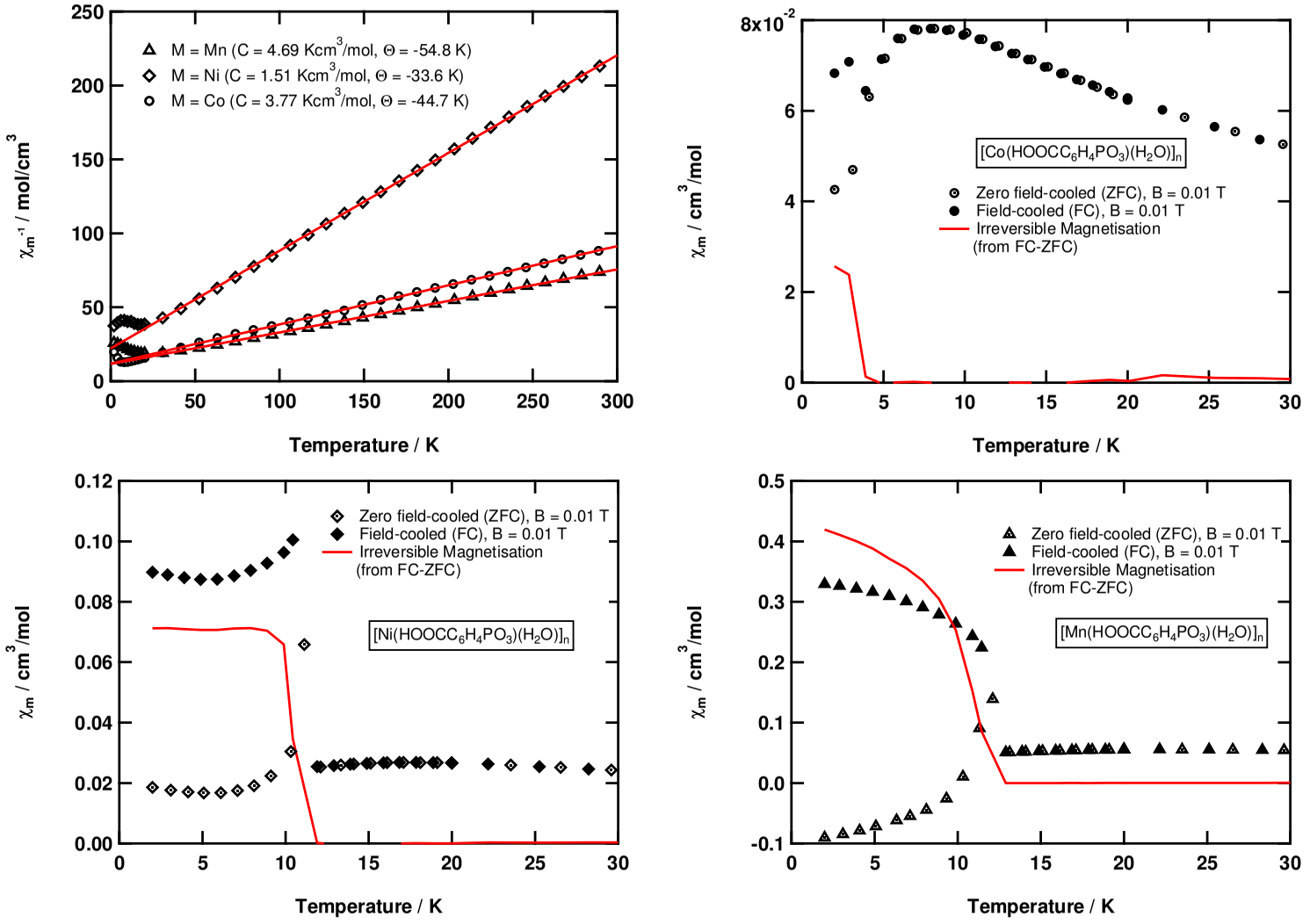

Figure 2.20: Measurement of the magnetic susceptibility of $[M(HOOCC_6H_4PO_3)(H_2O)]_n$, M = Mn, Co, Ni with a field of 1 T, χ^{-1} vs. T plot is shown normalized to one metal ion, simulation according to the Curie-Law for T > 20K; Temperature dependence of the ZFC (filled) and the FC (open) susceptibility of $[Co(HOOCC_6H_4PO_3)(H_2O)]_n$ (top right), $[Ni(HOOCC_6H_4PO_3)(H_2O)]_n$ (bottom left) and $[Mn(HOOCC_6H_4PO_3)(H_2O)]_n$ (bottom right) are shown; the full line represents the difference of FC and ZFC measurements

Table 2.3: top: Comparison of the cell parameters of different obtained metal phosphonate compounds with the same inorganic metal-oxygen part shown in figure 2.18; the parameters for the phenylphosphonate derivates are taken from literature [29–31]; the cell parameters of $[Ni(HOOCC_6H_4PO_3)(H_2O)]_n$ are obtained with a LeBay-Fit of powder diffraction data; bottom: Summary of magnetic parameters, the intraplanar superexchange can be estimated through molecular-field theory with J/k = -3Θ/2zS(S+1) with z=4; Neel temperature is taken from zero-field/field-cooled measurements shown in figure 2.20

Formula	$[M(C_6H_5PO_3)(H_2O)]_n$			$[M(meta\text{-}HOOCC_6H_4PO_3)(H_2O)]_n$		
Compound	M=Co [31]	M=Ni [29]	M=Mn [28]	M=Co **(12b)**	M=Ni **(12c)**	M=Mn **(12a)**
Sum formula	$C_6H_7CoO_4P$	$C_6H_7NiO_4P$	$C_6H_7MnO_4P$	$C_7H_7CoO_6P$	$C_7H_7NiO_6P$	$C_7H_7MnO_6P$
crystal system	orthorhombic			monoclinic		
space group	$Pmn2_1$			$P2_1/n$		
a / Å	5.6097(6)	5.5485(2)	5.734(2)	4.8556(1)	4.8031(1)	4.9628(5)
b / Å	14.305(2)	14.3919(5)	14.33(3)	31.8632(9)	32.0579(8)	31.943(4)
c / Å	4.8397(6)	4.7976(2)	4.945(2)	5.6722(2)	5.6196(1)	5.7787(6)
α / °	90	90	90	90	90	90
β / °	90	90	90	94.012(2)	92.820(2)	94.771(5)
γ / °	90	90	90	90	90	90
distance / Å	14.31	14.39	15.25, 16.05	15.55, 16.34	/	15.55, 16.44
C / Kcm^3/mol		1.26	4.56	3.77	1.51	4.69
Θ / K		-22.4	-46.0	-44.7	-33.6	-54.8
$\lvert J\rvert$/k / K (MF)		4.2	1.97	4.47	6.30	2.35
T_N / K	(4)	5	12.1	4	11	12

Table 2.4: Estimated values for the temperatures at which the maxima occur in the antiferromagnetic susceptibility of the quadratic Heisenberg lattices. The values attained by the susceptiblity at these temperatures are also given. From reference [81]

S	1/2	1	3/2	2	5/2	∞
$\frac{kT_{max}}{\|J\|S(S+1)}$	2.53	2.20	2.10	2.07	2.05	2.01
$\frac{\chi_{max}\|J\|}{Ng^2\mu_B^2}$	0.0469	0.0521	0.0539	0.0547	0.0551	0.0561
$\frac{\chi_{max}T_{max}}{C}$	0.356	0.344	0.340	0.340	0.339	0.338

ordering at low temperatures, but the temperature itself seems to be unaffected. With substituents in the meta-position of the phenylring, the canting is clearly enhanced.

To obtain a better understanding of the exchange coupling in the inorganic metal-oxygen part, the magnetic susceptibility measurements of $[M(HOOCC_6H_4PO_3)(H_2O)]_n$, with M = Mn, Ni measured at a field of 1 T are interpretated with a quadratic Heisenberg lattice approach. A high-temperature series expansion appropiate to a quadratic layer Heisenberg magnet is used to describe the paramagnetic regime of a static magnetic susceptibility measurement. Assuming that all metal ions are the same and that there is only one exchange constant, it provides an accurate method for determining the exchange constant $|J|$/k. In table 2.4 the estimated values for the temperatures at which the maxima occur in the idealized antiferromagnetic susceptibility of the quadratic Heisenberg lattice are given, from reference [81]. Furthermore, as a hint for the applicability of the model, the values of the fraction of $\chi_{max}T_{max}$/C are displayed, which only vary slowly with the spin quantum number S. In figure 2.21 the results are shown. The magnetic susceptibility of $[M(HOOCC_6H_4PO_3)(H_2O)]_n$, M = Mn, Ni is displayed as χ vs. T plot. From the temperature, at which the maximum in χ occurs the exchange coupling $|J|$/k is calculated. As can be seen from the value of the fraction of $\chi_{max}T_{max}$/C, the quadratic Heisenberg lattice model remains an approximation. Especially the value of the exchange coupling $|J|$/k is quite small, compared with the value obtained from the Θ_W-temperature with molecular-field theory. The occurence of a three-dimensional ordering at low temperatures quite close to the maxima values of χ in the χ vs. T plots is already proven by the zero-field and field cooled experiments shown in figure 2.20. The use of the maximum value of χ to determine the value of the exchange coupling $|J|$/k is deficient. Therefore the magnetic susceptibility measurements were simulated again with the high-temperature series expansion according to Lines [90] as can be seen in figure 2.21. The values ob-

Metal	Mn (S=5/2)	Ni (S=1)
χ_{max}/ cm^3/mol	0.054	0.026
T(χ_{max})/ K	20	18
$\frac{\chi_{max} T_{max}}{C}$	0.228	0.311
$\frac{\lvert J \rvert}{k}$ / K	1.11	2.73

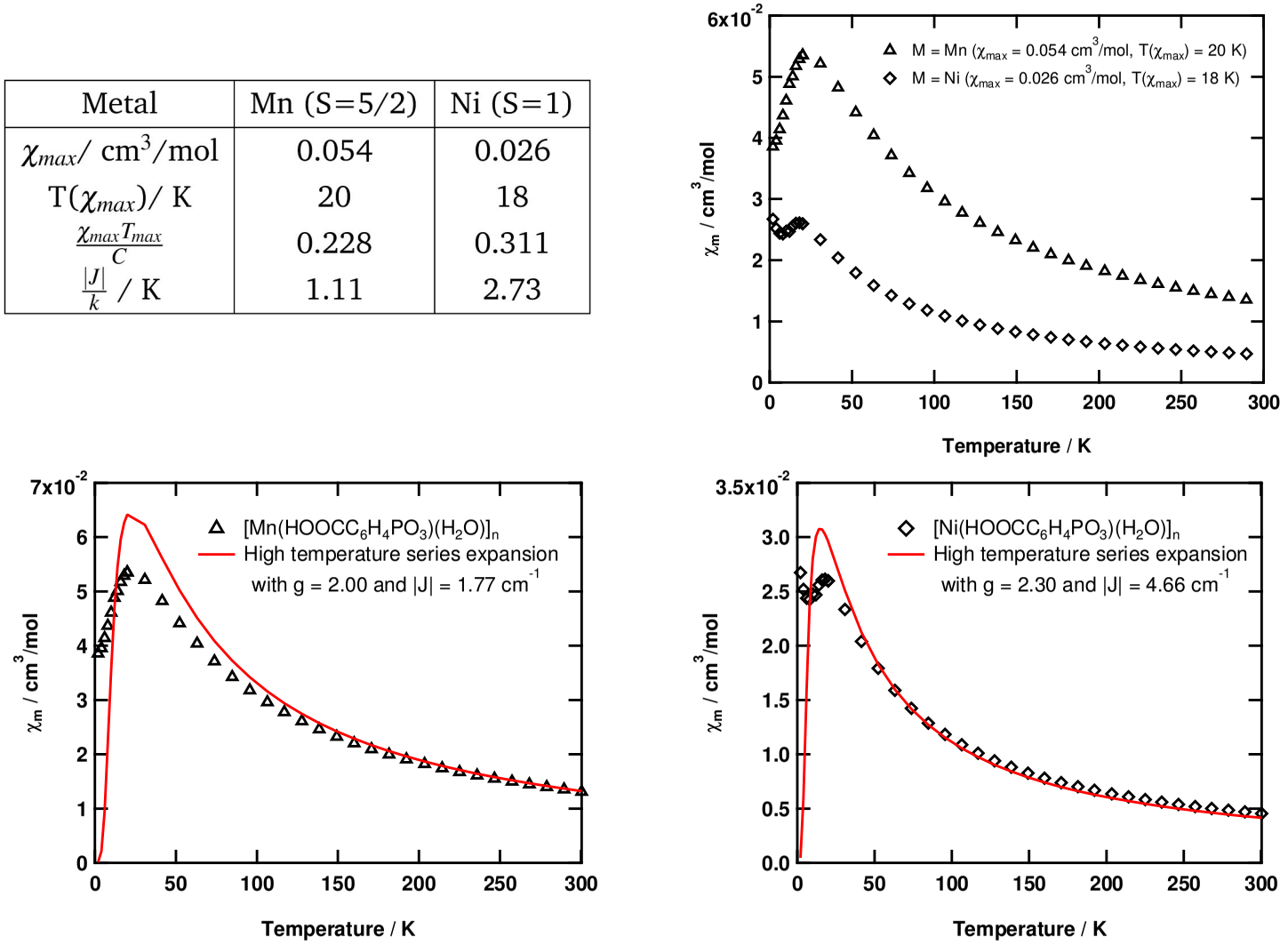

Figure 2.21: Top row: measurement of the magnetic susceptibility of $[M(HOOCC_6H_4PO_3)(H_2O)]_n$, M = Mn, Ni with a field of 1 T, χ vs. T plot is shown normalized to one metal ion; table shows results obtained with a quadratic heisenberg lattice approximation according to table 2.4; High temperature series expansion according to Lines [90] is applied on the magnetic susceptibility of $[Mn(HOOCC_6H_4PO_3)(H_2O)]_n$ with S = 5/2 (top) and $[Ni(HOOCC_6H_4PO_3)(H_2O)]_n$ with S = 1 (bottom)

tained for the exchange coupling $|J|$ and the g-value are displayed in table 2.6 on page 65. In comparison with the other methods used to describe the magnetic behaviour, the values determined with the high-temperature expansion seems to be more reasonable than the one obtained only form the maximum value of χ, although only the high-temperature part of the magnetic susceptibility is taken into account.

The following modification of the high-temperature series expansion describing the quadratic Heisenberg lattice is used to interpretate also the magnetic behaviour of the two-dimensional layered cobalt(II) compounds, although they usually can not be described with Heisenberg model systems because of the degeneracy of triplet ground state $^4T_{1g}$. From a theoretical point of view, the analysis of the magnetic properties of cobalt(II) compounds is in general a challenging subject because of the problems the orbital angular momentum causes. According to Lloret et al. [91] it is possible in the limit of weak magnetic coupling compared to spin-orbit coupling to describe the magnetic properties of six-coordinated high-spin cobalt(II) compounds with an empirical expression. An axial distortion is taken into account, so that the variable parameters are Δ (axial distortion parameter: 0-1000 cm^{-1}), α (orbital reduction factor: 0.75-1.5) and λ (spin-orbit coupling: 90-180 cm^{-1}). Furthermore the magnetic coupling J is incorporated by a perturbational approach, so that the magnetic susceptibility in the whole temperature range can be described as a function of J, Δ, α and λ. The calculation of the magnetic susceptibility of a polynuclear compound requires the treatment of each cobalt(II) ion as a spin doublet S=1/2 with a value of the Lande factor g described by an empirical expression G(T,J). For many compounds like dimers, high-nucearity complexes, one-dimensional chains or two-dimensional layered sytems analytical expressions are known as local spin doublets. The Lande factor g has then to be replaced by the G(T,J) function and the spin value by an effective spin of 1/2, so that these expressions can also be applied on cobalt(II) compounds. This approach is used to describe the magnetic susceptibility of the two-dimensional layered cobalt(II) compounds $[Co(HOOCC_6H_4PO_3)(H_2O)]_n$, $[Co(meta\text{-}H_3CC_6H_4PO_3)(H_2O)]_n$ and $[Co(para\text{-}H_3CC_6H_4PO_3)\ (H_2O)]_n$, shown in figure 2.22. The agreement of the simulated data with the experimental one is really good and the obtained values for the exchange coupling J as well as for the parameters Δ, α and λ are reasonable as can be seen in table 2.6. The positive value of the distortion parameter Δ indicates that the ground state is a singlet ($^4A_{2g}$ from breaking the symmetry of the formerly $^4T_{1g}$ ground state in octahedral symmetry), and with values between 330 and 620 cm^{-1} it is in the expected range

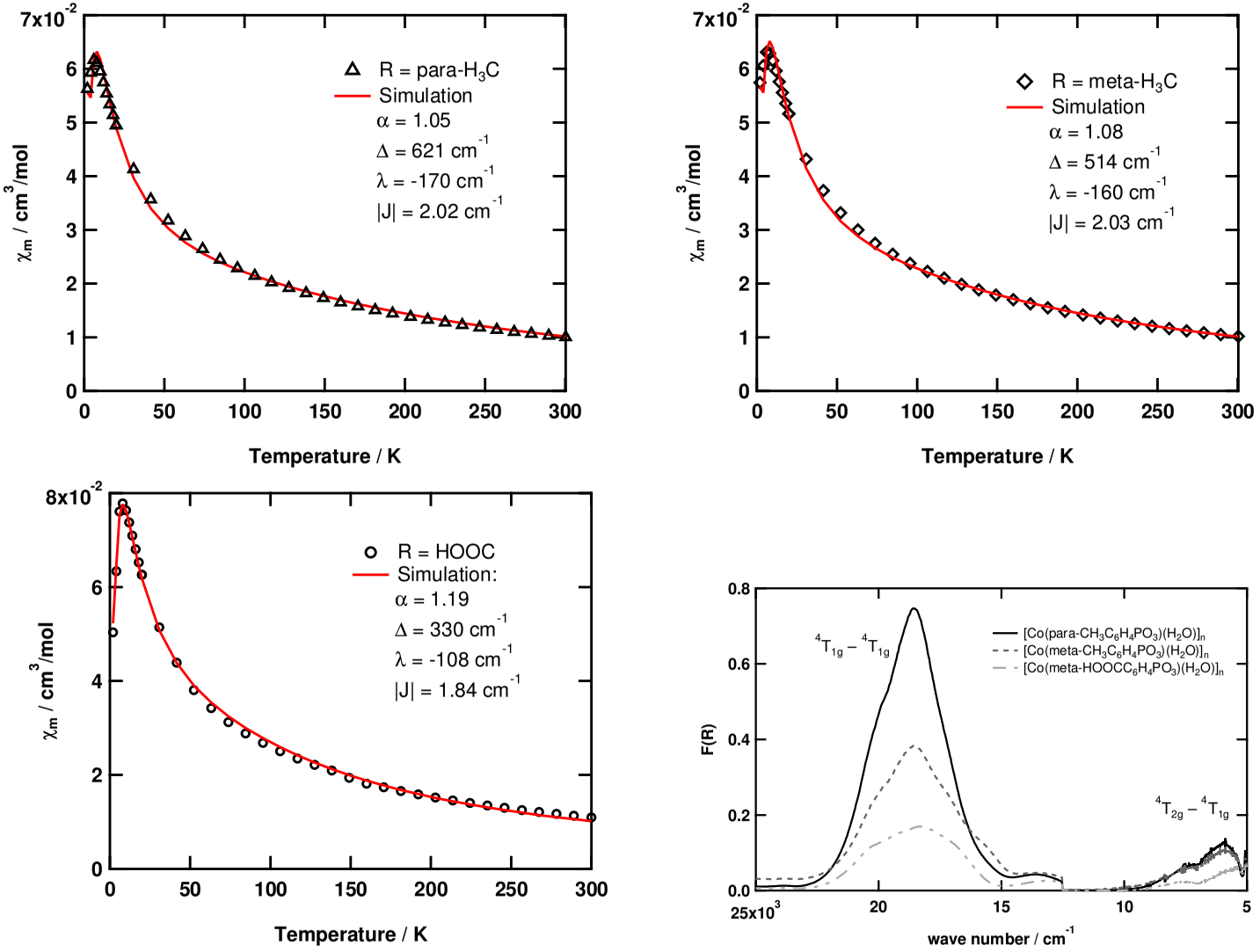

Figure 2.22: Modified high temperature series expansion according to Lloret et al. [91] is applied on the magnetic susceptibility of [Co(para-$H_3CC_6H_4PO_3$)$(H_2O)]_n$ (top left), [Co(meta-$H_3CC_6H_4PO_3$)$(H_2O)]_n$ (top right) and [Co($HOOCC_6H_4PO_3$)$(H_2O)]_n$ (bottom left); bottom right: part of the solid-state UV/Vis spectra (mixed with $BaSO_4$), the cobalt d-d-transitions are assigned in the spectra

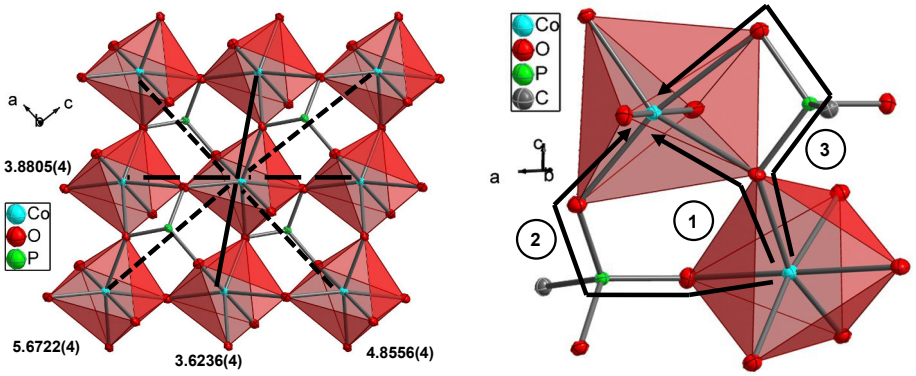

Figure 2.23: right: metal-metal distances in the inorganic metal-oxygen part, shown on $[Co(HOOCC_6H_4PO_3)(H_2O)]_n$; left: representation of exchange pathways that connect each of the cobalt ions to its nearest-neighbors: 1: Co-O-Co, dominant pathway for magnetic exchange; 2: μ_2-syn/syn-bridging phosphonate; 3: μ_2/κ^2-bridging phosphonate

for cobalt(II) compounds. The same is true for the values of α and λ. The influences of the spin-orbit coupling and of the distortion of the octahedral surrounding can also be seen in the solid-state UV/Vis spectra of the compounds shown in figure 2.22. Two d-d-transitions ($^4T_{1g}(^4F)$-$^4T_{1g}(^4P)$ and $^4T_{2g}(^4F)$-$^4T_{1g}(^4F)$) of the cobalt(II) ion can be assigned in a perfect octahedral surrounding, a possible third one ($^4A_{2g}(^4F)$-$^4T_{1g}(^4F)$) is a two photon process and usually very weak. The two observed transitions are broad with additional shoulders indicating the further splitting of the states due to the distortion of the octahedral surrounding and the spin-orbit coupling.

There are more reasons why the quadratic Heisenberg lattice is in general an approximation to describe the magnetic behaviour in these layered two-dimensional hybrid inorganic metal phenylphosphonate compounds. First of all, the layers are not planar, but crenellated. As a result, the metal-metal distances are not equivalent within the four neighbours as can be seen on the left site in figure 2.23. The assumption of only one exchange coupling is already an approximation. Another reason is also displayed in figure 2.23, on the right side the possible exchange pathways through the phosphonate linker are shown. Although the exchange interaction through the metal-O-metal bridge, labelled as pathway one, is the most direct and thought to be dominant, there are two other possible pathways. These chairlike O-P-O bridges, labelled two and three, are known to be the only pathways mediating magnetic exchange in compounds like $VO(O_3PC_6H_5)(H_2O)$ [92], but they require proper symmetry and geometrical arrangements [4]. So these two pathways are expected to give only small contributions to the exchange be-

tween nearest-neighbor metal ions, but they link the metal ion also to the next-nearest neighbors. The assumption of only four neighbors is another approximation. Important is the occurence of a three-dimensional ordering at low temperatures quite close to the maxima values of χ in the χ vs. T plots. Not only that the relationship used to determine $|J|$/k is established by a high-temperature expansion, also the three-dimensional canted antiferromagnetic ordering questions the assumption of a two-dimensional lattice. Two mechanism for the occurence of the three-dimensional canted antiferromagnetic ordering in these systems are discussed in the literature [29], a three-dimensional ordering is excluded in the two-dimensional quadratic Heisenberg lattice. The spin canting may be a result of single-ion anisotropy or of an antisymmetric exchange. The former requires the presence of two equivalent sites for the magnetic ions in the crystal, but the direction of their anisotropy axes should be different. The whole families of layered phosphonate compounds [33] gives confidence that the latter effect plays the most important role. The manganese (II) ion is often an example for a Heisenberg ion due to its ground state $^6S_{5/2}$, which is considered to be isotropic. In a crystal field second order spin-orbit coupling mixes the $^4T_{1g}$ excited state into the $^4A_{1g}$ ground state, resulting in a zero-field splitting of the lowest electronic levels. This mimics the effect of a static magnetic field along the principal axis of the local ligand field, which constrains the magnetic moments to that direction, what is called single-ion anisotropy. The near-neighbor antiferromagnetic isotropic exchange does not align the magnetic moments in an exactly antiparallel fashion, so that they make a small angle to each other. The symmetry requirements for a spin-canting phenomenon exclude the presence of an inversion center between the interacting magnetic ions. Already the orthorhombic space group $Pmn2_1$, typical for all metal phenylphosphonate compounds as can be seen in table 2.2, is sufficiently low that this antisymmetric exchange interaction for weak ferromagnetism, proposed by Dzyaloshinsky [93] and Moriya [94], can occur. The assumption of the isotropic Heisenberg model in general is the most important approximation.

Another approach to describe the magnetic behaviour of low-dimensional magnetic systems was developed by Souletie et al. [95]. In the so called noncritical scaling approach, the temperature dependence of χ*T exhibits a power law with a negative critical exponent γ depending on the spin space and the lattice dimensionality as can be seen in table 2.5 and a negative critical temperature T_C. Unlike the classical phase transition approach, non-singular solutions are deduced if spin correlations exist, that however are not large enough to trigger a long range order at T$\neq$0. The concept of "universality class" is extended to these systems that stand

Table 2.5: Some values of the critical exponent γ, according to the spin state (n) and the lattice dimensionalities (d). The mean field value γ=1 is observed for all n at d≥4. γ diverges for each n, at a lower critical dimensionality d_c(n). Table according to reference [95]

	n=1 (Ising)	n=2 (XY)	n=3 (Hbg)	n=∞ (sph.)
d=1	∞		-1.25S	
d=2	1.75	KT	∞	
d=3	1.25	1.32	1.387	2
Mean field	1	1	1	1

at or below a lower critical dimensionality. Besides the applicability for ferromagnetic Heisenberg chains, the authors also showed that the dimensionality of the phase transition in layered dicarboxylate-based materials can be analyzed [96]. Under these considerations the magnetic behaviour of $[Ni(C_6H_5PO_3)(H_2O)]_n$ was reviewed [33].

The magnetic susceptibility measurement of $[Ni(HOOCC_6H_4PO_3)(H_2O)]_n$ is analysed with the power law formulated as χ*T = C*(1-T_C/T)$^{-\gamma}$ [95]. As can be seen in figure 2.24, the simulation nicely agrees with the χ*T vs. T data. From the simulation the following parameters are obtained: Curie constant C = 1.484(6) Kcm^3/mol, T_C = -14(1) K, and γ=2.0(1). The inset shows the magnetic data measured at B = 0.01T, where the canted antiferromagnetic ordering could be observed in zero-field cooled (ZFC) and field-cooled (FC) measurements. The simulation of the data measured at B = 1T describes also the overall behaviour down to the ordering temperature of 11 K. The $\Delta Log_{10}(T)/\Delta Log_{10}(\chi*T)$ vs. T plot gives a straight line in the range where the model is valid according to the formula $\Delta Log_{10}(T)/\Delta Log_{10}(\chi*T) = (T-T_C)/(\gamma*T_C)$. From the intersection with the temperature axis the T_C value can be obtained and at T = 0 the γ^{-1} value is passed. Although the determination of these values is in this plot quite simple, one can see that the errors due to the differentiation are large compared to the χ*T vs. T plot. That is why the simulation was carried out on the χ*T data and with the obtained parameters the simulation in the $\Delta Log_{10}(T)/\Delta Log_{10}(\chi*T)$ vs. T plot is plotted again to confirm the applicability of the scaling approach. The inset shows the agreement with the zero-field cooled (ZFC) and field cooled (FC) data, which is good again down to the ordering temperature of 11 K. The values obtained from the simulation C = 1.484(6) K*cm^3/mol, T_C = -14(1) K, and γ = 2.0(1) are similar to the one described for $[Ni(C_6H_5PO_3)(H_2O)]_n$. The Curie constant is in the typicial range for a nickel(II) ion in an octahedral environment and furthermore a

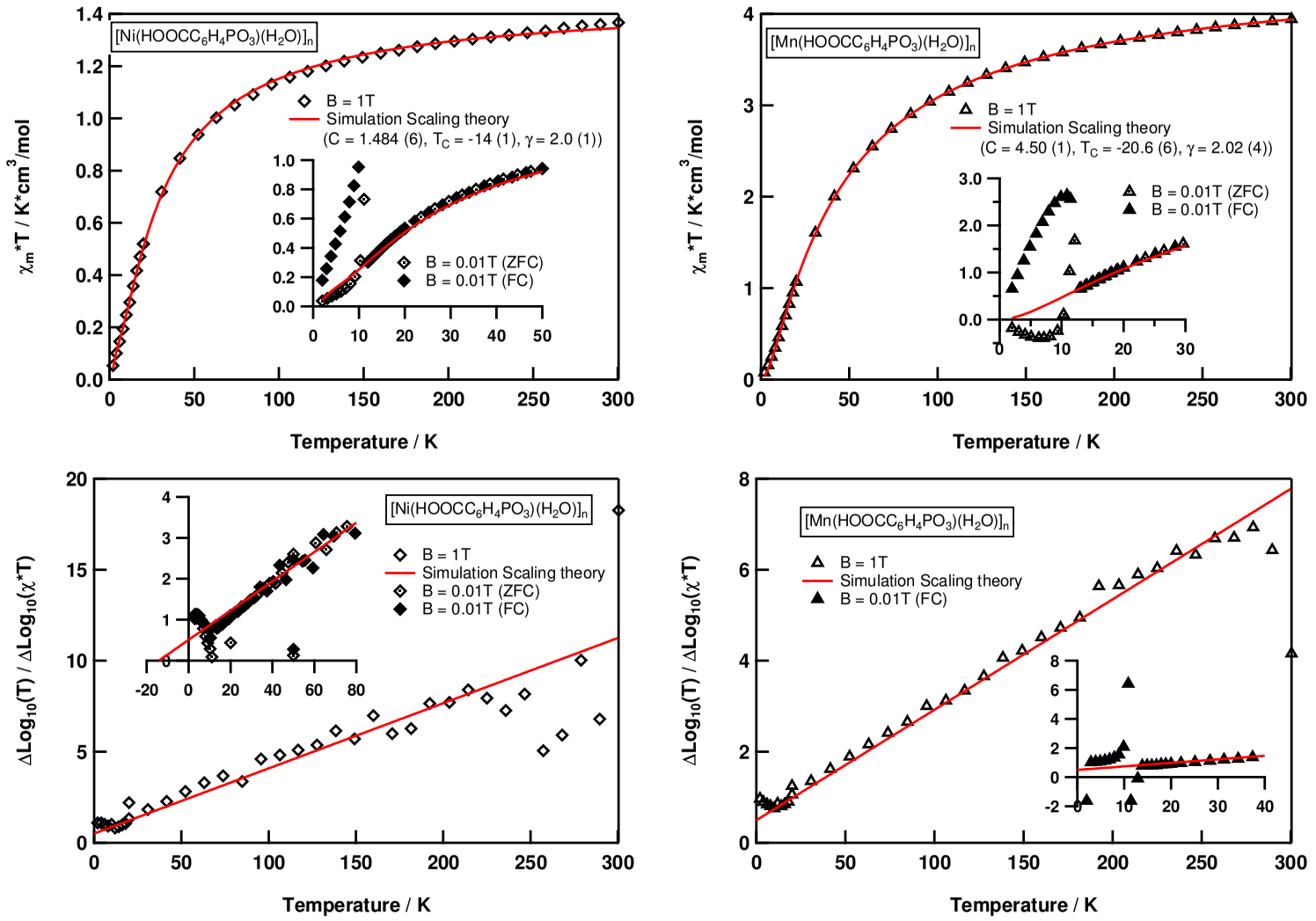

Figure 2.24: top: Measurements of the magnetic susceptibility of $[Ni(HOOCC_6H_4PO_3)(H_2O)]_n$ **(12c)** (left) and $[Mn(HOOCC_6H_4PO_3)(H_2O)]_n$ **(12a)** (right) are shown as a χ*T vs. T plot, Simulation according to the scaling theory with a power law formulated χ*T = C*(1-T_C/T)$^{-\gamma}$, inset shows agreement with ZFC and FC data; bottom: $\Delta Log_{10}(T)/\Delta Log_{10}(\chi*T)$ vs. T plots are shown, visualizing the region were the scaling model is appropiate, there it gives a straight line intersecting the temperature axis at a negative T_C value and the T=0 axis at γ^{-1}.

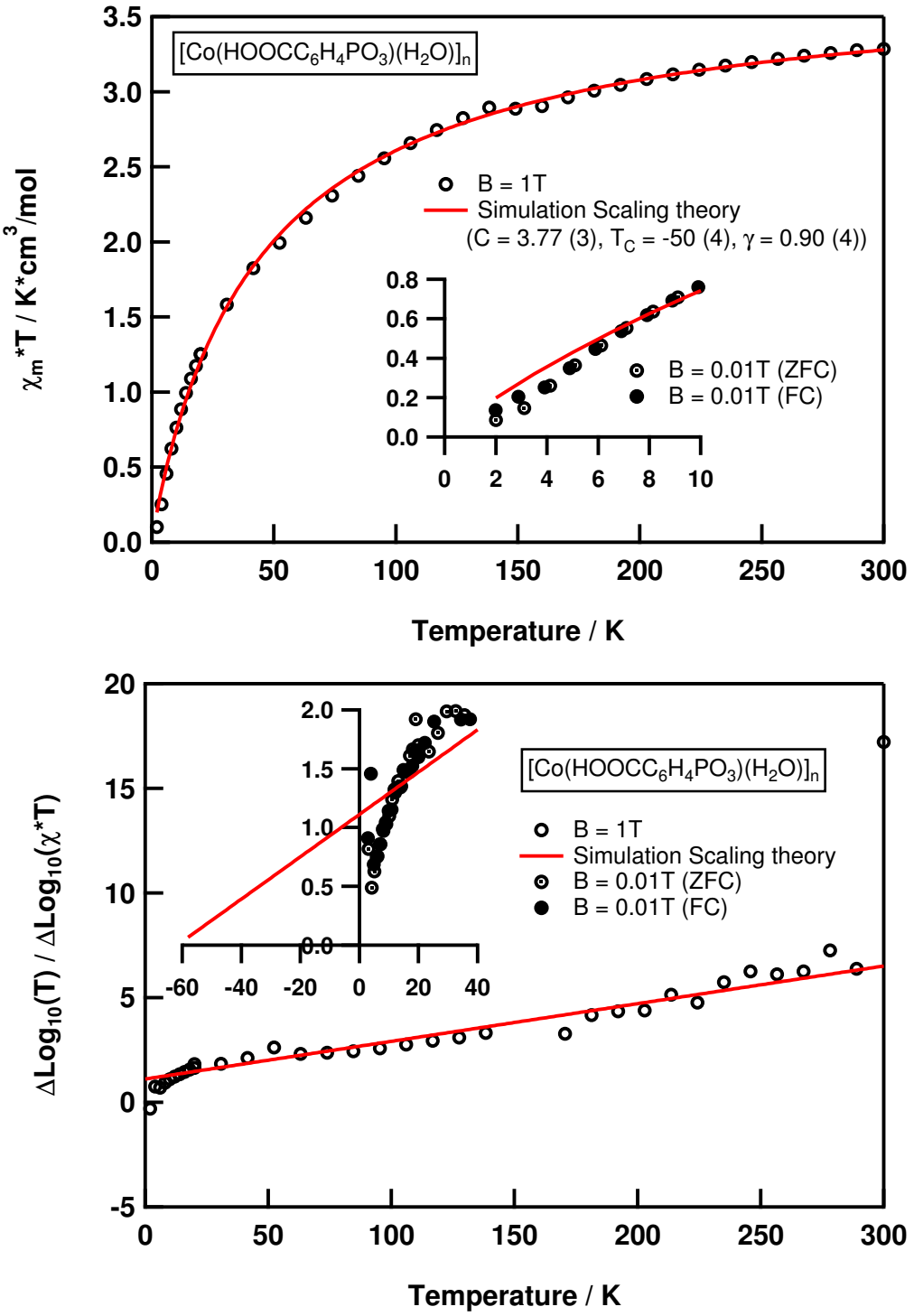

Figure 2.25: top: Measurement of the magnetic susceptibility of $[Co(HOOCC_6H_4PO_3)(H_2O)]_n$ **(12b)** is shown as a χ*T vs. T plot, Simulation according to the scaling theory with a power law formulated χ*T = C*(1-T_C/T)$^{-\gamma}$, inset shows agreement with ZFC and FC data; bottom: $\Delta Log_{10}(T)/\Delta Log_{10}(\chi*T)$ vs. T plot is shown, visualizing the region were the scaling model is appropiate, there it gives a straight line intersecting the temperature axis at a negative T_C value and the T=0 axis at γ^{-1}.

similar value was obtained by applying the Curie-Weiss law. The transistion temperature with 14 K is too high compared to the measured temperature obtained by the zero-field cooled and field cooled experiments, but this tendency is found also in $[Ni(C_6H_5PO_3)(H_2O)]_n$. There the ordering temperature T_C is found to be 5 K, but the simulation gives 11 K. As can be seen in table 2.5, the γ value of 2.0 is too high for a two-dimensional system showing some long-range order. But as it is argued in the literature for $[Ni(C_6H_5PO_3)(H_2O)]_n$, the power law analysis indicates that the magnetic behaviour has a strong three-dimensional character.

The same 3D behaviour is found for $[Mn(HOOCC_6H_4PO_3)(H_2O)]_n$ shown in figure 2.24. As can be seen in the inset of figure 2.24, the simulated curve according to the power law describes nicely the overall magnetic behaviour down to the temperature, where the ordering occur. Again, the Curie constant C = 4.50(1) Kcm^3/mol is in the expected range of a manganese (II) ion in an octahedral environment and a similar value was obtained by applying the Curie-Weiss law. The transition temperature with 20 K is too high compared to the temperature obtained by the zero-field cooled and field cooled experiments (T = 12K). Also the γ value of 2.02, compared to the values in table 2.5, is too high for a two-dimensional system showing some long-range order. Again the power law analysis indicates that the magnetic behaviour has a strong three-dimensional character.

For the cobalt compound $[Co(HOOCC_6H_4PO_3)(H_2O)]_n$, the overall magnetic behaviour is different. As can be seen in figure 2.25, the simulated curve according to the power law describes nicely again the magnetic susceptibility in the χ*T vs. T plot and also the straight line in the $\Delta Log_{10}(T)/\Delta Log_{10}(\chi*T)$ vs. T plot confirms that the noncritical scaling approach is applicable. The Curie constant C = 3.77(3) $K*cm^3/mol$ is in the expected range of a cobalt (II) ion in an octahedral environment and an identical value was obtained by applying the Curie-Weiss law. The obtained values for T_C and γ differ strongly from the ones obtained for the isostructural nickel and manganese compound. The T_C value is with 50 K quite high, the γ value is with 0.90 quite low. The power law analysis indicates that $[Co(HOOCC_6H_4PO_3)(H_2O)]_n$ belongs to the systems that are at or below a lower critical dimensionality for a long-range ordering. Any three-dimensional character of the magnetic behaviour can be excluded clearly from the low γ value. However, due to the strong anisotropy of the cobalt(II) ion a two-dimensional magnetic order cannot be ruled out.

Table 2.6: Comparison of the different methods used to describe the magnetic properties of the different obtained metal phosphonate compounds with the same inorganic metal-oxygen part; **1.** Neel temperature T_N is taken from zero-field/field-cooled measurements; **2.** Curie-Weiss law: the intraplanar superexchange can be estimated through molecular-field theory (MF) with J/k = -3Θ/2zS(S+1) with z=4; **3.** quadratic heisenberg lattice approximation (QH) according to reference [81]; **4.** high-temperature expansion (HTE) of the quadratic heisenberg lattice according to reference [90]; **5.** modification for cobalt(II) compounds according to [91]; **6.** scaling theory (ST) according to reference [33, 95]

Formula		$[Co(H_3CC_6H_4PO_3)(H_2O)]_n$		$[M(meta\text{-}HOOCC_6H_4PO_3)(H_2O)]_n$		
Compound		para **(11a)**	meta **(11b)**	M=Co **(12b)**	M=Ni **(12c)**	M=Mn **(12a)**
Sum formula		$C_7H_9CoO_4P$		$C_7H_7CoO_6P$	$C_7H_7NiO_6P$	$C_7H_7MnO_6P$
1.	T_N / K	(3)	4	4	11	12
2.	C / Kcm^3/mol	3.61	3.66	3.77	1.51	4.69
	Θ / K	-59.9	-57.1	-44.7	-33.6	-54.8
	$\|J\|$/k / K (MF)	5.99	5.71	4.47	6.30	2.35
3.	$\|J\|$/k / K (QH)	/	/	/	2.73	1.11
4.	g	/	/	/	2.3	2.0
	$\|J\|$ / cm^{-1}	/	/	/	4.66	1.77
5.	$\|J\|$ / cm^{-1}	2.02	2.03	1.84	/	/
	α	1.05	1.08	1.19	/	/
	Δ / cm^{-1}	621	514	330	/	/
	λ / cm^{-1}	-170	-160	-108	/	/
6.	C / Kcm^3/mol (ST)	/	/	3.77	1.48	4.50
	T_C / K (ST)	/	/	-50	-14	-21
	γ	/	/	0.90	2.0	2.0

In table 2.6 the results of the different methods to describe the magnetic behaviour of the two-dimensional layered hybrid inorganic metal phenylphosphonate derivate compounds are summarised. The Weiss temperature Θ already indicates that the main exchange coupling in this systems is an antiferromagnetic one, as expected compared to the metal phenylphosphonate compounds known from literature. The limitations of the quadratic Heisenberg lattice approach were already discussed in detail, thus due to the long-range ordering at low temperatures the values obtained for the exchange coupling J are deficient. An improvement is made by the use of the explicit high-temperature expansion and especially the modification for the cobalt compounds describes well the magnetic behaviour probably due to the fact that the ordering in the cobalt compounds is at lower temperatures, if at all. The interpretation according to the non-critical scaling approach gives a nice inside especially in the nature of the long-range ordering at low temperatures. Clearly the difference between the magnetic behaviour of the nickel and manganese compound of $[M(meta\text{-}HOOCC_6H_4PO_3)(H_2O)]_n$, where the long-range ordering has a strong three-dimensional character and the isostructural cobalt compound can be seen, where a two-dimensional ordering is assumed due to the strong anisotropy.

Unfortunaly $[Mn(HOOCC_6H_4PO_3)(H_2O)]_n$ **(12a)** and $[Co(HOOCC_6H_4PO_3)(H_2O)]_n$ **(12b)** were already published by Rueff et al. [77]. In their paper: Meta-phosphonbenzoic Acid: A Rigid Heterobifunctional Precursor for the Design of Hybrid Materials, they presented the crystal structure of $[M(HOOCC_6H_4PO_3)(H_2O)]_n$ (M = Co, Mn, Zn) as well as the crystal structure of the free meta-phosphonobenzoic acid and a second zinc compound. They described an alternate ligand synthesis, but they presented also some susceptibility measurements of $[M(HOOCC_6H_4PO_3)(H_2O)]_n$ (M = Co, Mn). However, their interpretation of the magnetic data is not complete. They simply simulated the susceptibility measurements by a modified Fisher law (for 1D chains) by adding an intrachain coupling without mentioning the canted antiferromagnetic behaviour at all.

2.1.5.2 Second Modification: Edge-sharing Metal-Oxygen Octahedra

Up to now, independently of the used ligand 4-Tolylphosphonic acid **(2c)** , 3-Tolylphosphonic acid **(2b)** or 3-Phosphonbenzoic acid **(3b)** the inorganic part of the obtained two-dimensional layered structure consists of corner-sharing metal oxygen octahedra. The so far introduced extended inorganic hybrid materials (I^2O^0) resemble closely the already known metal phenylphosphonate compounds with the general formula $[M(C_6H_5PO_3)(H_2O)]_n$. In the next part, two compounds with the general formula $[M(para\text{-}HOOCC_6H_4PO_3)]_n$ with M being cobalt **(13)** or copper **(14)** and 4-Phosphonbenzoic acid **(3c)** as ligand will be presented. In these "binary" compounds the metal oxygen octahedra are edge-sharing resulting that every oxygen atom of the phosphonate ligand is triply-bridging (two metal ions and the phosphorus). The synthesis of these compounds is carried out at a higher temperature T = 200 °C, so that the term high-temperature modification is used to describe the new linkage in the inorganic part of these extended inorganic hybrid materials (I^2O^0). In the literature no similar compound with the phenylphosphonate ligand is reported. Going back to purely inorganic compounds like phosphates, the equivalent compounds $CuHPO_4$ and $CoHPO_4$ are known [97], but they do not exhibit a two-dimensional layered structure. More relevant is a series of maricite type structures with the general formula $NaMPO_4$ (M = Mn, Fe, Co, Cu) [98]. Their chains of edge-sharing octahedra are separated by the non-magnetic sodium ions. For $NaCuPO_4$ even a field-induced antiferromagnetic to ferromagnetic transition could be found [99]. Nevertheless, no layered two-dimensional material with edge-sharing octahedra in the inorganic part of phosphate or phenylphosphonate compounds is reported so far.

It is especially noteable that in all reported copper phenylphosphonate structures, the copper ion is only five-coordinated and in distorted tetragonal pyramidal symmetry [29]. In $[Cu(C_6H_5PO_3)(H_2O)]_n$ all three oxygen atoms of the phosphonate group are bonded to copper ions, one of them bridges two copper ions, thus defining copper dimers forming four-membered parallelogram-shaped rings Cu-O-Cu-O in the plane. Two next-nearest neighbouring copper ions are linked by O-P-O bridges. Due to the special linkage in the inorganic copper oxygen layers, the phenyl rings of adjacent layers are approximately perpendicular to each other [100]. Even in dehydrated samples of $[Cu(RPO_3)]_n$ with R = CH_3 or CH_2CH_3, the five-coordination of the copper ions is retained [101]. In contrast to the reported copper phenylphosphonate structure, here a six-coordinated copper ion is found in $[Cu(para\text{-}HOOCC_6H_4PO_3)]_n$.

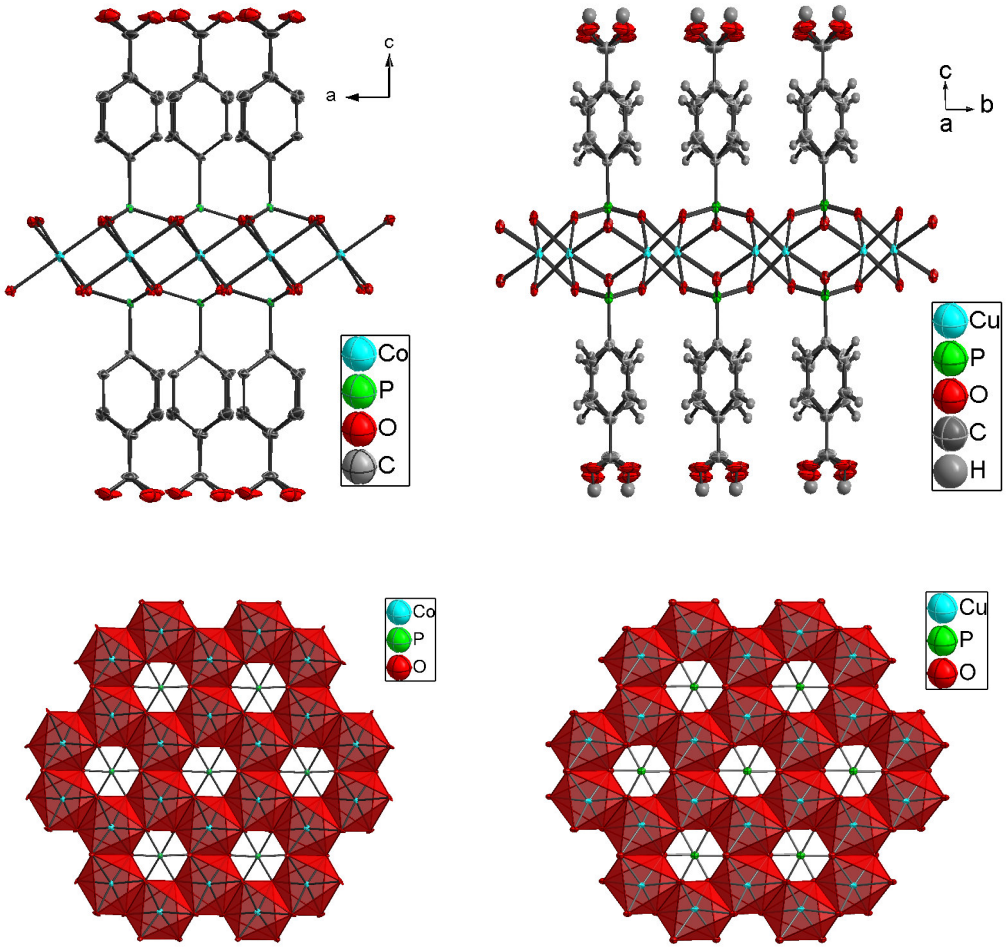

Figure 2.26: Part of the crystal structure of $[M(para\text{-}HOOCC_6H_4PO_3)]_n$ with M=Co **(13)** (left, C 2) and M=Cu **(14)** (right, C 2/m) are shown; top: two different views on the extended inorganic hybrid materials. They crystallise in different space groups, but the overall composition is quite similar. Phenyl rings are disordered over two positions; bottom: inorganic metal-oxygen part built of edge-sharing metal-oxygen octahedra, all oxygen atoms are triple-bridging. Overall a honeycomb arrangement of the metal ions is realised

The crystal structure of $[M(para\text{-}HOOCC_6H_4PO_3)]_n$ with M = Co **(13)** (space group: C 2) and M = Cu **(14)** (space group: C 2/m) consists of inorganic layers of MO_6 octahedra, which edge-share into a continuous sheet as shown at the bottom of figure 2.26. The overall arrangement of the metal ions is in a so called honeycomb motive and the resulting layers are completely flat. The phosphonates cap the layers alternately above and below the plane of the layer as can be seen at the top of figure 2.26. As for other metal phenylphosphonate derivates, the phenyl rings point into the interlayer space, defining a hydrophobic bilayer region. Furthermore, it has been found that the phenyl rings are disordered between two orientations. The new introduced carboxilic acid

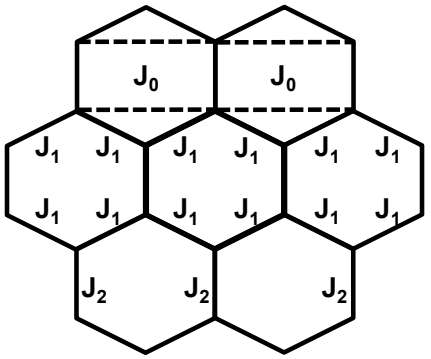

Figure 2.27: Scheme of the honeycomb motive with possible coupling scheme adopted for the compounds $[M(para\text{-}HOOCC_6H_4PO_3)]_n$; J_0 = 0 (assumption), magnetic properties depend on the ration between J_1/J_2, two limiting cases: for $J_1 \gg J_2$: one-dimensional chain compound, for $J_2 \gg J_1$: dimer approximation

is not involved in building up the inorganic part, as for the meta-derivate in $[M(meta\text{-}HOOCC_6H_4PO_3)(H_2O)]_n$ (M=Mn, Ni, Co), it stabilizes the hydrophobic bilayer region by hydrogen-hydrogen bonding between adjacent layers. In the case of the cobalt derivate $[Co(para\text{-}HOOCC_6H_4PO_3)]_n$, the symmetry of the CoO_6 octahedra is somewhat distorted as can be seen in the bond lengths and angles listed in figure 2.30, but it is less than in the already presented compounds $[Co(RC_6H_4PO_3)(H_2O)]_n$ in section 2.1.5.1. In the case of the copper derivate $[Cu(para\text{-}HOOCC_6H_4PO_3)]_n$, the CuO_6 octahedra are elongated due to a Jahn-Teller distortion as shown in figure 2.28, where the Jahn-Teller axis are marked in red.

In general the interest in materials based on a honeycomb lattice is based on the finding of topological insulator behaviour in some of these materials like graphene [102, 103] or bismuth telluride as well as the similarity to the Kagome lattice providing magnetic frustated systems [104]. The honeycomb motive found in the inorganic metal oxygen layers of the compounds $[M(para\text{-}HOOCC_6H_4PO_3)]_n$ is not a regular one, which leads to some interesting consequences concerning the magnetic properties [105]. In figure 2.27 a scheme of the adopted honeycomb motive is shown with assigned possible exchange couplings J_0, J_1 and J_2. J_0, the coupling to the next-nearest neighbor is not significant in the compounds with the general formula $[M(para\text{-}HOOCC_6H_4PO_3)]_n$, because the linkage between the next-nearest neighbors is a syn-anti μ_2-O-P-O bridge, which is considered to be weak, so in the present work J_0 is set to zero. The ratio between J_1/J_2 determines the magnetic properties in these not regular formed honeycomb motives. Two

limiting cases can be found, for $J_1 \gg J_2$ magnetically a one-dimensional chain compound is realised, whereas for $J_2 \gg J_1$ an approximation as dimer is appropiate. All cases with $J_1 \approx J_2$ need a two-dimensional model.

The magnetic properties of both compounds discussed here are completely different. For $[Cu(para\text{-}HOOCC_6H_4PO_3)]_n$, the measurement of the magnetic susceptibility is shown in figure 2.28. For $[Cu(C_6H_5PO_3)(H_2O)]_n$ [29], the main interaction between near-neighbor copper ions is found in the four-membered parallelogram-shaped Cu-O-Cu-O rings, so that a dimer model is sufficient to simulate the magnetic behaviour. In $[Cu(para\text{-}HOOCC_6H_4PO_3)]_n$, all copper ions are connected in four-membered parallelogram-shaped Cu-O-Cu-O rings as can be seen at the bottom of figure 2.28. Two different parallelogram-shaped Cu-O-Cu-O rings can be distinguished due to the Jahn-Teller distortion of the copper ions. In one type of four-membered Cu-O-Cu-O ring, two edges comprises the Jahn-Teller axis of two copper ions, marked in red. The bridging oxygen atom is labelled with O2 and the copper-copper distance is 2.84 Å (dark green). The second type of four-membered Cu-O-Cu-O ring is built of the oxygen atoms labelled with O1 and all four edges have equal lengths. The copper-copper distance is 2.92 Å (light green). Overall the honeycomb motive of the copper ions in the inorganic metal oxygen part is not regulary, but elongated in one direction, perpendicular to the elongated Jahn-Teller distortion of every single copper ion. The magnetic relevant orbital of the copper ions is the $d_{x^2-y^2}$-orbital, which is also perpendicular to the Jahn-Teller axis (elongation in z-direction). Therefore again just one type of four-membered parallelogram-shaped Cu-O-Cu-O rings is responsible for the magnetic behaviour of $[Cu(para\text{-}HOOCC_6H_4PO_3)]_n$, the one is Cu-O1-Cu-O1 with the longer copper-copper distance marked in light green. These rings are well-separated in the two-dimensional layered structure, so that also here a dimer model is appropiate to describe the magnetic properties as can be seen at the top of figure 2.28. Compared with the scheme in figure 2.27, the limiting case of $J_2 \gg J_1$ is realised here, so that only one exchange coupling called J is sufficient. The value of the exchange coupling J obtained in the simulation is -29.2 cm^{-1}. According to the structural and magnetic relationship established by Hatfield and Hodgson [106], with a value of the Cu-O1-Cu angle of 95.7° an exchange coupling constant of +170 cm^{-1} is expected in case of double hydroxo-bridged copper dimers like $[Cu(bipy)OH]_2(NO_3)_2$ [107]. From that, one can clearly see that the bridging oxygen atom O1 of the phosphonate ligand has not a simple p-character. The g-value obtained in the simulation is with 2.47 a bit too high, what can be explained with some underlying paramagnetic impurity not taken into account in the simulation.

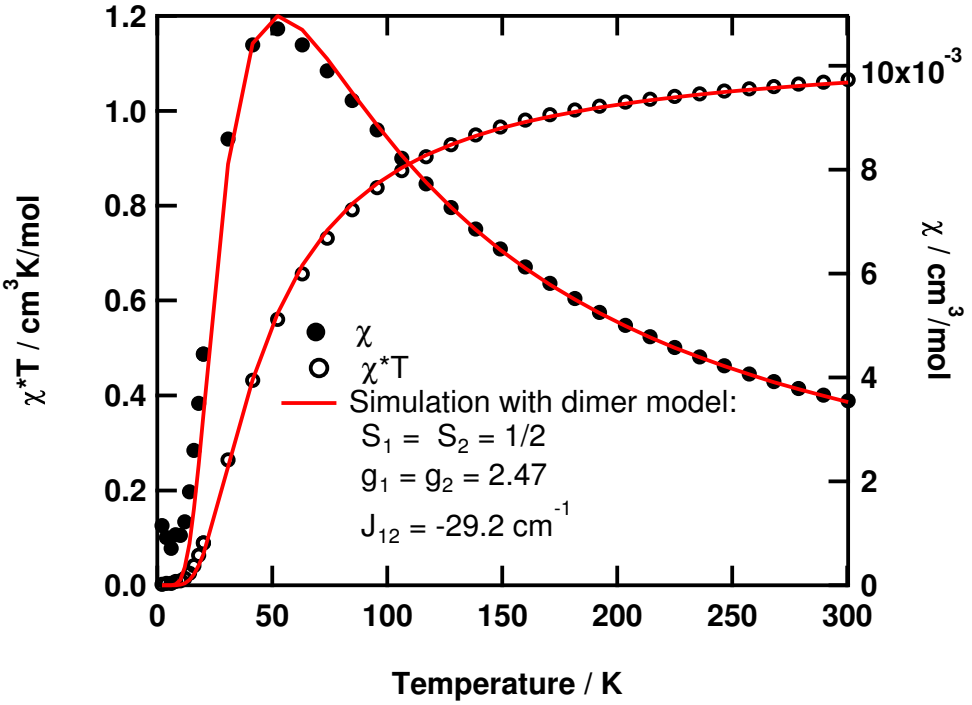

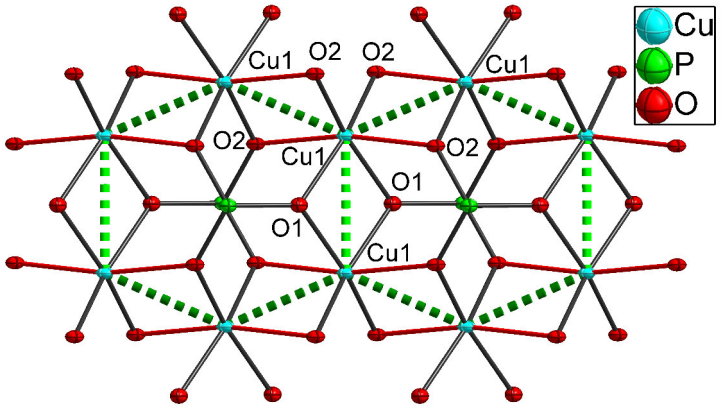

atoms	bond length / Å	atoms	angle /°
Cu1-O1	1.970(3)	Cu1-O1-Cu1	95.7(1)
Cu1-O2 (J.T., red)	2.549(4)	Cu1-O2-Cu1	77.3(1)
Cu1-O2 (not J.T., black)	1.935(3)		
Cu1-Cu1 (dark green)	2.84		
Cu1-Cu1 (light green)	2.92		

Figure 2.28: top: Measurement of the magnetic susceptibility of [Cu(para-$HOOCC_6H_4PO_3$)]$_n$ **(14)** with a field of 1T, the simulation is based on a dimer model, bottom: Cut off the inorganic metal-oxygen part of the crystal structure with labelling of atoms, selected bond lengths, distances and angles are listed

For the cobalt(II) derivate of $[M(para\text{-}HOOCC_6H_4PO_3)]_n$ **(13)** the measurements of the magnetic susceptibility at fields of 0.1 T and 1 T are shown in figure 2.29. Displayed are the χ_m vs. T, χ_m^{-1} vs. T and the χ_mT vs. T plots as well as the heat capacity vs. T plot. Clearly a phase transition at 11K can be deduced from all measurements. The phase transition and the low temperature magnetic behaviour were further investigated by the measurements of the dynamic susceptibilities χ_m' and χ_m" as well as magnetisation measurements shown in figure 2.29. No out-of phase signal (χ_m") was detected and no influence of the wave frequency ν could be found, so that a long-range weak ferromagnetic order could be excluded. The S-shaped characteristics of the low-temperature magnetisation curves reveal a more complex behaviour below 10K, which could be some metamagnetism [108]. The term of metamagnetism is widely used today, but here it describes a field-induced phase transition in a highly anisotropic magnetic system. When a magnetic field is applied at low temperatures, a first-order phase transition is observed from a state with a low magnetisation (i.e. net magnetic moment) and low susceptibility, to a state with a relatively high magnetisation and low susceptibility. Two microscopic properties are said to be essential characteristics of a metamagnet: strong anisotropy and competing interactions. Both are realised in $[Co(para\text{-}HOOCC_6H_4PO_3)]_n$, the scheme of the honeycomb motive shown in figure 2.27 reveals that there are different exchange couplings J_0, the next-nearest neighbor interaction, as well as J_1 and J_2, the nearest-neighbor interactions.

Selected cobalt-cobalt distances and bond angles are shown in figure 2.30. Furthermore, the high-spin cobalt(II) ion is a highly anisotropic ion, so that more cobalt(II) compounds exhibit a metamagnetic behaviour like $CoCl_2$*$2H_2O$ or $CoBr_2$*$2H_2O$. These are linear chain compounds, which crystallise in the monoclinic space group C2/m. The linear chains of $CoCl_2$*$2H_2O$ or $CoBr_2$*$2H_2O$ run parallel to the c axis and the intra-chain spin-spin interactions are much stronger than the inter-chain interactions, so that the anisotropy is such that the spins lie along the b axis. Both literature known compounds order antiferromagnetically in zero-field at T_N = 17.5 K for the chloride and T_N = 9.5 K for the bromide derivate. The copper derivate $[Cu(para\text{-}HOOCC_6H_4PO_3)]_n$ crystallises in the same space group C2/m, also the space group of the cobalt derivate $[Co(para\text{-}HOOCC_6H_4PO_3)]_n$, C 2, is quite similar. Although no further structural similarity can be found with $[Co(para\text{-}HOOCC_6H_4PO_3)]_n$, the antiferromagnetic ordering temperature T_N = 11 K is in the same range compared to $CoCl_2$*$2H_2O$ or $CoBr_2$*$2H_2O$. The magnetisation measured as a function of field below temperatures of 8 K displays a discontinuity, so that one successive phase transition is observed as shown in fig-

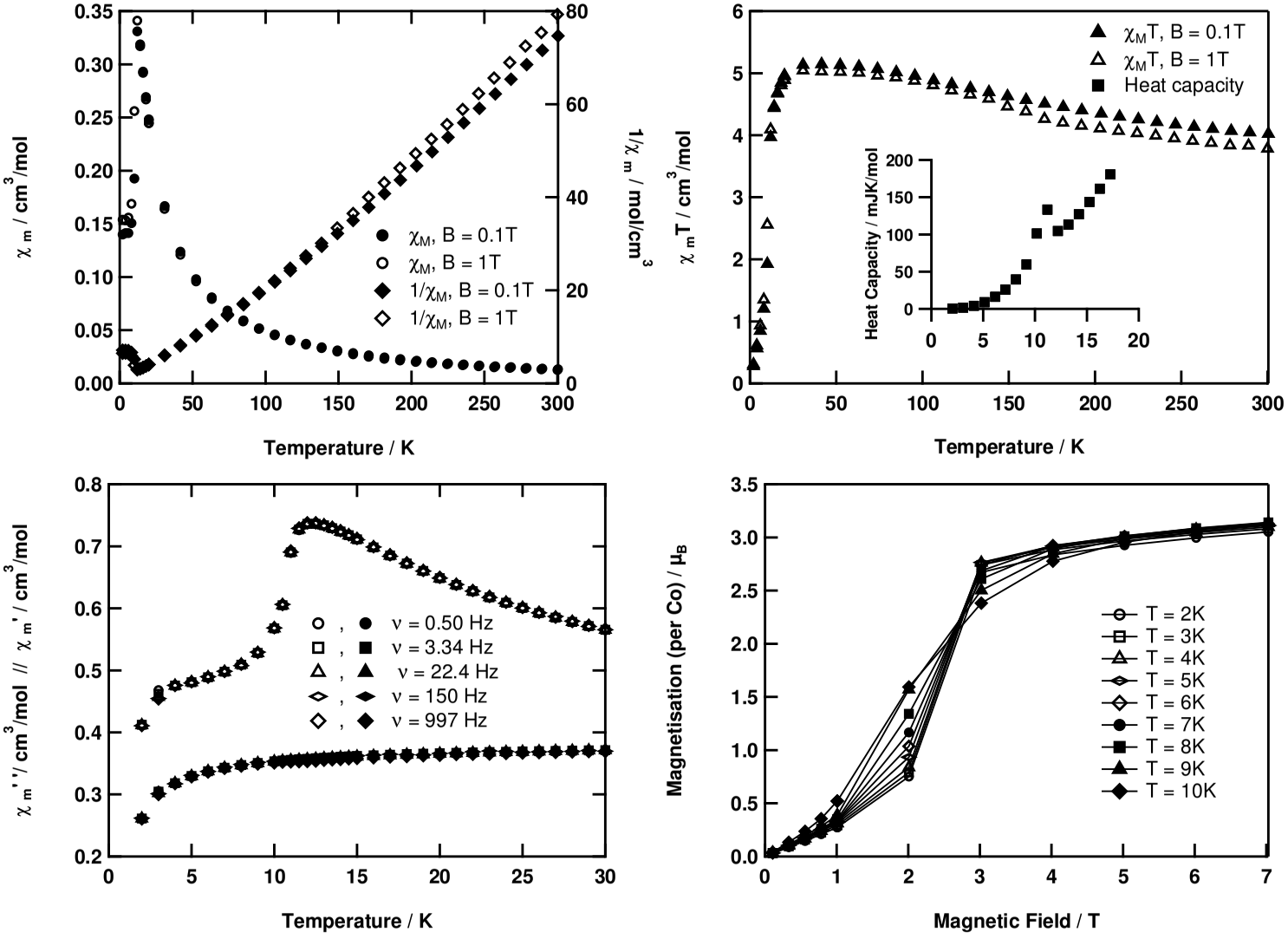

Figure 2.29: top left: Measurements of the magnetic susceptibility of $[Co(para\text{-}HOOCC_6H_4PO_3)]_n$ **(13)** with a field of 0.1T and a field of 1T are shown as χ_m vs. T and as χ_m^{-1} vs. T plots; top right: χ_mT vs. T plot of the magnetic susceptibility is shown, inset shows the total heat capacity vs. T, a phase transition at 11K is proven; bottom left: Measurement of the dynamic magnetic susceptibility with a static field of 3 Oe, no out-of phase signal (χ_m") was detected, no influence of the wave frequency *v* can be seen; bottom right: magnetisation measurements reveal a more complex behaviour below 10K

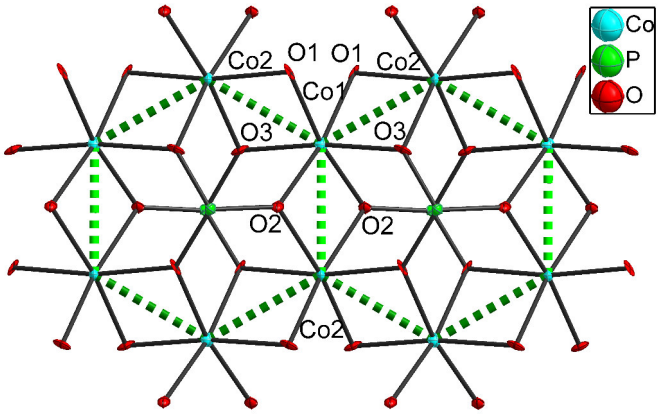

atoms	bond length / Å	atoms	angle /°
Co1-Co2 (dark green)	2.832(1)	Co1-O1-Co2	84.54(12)
Co1-Co2 (light green)	2.822(1)	Co1-O2-Co2	84.55(19)
		Co1-O3-Co2	85.04(13)

Figure 2.30: Cut off the inorganic metal-oxygen part of the crystal structure of [Co(para-$HOOCC_6H_4PO_3$)]$_n$ **(13)** with labelling of atoms; selected distances and angles are listed

ure 2.29. Measurements on single crystals would allow one to assign the easy axis in this system and then an appropiate magnetic model could be developed, what is not possible up to now due to the poor crystal quality of the sample. Nevertheless, it is proven by the experimental results that [Co(para-$HOOCC_6H_4PO_3$)]$_n$ exhibits a metamagnetic behaviour.

2.1.5.3 Summary: Two-dimensional Layered Systems build of Phosphonates

In this chapter entitled "Two-dimensional layered structures: Two modifications depending on the used phosphonate derivate", seven different two-dimensional layered divalent phosphonate structures have been discussed. The first modification of the extended inorganic hybrid materials was the corner-sharing metal-oxygen octahedra already known from the divalent phenylphosphonate compounds. Five new compounds with this binding motive in the inorganic metal-oxygen part were synthesized and fully characterised. They are divided in two series: the first one is described with the general formula [Co(R-$C_6H_4PO_3$)(H_2O)]$_n$ with R = para-H_3C, meta-H_3C and meta-HOOC. A dependence of the substituent can be found for the "strength" of the canted antiferromagnetic ordering at low temperatures, but the temperature itself seems to be unaffected. Enhancement of the

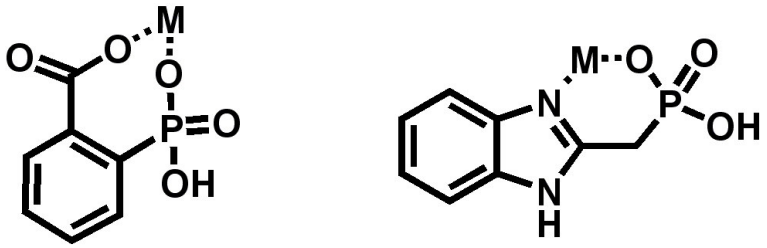

Figure 2.31: The consequence of the two functional groups in close proximity is schematically shown, the metal ion can be chelated in a seven-membered ring in case of the ortho-phosphonbenzoic acid shown right and a six-membered ring in case of the (1H-benzimidazol-2-yl-methyl)phosphonic acid shown left

canting is observed for compounds with substituents in the meta-position of the phenylring. The second series of compounds has the general formula [M(meta-$HOOCC_6H_4PO_3)(H_2O)]_n$ with M = Mn, Co and Ni. Overall the magnetic behaviour is quite similar to the one reported for the phenylphosphonate compounds. They are examples of canted antiferromagnets and the ordering temperatures T_N are similar to the one reported for the phenylphosphonate compounds except for the nickel derivate, where the temperature is higher. In general the magnetic behaviour was analysed using methods like the quadratic heisenberg lattice approximation or a non-critical scaling approach. Advantages and limitations of these models to describe the magnetic behaviour in these two series was extensively discussed.

A different modification of extended inorganic hybrid materials was realised with para-phosphonbenzoic acid as ligand. Edge-sharing of the metal-oxygen octahedra was found resulting so far not reported "binary" compounds with the general formula $[M(para\text{-}HOOCC_6H_4PO_3)]_n$, M = Co or Cu. The inorganic metal-oxygen part is described best with a honeycomb motive. In $[Cu(para\text{-}HOOCC_6H_4PO_3)]_n$, the inequality of exchange paths limits the honeycomb motive, thus a dimer model is appropiate to describe the magnetic behaviour. The magnetic behaviour of $[Co(para\text{-}HOOCC_6H_4PO_3)]_n$ is complex suggesting metamagnetic properties.

2.1.6 2 D - Layered Structures: Introduction of a Functional Group in Close Proximity

The ortho-derivate of the phosphonbenzoic acid is an interesting ligand, having the carboxilic acid and the phosphonic acid group in close proximity to each other, so it is expected that also the carboxilic acid is involved in the coordination of

the metal ion. This is in contrast to the already described compounds with the meta- and para-derivates, where the carboxilic acid group enhances just the stability of the hydrophobic organic bilayer region by hydrogen-hydrogen bonding. In the case of the ortho-derivate, the metal ion could be chelated in a seven-membered ring as schematically shown in figure 2.31. The exceptional position of the ortho-phosphonbenzoic acid was already discussed by the describtion of the titration curves in figure 2.3. Due to the close proximity of the carboxilic acid group and the phosphonic acid group an intramolecular ring closure can occur, that has a great influence on the pH-value. One two-dimensional layered structure could be obtained and is presented in the next paragraph. The second potential ligand already introduced is an aliphatic phosphonic acid with an additional benzimidazole residue in close proximity of the phosphonic acid group, namely (1H-benzimidazol-2-yl-methyl)phosphonic acid. Here again the second functional group is intended to coordinate to the metal ion, because a stable six-membered ring would be established as shown in figure 2.31. One compound with the aliphatic phosphonate compound could be characterised, however, it is not a two-dimensional layered compound, but a dimer.

2.1.6.1 A new motive in a two-dimensional layered structure: [Co(ortho-OOC $C_6H_4PO_3H)(H_2O)]_n$

As intended with the second functional group introduced in close proximity of the phosphonic acid, the carboxylate is also involved in the coordination of the metal ion in $[Co(ortho\text{-}OOCC_6H_4PO_3H)(H_2O)]_n$ **(15)**. The two times deprotonated ortho-phosphonbenzoic acid serves as a penta-dentate ligand using two of its three phosphonate oxygen atoms and the two carboxylate oxygen atoms to coordinate to the cobalt(II) ions. The remaining phosphonate oxygen is still protonated. One of the phosphonate oxygen atoms acts as a κ^2-bridge between two cobalt(II) ions resulting edge-sharing dimers of cobalt-oxygen octahedra. The octahedral coordination sphere of cobalt(II) is completed by a water molecule. The cobalt-cobalt distance within the dimer is 3.1806(4) Å and the Co-κ^2-O-Co angle is 98.79(5)°. These dimers are connected by both the carboxylate and the phosphonate groups, leading to a two-dimensional inorganic layer as shown in figure 2.32. Neighbouring layers are only connected through van der Waals interactions, resulting again a purely organic bilayer region. This compound is a further example of an extended inorganic hybrid material (I^2O^0).

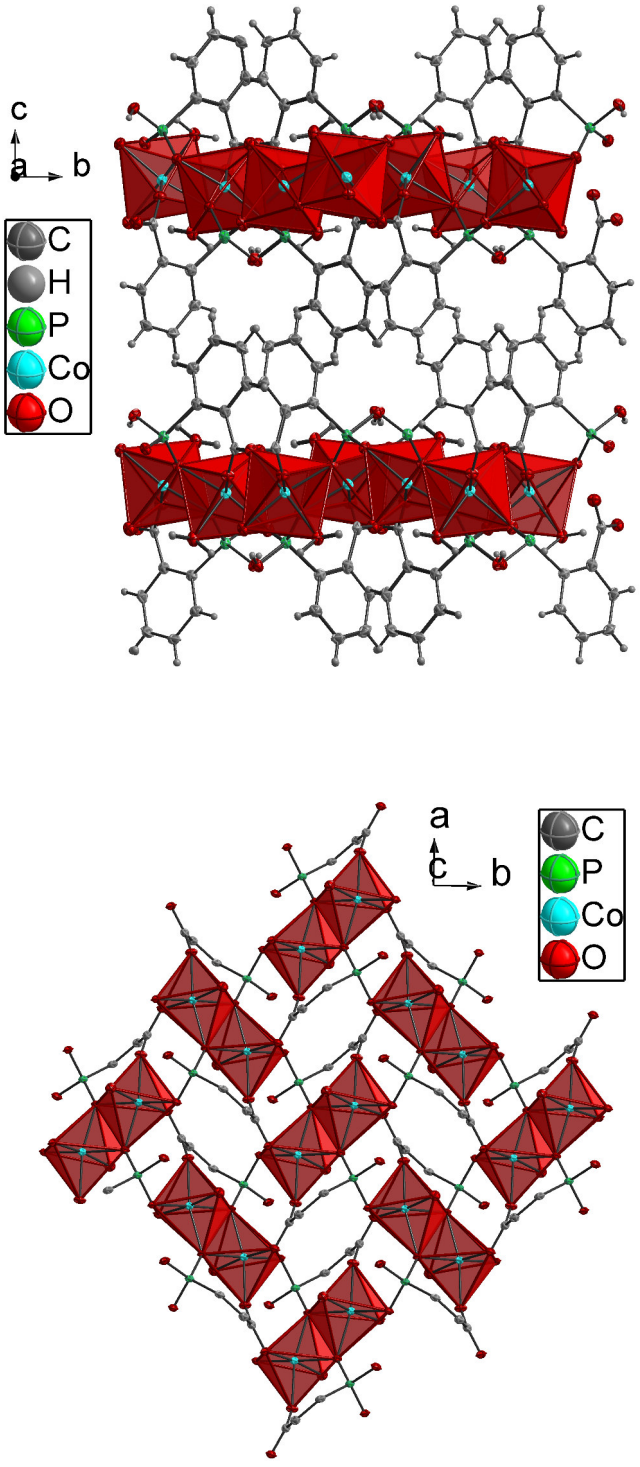

Figure 2.32: Part of the crystal structure of $[Co(ortho\text{-}OOCC_6H_4PO_3H)(H_2O)]_n$ **(15)**, left: new example of a layered extended inorganic hybrid material (I^2O^0) with a hydrophobic organic bilayer region, right: Cut-out of the inorganic metal-oxygen part, dimers of edge-sharing cobalt-oxygen octahedra are further linked in a two-dimensional layered structure, hydrogen atoms are omitted for clarity

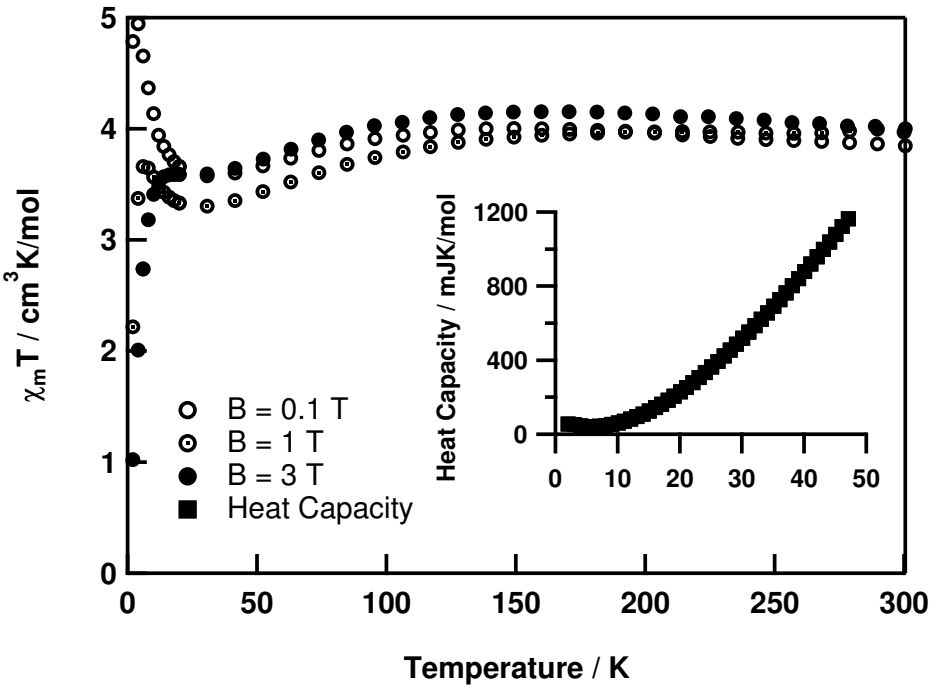

Figure 2.33: Measurements of the magnetic susceptibility of [Co(ortho-$OOCC_6H_4PO_3H)(H_2O)]_n$ **(15)** with a field of 0.1T, 1T and 3T are shown as χ_mT vs. T plots, inset shows the total heat capacity vs. T, no phase transition can be found

The compound was already published by Zheng et al. [109] as part of the isomorphous series with the general formula $[M(OOCC_6H_4PO_3H)(H_2O)]_n$ with M = Mn, Co, Ni. They intepretated the magnetic behaviour as a chain compound due to the fact that the exchange coupling through the double carboxylate and phosphonate bridge is the dominat one and for the manganese derivate they obtained resonable simulation parameters with a dominant antiferromagnetic interaction of -0.53 cm^{-1}. But in the case of the cobalt derivate their fitting procedure was not successful, because the κ^2-bridge between two cobalt(II) ions mediates a ferromagnetic interaction that has a comparable strength to the antiferromagnetic interaction mediated through the chain. These competing interactions can be clearly seen in the χ_mT vs. T plot measured at different fields shown in figure 2.33. The inset displays the heat capacity measurement and no hint for a phase transition can be found. All attemps to simulate this compound according to Lloret et al. [91], taking into account the spin-orbit coupling effects known for cobalt(II) ions in general [110], remain unsuccessful because of the present ferromagnetic interaction. Nevertheless, the presented approach of introducing a second functional group in close proximity to the phosphonate is successful in building up new two-dimensional layered materials with interesting magnetic properties.

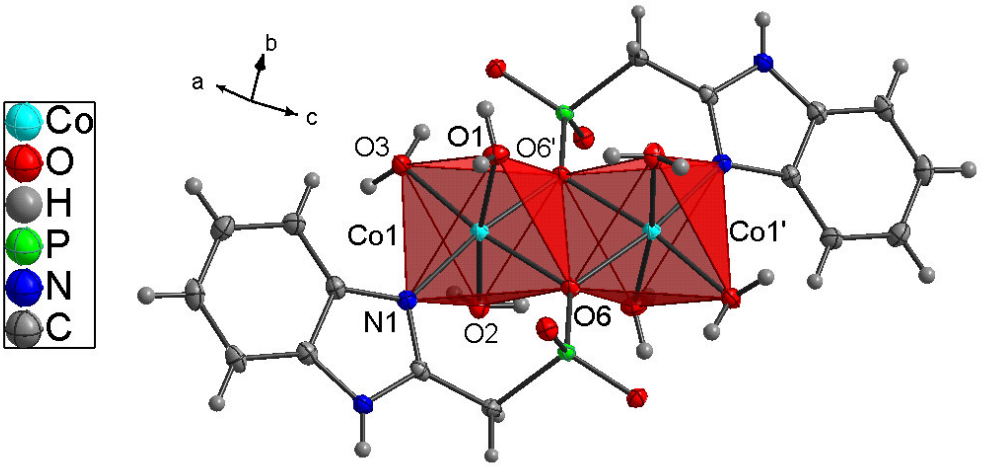

Figure 2.34: Part of the crystal structure of $[Co_2(H_2O)_6(O_3PCH_2C_7H_5N_2)_2]$*$6H_2O$ **(16)**

2.1.6.2 No two-dimensional layered structure, but a dimer: $[Co_2(H_2O)_6(O_3PCH_2C_7H_5N_2)_2]$*$6H_2O$

Again, as intended with the second functional group introduced in close proximity of the phosphonic acid, the benzimidazole residue is also involved in the coordination of the metal ion in $[Co_2(H_2O)_6(O_3PCH_2C_7H_5N_2)_2]$*$6H_2O$ **(16)**. But the presented compound is just a cobalt dimer, which is double bridged by a κ^2-O of the phosphonate ligand. The benzimidazole residue is coordinating to the cobalt(II) and a stable six membered ring is established. Three water molecules complete the octahedral coordination sphere of the cobalt(II) and due to the κ^2-O binding mode of the phosphonate ligand, the dimer can be described as two edge-sharing octahedra, shown in figure 2.34. The overall coordination geometry is not perfectly octahedral, but the distortion is comparable small e.g. the angles between O1-Co1-O2, O3-Co1-O6 and N1-Co1-O6' are in the range of 170.80(4)-172.51(4)°. The Co-Co intradimer distance is 3.204(1) Å and the Co-κ-O6-Co angle is 99.44(5)°. Overall the dimer is well isolated in the solid-state, see figure 2.35.

A similar 3d transition metal dimer with a double bridged κ^2-O of the phosphonate ligand, $[Mn_2(((C_7H_5N_2)CH_2)_2NCH_2PO_3)_2(H_2O)_2]$, also substituted with benzimidazole residues, was already reported in the literature [83]. The metal was in this case manganese(II). The manganese-manganese intradimer distance was 3.358 Å and the Mn-κ^2-O-Mn angle was 102.8°. There a weak ferromagnetic interaction was reported.

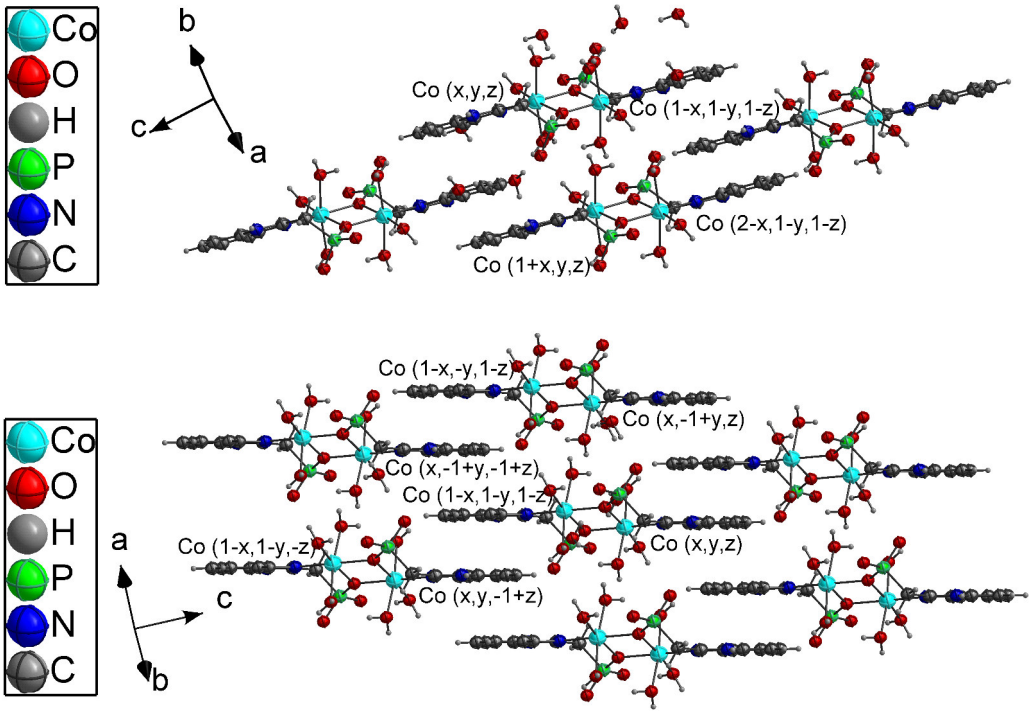

atoms	distance / Å
Co (x,y,z) - Co (1-x,1-y,1-z)	3.204(1)
Co (1-x,1-y,1-z) - Co (1+x,y,z)	6.389(4)
Co (x,y,z) - Co (1+x,y,z)	7.405(4)
Co (x,y,z) - Co (x,-1+y,z)	8.920(5)
Co (1-x,1-y,1-z) - Co (x,-1+y,z)	8.960(4)
Co (1-x,1-y,1-z) - Co (x,y,-1+z)	9.922(4)
Co (1-x,1-y,1-z) - Co (x,-1+y,-1+z)	10.480(4)

Figure 2.35: Part of the crystal structure of $[Co_2(H_2O)_6(O_3PCH_2C_7H_5N_2)_2]$*$6H_2O$ **(16)**; Packing of the dimers is shown with selected Co-Co distances; top: Packing in the ac-crystal plane; bottom: Packing in the bc-crystal plane

A weak ferromagnetic coupling can also be found in all compounds presented in this work, when the metal ions are bridged by κ^2-oxygens of a (hydrogen)phosphonate, namely $[Mn(meta\text{-}HOOCC_6H_4PO_3H)_2(H_2O)_2]_n$ **(9)** and $[Co(ortho\text{-}OOCC_6H_4PO_3H)(H_2O)]_n$ **(15)**. The magnetic susceptibility measurement of $[Co_2(H_2O)_6(O_3PCH_2C_7H_5N_2)_2]$*$6H_2O$ **(16)** is shown as χ_mT vs. T and χ_m vs. T in figure 2.36. Clearly again the ferromagnetic interaction can be seen at low temperatures, whereas the steady decrease with decreasing temperatures at higher temperatures has to be caused by the effect of spin-orbit coupling [110], since interdimer interactions can be excluded due to the good separation in the solid state. A simulation approach according to Lloret et al. [91], taking into account the influence of

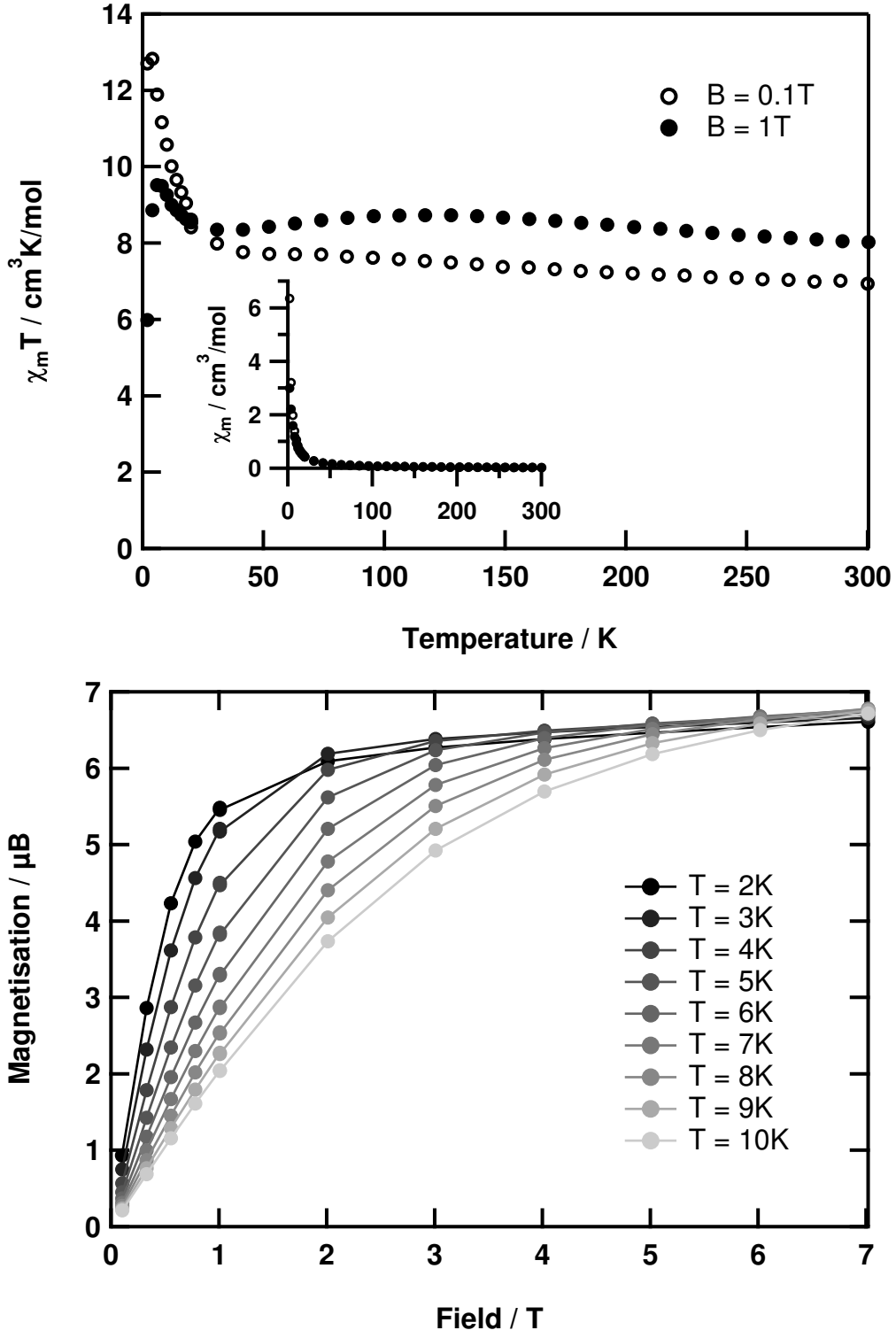

Figure 2.36: top: measurements of the magnetic susceptibility of $[Co_2(H_2O)_6(O_3PCH_2C_7H_5N_2)_2]*6H_2O$ **(16)** with a field of 0.1T and 1T are shown as χ_mT vs. T plots, inset shows the χ_m vs. T plots, bottom: field dependence of the magnetisation at different temperatures is shown

the spin-orbit coupling, was not successful, due to the ferromagnetic interaction present in this compound.

The question why this compound is only a dimer and not as intended a higher dimensional material might be answered by the fact that it was not obtained directly from the solvothermal reaction. It crystallised some days later from the mother liquid. By filtering off all insoluble material obtained during the reaction, probably of a higher dimensionality, the reaction conditions (ratio of metal to ligand, pH-value) were changed, so that then the dimer formation was favoured especially at room temperature. Although the benzimidazole residue is comparable bulky, several compounds are reported where the benzimidazole residue is even double bridging [111]. Probably depending on the temperature during the solvothermal reaction, other compounds of different dimensionalities could be realised with (1H-Benzimidazol-2-yl-methyl)phosphonic acid **(6)** as ligand.

2.1.7 3 D - Network Structures: The Choosen Approaches

Up to now the presented approach concerning the control of the dimensionality of the resulting compound by adjusting the pH-value during the reaction worked nicely, especially for the meta- and para-derivate of the phosphonbenzoic acid. Starting with the zero-dimensional compounds in highly acidic pH-range, over one-dimensional chain compounds obtained by a first deprotonation of the appropiate ligand to the two-dimensional layered compounds obtained by a second deprotonation step of the appropiate ligand, the dimensionality could clearly be influenced by the choosen reaction conditions. So by the complete deprotonation of the appropiate phosphonate ligand, mainly the phosphonbenzoic acid derivates, a three-dimensional network compound should be obtained. However, from these simple reaction conditions no three-dimensional network compound could be characterised up to now.

Taking a closer look on all obtained compounds with the meta- and para-derivates of the phosphonbenzoic acid obtained so far, it is remarkable that all are neutral compounds. Thus the charge balance is always realised by the deprotonating of the phosphonbenzoic acid derivate. In no case a counterion is incooperated in the structure and seldom a coordinated solvent molecule like water. With the complete deprotonation of the phosphonbenzoic acid, a three time negatively charged linker is created. With divalent transition metal ions used so far, no simple neutral composition of the resulting compound would be possible. For a simple metal

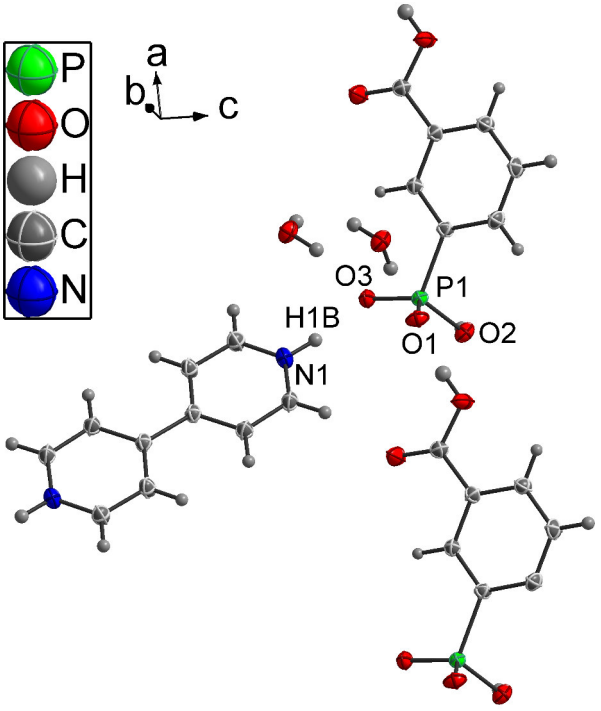

Figure 2.37: Part of the crystal structure of $[(HNC_5H_4C_5H_4NH)(HOOCC_6H_4PO_3H)_2]$ $*2H_2O$ **(17)**; Cocrystal of protonated 4,4'-Bipyridine and one time deprotonated hydrogenphosphonate anion is built of extended hydrogen-hydrogen bonding

to ligand ratio of one to one, an incooperation of an additional positive charged counterion would have been necessary.

Two possible approaches are presented in this section that should overcome this problem and lead to three-dimensional network structures. The first one is the use of the well-known divalent transition metal ions and the just two times deprotonated phosphonbenzoic acid, leading to two-dimensional layered compounds, as already presented. The linkage to a three-dimensional network structure is done by neutral co-ligands like 4,4'-Bipyridine which can in principle replace the coordinated water molecule still present in the first modification of the two-dimensional layered materials. The second approach is the use of higher charged metal ions.

2.1.7.1 Linkage of two-dimensional Layers with Co-Ligands

By using divalent transition metal ions and the just two times deprotonated metaphosphonbenzoic acid, two-dimensional layered compounds with the general for-

mula $[M(HOOCC_6H_4PO_3)(H_2O)]_n$ (M = Mn, Co, Ni) are obtained as already presented in section 2.1.5.1. The neutral co-ligand 4,4'-bipyridine was added to the starting reaction media to link the layers. This one pot synthesis was choosen due to the fact that the two-dimensional layered compounds are extremely insoluble (even under solvothermal conditions again) and a two-step procedure was not possible. However, no crystalline material could be obtained directly from the solvothermal reactions and just a co-crystal of protonated 4,4'-bipyridine and one time deprotonated hydrogenphosphonate ligand could be isolated from the mother liquid. Probably the 4,4'-bipyridine is too rigid as co-ligand and further co-ligands should be tested in the future for building up three-dimensional network structures.

2.1.7.2 Use of Higher Charged Metal Ions like Lanthanides

This approach of using higher charged metal ions like the lanthanides was successfully proven by Rueff et al. with the preparation of the three-dimensional network compound Eu(para-$O_3PC_6H_4COO$) [112]. As intended, by a simple one to one reaction of the lanthanide precursor, $Eu(NO_3)_3$ * 5 H_2O, with the ligand para-phosphonbenzoic acid, a neutral three-dimensional network was obtained. The crystal structure of [Eu(para-$O_3PC_6H_4COO$)] was solved by a combination of x-ray powder diffraction and electron diffraction due to the fact that the crystal quality was not good enough for single crystal x-ray analysis. The europium(III) ions have a sevenfold coordination sphere, where five oxygen atoms are provided by three different phosphonate ligands and two oxygen atoms by the carboxylate. The luminescence behaviour in comparison to the phenylphosphonate compound $[Eu(O_3PC_6H_5)(HO_3PC_6H_5)]$ is reviewed, but no magnetic measurement is reported.

In contrast to the published three-dimensional network compound [Eu(para-O_3P C_6H_4COO)], in this work only a dimeric praseodymium compound with the general formula $[Pr_2(H_2O)_8(HOOCC_6H_4PO_3H)_6]$ **(18)** could be obtained under similar reaction conditions. A part of the crystal structure is shown in figure 2.38. Clearly the κ^2-bridging mode of two phosphonate ligands can be seen, resulting in edge-sharing of the coordination polyhedrons. The praseodymium(III) ions are ninefold coordinated, where five oxygen atoms are provided by four different (hydrogen)phosphonate ligands and four oxygen atoms by coordinated water molecules. Two different deprotonation states of the meta-phosphonbenzoic acid

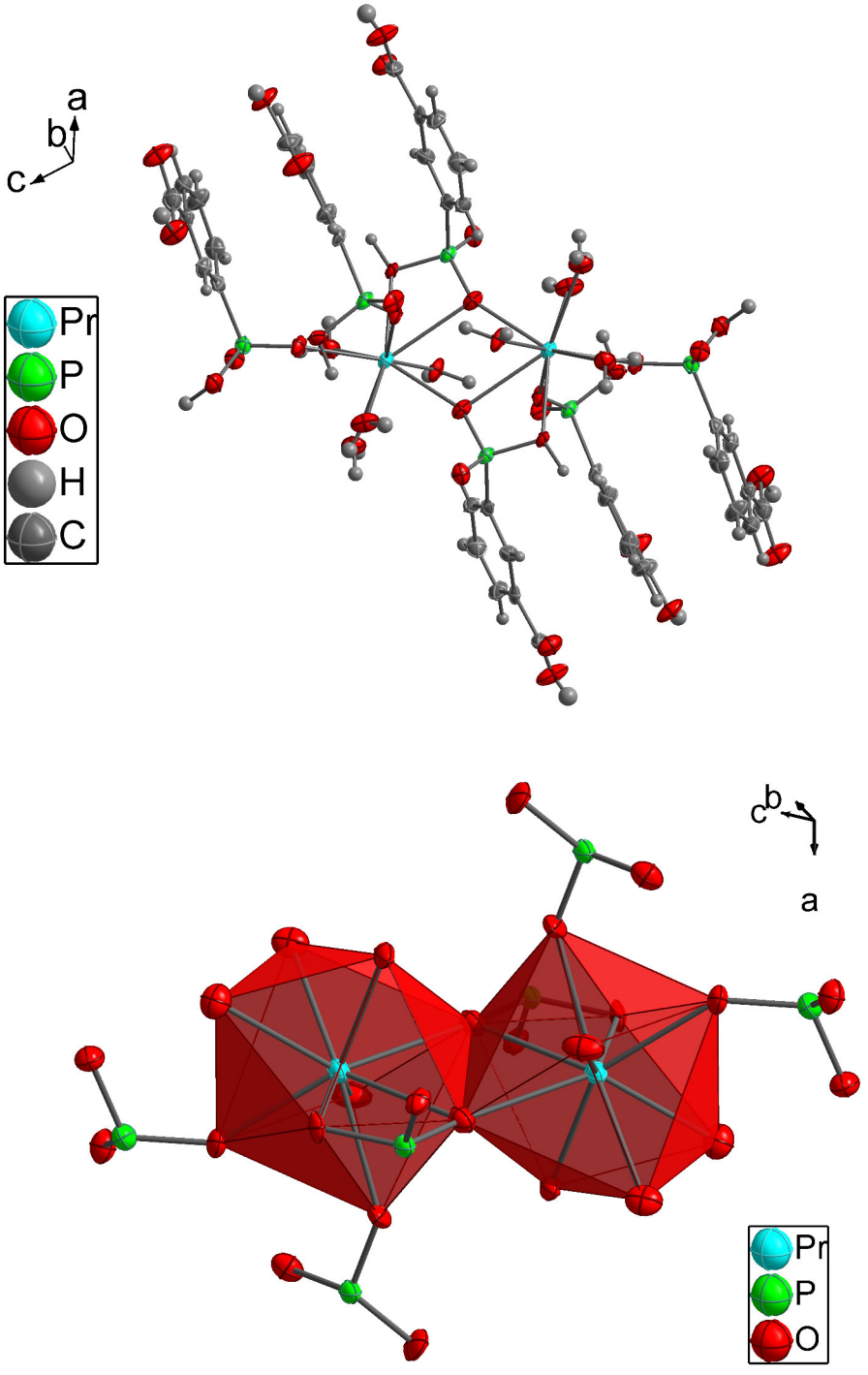

Figure 2.38: Part of the crystal structure of $[Pr_2(H_2O)_8(HOOCC_6H_4PO_3H)_6]$ **(18)**; the ninefold coordination sphere of the praseodymium(III) ion is shown, again a κ^2-oxygen of a phosphonate ligand is bridging the two praseodymium ions resulting an edge-shared coordination sphere

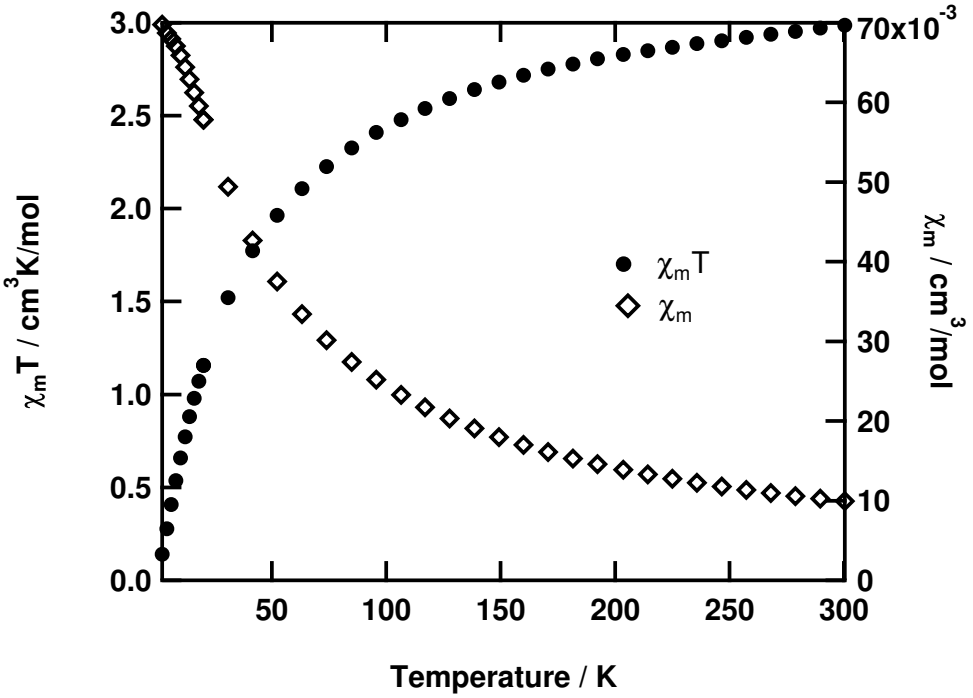

Figure 2.39: Measurements of the magnetic susceptibility of $[Pr_2(H_2O)_8(HOOC C_6H_4PO_3H)_6]$ **(18)** with a field of 1 T is shown as χ_mT vs. T plot and χ_m vs. T plot

can be found in the structure. The κ^2-bridging phosphonate ligand is two times deprotonated whereas the simple one-time coordinating ligands are only one time deprotonated hydrogenphosphonate ligands. The carboxilic acid group is in all cases protonated and involved in hydrogen-hydrogen bonding to adjacent dimers. The isostructural compound $[La_2(H_2O)_8\ (HOOCC_6H_4PO_3H)_6]$ with lanthanum as metal ion is already published [113].

The measurement of the magnetic susceptibility of $[Pr_2(H_2O)_8(HOOCC_6H_4PO_3H)_6]$ with a field of 1 T, shown as χ_mT vs. T plot and as χ_m vs. T plot, can be seen in figure 2.39. It is well known that for systems containing lanthanoid ions in general, the effects of the magnetic exchange coupling are much weaker than those of transition-metal ions, because the f orbitals are well shielded by outer s and p orbitals and less extended than d orbitals. Moreover, analysis of the magnetic interaction between rare-earth ions, except Gd(III) [114], are difficult since the magnitude of these interactions is comparable with that of the crystal field acting on the ion due to the large orbital contribution. As a result, isolation of the single-ion magnetic anisotropy from the exchange contribution in the analysis of the temperature dependence of the magnetic susceptibility is not possible. As far as praseodymium(III) is concerned, it possesses rather large unquenched orbital

angular momentum associated with the internal nature of the valence f orbitals and simultaneously has orbitally degenerate ground states, which are facile to be split by spin-orbit coupling and crystal-field effects. Although the χ_mT product decrease with decreasing temperature as can be seen in figure 2.39, antiferromagnetic coupling between adjacent praseodymium(III) ions could not be explicitly deduced due to the existence of strong spin-orbit coupling for lanthanide atoms. The decrease in χ_mT possibly originates in the thermal depopulation of the highest Stark components deriving from the splitting of the free-ion ground state $^3H_4$ by the crystal field [4]. Accordingly, any weak exchange interaction within the structure is masked by crystal-field effects.

Whereas lanthanum and praseodymium as ligther lanthanide(III) ions have bigger ionic radii and favour a ninefold coordination in the dimeric complex, the heavier europium(III) with a smaller ionic radius is satisfied with a sevenfold coordination sphere in the three-dimensional network structure. The influence of the phosphonbenzoic acid derivate has to be investigated in the future. Although the success of this approach for building up three-dimensional network structures is proven, the use of further three times charged metal ions should be exploited in the future.

2.1.8 PART 1: Summary Extended Inorganic Hybrids

It is remarkable that the presented concept, how to influence the dimensionality of the resulting compound, worked so nicely in case of the meta **(3b)** and para **(3c)** derivate of the phosphonbenzoic acid. The pH value adjusted during the reaction mainly determined the dimensionality of the product. In acidic conditions only a hydrogenphosphonate ligand with a protonated carboxilic acid group was realised, that in very acidic conditions was not bound to the metal(II) ions, but acted just as a counterion, e.g. in $[Ni(H_2O)_6$(meta-$HOOCC_6H_4PO_3H)_2]$*(meta-$HOOCC_6H_4PO_3H_2)_2$ **(7)** and $[M(H_2O)_6$(para-$HOOCC_6H_4PO_3H)_2]$*4(H_2O), M = Co **(8a)** and Ni **(8b)** . In acidic conditions, the hydrogenphosphonate ligand coordinated the metal(II) ions and two one-dimensional hybrid inorganic chain compounds (I^1O^0) were obtained. With $[Mn$(meta-$HOOCC_6H_4PO_3H)_2(H_2O)_2]_n$ **(9)**, an example of a rare linear alternating chain compound was presented. In contrast $[Co$(para-$HOOCC_6H_4PO_3H)_2(H_2O)]_n$ **(10)** was a linear regular chain, that displayed a spin-flop behaviour due to canted antiferromagnetic exchange interactions. Both are interesting examples of low-dimensional magnetic materials.

For two-dimensional compounds, two protons of the phosphonbenzoic acid

derivate have to be removed. Although the carboxilic acid group is clearly more acidic than the second proton of the phosphonic acid, under the mentioned conditions only two-dimensional extended hybrid inorganic compounds (I^2O^0) were obtained, where the phosphonate group is completely deprotonated and the carboxilic acid group is still protonated. Two different modifications of the two-dimensional extended hybrid inorganic compounds (I^2O^0) were found, depending on the used phosphonbenzoic acid derivate. The first modification was with meta-phosphonbenzoic acid as ligand. A series of compounds was obtained with the general formula $[M(meta\text{-}HOOCC_6H_4PO_3)(H_2O)]_n$ with M = Mn **(12a)** , Co **(12b)** and Ni **(12c)** . The inorganic layers consist of corner-shared metal oxygen octahedra, where an additional water molecule is needed to fulfill the coordination spheres. They are examples of canted antiferromagnets at low temperatures. The second modification was with para-phosphonbenzoic acid as ligand. The compounds with the general formula $[M(para\text{-}HOOCC_6H_4PO_3)]_n$ with M = Co **(13)** and Cu **(14)** consist of edge-shared metal oxygen octahedra with no further coordinated water molecules. The metal ions are arranged in a honeycomb motive and the resulting magnetic properties were discussed.

At this point it is important to emphasise again the influence of the choosen phosphonbenzoic acid ligand itself. Although the pH-value adjusted in the reaction media determines mainly the dimensionality of the resulting compound, the composition of the compound depends strongly on the used derivate. Ranging from zero-dimensional (I^0O^0, co-crystallisation of $M(H_2O)_6$ with the deprotonated phosphonate ligands), over one-dimensional (I^1O^0, chain structures) to two-dimensional (I^2O^0, layered structures), in all dimensionalities different compositions of the compounds are realised, depending on the used derivate of the phosphonbenzoic acid. The described pairs of hydrogen-bonded carboxilic acid groups act as synthons in building up extended inorganic hybrid materials. So, they determine the final composition as well as packing effects in general. Furthermore, the presented extended inorganic hybrid materials (1D: I^1O^0 and 2D: I^2O^0) can be classified as multi-functional and multi-dimensional materials. With the carboxilic acid groups an additional functionality is present, that is not involved in building up the extended inorganic hybrid materials.

In this work, the sterical influence of a methyl group of tolylphosphonic acid ligands on the resulting compound was investigated. Two new two-dimensional extended hybrid inorganic compounds (I^2O^0), $[Co(meta\text{-}CH_3C_6H_4\ PO_3)(H_2O)]_n$ **(11b)** and $[Co(para\text{-}CH_3C_6H_4PO_3)(H_2O)]_n$ **(11a)** were described. Here, the in-

organic layers consist again of corner-shared metal oxygen octahedra, where an additional water molecule is needed to fulfill the coordination spheres.

With a second functionality in close proximity to the phosphonic acid group, it is possible to obtain new two-dimensional layered materials (I^2O^0) with interesting linkage of the metal coordination polyhedra. An example is [Co(ortho-$OOCC_6H_4PO_3H)(H_2O)]_n$ **(15)**, here the ortho-derivate of the phosphonbenzoic acid **(3c)** is used as ligand. The exciting magnetic behaviour with different competing interactions was discussed. Furthermore, new compounds with lower dimensionalities can be obtained as the dimeric complex $[Co_2(H_2O)_6(O_3PCH_2C_7H_5N_2)_2]$*$6H_2O$ **(16)** with (1H-Benzimidazol-2-yl-methyl)phosphonic acid **(6)** as ligand.

Up to now, it was not possible to obtain a three-dimensional network compound (I^2O^1), whether a homometallic one nor a heterometallic one. Two approaches were described to overcome this problem. With the choice of an appropiate neutral co-ligand it might be possible to connect the two-dimensional extended hybrid inorganic compounds (I^2O^0). The success of the use of higher charged metal ions was already proven by the synthesis of Eu(para-$O_3PC_6H_4COO$) [112]. Here, with $[Pr_2(H_2O)_8(HOOC\ C_6H_4PO_3H)_6]$ **(18)**, a dimer is presented that consists as well of lanthanoide ions.

2.2 Coordination Polymers build of Carboxylate Ligands

This section is a completion to the main topic of extended inorganic hybrid materials build of phosphonate ligands. As already discussed in the introduction, hybrid inorganic-organic framework materials can be divided in the class of extended inorganic hybrids, where the presented phosphonate compounds play an important role, and in the class of coordination polymers. Here three different carboxylate bridged coordination polymers will be presented. The first one is a layered coordination polymer (I^0O^2) build of iron(II/III) ions, formiate ligands and γ-picoline as co-ligand. The second and third example are ladder-like chains (I^0O^1) of transition metal ions with acetate ligands and 4,4'-bipyridine as co-ligand.

In case of the smallest carboxylate, it is quite typical to have chain or layered structures for the divalent metal formiate hydrate salts like $Cu(HCOO)_2$*$4H_20$ [19]. By dehydratisation, three-dimensional coordination polymers are accessible like anhydrous manganese(II) formiate [20]. It is remarkable that the coordination sphere of the metal ions in most of the formiate compounds is completely saturated by oxygen donor atoms, wheter of the formiate itself or of water or other solvent molecules like alcohols. Only some exceptions can be found in the literature. In general the typical three-nuclear metal carboxylate cores bridged by a μ_3-oxo-bridge with apical nitrogen donors like pyridine are also accessible with the formiate [115], but these compounds are zero-dimensional (I^0O^0). There are only two coordination polymers with the formiate ion known with additional nitrogen donors, one is the two-dimensional sheet compound with the formula $[Fe^{II}_2Fe^{III}_2(HCOO)_{10}(C_6H_7N)_6]_n$, which can be classified as I^0O^2 material and which is discussed in section 2.2.1. The second example is a formiate chain compound which can be classified as I^0O^1 material, where trimeric manganese units are built of pyridyldioximato ligands and formiate ligands which are further connected by formiate [116]. Interestingly, by replacing the formiate by acetate or benzoate, the linkage of the trimeric manganese units is not possible and only zero-dimensional materials can be obtained. In case of the acetate in general, a lot of different coordination polymers are known due to the fact that small acetate clusters are used as secondary building units (SBU), like the paddlewheel complexes $[M_2(CH_3COO)_4]$, the basic zinc acetate structure $[Zn_4(CH_3COO)_6]$ or oxo-centered trimeric structures $[M_3(\mu_3\text{-}O)(CH_3COO)_6]$ [117]. With rigid ditopic nitrogen-donor ligands, also 4,4'-bipyridine, several classes of coordination polymers were build [118]. Two new derivates of the unexploited windmill motive as SBU with 4,4'-bipyridine resulting a double ladder chain are presented in section 2.2.2.

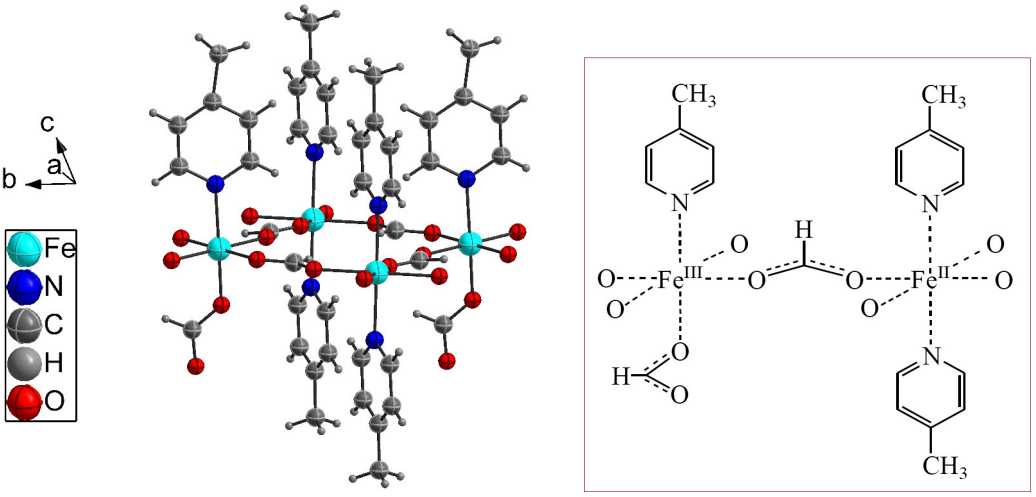

Figure 2.40: left: smallest crystallographic unit of $[Fe^{II}_2Fe^{III}_2(HCOO)_{10}(\gamma\text{-}C_6H_7N)_6]_n$ with four iron centers is shown in a ball and stick representation, right: scheme of the smallest magnetic unit with one iron(II) and one iron(III)

2.2.1 An interesting 2D Iron Formiate Layered Compound

The presented compound with the general formula $[Fe^{II}_2Fe^{III}_2(HCOO)_{10}(C_6H_7N)_6]_n$ **(19)** was already published by E. Rentschler et al. [119]. Although it is well-known as compound, the unusual magnetic behaviour is still not completely understood. With the here presented new methods like the single crystal SQUID measurement or the pressure dependent studies of the magnetic susceptibility, a deeper insight can be obtained. The compound will be shortly introduced, to give some background information for the afterwards presented new results.

$[Fe^{II}_2Fe^{III}_2(HCOO)_{10}(\gamma\text{-}C_6H_7N)_6]_n$ consists of alternating iron(II)- and iron(III)-sites, which are connected into a two-dimensional layered system by formiate ligands. The octahedral coordination sphere of every iron(II) is completed by two γ-picoline molecules whereas the coordination sphere of every iron (III) is completed by one γ-picoline ligand and one formiate ligand as can be seen in figure 2.40. The π-systems of the picoline molecules of neighbouring layers overlap, so that a π-π-stacking is observed. A structural phase transition is found at 20 K by single crystal synchrotron X-ray studies shown in figure 2.41. Here, two neighbouring iron-formiate layers are shown in top-view (on the 001 plane), one in red and one in black. On the left side is the high temperature modification displayed, where just short π-π-interations (within three γ-picoline residues) between the two neighbouring layers can be observed. Shown at the right side of figure 2.41 is the low temperature modification, where one γ-picoline residue on Fe(2) is reoriented, so that a long overlapping π-π-system between the two neighbouring layers

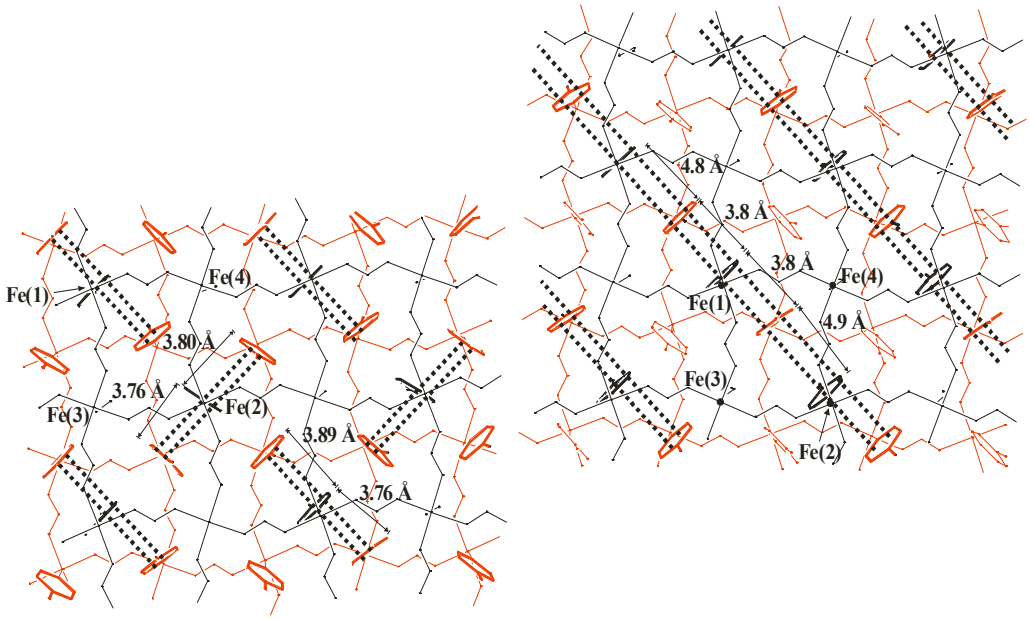

Figure 2.41: Structural transition of $[Fe^{II}_2Fe^{III}_2(HCOO)_{10}(\gamma\text{-}C_6H_7N)_6]_n$ at 20 K found by single crystal synchrotron X-ray studies; two neighbouring layers are displayed in top-view on the 001 plane; a change in the overlapping π-π-stacking can be seen due to a rotation of the γ-picoline residue on Fe(2); left: high temperature modification, short π-π stacking, only three γ-picoline residues are connected; right: low temperature modification: extended π-π stacking

is created. Especially interesting is, that this structural transition effects mainly the weakly bonded π-π-stacking of the γ-picoline residues and not the iron-formiate connection.

Furthermore, in the measurement of the magnetic susceptibility a sharp peak is observed at 20 K, typical of a magnetic phase transition, as already shown by Rentschler et al. [119]. The magnetic phase transition was also proven by temperature dependent measurements of the magnetisation, where even a hysteresis could be found at low temperatures. Additionally in temperature dependent mößbauer measurements, the magnetic splitting of the iron(II) and iron(III) signals could be found at low temperatures. The specific heat measurement shown in figure 2.42 suggests that both phase transitions, the structural one and the magnetic one, coincidence due to the fact that only one λ-shaped maximum is observed at 20 K. To what extend the change in the π-π stacking of the γ-picoline residues, namely the structural phase transition, affects the exchange couplings of the mixed-valence iron(II/III) species in and between the iron-formiate layers has still to be clearified.

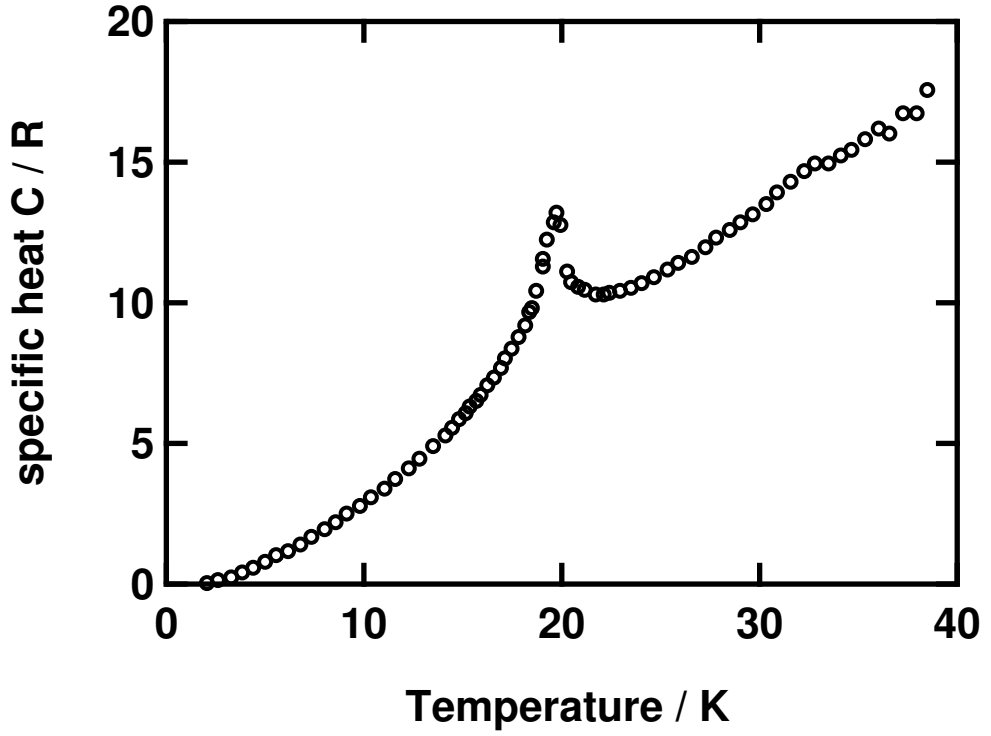

Figure 2.42: Measurement of the specific heat of $[Fe^{II}_2Fe^{III}_2(HCOO)_{10}(\gamma\text{-}C_6H_7N)_6]_n$; no correction for the lattice contribution ($\propto T^3$) was applied

In cooperation with T. G. and V. K. of the group of Prof. F., also University of Mainz, the pressure dependent behaviour of the magnetic susceptibility of $[Fe^{II}_2Fe^{III}_2(HCOO)_{10}$-$(C_6H_7N)_6]_n$ was investigated. A homemade pressure cell, using silicon oil as pressure-transmitting medium, was used. The cell has a weight of 8 g, a range of pressure 0-1.3 GPa can be applied with an accuracy ≈0.025 GPa, and non-hydrostaticity less than 0.05 GPa. Cylindrically shaped sample dimensions are 1 mm in diameter and 5-7 mm in length. The pressure was calibrated using the transition temperature of superconducting tin of purity 0.9999. A summary of the results is depicted in figure 2.43. Whereas an increase of the ordering temperature was expected with increasing pressure, because in a simple picture the shorter the interlayer and the intralayer distances of the mixed-valence iron(II/III) species, the larger the magnetic interactions, the magnetic behaviour is nearly unaffected by the increase in pressure. It is found, that the maximum in the χ*T vs. T plot of $[Fe^{II}_2Fe^{III}_2(HCOO)_{10}(C_6H_7N)_6]_n$ decreases with increasing pressure, as can be seen in figure 2.43. As a first approximation, the high-temperature behaviour is simulated with a simple dimer model $[Fe^{II}Fe^{III}(HCOO)_5(C_6H_7N)_3]$, which is schematically shown in figure 2.40, according to the Heisenberg-Dirac-van-Vleck Hamiltonian $\hat{H} = -2\sum_{i,j} J_{ij}S_iS_j$. So, the intralayer exchange coupling

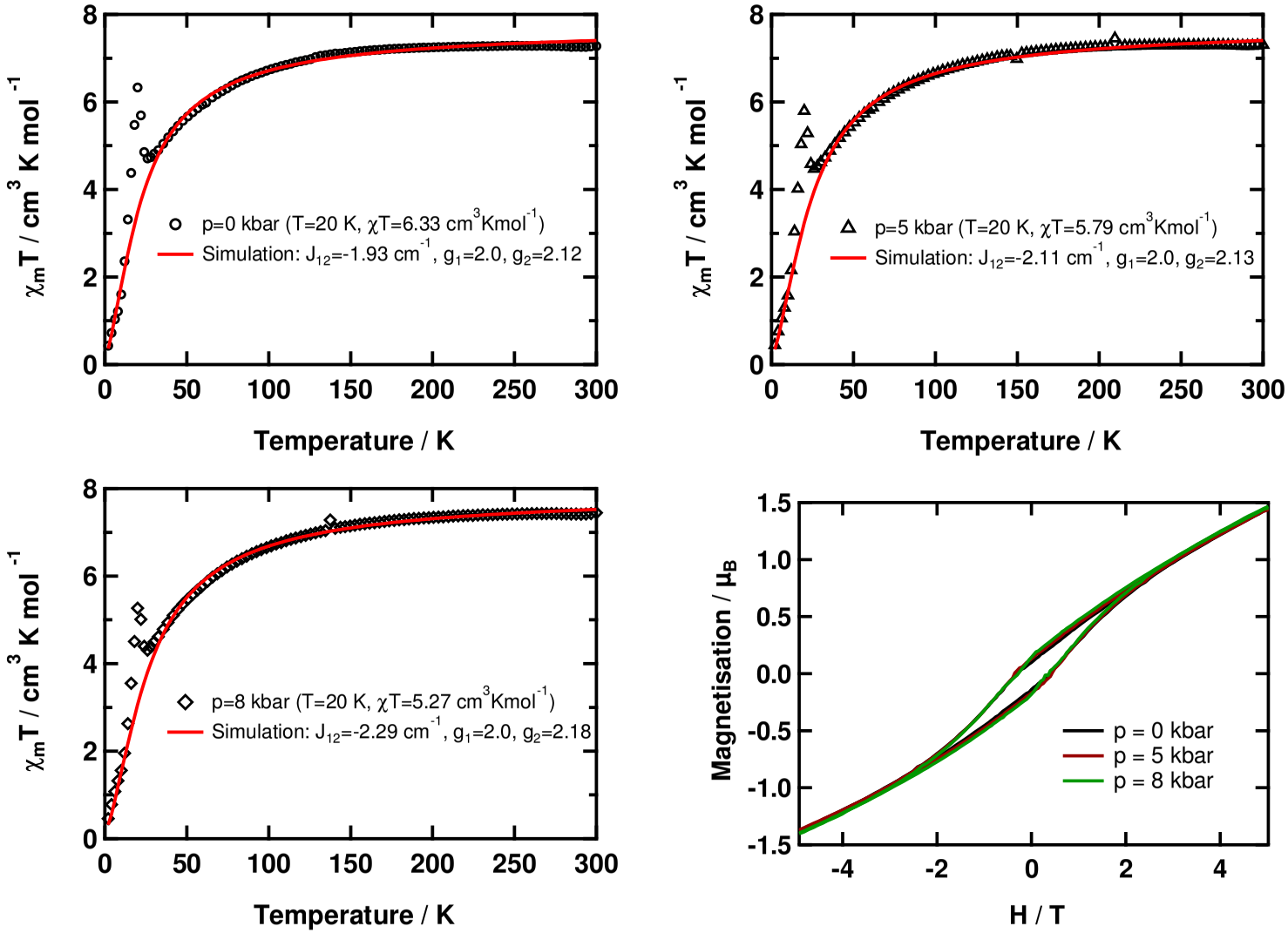

Figure 2.43: Measurement of the magnetic susceptibility of $[Fe^{II}_2Fe^{III}_2(HCOO)_{10}(C_6H_7N)_6]_n$ under different applied pressures at B = 1 T; the total mass of the sample could not be determined correctly due to the sample preparation in inert atmosphere, so a mass of 6.30 mg was assumed to match the measured data points; only the high-temperature region was simulated according to a dimer model according to the Heisenberg-Dirac-van-Vleck Hamiltonian $\hat{H} = -2\sum_{i,j} J_{ij} S_i S_j$; bottom right: field dependent measurements of the magnetisation under different applied pressures at T = 4.2 K, even a hysteresis is observed

J_1 can be estimated. The simulations reveal that the intralayer exchange coupling J_1 is increased, a result that was also observed in layered copper(II) compounds [120]. More appropiate model systems for the describtion of the magnetic susceptibility behaviour will be discussed in the future, also taking into account the observed hysteresis at low temperatures. But up to now, the nature of the magnetic phase transition is not clear, because a long-range antiferromagnetic order explains the decrease in the χ*T value at low temperatures, but not the occurence of a hysteresis, which is a typical feature of a ferromagnetic or ferrimagnetic order.

During the internship in the group of Prof. A. in Nagoya (Japan) the layered compound $[Fe^{II}_2Fe^{III}_2(HCOO)_{10}(C_6H_7N)_6]_n$ was also investigated by single crystal magnetic measurements and conductivity measurements. Before the presentation of the results, one has to admit that they are still preliminary ones due to several problems in the experimental setup in combination with the poor crystal quality of the compound so that up to now no further investigations were possible.

For the single crystal magnetic measurements of $[Fe^{II}_2Fe^{III}_2(HCOO)_{10}(C_6H_7N)_6]_n$, several indexed single crystals were mounted at the same time on the sample holder due to the fact that the crystal quality was poor. Already one "single crystal" was grown together as stack of thin sheet-like single crystals, so that the indexing of the crystal planes was only certain for the 001 plane, so that two measurements with different orientations have been possible (parallel to the 001 plane and perpendicular to the 001 plane) as can be seen in figure 2.44. A second problem in the single crystal measurement of $[Fe^{II}_2Fe^{III}_2(HCOO)_{10}(C_6H_7N)_6]_n$ is the low space group the compound crystallises in, $P\bar{1}$. Although β and γ are close to 90°, the approximation with an orthorhombic crystal system for reasons of practical realisation in the orientation of the single crystals (three 90° angles) is a rough one due to the fact that α is 65.8°.

In general, the same temperature dependence of the rotation dependent measurements of χ_m can be found compared with the powder measurement, χ_m passes through a maximum value for temperatures below 25 K. Also the values obtained for χ_m in the single crystal measurements matches the powder measurement which should be the average value of all orientations. This shows that the measurements of the SQUID is precise even when the mass of the sample is quite low (below 0.1 mg). In the first orientation, the applied magnetic field was at the beginning parallel to the 001 plane and after 90° perpendicular to the 001 plane and after 180° again parallel to the 001 plane and so on. The result of the rotation dependent measurements is shown at the top of figure 2.44. Clearly the anisotropy of

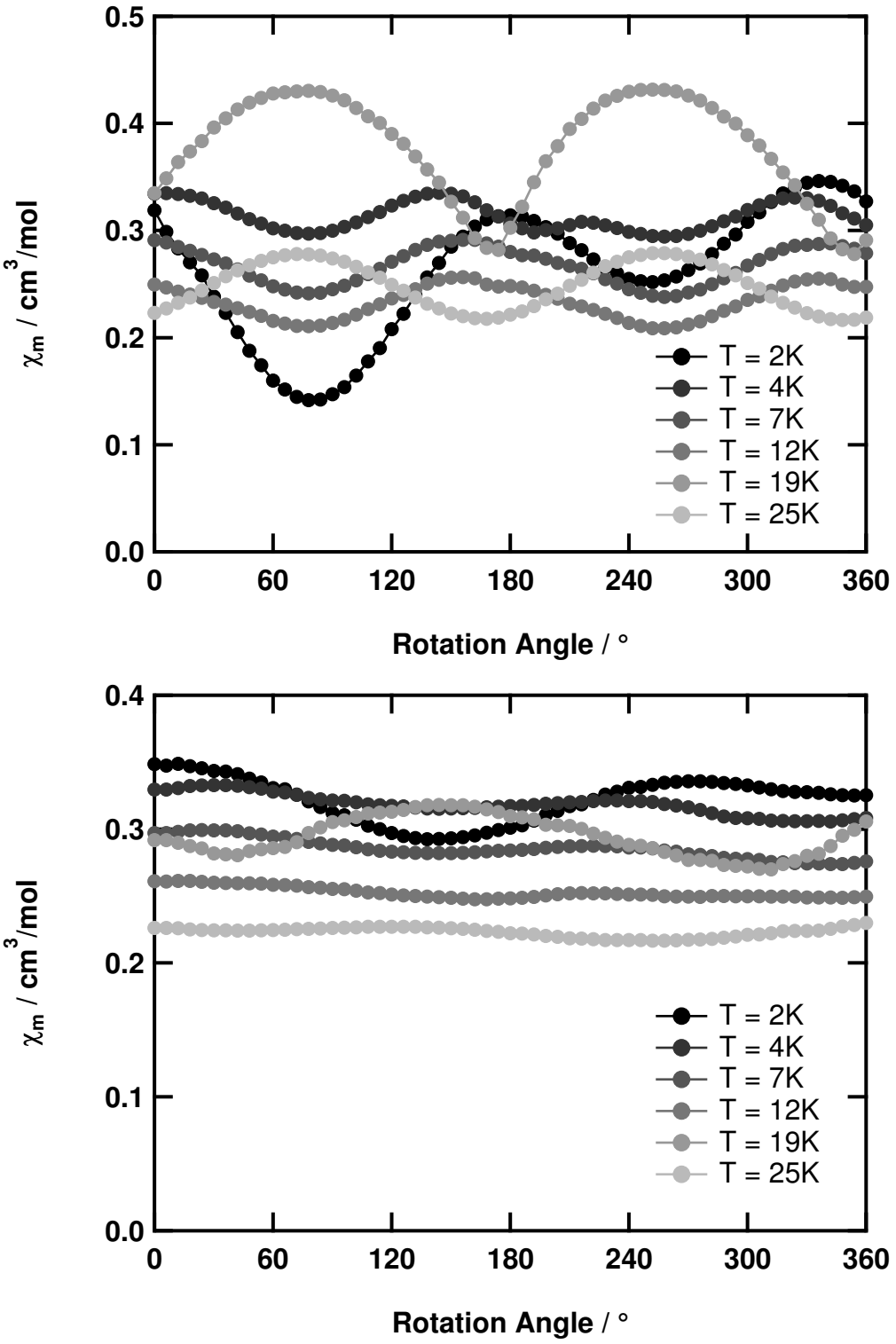

Figure 2.44: Rotation dependence of the magnetic susceptibility of $[Fe^{II}_2Fe^{III}_2(HCOO)_{10}(C_6H_7N)_6]_n$ measured with a static field of 1 T; top: single crystals were so oriented that the magnetic field is parallel to the 001 crystal plane at the beginning of the measurement; bottom: single crystals were so oriented that the magnetic field is always perpendicular to the 001 plane

the system can be seen with the appearance of a broad maxima occuring at 78° and 258° and a steep minima occuring at 174° and 354° at T = 19 K. Below T = 19 K, the orientation of the measurement is exactly opposite to the orientation above T = 19 K, where a maximum was observed there is now a minimum. If the maximum of the susceptibility measurement at low temperatures is the preferred "easy" axis or if the maximum of the susceptibility measurement at low temperatures is the non-preferred "hard" axis of the system, depends on the nature of the established long-range order. Also, a correlation of the anisotropy with the axes of the crystal structure is not possible. Nevertheless, it is proven that with the phase transition the preferred orientation of the anisotropy is rotated by 90°. In general a rotation symmetry is retained, that means that values of the rotation angles and the rotation angles + 180° are the same, except for T = 2 K, there this rotation symmetry is broken. In the second orientation, the applied magnetic field was all the time perpendicular to the 001 plane. The result of the rotation dependent measurements is shown at the bottom of figure 2.44 and as expected from the experimental setup, nearly no anisotropy can be seen due to the fact that the mounted crystals are not orientated in this direction, except for T = 19 K and T = 2 K, there some anisotropy can be seen (temperatures with the strongest changes). Further investigations of "real" single crystals would be very interesting, because closer insights in the nature of the long-range magnetic behaviour occuring at low temperatures could be obtained.

The conductivity measurements were carried out with home-made sample holders which could be evaporated, so that the air-sensitive sample $[Fe^{II}_2Fe^{III}_2(HCOO)_{10}(C_6H_7N)_6]_n$ was not destroyed during the measurements. Some grown together stacks of single crystals were fixed on an interdigitated electrode with tape as can be seen at the bottom right of figure 2.45 and contacted at two points with gold paste and gold wire to the voltameter. First different voltages were applied and the current was measured, as expected the current was very low (in the region of nano-ampere) and overall an ohmic behaviour was found as shown at the top left in figure 2.45. The contact of the sample to the interdigitated electrode is not perfect due to the fact that the sample is not flat, so the obtained values for the resistance R = 360 MΩ which corresponds to a specific resistance $\rho = R * (height * width/length)$ = 7 MΩcm and a conductivity $\sigma = 1/\rho$ = 1.39E-7 S/cm should be considered carefully. Furthermore, temperature dependent measurements were carried out, for that a thermo-couple was linked to the sample, so that the temperature of the sample could be determined. The cooling procedure was realised by bringing the evacuated sample holder in a dewar of liquid nitrogen and the heating procedure

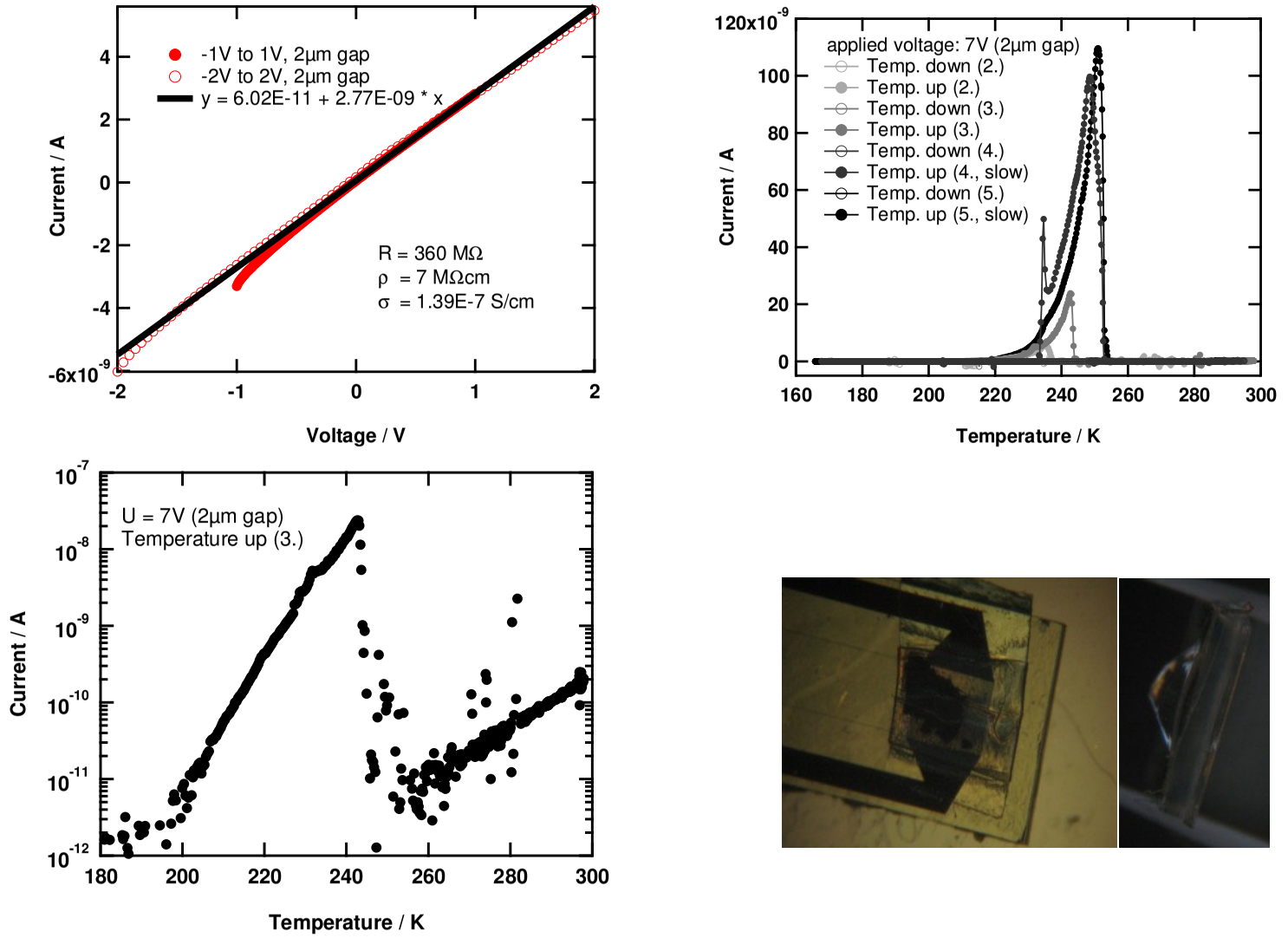

Figure 2.45: Measurement of the conductivity of $[Fe^{II}_2Fe^{III}_2(HCOO)_{10}(C_6H_7N)_6]_n$ with a interdigitated electrode shown at the bottom right; a nearly ohmic behaviour is found, shown at the top left; temperature dependent measurement of the current with an applied voltage of 7 V are shown at the top right; logarithmic scale of the current for a selected cycle is shown at the bottom left

was the removal of the dewar again. A constant voltage of 7 V was applied and the current was measured during cooling and heating cycles, the results are shown at the top right of figure 2.45. By lowering the temperature the current was also lowered, a behaviour that meets the expectations. Below 180 K the signal was lost (in the range of pico-amperes). By heating up the sample a different behaviour occurred, above 200 K the current increased much faster up to a temperature between 220 K and 250 K depending on the cycle number. Then it droped again to similar values obtained during the cooling cycle, although the temperature was further increased. A selected heating cycle is shown in a logarithmic scale at the bottom left of figure 2.45. In a first approximation two Arrhenius laws ($f(T) = A * exp(\Delta E/kT)$) can be simulated in the two different temperature regions 206 K - 240 K and 280 K - 298 K. For the low temperature region a high value for A is found with 1.9E+9 and an energy difference ΔE of 1.3E-19 J ($\approx$ 0.8 eV). For the high temperature region a low value of A is found with 2.5 and also the energy difference ΔE is smaller with 9.6E-20 J ($\approx$ 0.6 eV). The value of A is a hint for the mobility of the charge carrier, whereas the energy difference ΔE describes the band gap of the system, which is here comparable to the band gap in germanium.

To understand the conductivity behaviour of $[Fe^{II}_2Fe^{III}_2(HCOO)_{10}(C_6H_7N)_6]_n$ it is important to consider again the mixed-valence state realised in this compound. The blue colour is a hint for some metal-metal charge transfer, but it can be clearly seen in the mößbauer measurements, that the system is localised over a broad range of temperatures. Therefore, it can be classified as class I material according to Robin and Day [121]. The localised state (fixed oxidation states of each iron site) explains the overall low conductivity of being nearly an insulating material. Nevertheless, in the literature an ion-radical salt (also class I material) is known, where the conductivity was drastically increased by applying a large voltage and that the charge was partly delocalised [122]. Probably due to the high voltage applied, also a phase transition could occur in $[Fe^{II}_2Fe^{III}_2(HCOO)_{10}(C_6H_7N)_6]_n$, where the charge would be partly delocalised, explaining the higher conductivity. Further investigations are needed to clearify the conductivity behaviour of $[Fe^{II}_2Fe^{III}_2(HCOO)_{10}\ (C_6H_7N)_6]_n$. It is planned to repeat the conductivity measurements with a physical properties measurement system (PPMS), here the sample is contacted at four points, so that e.g. the contact resistance plays no role. So far, the air-sensitivity of the compound makes further investigations difficult. Nevertheless, in general due to the methods presented, new insigths were gained in the interesting magnetic behaviour of $[Fe^{II}_2Fe^{III}_2(HCOO)_{10}(C_6H_7N)_6]_n$.

2.2.2 Two Double-Ladder Chains build of Acetate and Bipyridine

The presented compounds with the general formula $[M_2(CH_3COO)_4(C_{10}H_8N_2)_2]_n$ (M = Fe, Co) with iron(II) **(20a)** and cobalt(II) **(20b)** as metal ions can be described as double-ladder chains, with two bidentately bridging acetate groups forming the double ladder step and chains of 4,4'-bipyridine forming the ladder stringer. Interestingly, there is also a second coordination mode of the acetate group in the compound present to complete the octahedral coordination sphere of the metal ions. Whereas one carboxylate bidentately bridges two metal atoms in a syn-syn fashion, the other is chelating one metal atom. This results in a distorted geometry of the metal ions as can be seen in the metal oxygen bonding angles (labeling according to figure 2.46). Due to the chelating coordination mode, the angle of O26-Fe1-O28 or O1-Co1-O3 is reduced to 58.86(9)° or 59.6(2)°, whereas the two bridging carboxylates open up the angle of O30-Fe1-O32 or O5-Co1-O7 to 124.3(1)° or 120.7(2)°. Both angles differ strongly from 90° for a perfect octahedral coordination, but the N1-Fe1-N10 and N17-Co1-N26 angles are with 176.6(1)° and 177.0° quite close to the expected 180° ones. The packing of the chains in the crystal is shown in figure 2.47 and selected metal-metal distances are listed. Due to the larger angle of the iron compound between the two bridging carboxylates (124.3(1)° compared to 120.7(2)° for the cobalt compound), the intrachain iron-iron-distance is with 3.960(1) Å shorter compared to the intrachain cobalt-cobalt distance (4.016(2) Å). In consequence also the distances to the neighbouring chains vary slightly, especially in the diagonal of the ac crystal plane (Fe (1-x, 1-y, 1-z) - Fe (x, -1+y, z): 8.195(1) Å and Co (x, -1+y, z) - Co (-x, 1-y, 1-z): 10.926(5) Å). But overall, the double-ladder chains build of acetate and bipyridine whether for iron or for cobalt are well separated in the solid state.

The binding motive $M_2(\mu\text{-OAc})_2(\eta^2\text{-OAc})_2$ is not unusual for the late 3d transition metals (M = Mn(II), Fe(II), Co(II), Ni(II) and Cu(II)), the same structure of a double-ladder chain build of acetic acid and 4,4'-bipyridine was already reported for manganese(II) [123] and copper(II) [80]. In these two structures the chains were additionally separated by a water molecule. Furthermore, the zinc(II) derivate $[Zn_2(\mu\text{-OAc})_2(\eta^2\text{-OAc})_2(C_{10}H_8N_2)_2]_n$ and a similar copper(II) compound $[Cu_2(\kappa^2\text{-OAc})_2(OAc)_2(C_{10}H_8N_2)_2]_n$, where the bridging acetate is, as the second acetate ligand, only coordinated in a monodentate way, were also reported [124]. For the sligthly different copper compound a weak antiferromagnetic interaction is found, what is surprisingly compared to the strong antiferromagnetic interaction in paddle-wheel complexes. In case of the manganese(II), a molecular system

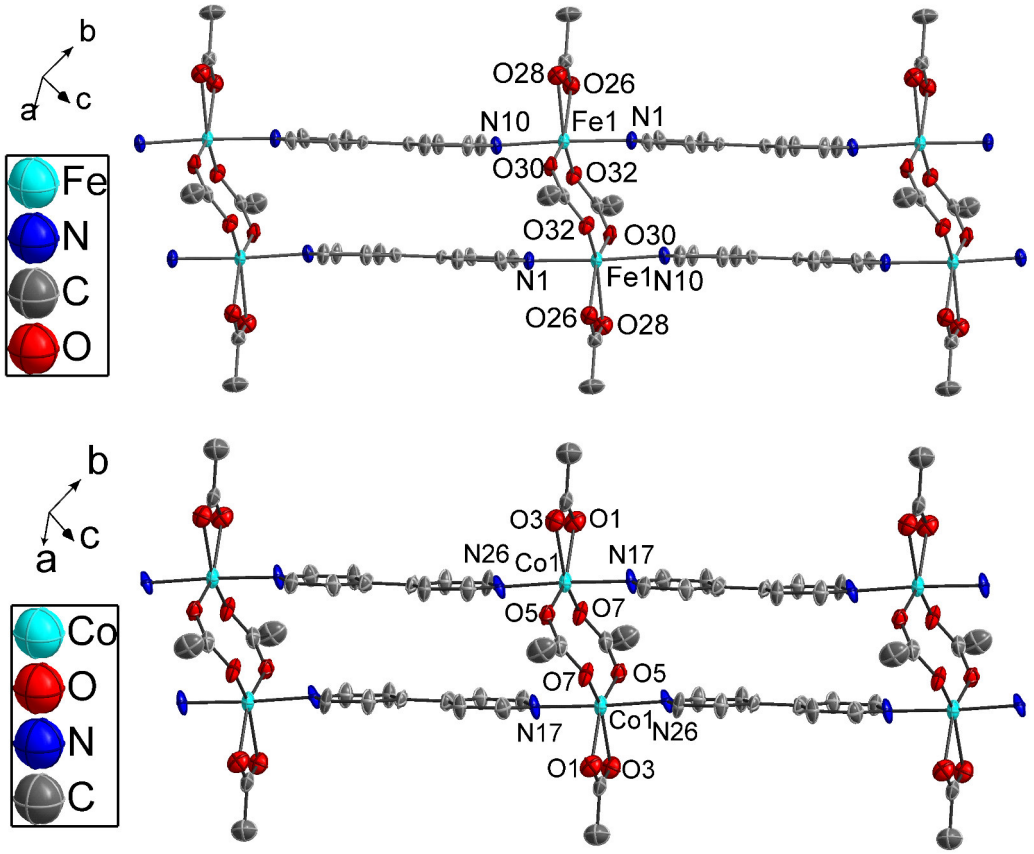

Figure 2.46: Part of the crystal structure of $[M_2(CH_3COO)_4(C_{10}H_8N_2)_2]_n$, shown for M = Fe(top) **(20a)** and Co **(20b)** (bottom); H atoms are omitted for clarity

with the dimanganese $Mn_2(\mu\text{-OAc})_2(OAc)_2$ motive was also reported [125], where a rigid organic clip with pyridines as monodentate coordination sites established a similar surrounding for the metal ions compared to the double-ladder chain. Here the magnetic behaviour was investigated and a small antiferromagnetic interaction of -1.6 cm^{-1} (for $S_1=S_2=5/2$ using the Hamiltonian $\hat{H} = -2\sum_{i,j} J_{ij} S_i S_j$) was found. For iron(II), the binding motive of two different carboxylate coordination modes, one bidentately bridging two iron atoms in a syn-syn fashion and the other chelating one iron atom is very prominent as model system for the methan monooxygenase enzymes (MMOs) [126]. Often bulky carboxilic acids were used, so that a windmill motive was obtained with a five coordinated iron species [127]. For cobalt(II) and nickel(II), there were compounds reported where the double-ladder chains were connected to a three dimensional network [111, 128]. In both cases polycarboxylate ligands, where again one carboxylate group bidentately bridges two metal atoms and another carboxylate chelates one metal atom, and 4,4'-bipyridine were used. For cobalt(II) the magnetic behaviour was investigated

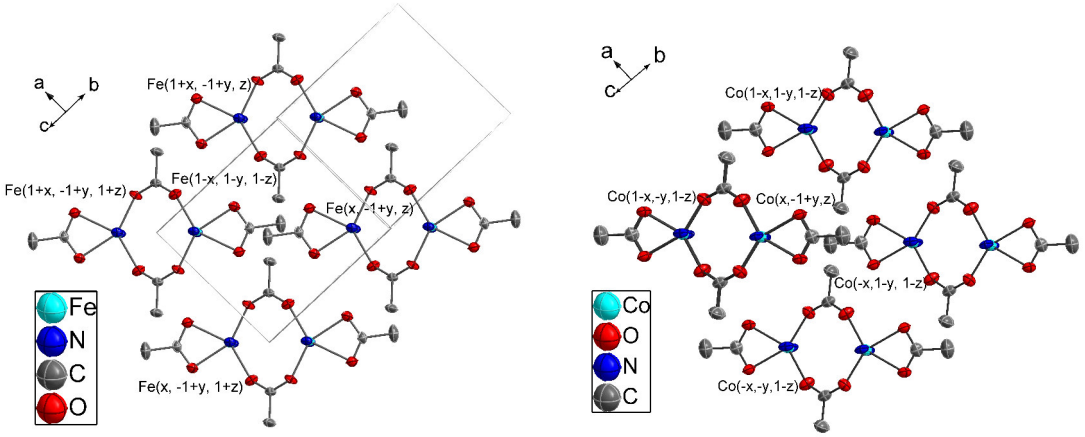

atoms	distance / Å
Fe (1-x, 1-y, 1-z) - Fe (1+x, -1+y, 1+z)	3.960(1)
Fe (1-x, 1-y, 1-z) - Fe (x, -1+y, 1+z)	6.660(1)
Fe (1-x, 1-y, 1-z) - Fe (x, -1+y, z)	8.195(1)
Fe (1-x, 1-y, 1-z) - Fe (1+x, -1+y, z)	8.225(1)
Co (x, -1+y, z) - Co (1-x, -y, 1-z)	4.016(2)
Co (x, -1+y, z) - Co (-x, -y, 1-z)	6.668(4)
Co (x, -1+y, z) - Co (-x, 1-y, 1-z)	10.926(5)
Co (x, -1+y, z) - Co (1-x, 1-y, 1-z)	7.971(5)

Figure 2.47: Packing of the double-ladder chains of $[M_2(CH_3COO)_4(C_{10}H_8N_2)_2]_n$, shown for M = Fe **(20a)** (left) and Co **(20b)** (right) with selected M-M distances labelled by symmetry; H atoms are omitted for clarity

and a weak antiferromagnetic interaction of -0.83 cm^{-1} (for $S_1=S_2=3/2$, isotropic dimer model with an additionally exchange coupling [129] zJ' = -0.09 cm^{-1}) is reported.

In general a ladder-chain is expected to have interesting magnetic properties, depending on the ratio between the magnetic exchange interaction through the ladder step (here called J_1) and through the ladder stringer (here called J_2). The Ising model of a ladder-chain predicts spin frustation effects when J_1 is antiferromagnetic, independently of the sign of J_2. So, the double chain behaves as a 1D ferromagnet when $J_2 > 2|J_1|$ or as a 1D antiferromagnet when $J_2 < 2|J_1|$. For $J_2 = 2|J_1|$ the system looks like a set of magnetically isolated spin centres giving rise to a Curie-like behaviour [130]. The reported values of the exchange coupling through the double acetate bridge are all weak and antiferromagnetic ($J_1 \approx$ -1 cm^{-1}) and also a weak and antiferromagnetic interaction can be expected through the bipyridine linkage.

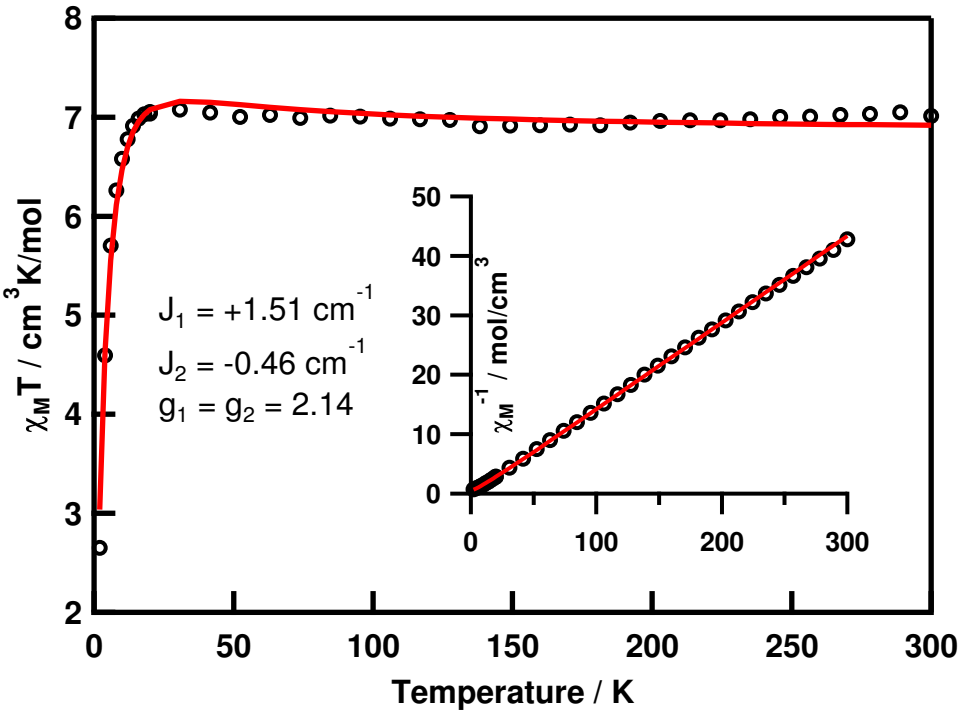

Figure 2.48: Measurement of the magnetic susceptibility of $[Fe_2(CH_3COO)_4(C_{10}H_8N_2)_2]_n$ at B=0.1T; Simulation of the magnetic data on basis of a simple dimer model (J_1 intradimer exchange coupling) with an additional mean-field interaction J_2

In figure 2.48 the measurement of the magnetic susceptibility versus temperature of $[Fe_2(CH_3COO)_4\ (C_{10}H_8N_2)_2]_n$ **(20a)** is displayed. As shown in the inset, the overall magnetic behaviour is Curie-like. The simulation of the magnetic data was done on basis of a dimer model (resembling one ladder step, J_1) with an additional mean-field term taking into account the interaction (J_2) through the bipyridine linkage [129]. The Heisenberg-Dirac-van-Vleck Hamiltonian $\hat{H} = -2\sum_{i,j} J_{ij} S_i S_j$ is applied. The χ_MT vs. T plot clarifies the sign of both interactions. Although both interactions are expected to be antiferromagnetic, it is only possible to simulate the data with J_1 being positive, but weak. As expected, J_2 is antiferromagnetic and even weaker as J_1.

For the cobalt derivate $[Co_2(CH_3COO)_4(C_{10}H_8N_2)_2]_n$ **(20b)** the situation is more complicated due to the influence of the spin orbit coupling. The simulation with a simple dimer model (for S_1=S_2=3/2 and g_1=g_2=2.48 with the Hamiltonian $\hat{H} = -2\sum_{i,j} J_{ij} S_i S_j$), again resembling one ladder step, is a reasonable first approximation as can be seen in figure 2.49. The obtained value for the exchange coupling J is with -1.26 cm^{-1} in the expected range. But the steady decrease in the χ_mT value with decreasing temperature can also be caused by the effect of spin-

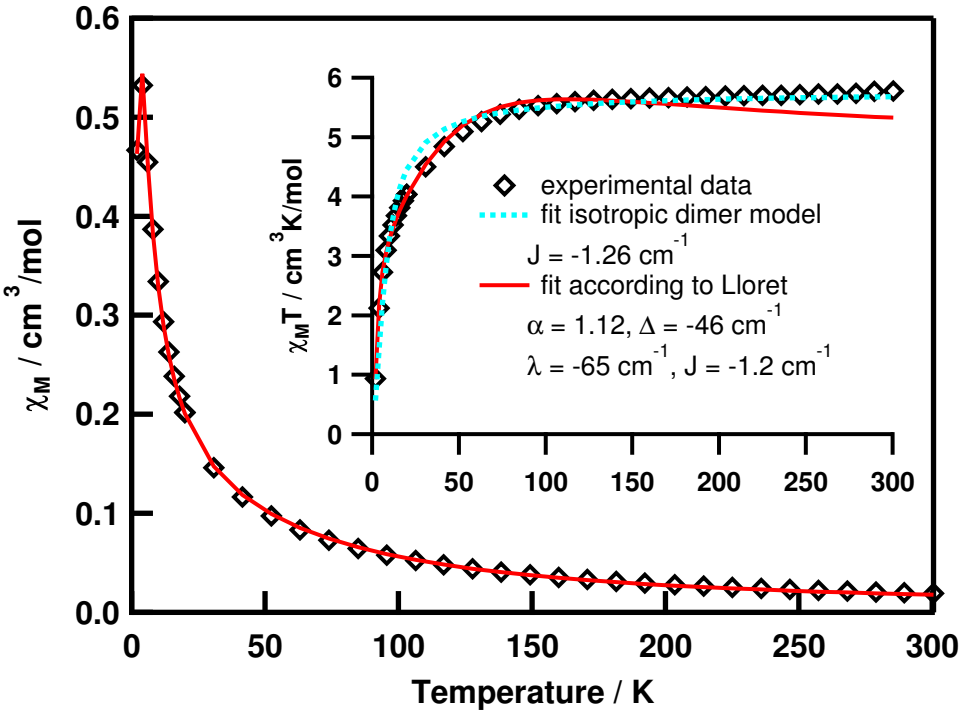

Figure 2.49: Measurement of the magnetic susceptibility of $[Fe_2(CH_3COO)_4(C_{10}H_8N_2)_2]_n$ at B=0.1T; Simulation of the magnetic data on basis of a dimer model modified for cobalt(II) compounds according to Lloret et al. [91]

orbit coupling [110], so that a second approach according to Lloret et al. [91] is applied. In the limit of weak magnetic coupling compared to spin-orbit coupling it is possible to describe the magnetic properties of six-coordinated high-spin cobalt(II) compounds with an empirical expression. An axial distortion is taken into account, so that the variable parameters are Δ (axial distortion parameter: 0-1000 cm^{-1}), α (orbital reduction factor: 0.75-1.5) and λ (spin-orbit coupling: 90-180 cm^{-1}). Furthermore the magnetic coupling J is incorporated by a perturbational approach, so that the magnetic susceptibility in the whole temperature range can be described as a function of J, Δ, α and λ. The calculation of the magnetic susceptibility of a polynuclear compound requires the treatment of each cobalt(II) ion as a spin doublet S=1/2 with a value of the Lande factor g described by an empirical expression G(T,J). For many compounds like dimers, high-nucearity complexes, one-dimensional chains or two-dimensional layered sytems analytical expressions are known in case of local spin doublets. Then the Lande factor g has to be replaced by the G(T,J) function and the spin value by an effective spin of 1/2, so that these expressions can also be applied on cobalt(II) compounds. A problem is still overparametrization, because four parameters (J, Δ, α and λ) are

applied in this model and often not so many parameters are needed. That is the reason why no mean-field correction term was added to describe the interaction through the bipyridine linker, a fifth parameter would have made the interpretation ambiguous. The values obtained for α, Δ and λ are all similar to the dimeric compound $[Co_2(bpym)_3(H_2O)_4]$ with bpym being 2,2'-bipyrimidine, introduced by Lloret et al. [91], where also a mixed nitrogen and oxygen donor atoms are present. Overall the distortion around the cobalt(II) ions is not so important, the value of Δ is quite small with 46 cm^{-1} and also the spin-orbit coupling constant λ is small. Furthermore the exchange coupling constant J is with -1.2 cm^{-1} quite close to the value obtained with the isotropic dimer model, so that in total the influence of the spin-orbit coupling is not that important in this compound.

In general, rigid ditopic nitrogen-donor ligands like 4,4'-bipyridine are often used in building up coordination polymers [118]. The advantage of using these rigid nitrogen-donor ligands is, that the assembly process can be controlled by the sterical constraints of these used co-ligand. Furthermore, several acetate bridged secondary building units (SBU) used as nodes in coordination polymers are known [117]. Here, two new metal ion derivates of the relatively unexploited windmill motive $[M_2(\mu_2\text{-}CH_3COO)_2(\eta^2\text{-}CH_3COO)_2]$ in coordination polymers were presented, which were further linked with 4,4'-bipyridine to a double-ladder chain compound. Interestingly magnetic interactions were expected due to the distorted coordination spheres of the metal ions, although the observed exchange interactions in $[Fe_2(CH_3COO)_4(C_{10}H_8N_2)_2]_n$ **(20a)** and $[Co_2(CH_3COO)_4(C_{10}H_8N_2)_2]_n$ **(20b)** were weak. Probably, it is possible to use other ditopic nitrogen-donor ligands for building up a new class of one-dimensional coordination polymers based on the new windmill motive.

2.2.3 PART 1: Summary Coordination Polymers

The here presented class of coordination polymers stand out due to the fact that the dimensionality of the compound can be controlled by the geometry of the node or secondary building unit (SBU) combined with the geometry of the linker. For $[Fe^{II}_2Fe^{III}_2(HCOO)_{10}(C_6H_7N)_6]_n$ **(19)**, the node is the iron species Fe(II/III) with an octahedral symmetry, and the linker is the formiate ion, which can be considered as a linear linker in this case. The γ-picoline is just a monodentate co-ligand, which limits the dimensionality of the compound to two-dimensional (I^0O^2). For $[Fe_2(CH_3COO)_4(C_{10}H_8N_2)_2]_n$ **(20a)** and $[Co_2(CH_3COO)_4(C_{10}H_8N_2)_2]_n$ **(20b)** , the presented windmill motive $[M_2(\mu_2\text{-}CH_3COO)_2(\eta^2\text{-}CH_3COO)_2]$ is as SBU the node with four possible contact points for the linker molecules. With linear ditoptic nitrogen-donor ligands ladder-like chain compounds (I^0O^1) are obtained. In general, the exchange interactions expected in coordination polymers is weak, because often the exchange path through the linker is long, e.g. in 4,4'-bipyridine. But with a careful selection of SBU and linker molecules it is possible to obtain interesting molecular magnetic materials.

In the case of the here presented extended inorganic hybrid materials, the dimensionality of the resulting metal phosphonate compounds were controlled by the pH-value adjusted during the reaction, because the degree of protonation of the phosphonate ligand was determining. In general, the exchange interactions expected in inorganic hybrid materials are strong, because often a superexchange through a single oxygen atom is possible. But often several competing exchange interactings are present, so that the observed magnetic behaviour is complicated. Independently of the used class of hybrid inorganic-organic framework materials, interesting molecular magnetic materials can be designed due to the fact that the dimensionality of the compounds can be controlled.

3

PART 2: Nitronyl-Nitroxide Radicals

Nitronyl-nitroxide radicals (NIT) are a class of stable radicals, that can be used as spin carriers in molecular magnetic materials. The unpaired electron is located in the π^*-orbital of the nitronyl-nitroxide unit. As a typical example the first nitronyl-nitroxide radical Phenyl-NIT, published by Ullman et al. [48] is described in section 3.1.1. The organic residue at the 2-position of the NIT radical can be manifold varied. The first purely organic ferromagnet build of only light elements like C, H, N and O should be mentioned, a nitronyl-nitroxide radical with a nitro-group NO_2 in para-position of the phenylring, namely 2-(4-nitrophenyl)-4,4,5,5-tetramethyl-4,5-dihydro-1H-imidazol-1-oxyl-3-N-oxide (short: pNO_2-NIT). At low temperatures (below 0.65 K), the β-phase pNO_2-NIT undergoes a phase transition to a ferromagnetic ordered state [52]. In this work, three new examples of nitronyl-nitroxide radicals are presented in section 3.1.2, where the additional functionality is an acidic one. The acidic character of the additionally introduced sulfonic acid group (SO_3H-NIT **(33)**) or phosphonic acid groups (in para: pPO_3H_2-NIT **(27a)** , in meta mPO_3H_2-NIT **(27b)**) has consequences for the nitronyl-nitroxide radical unit, what is investigated in detail for the first time.

With pPO_3H_2-NIT **(27a)** and mPO_3H_2-NIT **(27b)** , two perfect samples for the investigation of the spin shift in nitronyl-nitroxide radicals by EPR spectroscopy in general are obtained due to the phosphorus present in the second functional

group. The investigation of the spin density in pPO_3H_2-NIT **(27a)** and mPO_3H_2-NIT **(27b)** , depending on the protonation state of the additional phosphonic acid group, is presented in section 3.2.

Furthermore, the nitronyl-nitroxide radical group can coordinate directly metal ions. With this so called "metal-radical approach" [60], several interesting molecular magnetic materials have been discovered. The first example of a single chain magnet (short: SCM), an one-dimensional compound showing slow magnetic relaxation and hysteresis effects of dynamic origin without any evidence of a phase transition to three-dimensional magnetic order, was the cobalt nitronyl-nitroxide chain $[Co(hfac)_2(NITPhOMe)]_n$ [42]. A second functional group introduced at the 2-position of the nitronyl-nitroxide radical unit can as well coordinate to metal ions. Here, in this work the first metal complexes of the new acidic substituted nitronyl-nitroxide radicals pPO_3H_2-NIT **(27a)** and mPO_3H_2-NIT **(27b)** are presented. In section 3.3, the coordination of nickel(II) metal ions to the acidic, second functional group of the nitronyl-nitroxide radical is described. The magnetic exchange interactions of the metal ions and the metal-radical exchange interactions are investigated.

3.1 The pH-Dependendence of the Nitronyl-Nitroxide Unit

3.1.1 Revision of the Phenyl-NIT derivative

In the first publication of the synthesis of a nitronyl-nitroxide radical, the Phenyl-NIT derivative by Ullman et al. [48], already a qualitative describtion of several processes possible with the Phenyl-NIT is given. In figure 3.1 the most interesting part, the behaviour against different aqueous acids is depicted with a list of characteristic features of the different obtained species Phenyl-NIT **(IV)**, the protonated species $[NIT\text{-}H]^+$ **(V)** and the oxidized species $[Phenyl\text{-}NIT]^+$ **(VI)**. The different species were characterised by EPR and UV/Vis spectroscopy. The EPR spectra of a nitronyl-nitroxide radical is a quite characteristic five line pattern, because the radical is located in the π^*-orbital of the nitronyl-nitroxide unit. The electron spin (S = 1/2) interacts with the nuclear spin of the two nitrogen nuclei (I = 1), which are equivalent. The hyperfine coupling to the nitrogen nuclei is at room temperature A_{iso} = 7.5 G = 0.75 mT (isotropic case). At low temperatures (T = 20 K), an axial distorted spectra ($A_{iso} = 1/3*(2*A_\perp + A_{II})$) is obtained with a strong coupling parallel to the field, because the unpaired electron is located in a π^*-orbital of a

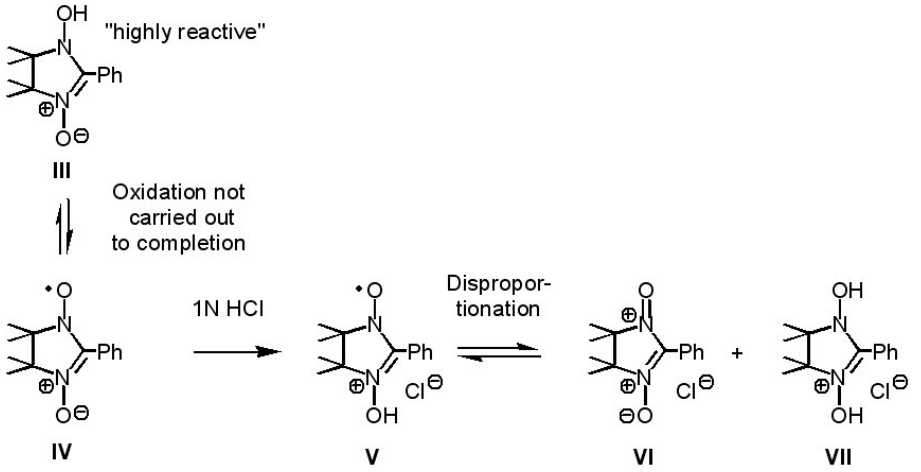

derivative	III	IV	V	VI / VII
EPR	/	five lines	reduced signal	diamagnetic
g	/	2.00651	2.00651	/
A_N/G	/	7.5	7.5	/
UV/Vis / nm	239, 317	238, 263, 360, 588	/	/

Figure 3.1: Processes, conditions and derivatives (III-VII) described by Ullman et al. [48]

nitronyl-nitroxide unit, derived of a p_z-orbital of the nitrogen atom. The g-value is close to the value of a free electron, $g_e = 2.0023$, as expected for an organic radical. In the UV/Vis spectra of nitronyl-nitroxide radicals typically three different transitions can be assigned (values were obtained in ethanolic solution). First a $\pi - \pi^*$-transition of the phenylring at 238 and 263 nm, second a $\pi - \pi^*$-transition of the NO group at 360 nm and third a $n - \pi^*$-transition of the NO group at 588 nm. Although the last transition is Laporte forbidden, so weak in intensity, it is responsible for the typical blue colour of nitronyl-nitroxides in general.

By now, also X-ray single crystal structures of Phenyl-NIT **(IV)** [131] and its oxidized form $[\text{Phenyl-NIT}]^+$ **(VI)** [132] are known. Parts of the crystal structures can be seen in figure 3.2, together with a comparison of selected bond lengths and torsion angles typical of the nitronyl-nitroxide radicals in general. Although the radical is delocalised in the nitronyl-nitroxide unit of Phenyl-NIT **(IV)**, differences in the N-O bond lengths and C-N bond lengths can be found in the solid state. In general the conjugation of the nitronyl-nitroxide unit is reflected in the N-O bond lengths, since the averaged N-O bond length $\approx$ 1.27(2) Å is smaller compared to those found in other nonconjugated dialkyl nitroxides, e.g. TEMPO (1.296 Å) [133]. In general the phenyl ring attached to the 2-position of the nitronyl-nitroxide unit stabilises the radical, because of an expansion of the aro-

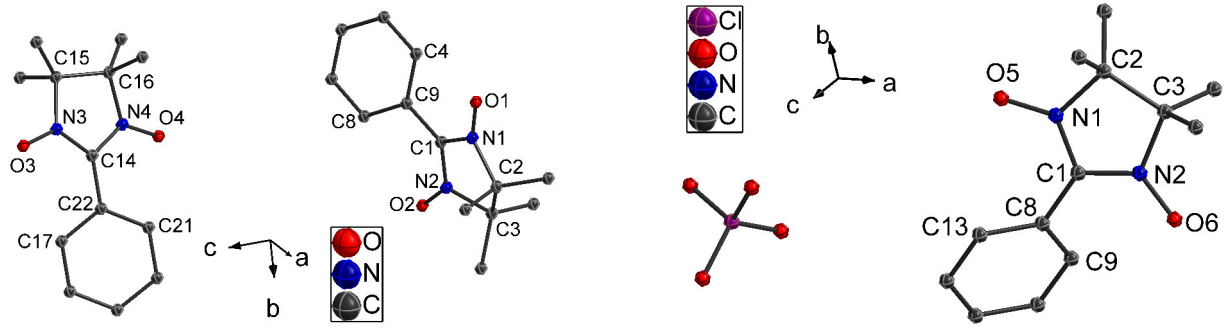

short CCDC	Phenyl-NIT MPIMZR01 [131]				[Phenyl-NIT]$^+$ FENCAC [132]	
/ Å	C1-N1	1.344(8)	C14-N3	1.336(8)	C1-N1	1.342(6)
/ Å	C1-N2	1.364(6)	C14-N4	1.373(8)	C1-N2	1.343(6)
/ Å	C2-N1	1.511(7)	C15-N3	1.503(5)	C2-N1	1.513(6)
/ Å	C3-N2	1.538(9)	C16-N4	1.488(6)	C3-N2	1.513(6)
/ Å	N1-O1	1.261(7)	N3-O3	1.278(9)	N1-O5	1.223(5)
/ Å	N2-O2	1.274(9)	N4-O4	1.269(9)	N2-O6	1.227(5)
/ °	C4-C9-C1-N1	24.5(9)	C17-C22-C14-N3	31.7(9)	C13-C8-C1-N1	38.4(6)
/ °	C8-C9-C1-N2	24.6(9)	C21-C22-C14-N4	28.1(9)	C9-C8-C1-N2	39.0(6)
/ °	N1-C2-C3-N2	25.9(6)	N3-C14-C15-N4	25.6(5)	N1-C2-C3-N2	3.7(4)

Figure 3.2: Part of the literature known crystal structures of Phenyl-NIT (two molecules in the asymmetric unit; labelling according to figure 3.1: **(IV)**) and its oxidized form [Phenyl-NIT]$^+$ (4,4,5,5-tetramethyl-1-oxo-2-phenyl-4,5-dihydroimidazolium perchlorate N(3)-oxide; labelling according to figure 3.1: **(VI)**, here the perchlorate salt is shown); H atoms are omitted for clarity; Selected bond lengths and torsion angles are listed

matic system. But the two ring systems, the phenyl ring and the imidazoline ring are not co-planar, they are twisted against each other. The reason for the twisting is the sterical hindrance of the oxygens of the NO-bond with the ortho-hydrogens of the phenyl ring [134]. This effect is known as atropisomerism and can lead to axial chirality. The differences in the C-C-C-N torsion angles, quite obvious in one of the two molecules of the Phenyl-NIT derivative **(IV)**, can be explained by the fact that the nitronyl-nitroxide unit N-O-C-N-O is in this moelcule not completely flat. Also the imidazoline ring itself is not flat as can be seen in the N-C-C-N torsion angle. The imidazoline ring seems to be quite flexible in general, so that packing effects may lead to the observed differences in bond lengths and torsion angles of the two Phenyl-NIT molecules.

Nitronyl-nitroxide free radicals are in an oxidation state intermediate between the hydroxylamino anion and the nitrosonium cation. As shown by electrochemical studies, the conversion of the nitronyl-nitroxide into the corresponding nitrosonium species requires a potential of only $\approx +0.4$ V (vs. Ag/AgN03) [135]. In the crystal structure of the oxidized species [Phenyl-NIT]$^+$ **(VI)**, the five-atom fragment 0-N-C-N-O is nearly planar, but again the five-membered heterocyclic ring is not planar, the tetramethylethylene moiety is twisted out as can be seen on the N-C-C-N torsion angle. The phenyl plane makes an angle of 39 $^\circ$ with the O-N-C-N-O plane, suggesting some weak resonance interaction between the ring π-system and the N-oxide N-oxonium π-system by additionally lowering the sterical hindrance of the ortho hydrogen atoms of the phenyl ring to the N-O bonds. As expected, here the N-O bond length (1.225(4) Å) is smaller than the one found in the corresponding free radical ($\approx$ 1.27(2) Å). This smaller distance is consistent with a higher bond order in the more oxidized compound and with the presence of the unpaired electron in an antibonding orbital in the free radical, since the conversion of the radical into the cation involves the loss of this unpaired electron.

In the case of the acidic substituted nitronyl-nitroxide derivatives the radical is intrinsically in acidic conditions, therefore it is important to get a deeper understanding of the possible behaviour of the Phenyl-NIT derivative at low pH-values. For that reason DFT calculations were carried out in cooperation with U. S. of the Ruhr university in Bochum, Germany. As a necessary precondition the geometry and the electronic structure of the Phenyl-NIT derivative were calculated. The calculated bond lengths for the N-O and C-N bonds of the nitronyl-nitroxide unit are with 1.273 Å and 1.360 Å quite close to the experimental data [131], concerning the general limitations of DFT calculations. The torsion angle of the imidazole and

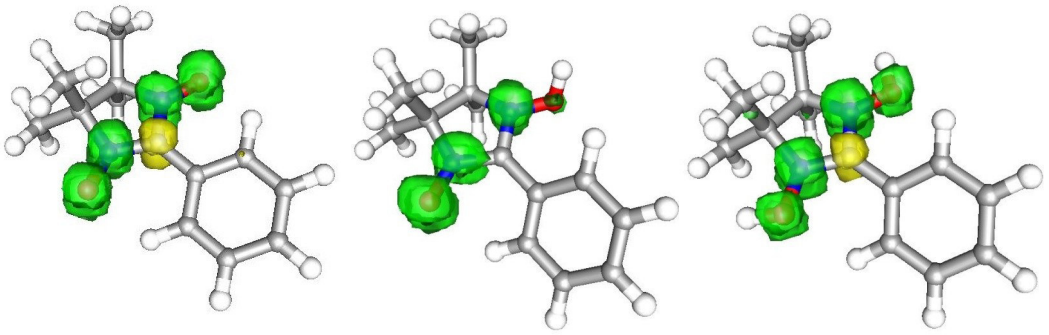

compound	Phenyl-NIT		Phenyl-NIT	$[NIT+H]^+$	$[NIT+2H]^{2+}$
method	TZV(P)	TZV(P)/TZVPP	TZV(P)/TZVPP/COSMO(methanol)		
O	0.3461	0.3432	0.3201	0.5136	0.1774
N	0.2772	0.2763	0.2948	0.2404	0.3901
C	-0.2165	-0.2104	-0.2053	-0.0157	-0.1437
N	0.2772	0.2762	0.2949	0.1886 (H)	0.3901
O	0.3460	0.3431	0.3200	0.0265 (H)	0.1775

Figure 3.3: Dependence of the spin density according to Mulliken on the protonation of the nitronyl-nitroxide unit; a comparison for the influence of the basis set and the solvent molecules is made for the Phenyl-NIT derivative

the phenyl ring is with 22.9 ° also quite close to the observed torsion angle in the crystal structure of Phenyl-NIT **(IV)**, shown in figure 3.2. Here, for the first time, also the at the nitronyl-nitroxide unit protonated species $[Phenyl\text{-}NIT+H]^+$ **(V)** and $[Phenyl\text{-}NIT+2H]^{2+}$ are calculated. As expected, for $[Phenyl\text{-}NIT+H]^+$ the nitronyl-nitroxide unit ONCNO-H is sligthly distorted with a N-O bond length of 1.380 Å for the protonated part and 1.255 Å for the non-protonated part. In contrast the C-N bond of the protonated part gets shorter with 1.333 Å and the C-N bond of the non-protonated part gets longer with 1.380 Å. The torsion angle is a bit larger with 37.4 °, but still in the expected range for nitronyl-nitroxide radicals in general. For the two times protonated species $[Phenyl\text{-}NIT+2H]^{2+}$ a symmetric structure is found again with N-O and C-N bond lengths of 1.332 Å and 1.361 Å and a torsion angle of 37.9 °.

The result of the DFT calculations can be seen in figure 3.3, first of all the influence of the basis sets and the solvent molecules is checked for the Phenyl-NIT derivative. Whereas the additionally polarisation functions of the TZVPP basis set have no influence on the spin density according to Mulliken, the consideration of

the solvent molecules in the frame of a COSMO model (conductor-like screening model) makes a difference with a decrease of the spin density of 0.025 in case of the oxygen atoms and of 0.01 in case of the ipso-carbon. In contrast, the spin density on the nitrogen atoms is increased by 0.02. The influence of the protonation of the nitronyl-nitroxide unit is by far more important. The first protonation of the nitronyl-nitroxide unit has a dramatical decrease of spin density on the protonated oxygen atom as consequence (from 0.32 to 0.03), whereas the spin density on the non-protonated oxygen is increased (from 0.32 to 0.51). Also the spin density on the nitrogen atoms is in total decreased, but the effect is less pronounced, and compared to the oxygen atoms, the spin density is still rather equally shared between the nitrogen atoms. More clearly the effect is seen on the ipso-carbon atom. Here again the decrease of the spin density is one order of magnitude. For the second protonation step, a contrary behaviour of the spin densities is predicted by the DFT calculations. As expected the spin density is again equally distributed, but here the spin density on the oxygen atoms is lowered in total, whereas it is increased on the nitrogen atoms and the ipso-carbon again.

For a comparison with experimental UV/Vis spectra, TDDFT calculations were done. Calculations of all three theoretical possible species were carried out, also taking into account the influence of the solvent molecules by the COSMO approach. The results are summarised in figure 3.4, where the experimental spectra of Phenyl-NIT (exp) at pH = 7 is shown in red. The calculated line spectra of all three theoretical considered species Phenyl-NIT (theo) **(IV)** (deep blue), $[NIT+H]^+$ **(V)** (light blue) and $[NIT+2H]^{2+}$ (green) are considered. The experimental UV/Vis spectra is a typical example of a UV/Vis spectra of a nitronyl-nitroxide radicals with three main transitions present ($\pi - \pi^*$-transition of the phenylring, $\pi - \pi^*$ transition of the NO-group and $n - \pi^*$ transition of the NO-group). Already the calculated spectra of the Phenyl-NIT derivative reproduces the main features of the three typicial transitions of the nitronyl-nitroxide radicals with two red-shifted transitions at 260 nm and 274 nm for the $\pi - \pi^*$-transition of the phenylring and a quite good single transition at 332 nm for the $\pi - \pi^*$ transition of the NO-group and last a blue-shifted weak transition at 511 nm for the $n - \pi^*$ transition of the NO-group. Nevertheless, also for the one-time protonated species $[NIT+H]^+$ a good agreement with the experimental spectra can be found, given that comparable many transitions are predicted. For the double-protonated species $[NIT+2H]^{2+}$ only a small region is predicted, where transition can occur. Especially for the region beyond 410 nm, no transitions are calculated, where the characteristic $n - \pi^*$ transition of the NO-group is expected, support-

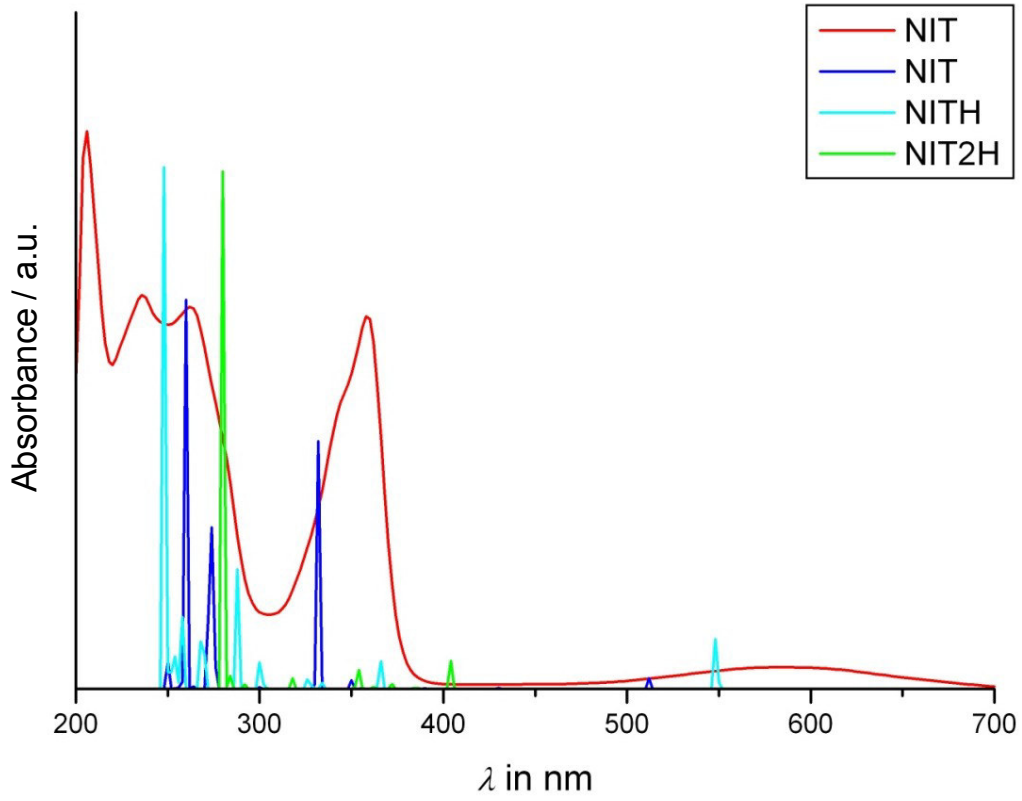

compound	most important peaks / nm						
	$\pi-\pi^*$ Phenyl			$\pi-\pi^*$ NO		$n-\pi^*$ NO	
Phenyl-NIT (lit)		238	263		360		588
Phenyl-NIT (exp)	206	236	263	345	358		583
Phenyl-NIT (theo)		260	274	332			511
$[NIT+H]^+$		248-258	269	288 301	327	365	549
$[NIT+2H]^{2+}$				280 317	355	405	

Figure 3.4: UV/Vis spectra of Phenyl-NIT (exp) compared with the UV/Vis spectra calculated for the three species Phenyl-NIT (theo), $[NIT+H]^+$ and $[NIT+2H]^{2+}$ with TDDFT; also the values of the reported spectra by Ullman et al. [48] are given: Phenyl-NIT (lit), values for ethanol as solvent

ing that any significant role of this species can be excluded. The experimental UV/Vis without any change of the pH-value is best reproduced by a mixture of the Phenyl-NIT (theo) and $[NIT+H]^+$, especially by taking into account that the occurence of more transition bands at lower pH-value, shown in figure 3.5, can only be explained with the one-time protonated $[NIT+H]^+$ **(V)** species.

The pH- and time dependent study of the UV/Vis spectra recorded in methanol is shown in figure 3.5. The spectra reveal that an additionally band around 450 nm occurs by lowering the pH-value. Without further change of the pH-value, this

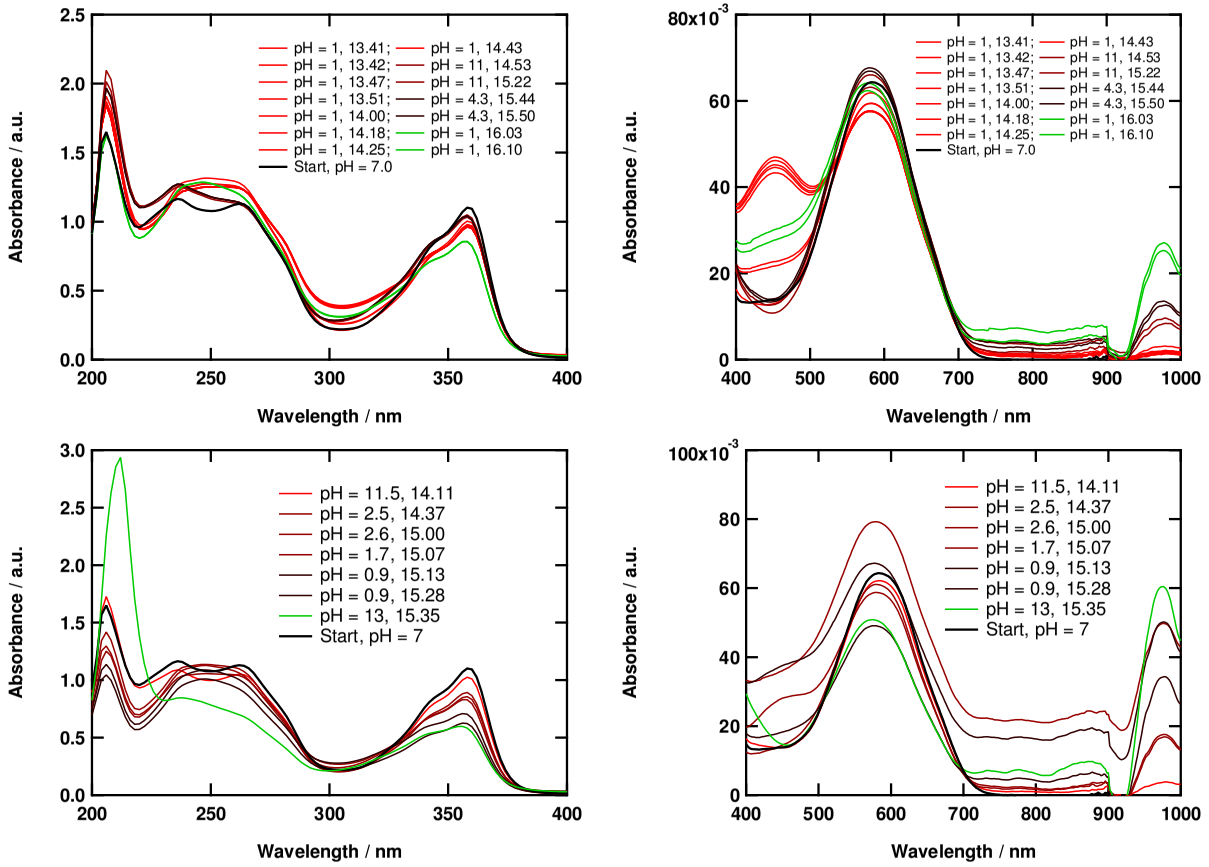

Figure 3.5: Comparison of the UV/Vis spectra of Phenyl-NIT in methanol shown (c = 0.1 mmol/L); two different scalings in 200-400 nm (left) and 400-1000 nm (rigth), top row: first sample was first acidified with diluted HCl, before the pH value was changed with NaOH and afterwards it was acidified again; bottom row: in the second sample the pH-value was first basic before the sample was acidified and again changed to basic conditions

band slowly decays. By increasing the pH-value again, the starting UV/Vis spectra is obtained. By a further decrease of the pH-value the band around 450 nm occurs again, but with less intensity. The same is true for a sample that is first made alkaline and then the pH-value is lowered. Here also an additionally band around 450 nm occurs, but again with less intensity. The experimental data confirm the occurence of the protonated species [Phenyl-NIT+H]$^+$ **(V)**.

For the first time experimental and theoretical results are presented for the proposed mechanism by Ullman et al. [48] of the behaviour of the Phenyl-NIT derivative at low pH-values. Solely on basis of the analysis of the resulting products, they stated that a disproportionation reaction takes place. The intermediate protonated Phenyl-NIT radical was proven simply by an EPR signal similar to the unprotonated Phenyl-NIT, but with reduced intensity. In the present work, the reaction of the protonated Phenyl-NIT is monitored at 450 nm in the UV/Vis spectra shown in figure 3.5. The UV/Vis spectra of the Phenyl-NIT radical is qualitative correctly reproduced by DFT calculations, supporting the reliability of the calculations in general. In addition, the spin density of the protonated Phenyl-NIT derivative is calculated. Although the equally distribution of the spin density is disturbed upon protonation, the values on the nitrogen atoms are not affected, thus a five-line pattern comparable to the EPR signal of the unprotonated Phenyl-NIT radical can be expected as was reported by Ullman et al.. Again DFT calculations nicely confirm the experimental results. The existence of a protonated nitronyl-nitroxide radical unit could be clearly proven, although this species is not stable in solution and undergoes a reversible disproportionation process in acidic conditions. By increasing the pH-value again the original UV/Vis spectra are reproduced in the experiment. In the future further time-dependent studies (UV/Vis and EPR spectroscopy) are planned to investigate the kinetic behaviour of the disproportionation reaction to gain an insight in the reaction mechanism.

3.1.2 Characterisation of the New Nitronyl-Nitroxide Radicals

Although a great variety of residues are known, that can be attached at the 2-position of the nitronyl-nitroxide radical unit, it is remarkable that except for the carboxilic acid derivative (COOH-NIT) [136, 137], no other acidic residue is reported in literature. In the working group of Prof. Dr. E. R. this gap in the literature was recognised already some time ago and the synthesis of new nitronyl-nitroxide radicals with acidic residues was aimed [138, 139]. As shown in figure 3.6, by

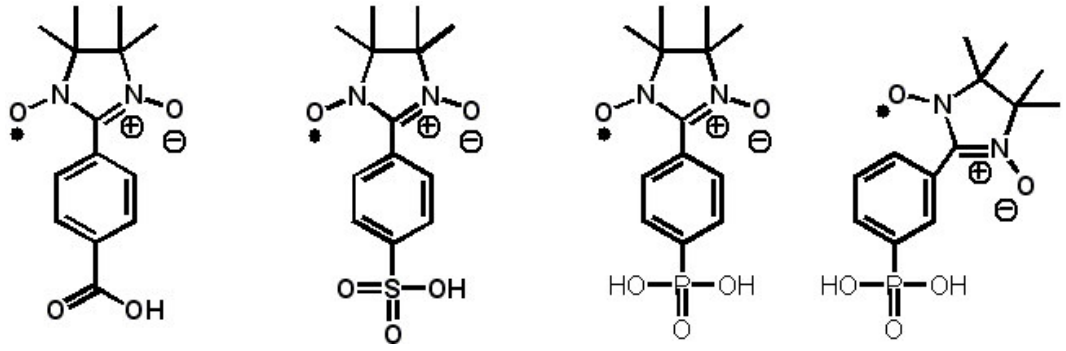

IUPAC name	4(3)-(4,4,5,5-tetramethyl-imidazoline-3-oxide-1-oxyl)-benzene-		
	carboxilic acid	sulfonic acid	phosphonic acid
Short	COOH-NIT	SO_3H-NIT **(33)**	p(m)PO_3H_2-NIT **(27a) (27b)**
Literature	[136]	[138]*	[139]*, (this work)
Oxygens	2	3	3
Charge	1-	1-	2-

Figure 3.6: Comparison of the four here disussed nitronyl-nitroxide radicals, which are the only nitronyl-nitroxide radicals known with acidic residues; *parts of the synthesis/characterisation are already described here; in parentheses information for the meta-derivative are given

now a series of three new nitronyl-nitroxide radicals with acidic residues can be presented. With the sulfonic acid group and the phosphonic acid group, two new acidic residues could be introduced in the phenylring of the nitronyl-nitroxide, which both possess three oxygen atoms that possibly can coordinate to metal ions in contrast to the carboxilic acid that exhibits only two. For the synthesis of new complexes, also the charge of the second functional group has to be taken into account. The carboxilic acid and the sulfonic acid can only be deprotonated one time in contrast to the phosphonic acid that can be deprotonated two times.

The syntheses of nitronyl-nitroxide radicals depends on the availability of the appropiate aldehyde compounds, as can be seen in the synthetic protocols shown for the SO_3H-NIT **(33)** derivative in figure 5.5 on page 181 and for the pPO_3H_2-NIT **(27a)** derivative in figure 5.4 on page 172. With the appropriate aldehyde, a condensation reaction with the bis(hydroxylamino)component **(22)** is carried out. The last step is the oxidation process to the stable radical species. Especially the syntheses of the Formyl-phosphonic acid derivatives **(25a)** , **(25b)** are challenging ones, because the Michaelis-Arbuzov reaction used is intolerant versus the aldehyde function so that an appropiate protective group has to be choosen. Furthermore, the reaction has to be carried out at higher temperatures ($\approx 200°C$). For

Table 3.1: Simulation parameters of the X-Band spectra presented in figure 3.8 with an assumed rhombic g-value and an axial hyperfine coupling to the ^{14}N nuclei

Sample	g_x	g_y	g_z	A_{xx}/mT	A_{yy}/mT	A_{zz}/mT
pPO_3Na_2-NIT	2.0122	2.0110	2.0036	0.42	0.42	1.85
pPO_3H_2-NIT	2.0122	2.0110	2.0037	0.42	0.42	1.79
mPO_3Na_2-NIT	2.0120	2.0110	2.0036	0.42	0.42	1.84
mPO_3H_2-NIT	2.0120	2.0110	2.0036	0.42	0.42	1.78

4-(Formyl)benzenesulfonic acid **(31)** no synthesis procedure was reported in the literature, but one was already developed in our working group [138]. The condensation reaction with the bis(hydroxylamino)component **(22)** was carried out in methanol or ethanol depending on the solubility of the starting aldehyd derivatives and the insolubility of the condensation products. Only by precipitation the condensation products can be obtained. In solution an acid-induced side reaction takes places depending on the reaction conditions [138]. For the oxidation process two procedures depending on the used oxidising agent, PbO_2 or $NaIO_4$, were developed. Both have their limitations, because the solubility of the acidic derivatives of the nitronyl-nitroxide radical is in general poor in most organic solvents. Furthermore, the intrinsic tendency of the second functional group (phosphonic acid or sulfonic acid) to coordinate metal ions lead to partly dissolution of the PbO_2 oxidising agent and a contamination of the nitronyl-nitroxide radical with lead oxide. As discussed in section 3.1.2.2, the free acid form of the nitronyl-nitroxide radicals is not stable in solution. The isolation of the sodium salts by the oxidation procedure with $NaIO_4$ is preferred. The obtained nitronyl-nitroxide radicals were completely characterised and pure enough for further reactions, although no purification process was applied.

3.1.2.1 X-band EPR spectra

In cooperation with Y. A. and D. H. from Max Planck Institute for Polymer Science in Mainz, the X-band EPR spectra of the two phosphonate substituted nitronyl-nitroxide radicals (meta and para) in two forms (free acid and di-sodium salt) were measured at low temperatures. The spectra of the free acids **(27b)** , **(27a)** and the two salts **(28b)** and **(28a)** are shown in figure 3.7. In figure 3.8, the simulation with a rhombic g-value and an axial hyperfine coupling to the ^{14}N is shown. The values are summarised in table 3.1.

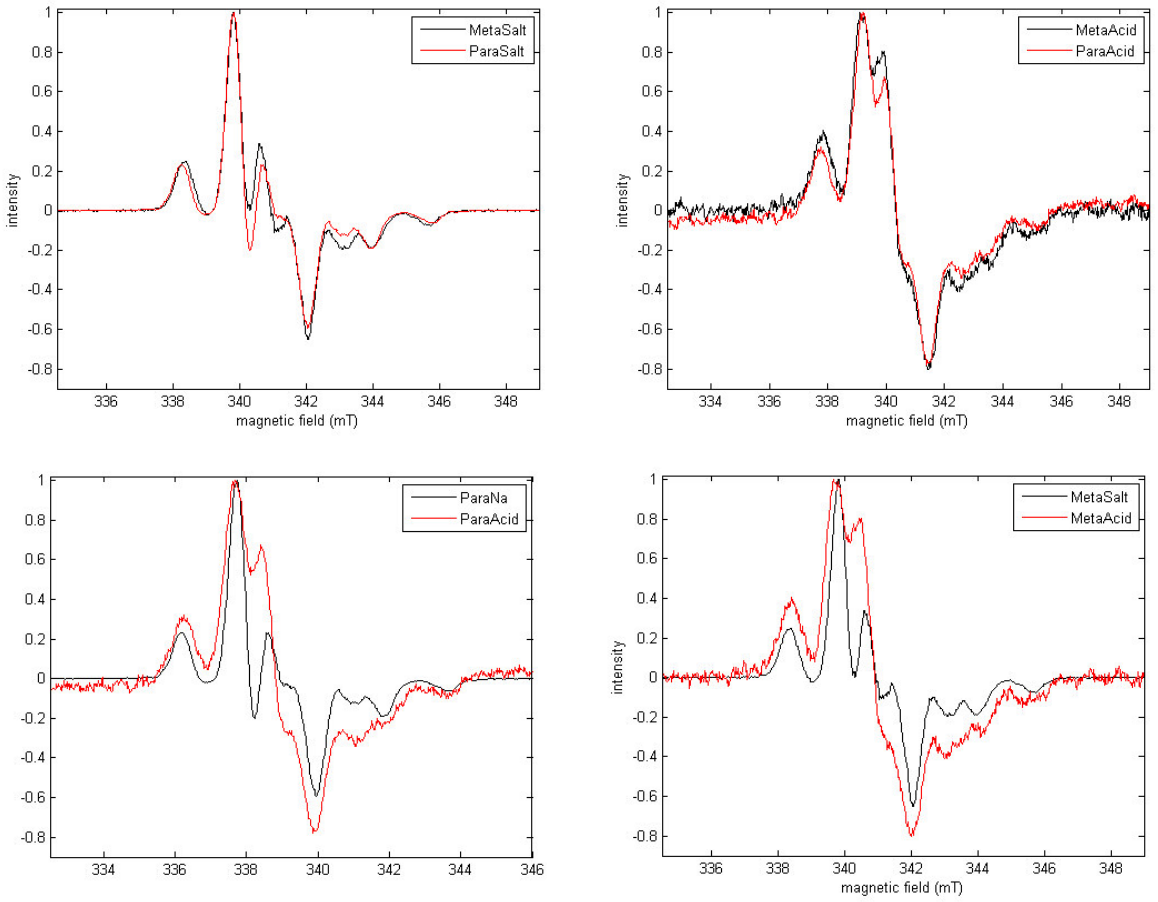

Figure 3.7: Comparision of the X-Band spectra measured at 20 K of pPO_3H_2-NIT **(27a)** , mPO_3H_2-NIT **(27b)** , pPO_3Na_2-NIT **(28a)** and mPO_3Na_2-NIT **(28b)** ; top left: comparison of the two sodium salts, top right: comparison of the two acids; bottom left: comparison of the two para-derivatives (sodium salt and acid); bottom right: comparison of the two meta-derivatives (sodium salt and acid); no influence concerning the solvent difference of the pPO_3H_2-NIT **(27a)** sample could be determined

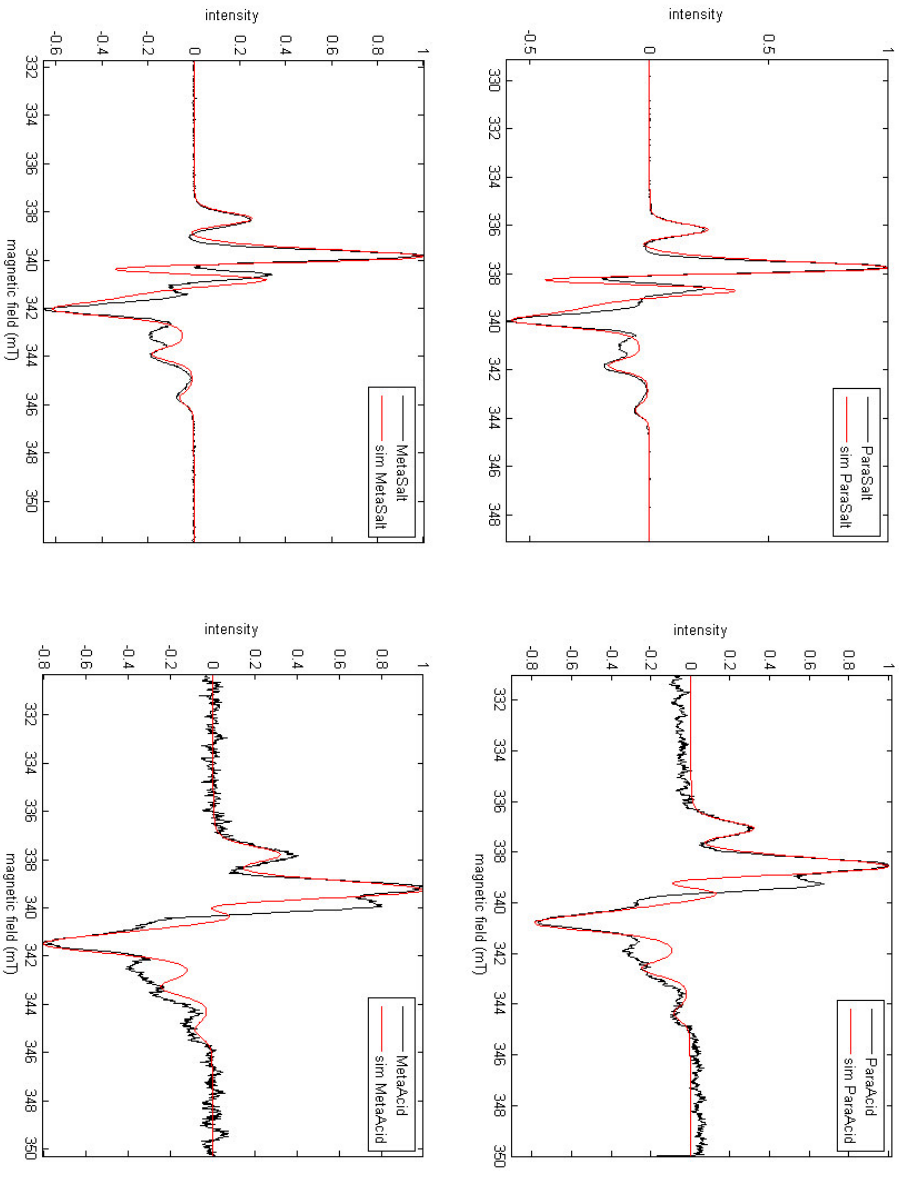

Figure 3.8: top left: Simulation of the X-Band spectra measured at 20 K of pPO_3Na_2-NIT **(28a)** , top right: Simulation of the X-Band spectra of pPO_3H_2-NIT **(27a)** ; bottom left: Simulation of the X-Band spectra of mPO_3Na_2-NIT **(28b)** ; bottom right: Simulation of the X-Band spectra of mPO_3H_2-NIT **(27b)**

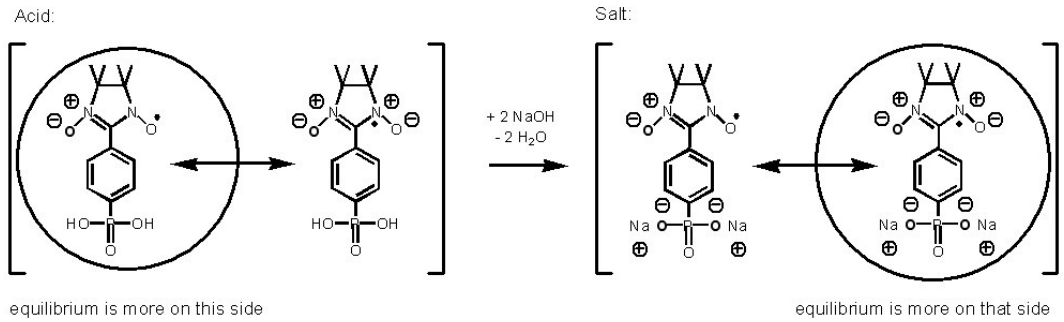

Figure 3.9: Schematic drawing of the different mesomeric structures of the nitronyl-nitroxide unit dependent on the deprotonation stage of the phosphonic acid

Typicial for EPR spectra of nitronyl-nitroxide radicals is, that at low temperatures an axial distortion of the five line pattern is observed. The coupling of the electron spin (S=1/2) to the two equivalent nitrogen atoms (nuclear spin (I=1)) has a large z-contribution, because the radical is located in a π^*-orbital of a nitronyl-nitroxide unit, derived of a p_z-orbital of the nitrogen atom. The isotropic g-value, calculated according to $g_{iso} = 1/3*(g_x+g_y+g_z) = 2.0089$, is close to the value of a free electron, $g_e = 2.0023$, as expected for an organic radical. The effect that the hyperfine coupling to the nitrogen is larger in the case of the di-sodium salt, by deprotonating the acidic second functionality, is also found by Barone et al. in the case of simple nitroxide radicals 3-carboxy-PROXYL and 4-carboxy-TEMPO [140]. Due to the negative charge present in the periphery of the nitronyl-nitroxide unit, a polar structure with more radical character on the nitrogen of the nitronyl-nitroxide radical is stabilisied. A scheme for the present structures can be found in figure 3.9. No significant difference in the spectra is found, whether the phosphonic acid is attached in para or meta-position of the phenyl ring. But a difference in signal intensity is found, depending on the protonation state of the phosphonic acid group. Although all EPR samples had the same concentration, the signal-to-noise ratio is better in the case of the di-sodium salt derivatives compared to the free acids. Again the disproportionation reaction of nitronyl-nitroxide radicals at low pH-values, already described by Ullman et al. [48], is an explanation.

3.1.2.2 UV/Vis-spectra

For the acidic substituted nitronyl-nitroxide radicals pPO_3H_2-NIT **(27a)** and mPO_3H_2-NIT **(27b)** a disproportonation side reaction is assumed in solution, quite similar to the already presented results for the Phenyl-NIT derivative in acidic conditions in section 3.1.1. Due to the pK_A-value of phenyl phosphonic acid in general

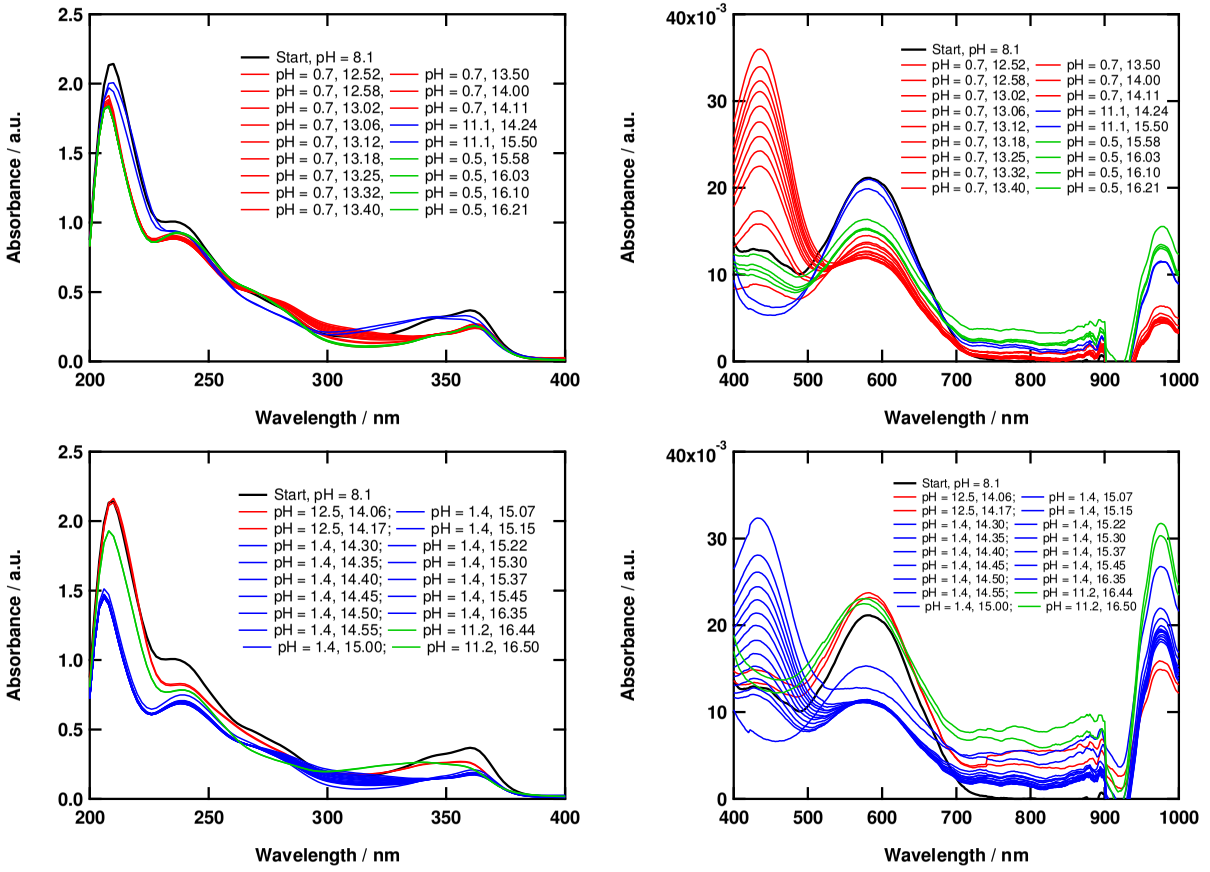

Figure 3.10: Comparison of the UV/Vis spectra of meta-PO_3Na_2 **(28b)** in methanol shown (c = 0.1 mmol/L); two different scalings in 200-400 nm (left) and 400-1000 nm (rigth), top row: first sample was first acidified with diluted HCl, before the pH value was changed with NaOH and afterwards it was acidified again; bottom row: in the second sample the pH-value was first basic before the sample was acidified and again changed to basic conditions

Table 3.2: Comparsion of the experimental UV/Vis data depending on pH-value and time of mPO_3Na_2-NIT **(28b)** and pPO_3Na_2-NIT **(28a)** ; see also figure 3.10 and 3.11; sh: shoulder; ÷: not measured

compound	most important peaks / nm						
	$\pi-\pi^*$ Phenyl			$\pi-\pi^*$ NO		$n-\pi^*$ NO	
Phenyl-NIT (Start)	206	236	263	345	358		583
mPO_3Na_2-NIT (Start)	210	238	sh	348	360	438	582
mPO_3Na_2-NIT (acidic)	208	236		348	362	438	580
mPO_3Na_2-NIT (basic)	210	238		342	358		582
pPO_3Na_2-NIT (Start)	÷	232	sh	348	364	sh	582
pPO_3Na_2-NIT (acidic)	÷	228	250	350	366	460	580
pPO_3Na_2-NIT (basic)	214	228	252	342	362	530	sh

(1.83 and 7.07 [74]), a protonation of the nitronyl-nitroxide unit can occur intrinsically, so that in solution in a protic solvent even a zwitterionic species (short: NIT**H**-C_6H_4-PO_3H) can be realised. The results of the pH- and time-dependent UV/Vis studies of the di-sodium salts pPO_3Na_2-NIT **(28a)** and mPO_3Na_2-NIT **(28b)** are summarised in table 3.2. The UV/Vis spectra of pPO_3Na_2-NIT are shown in figure 3.11 and of mPO_3Na_2-NIT in figure 3.10. Already without any change of the pH-value, additionally bands or shoulders to the three typicial transition of a nitronyl-nitroxide radical ($\pi-\pi^*$-transition of the phenylring, $\pi-\pi^*$ transition of the NO-group and $n-\pi^*$ transition of the NO-group) can be assigned. The occurence of the additionally peak or shoulder around 440 nm is attributed to the zwitterionic species NIT**H**-C_6H_4-PO_3H. By acidification, the band at 438 nm is increased first in the case of the mPO_3Na_2-NIT derivative. Then without changing the pH-value, a decay of this band is observed, comparable to the described behaviour of the Phenyl-NIT derivative. In alkaline conditions, the band at 438 nm is completely absent, but it can be recovered by acidification. The behaviour of the pPO_3Na_2-NIT is completely different. By acidification, the shoulder around 440 nm is increased to a band, but the intensity is still low compared to the $n-\pi^*$ transition of the NO-group at 580 nm. Furthermore, no decay in the observed time frame was monitored. In alkaline conditions, strong shifting of the bands occur, so that an unambiguous assignment of the bands is difficult. Probably, here a more complex reaction mechansim is realised. To get a deeper insigth in the general behaviour of the nitronyl-nitroxides unit under acidic conditions, other acidic substituted nitronyl-nitroxide radicals (COOH-NIT and SO_3H-NIT) will be examined in the future.

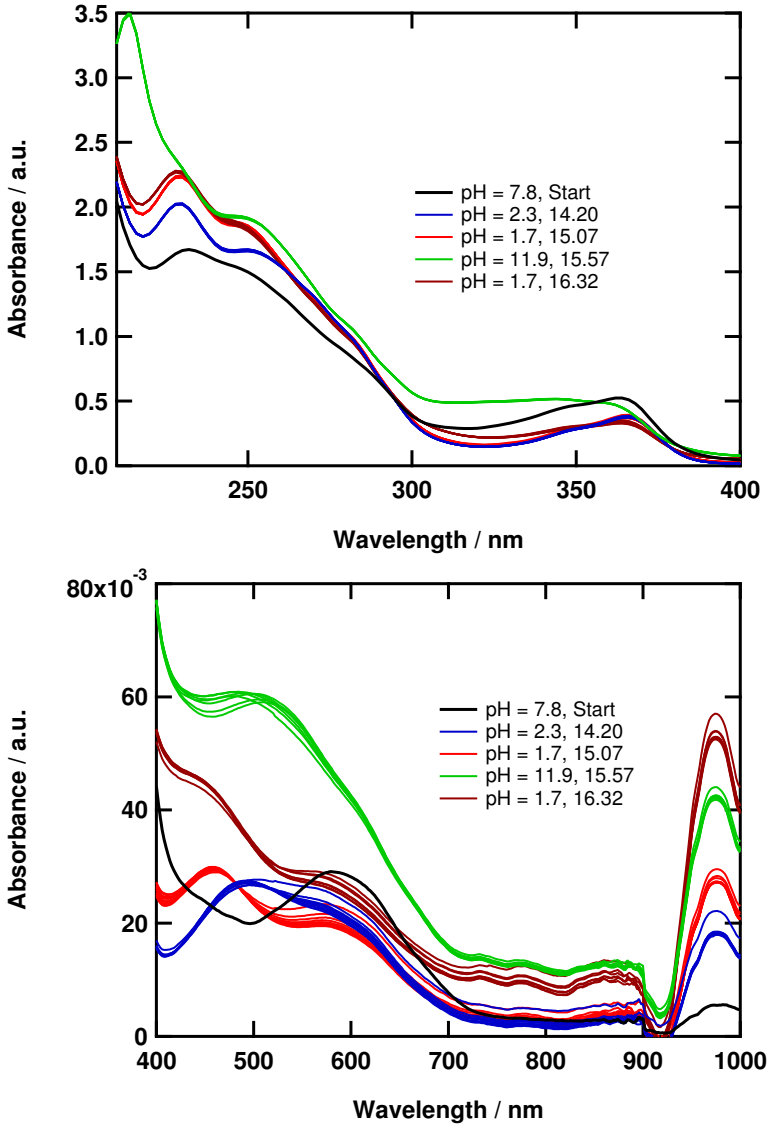

Figure 3.11: Comparison of the UV/Vis spectra of para-PO_3Na_2 **(28a)** in methanol shown (c = 0.1 mmol/L); two different scalings in 200-400 nm (top) and 400-1000 nm (bottom), sample was first acidified with diluted HCl, before the pH value was changed with NaOH and afterwards it was acidified again

3.1.2.3 Cyclovoltammetric measurements

First the starting potential of the cyclovoltammetry was determined in a so called open circuit measurement. For the two sodium salts the starting potential is around -0.790 V, whereas the starting potential for the two acids is higher with around -0.420 V. Several redox waves can be assigned in the total range of the cyclovaltommetric measurement, the one we are interested in is between 0.2 V and 0.4 V (vs. ferrocenium/ferrocen standard) shown in figure 3.12. This is a reversible one electron transition of [N-O]$^{\bullet}$ to [N=O]$^{+}$ located on the nitronyl-

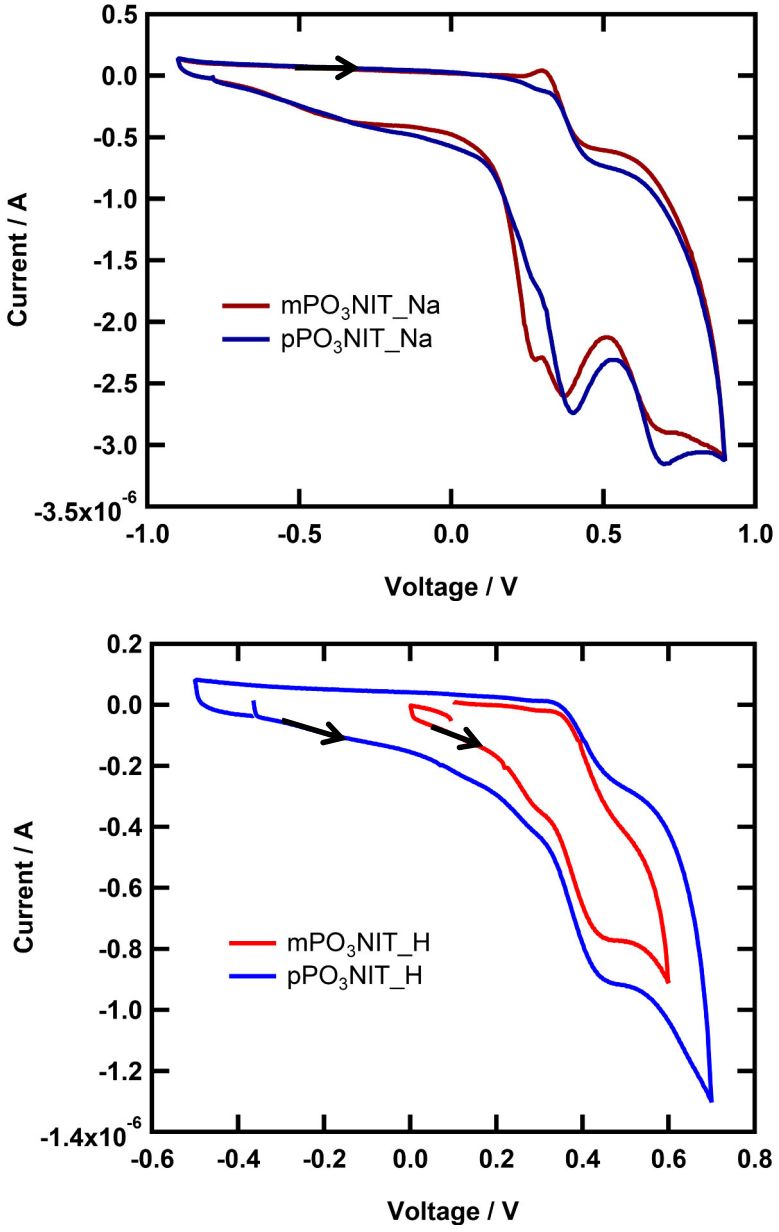

	meta	para
Acid	(0.142 V) 0.282 V	(0.124 V) 0.292 V
Salt	(0.136 V) 0.233 V (0.510 V)	(0.132 V) 0.253 V (0.510 V)

Figure 3.12: Cyclovoltammetric measurements with following parameters: scanrate 50mV/s; the standard ferrocenium/ferrocen potentials are 0.100 V for pPO_3Na_2-NIT, 0.103 V for mPO_3Na_2-NIT, 0.106 V for pPO_3H_2-NIT and 0.113 V for mPO_3H_2-NIT; standard potentials vs. ferrocenium/ferrocen are listed

nitroxide unit. In comparison the redox wave for the sodium salt of the COOH-NIT derivative is found at a potential of 0.34 V [138]. At the top of figure 3.12 the cyclovoltammetric measurements of the two sodium salts pPO_3Na_2-NIT **(28a)** and mPO_3Na_2-NIT **(28b)** are shown, whereas the cyclovoltammetric measurements of the two acids pPO_3H_2-NIT **(27a)** and mPO_3H_2-NIT **(27b)** are displayed at the bottom of figure 3.12. The standard potential vs. ferocenium/ferrocene of the one reversible transition with two shoulders in the case of the two sodium salts and of one reversible transition with one shoulder in the case of the two acids are also listed. So far two conclusions can be drawn from the cyclovoltammetric measurements: In the meta substitutated radicals mPO_3Na_2-NIT and mPO_3H_2-NIT, the [N-O]$^\bullet$ to $[N{=}O]^+$ transitions have a lower standard potential compared to the para substituted radicals pPO_3Na_2-NIT and pPO_3H_2-NIT. A possible interpretation is that the phosphonic acid group known as electron withdrawing group has a stronger effect in para-position to the nitronyl-nitroxide unit than in meta-position. Thus, the [N-O]$^\bullet$ to $[N{=}O]^+$ oxidation need a higher potential to occur. The second observation is that the two acids pPO_3H_2-NIT and mPO_3H_2-NIT have higher standard potentials compared to the two salts pPO_3Na_2-NIT and mPO_3Na_2-NIT. This can be explained by the fact that less free electrons are already located on the compound, so that again a higher potential is needed for the [N-O]$^\bullet$ to $[N{=}O]^+$ oxidation to occur. The measurements of the sulfonic acid derivative and the sulfonate derivative of the nitronyl-nitroxide radical SO_3H-NIT **(33)** and SO_3Na-NIT **(34)** are to be done, so that also the difference in the acidic substituents can be determined.

The syntheses and characterisation of three new nitronyl-nitroxide radicals is presented in this section. With the sulfonic acid in SO_3H-NIT **(33)** and the phosphonic acid in pPO_3H_2-NIT **(27a)** and mPO_3H_2-NIT **(27b)** , two new acidic substituents are introduced in nitronyl-nitroxide radicals. Similar to the already presented results for the Phenyl-NIT derivative in acidic conditions in section 3.1.1, a disproportonation side reaction is assumed for the acidic substituted nitronyl-nitroxide radicals in solution. For the first time, experimental results are obtained where a zwitterionic species is proven, due to the protonation of the nitronyl-nitroxide unit by the acidic substituent. For pPO_3H_2-NIT **(27a)** and mPO_3H_2-NIT **(27b)** , a detailed investigation on the shift of the spin density is presented in section 3.2. The pH-value dependency of the surrounding media is discussed since it influences the second functional acidic group. Finally, first mainly dinuclear complexes with the new nitronyl-nitroxide radicals are described in section 3.3 and their magnetic behaviour is investigated.

3.2 Investigation of the Spin Density in Acidic Substituted Nitronyl-Nitroxide Radicals

The knowledge of the spin density distribution in molecules is crucial for the understanding of the magnetic behaviour, especially in organic radicals where various close contacts between the molecules add up to the final magnetic interaction. The spin density is defined as fraction of a spin that is located somewhere in considered molecule. It has a certain shape (often it resembles molecular orbitals) and a sign depending on its orientation concerning an external magnetic field or a reference field in general [141]. For the experimental investigation of the spin density of a molecule, some methods are known in literature. Due to their magnetic moment, neutrons are a unique tool for spin-density studies. In scattering experiments, neutrons are scattered on the one side by nuclear interactions with the nuclei and on the other side by magnetic interactions with the spin density. In a first step the precise crystal structure at low temperature is determined by using conventional unpolarised neutrons. Then, in a second step a polarised neutron beam is used to measure the so called flipping ratio, that is the ratio of scattered intensities for "up" (parallel to the applied field) and "down" (antiparallel to the applied field). From these two measurements the spin density at every point of the crystal structure can be calculated as reported for the p-(methylthio)phenyl nitronyl-nitroxide radical [142]. Another method of choice is the paramagnetic NMR spectroscopy [143]. The signal broadening typically observed in a paramagnetic NMR spectra is due to the effect of the electron spin on the nuclear spin relaxation, while the signal shift in general can be thought of being mainly determined by the average local magnetic field of the unpaired electrons which in turn is related to the spin density. However, the contributions to the isotropic and anisotropic shifts are manifold and only with the help of theoretical calculations a spin density map can be determined. The last technique mentioned here is EPR spectroscopy, allowing the determination of spin density distributions hidden in solvent-solute interactions as reported for several nitronyl-nitroxide radicals [144]. Unfortunately, all of these methods have their limitations, so the high cost of polarised neutron diffraction experiments and the strict sample requirements on large single crystals render the technique useless for routine characterisation and does not permit a precise determination of the vanishing spin densities on some molecular regions which are at the limit of the experimental accuracy. The EPR spectroscopy on the other side does not provide the sign of the spin densities, it gives the absolute values and in general only the density on nuclei for isotopes

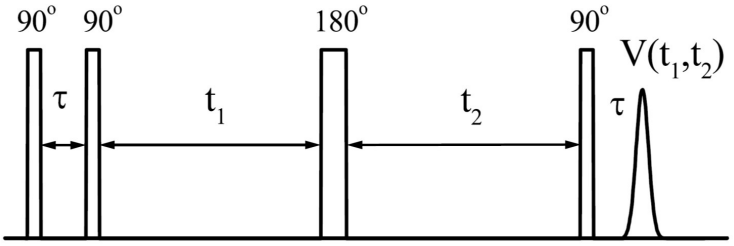

Figure 3.13: Pulse sequence of the HYSCORE experiment, the stimulated echo signal amplitude $V(t_1, t_2)$ is measured as a function of two delays, t_1 (between the second 90° pulse and the (third) mixing pulse of 180°) and t_2 (between the (third) mixing pulse of 180° and the fourth (90°) pulse), scheme according to literature [145]

having a nuclear spin that is unequal zero. Therefore, often combinations of several techniques are needed as well as theoretical calculations to fully understand the spin density distribution.

The two phosphonic acid substituted nitronyl-nitroxide radicals, the para **(27a)** and the meta **(27b)** derivative, introduced in this work are perfect samples for the investigation of the spin shift in nitronyl-nitroxide radicals in general by EPR spectroscopy. With the phosphorus nuclei present in the second functional group, an intrinsic sensor of the spin density is incooperated in the molecule due to the nuclear spin of 1/2. Although already nitronyl-nitroxide radicals with a secondary functional group containing also phosphorus atoms as part of a phosphine or phosphinoxide group are known [146], the here presented derivatives with a phosphonic acid group have the advantages that they are air-stable (compared to the phosphine group) and that the electron withdrawing character of the group can be changed by the pH-value of the surrounding media. The EPR technique used here is called HYSCORE, what is the abbreviation for two-dimensional hyperfine sublevel correlation spectroscopy. The advantage of this technique is that the hyperfine couplings to the different nuclei present in the nitronyl-nitroxide radical (^{14}N, ^{13}C, ^{1}H, ^{31}P) are well separated by a good spectral resolution [145]. The shown pulse sequence in figure 3.13 is used in a typical HYSCORE experiment. The first two $\pi/2$ pulses create some nuclear coherences that evolve in the first time domain t_1, which are mixed again by an inversion pulse π. In the second time domain t_2, the nuclear coherences evolve again before the fourth pulse of $\pi/2$ generates the signal again. A double fourier transformation of both time domaines t_1 and t_2 gives the two-dimensional frequency dependent spectra with the axis ν_1 and ν_2.

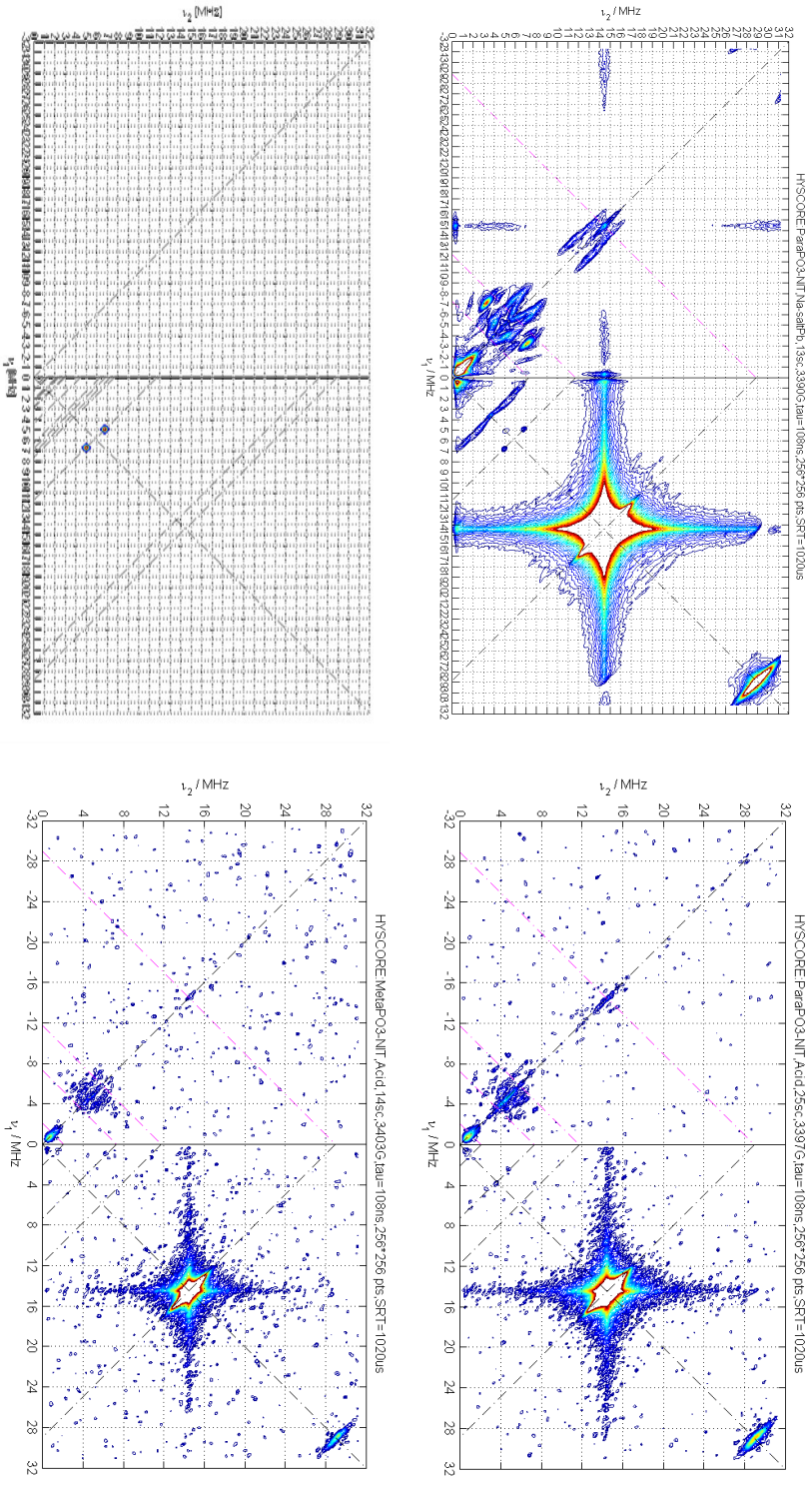

Figure 3.14: top left: HYSCORE measurement of the di-sodium salt of pPO_3-NIT radical, 13 scans, τ=108 ns; bottom left: simulation result for the phosphorus coupling with parameters obtained in the W-band ENDOR measurements shown in table 3.3; top right: HYSCORE measurement of the pPO_3H_2-NIT radical, 25 scans, τ=108 ns; bottom right: HYSCORE measurement of the mPO_3H_2-NIT radical, 14 scans, τ=108 ns

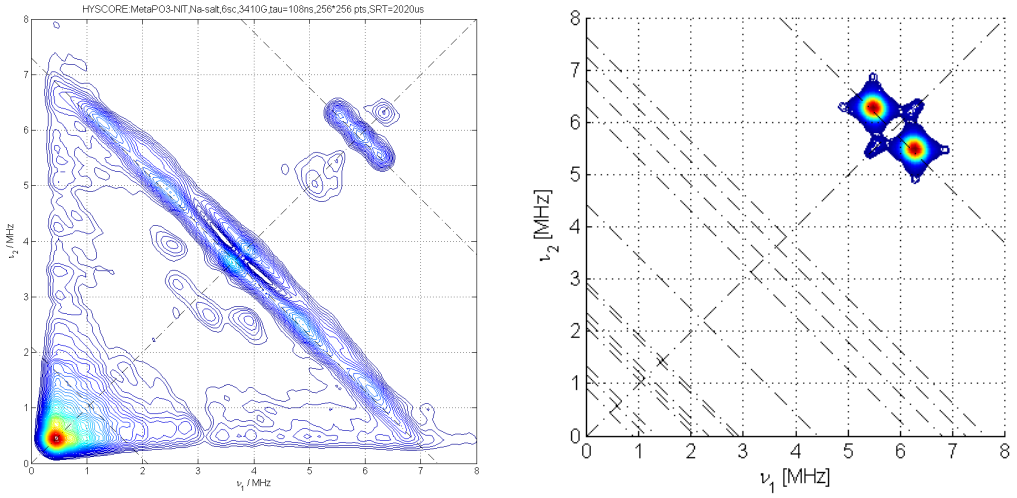

Figure 3.15: left: HYSCORE measurement of the di-sodium salt of mPO_3-NIT radical, 6 scans, τ=108 ns; right: simulation result for the phosphorus coupling with parameters obtained in the W-band ENDOR measurements shown in table 3.3

In cooperation with Y. A. and D. H. from Max Planck Institute for Polymer Science in Mainz, the X-band HYSCORE spectra and W-band ENDOR spectra were obtained. The results of the X-band HYSCORE spectra can be seen in figures 3.14 and 3.15. As already explained in section 3.1.1 for the X-band EPR measurements, the acidic form of the nitronyl-nitroxide radicals pPO_3H_2-NIT and mPO_3H_2-NIT is not stable in solution and so the intensity of the EPR signal in total is lowered. Unfortunately the signal is even too low to obtain any useful information in the HYSCORE spectra as can be seen at the right side of figure 3.14. In contrast, the di-sodium salts of the nitronyl-nitroxide radicals pPO_3Na_2-NIT and mPO_3Na_2-NIT give nice spectral information in the HYSCORE spectra. Both HYSCORE spectra are very similar, except for the region of the phosphorus coupling. Therefore this region is additionally shown for the mPO_3Na_2-NIT in figure 3.15. Every nucleus has an off-diagonal line at the appropiate resonance frequency and depending on the hyperfine coupling strength, the signal is located in the left part of the spectra (strong coupling regime) or in the right part of the spectra (weak coupling regime). If the hyperfine coupling is very anisotropic, then the signal intensity is not exactly on the line, but curved away from the line. The quite prominent signal in the right part of the spectra is the proton signal and in the top right corner even the double proton signal can be seen. Three off-diagonals are drawn for orientation in the HYSCORE spectra of pPO_3Na_2-NIT (top left in figure 3.14), the first one being the ^{14}N resonance line is at the highest frequency of $\approx$29 MHz. The signal can be found in the strong coupling regime (on the left side). It is highly

anisotropic, therefore it is curved away from the resonance line. The next off-diagonal at ≈11.5 MHz belongs to the ^{31}P nucleus, and the coupling is more or less isotropic reflected by the fact that the signals are exactly on the line. The last off-diagonal at ≈7 MHz is at the resonance frequency of the ^{13}C nuclei and again a small anisotropic behaviour can be seen. As well the ^{31}P signal as the ^{13}C signal can be found in the weak coupling regime in the right part of the spectra.

The shift of the spin density from the nitronyl-nitroxide unit to the second functional group by substituting with electron-withdrawing groups can be detected by the amount of spin density located at the phosphorus. Therefore, the hyperfine coupling to the ^{31}P nucleus in the HYSCORE spectra is the most important one. To simulate in detail the hyperfine coupling to the ^{31}P nucleus in the HYSCORE spectra, W-band ENDOR spectra were measured additionally. ENDOR stands for electron nuclear double resonance [147], and here the EPR sample is simultaneously irradiated with two resonant fields, so that nuclear spin transitions in paramagnetic molecules are induced by means of a suitable radio frequency field and are detected by a change in the EPR signal intensity. Thereby additional selection rules need to be fulfilled, so that the resolving power of EPR in general is improved taking into account that an unpaired electron in an organic π-radical is delocalised over a larger π system resulting couplings with all magnetic nuclei, producing an (integral) multispin ensemble. Due to the normally drastical limited numbers of lines in ENDOR spectra compared to cw EPR spectra, all hyperfine coupling constants can be extracted without difficulty and usually unambiguously. Several advantages of using a high-field W-band ($\nu \approx 95$ GHz) compared to a X-band spectrometer ($\nu \approx 10$ GHz) are known. The most important are that spin systems with larger zero-field splittings due to the larger microwave quantum energy $h\nu$ are accessible. Furthermore, the higher spectral resolution of the g-factor, which increases also with irradiation frequency ν and external magnetic field B_0, so that orientation selectivity and sensitivity are increased or that EPR spectra are simplified due to the reduction of second-order effects in general at higher fields. In the case of the two p(m)PO_3Na_2-NIT radicals, especially the higher resolution of the g-factor was needed, so that an orientation dependent measurement of the ^{31}P hyperfine coupling was possible in a powdered (isotropic) sample. The result of the W-band ENDOR measurements can be found in figure 3.17 (pPO_3Na_2-NIT) and in figure 3.18 (mPO_3Na_2-NIT). The obtained orientation dependent parameters are summarised in table 3.3. With the help of this parameters the spin density in s-type and p-type orbitals of the phosphorus can be calculated according to the formulas (3.1) and (3.2) [148].

Table 3.3: Simulation parameters of the W-Band ENDOR spectra of pPO_3Na_2-NIT **(28a)** and mPO_3Na_2-NIT **(28b)** presented in figures 3.17 and 3.18 with an assumed rhombic hyperfine coupling to the ^{31}P nucleus; to clearify the labelling of the axis according to Angeloni et al. [149], a schematic drawing of the nitronyl-nitroxide radicals is given

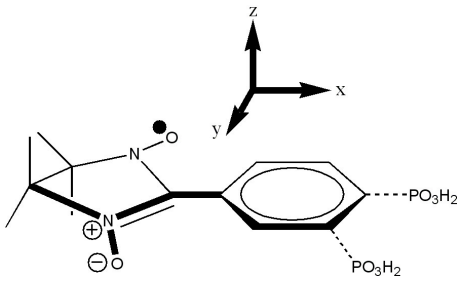

Sample	n	A_n/MHz	A_{iso}/MHz	T_n/MHz	T / MHz	ρ_S / %	ρ_P / %
pPO_3Na_2-NIT	x	1.63	1.71	-0.08	0.070	0.013	0.019
	y	1.85		0.14			
	z	1.65		-0.06			
mPO_3Na_2-NIT	x	0.97	0.85	0.12	0.115	0.006	0.031
	y	0.62		-0.23			
	z	0.96		0.11			

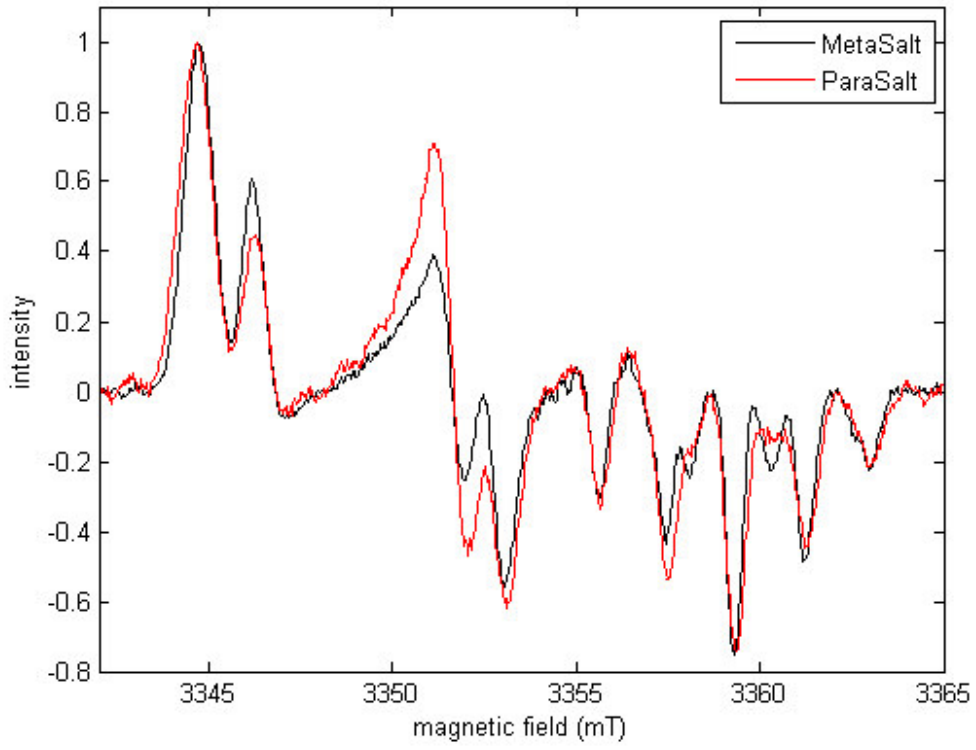

Figure 3.16: Comparision of the W-Band spectra measured at 20 K of pPO_3Na_2-NIT **(28a)** and mPO_3Na_2-NIT **(28b)**

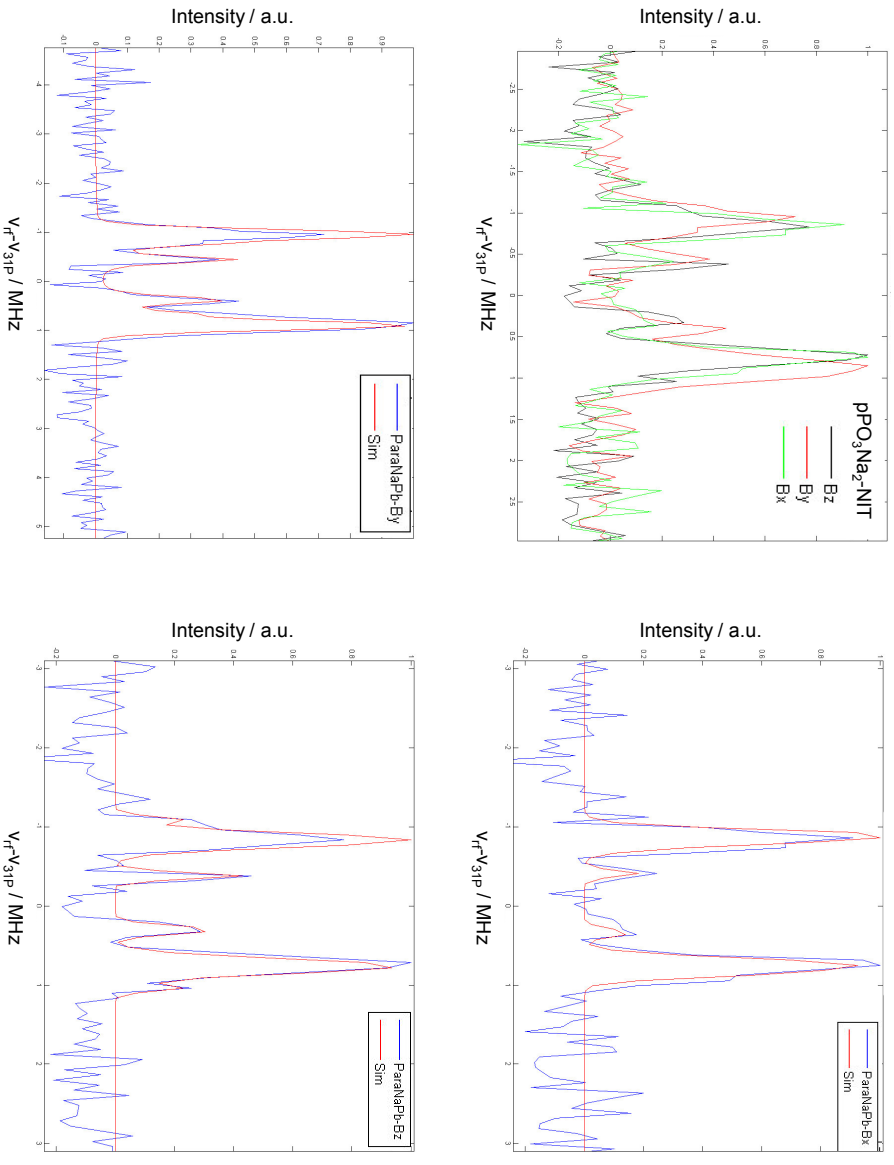

Figure 3.17: ENDOR W-Band spectra of the para-PO_3Na_2 derivative at low temperatures; top left: Comparison of all three direction is shown; top right: measurement in x-direction; bottom left: measurement in y-direction; bottom right: measurement in z-direction

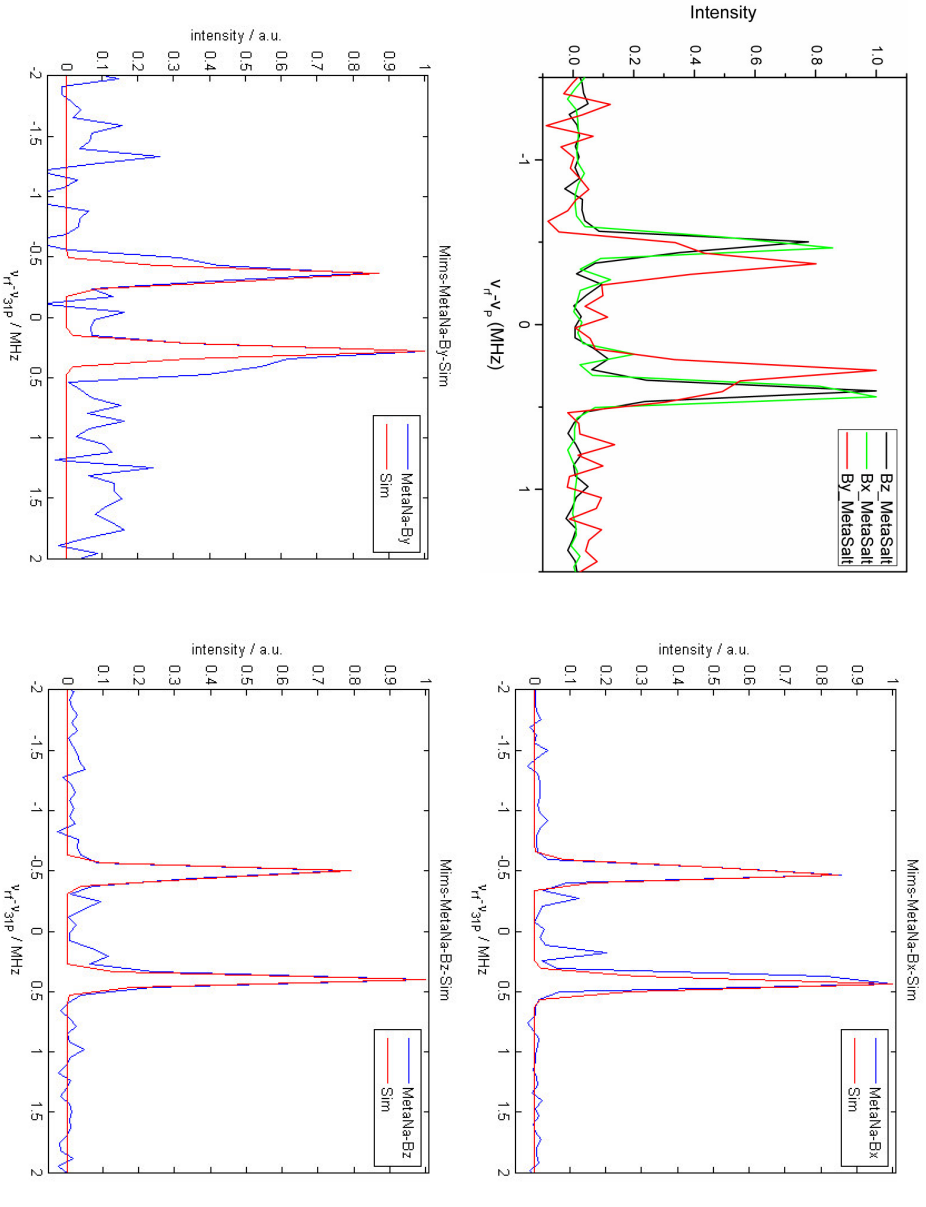

Figure 3.18: ENDOR W-Band spectra of the meta-PO_3Na_2 derivative at low temperatures; top left: Comparison of all three direction is shown; top right: measurement in x-direction; bottom left: measurement in y-direction; bottom right: measurement in z-direction

Table 3.4: Mulliken Spin densities of the different calculated spezies

	NIT-PO_3H_2	NIT-PO_3H^-	NIT-PO_3^{2-}	NIT**H**-PO_3H_2	NIT**H**-PO_3H^-	NIT**H**-PO_3^{2-}
N1	0.29399	0.29510	0.27384	0.20372	0.17445	-0.00128
N2	0.29399	0.29443	0.27424	0.23072	0.13480	0.00005
O1	0.32424	0.32164	0.32893	0.51154	0.51571	0.32552
O2	0.32427	0.32067	0.32924	0.02922	0.02572	0.00007
C	-0.21105	-0.20594	-0.18146	-0.01529	0.01495	0.00147
P	-0.00037	0.00171	0.00278	-0.00032	-0.00669	-0.14296
O3	0.00007	-0.00052	-0.00305	0.00039	0.01134	0.51268
O4	-0.00154	-0.00093	-0.00103	0.00002	0.00871	0.30602
O5	0.00005	-0.00075	-0.00089	0.00004	-0.00006	-0.00112

$$\rho_S = \frac{A_{iso} * g_e}{a_{0,^{31}P} * g_{iso}} \tag{3.1}$$

$$\rho_P = \frac{T * g_e}{b_{0,^{31}P} * g_{iso}} \tag{3.2}$$

with g_e = 2.0023 and
$a_{0,^{31}P}$ = 474.79 mT = 13 306 MHz, $b_{0,^{31}P}$ = 13.09 mT = 367 MHz

By taking a closer look on the spin density and more detailled on the distribution in s-type and p-type orbitals at the ^{31}P of the phosphonate substituted nitronyl-nitroxide radicals, a difference depending on the substitution pattern is clearly seen. At the nitronyl-nitroxide unit the radical is located in a π^*-orbital of the N-O bond, as proven by the hyperfine coupling to the ^{14}N-nucleus, where the z-component is the distinguished one. At the phosphorus, as shown in table 3.3, the y-component is the distinguished one. For the para-substituted derivative pPO_3Na_2-NIT, the y-component has the biggest contribution, whereas for the meta-substituted the y-component is still the distinguished one, but has the smallest contribution. Overall, the isotropic hyperfine coupling of the para-substituted derivative pPO_3Na_2-NIT (A_{iso} = 1.71 MHz) is twice the isotropic hyperfine coupling of the meta-substituted derivative mPO_3Na_2-NIT (A_{iso} = 0.85 MHz). In consequence the spin density in s-type orbitals located on the phosphorus of the para-derivative pPO_3Na_2-NIT (ρ_S = 0.013%) is also twice the spin density in s-type orbitals located on the phosphorus of the meta-derivative mPO_3Na_2-NIT (ρ_S = 0.006%). This is compensated by the difference in spin density of the p-type orbitals located on the phosphorus of the para-derivative pPO_3Na_2-NIT (ρ_P = 0.019%) and

the meta-derivative mPO_3Na_2-NIT (ρ_P = 0.031%), so that overall the total spin density located on the phosphorus is more or less identical (pPO_3Na_2-NIT: ρ_{tot} = 0.032%; mPO_3Na_2-NIT: ρ_{tot} = 0.037%).

The determined spin densities can be compared with results of DFT calculations, having in mind that the EPR spectroscopy is not sensitive concerning the sign of the spin density. The DFT calculations were carried out again in cooperation with U. S. of the Ruhr university in Bochum, Germany. As a necessary precondition the geometry and the electronic structure of the para-substituted NIT-derivatives pPO_3Na_2-NIT **(28a)** , pPO_3NaH-NIT and pPO_3H_2-NIT **(27a)** and their protonated counter-parts pPO_3Na_2-NIT**H**, pPO_3NaH-NIT**H** and pPO_3H_2-NIT**H** were calculated. Then the spin density according to Mulliken, shown in table 3.4, was calculated. As shown with the calculated spin densities, an increased spin shift from the nitronyl-nitroxide unit to the second functional group is expected with deprotonating of the phosphonic acid. Whereas in pPO_3H_2-NIT the spin density on the phosphorus is really small with -4*10^{-4}, it is increased by nearly an order of magnitude in pPO_3Na_2-NIT to 3*10^{-3}. In prinicple in the protonated species the same tendency can be found, although the species with the highest theoretical spin density at the phosphorus pPO_3Na_2-NIT**H** is unlikely to exist, so that the zwitter-ionic species pPO_3H-NIT**H**, which exists in solution as proven by the UV/Vis-spectra in figure 3.11 on page 124, has the highest theoretical spin density at the phosphorus with -7*10^{-3}. Nevertheless, the experimental values for the pPO_3Na_2-NIT derivative (ρ_S = 1*10^{-4}, ρ_P = 2*10^{-4}; ρ_{tot} = 3*10^{-4}) as well as for the mPO_3Na_2-NIT derivative (ρ_S = 6*10^{-5}, ρ_P = 3*10^{-4}; ρ_{tot} = 3*10^{-4}) are lower than predicted by DFT calculations, but in general they match the expected range.

3.3 Complexes with the New Nitronyl-Nitroxide Radicals

With the co-ligands presented in figure 3.19, ^{Pr}HPTB **(38)** and ^{Pr}EPTG **(36)**, dimeric complexes with the COOH-NIT radical are reported by Jung et al. [71, 72, 139]. These are nice examples of compounds, where the nitronyl-nitroxide unit is not bound directly to the metal ions, but through the additional functional group introduced in the phenyl ring. A weak antiferromagnetic interaction of the nitronyl-nitroxide radical unit with a copper(II) dimer in case of the ^{Pr}HPTB co-ligand [71] and with a nickel(II) dimer in case of the ^{Pr}EPTG co-ligand [139] was proven. Therefore, ^{Pr}HPTB **(38)** and ^{Pr}EPTG **(36)** were also choosen as co-ligands for building up dimeric complexes with the new nitronyl-nitroxide radicals

pPO_3H_2-NIT **(27a)** and mPO_3H_2-NIT **(27b)** as well as SO_3H-NIT **(33)**.

In the literature one dimeric cobalt(III) complex bridged by a phenylphosphonate ligand is known, where a quite similar co-ligand to ^{Pr}HPTB **(38)** is used, 2,6-bis[(bis(2-pyridylmethyl)amino)methyl]-4-methylphenol (short: Hbpmp) [150]. Here the phenylphosphonate ligand serves as inhibitor for the hydrolysis reaction of a phosphate monoester and a structural characterisation of the reactive dimeric complex was possible. Deeper insight in the general mechanism of the hydrolysis of phosphate monoesters and diesters and the role of simple mononuclear and dinuclear metal complexes in the hydrolysis reaction was gained, important to obtain an understanding of many enzymes that hydrolyse phosphate esters in nature that are activated by two or more metal ions like alkaline phosphatase, purple acid phosphatase, inositol monophosphatase or D-fructose 1,6-biphosphate 1-phosphatase. Since cobalt(III) in the low-spin state is diamagnetic, no magnetic interaction mediated through the phosphonate group could be determined. But in the literature a series of phosphate diester bridged cobalt(II-II, II-III, III-III) dimers with Hbpbp, again a quite similar co-ligand to Hbpmp and ^{Pr}HPTB, is reported [151]. There, in case of the homovalent cobalt(II) complexes, the magnetic couplings were investigated and it is reported that mainly the Co-O-Co angle of the phenolic co-ligand determines the nature and strength of the interaction (quite similar to the well-known relationship for dimeric copper complexes by Hatfield and Hodgson [106]). The additional bridges of the phosphate diesters seem not to influence the magnetic properties. Again, the similarity to known dicobalt metallohydrolases is shown and the dimeric complexes serves as spectroscopic models for the naturally occurring enzymes.

Unfortunately all synthetic approaches to crystallise complexes with the ^{Pr}HPTB ligand and the new nitronyl-nitroxide radicals pPO_3H_2-NIT and mPO_3H_2-NIT as well as SO_3H-NIT failed up to now, although different metal ions (Co(II), Ni(II) or Cu(II)), counterions (Cl^-, Br^-, ClO_4^-, PF_6^-, BF_4^- or $B(C_6H_5)_4^-$) and solvent combinations (solvent 1: CH_3OH, CH_3CH_2OH or CH_3CN is mixed by diffusion with solvent 2: $(CH_3CH_2)_2O$ or CH_2Cl_2) were tried. Probably the combination of a third oxygen atom in the second functional group (phosphonate or sulfonate) instead of only two oxygens of the carboxylate with the sterical demanding benzimidazole residues in the co-ligand ^{Pr}HPTB hinders the crystallisation of the desired compounds. Already in the case of the COOH-NIT coordinated complexes with ^{Pr}HPTB, the metal ion coordination sphere is not octahedral but just trigonal-bipyramidal (five-coordinated) due to the sterical demand of the bulky benzimi-

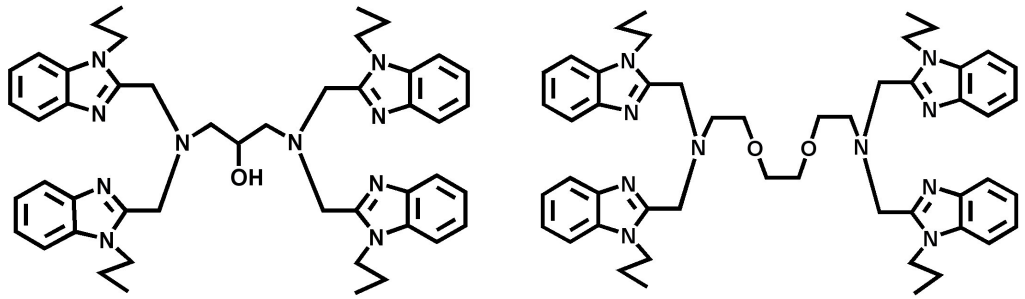

IUPAC name	N,N,N',N',-tetrakis[(2-benzimidazolyl)methyl]- 1,3-diaminopropan-2-ol	1,2-di(2-aminoethoxy)ethan
Short	^{Pr}HPTB **(38)**	^{Pr}EPTG **(36)**
Donoratoms	4 N (benzimidazole) 2 N (amine) 1 O (OH)	4 N (benzimidazole) 2 N (amine) 2 O (ether)
Charge	1-	0
Complexes with		
COOH-NIT	[71, 72]	[139]
SO_3H-NIT **(33)**	/	/
pPO_3H_2-NIT **(27a)**	/	this work
mPO_3H_2-NIT **(27b)**	/	this work

Figure 3.19: Comparison of the used co-ligands; left: ^{Pr}HPTB **(38)**; right: ^{Pr}EPTG **(36)**; both co-ligands provide two dipodal N-N'-N moieties with a central amino nitrogen and two imidazole nitrogen atoms, whereas the backbones are different: ^{Pr}HPTB has only three atoms in the backbone with an attached hydroxyl group, ^{Pr}EPTG has a flexible aliphatic chain between the nitrogen atoms including two ether groups

dazole residues [72].

In contrast to the co-ligands described above, the main advantage of using ^{Pr}EPTG as co-ligand to build up dimeric complexes is that the exchange-coupling of the metal ions through the co-ligand is not further possible. With ^{Pr}HPTB only in the case of a ferromagnetic interaction of the homovalent copper dimer a ground state unequal zero could be realised and a significant interaction with the nitronyl-nitroxide radical unit could be detected [71]. By changing the hydroxyl group in ^{Pr}HPTB to an aliphatic di-ether bridge in ^{Pr}EPTG, the superexchange between the metal ions is not possible anymore. The overall set of donor atoms is only sligthly changed (eigth in total instead of seven) as can be seen in figure 3.19, but the main difference is that the charge of the ligand is changed. Whereas ^{Pr}HPTB is one time negatively charged when it coordinates with the hydroxyl group, ^{Pr}EPTG is still

neutral when incooperated in a complex. For dimeric complexes with the COOH-NIT radical, this makes a large difference. Whereas in the case of ^{Pr}HPTB an exchange-coupled dimeric copper complex with one additionally bridging COOH nitronyl-nitroxide radical is obtained [71], for ^{Pr}EPTG only an "open" dimer copper complex with two COOH-NIT radicals can be isolated. In the latter case no intramolecular exchange coupling is realised at all [139]. With nickel(II) as metal ion the choice of the co-ligand is also crucial for building up the desired dinuclear complexes. With ^{Pr}HPTB, no dimeric nickel complex with COOH-NIT is reported. Probably the favoured octahedral coordination sphere of nickel(II) can not be realised with the bulky benzimidazole residues of ^{Pr}HPTB and the sterically demanding nitronyl-nitroxide derivative. In contrast the aliphatic methylene chain between the di-ether oxygen bridge of the ^{Pr}EPTG co-ligand opens the coordination pocket for the two nickel ions, so that the COOH-NIT radical can be coordinated. Additionally a chloride ion is coordinated to complete the octahedral coordination sphere of the nickel(II) ions. Again an exchange-coupled homovalent metal ion dimer is achieved. Here the observed nickel-nickel coupling through the Ni-Cl-Ni bridge is ferromagnetic in nature, so that again a significant coupling with the nitronyl-nitroxide radical unit could be determined [139].

The successfull attemps for building up complexes with ^{Pr}EPTG as co-ligand and the new nitronyl-nitroxide radicals pPO_3H_2-NIT **(27a)** and mPO_3H_2-NIT **(27b)** are presented in the following sections. Unfortunately with the SO_3H-NIT derivative **(33)** no complex could be crystallised up to now, probably the third oxygen atom of the sulfonate group prevent the coordination of smaller counterions as in the case of presented phosphonate complexes. With only one negative charge of the sulfonate group and the neutral ^{Pr}EPTG co-ligand, three counterions would be needed for charge compensation of the dimeric metal(II) ion complexes, what makes the incorporation in a crystal packing complicated.

3.3.1 Complexes of Para Substituted Phenylphosphonic Acids with ^{Pr}EPTG

In this section the coordination of the pPO_3Na_2-NIT derivative **(28a)** with the ^{Pr}EPTG co-ligand is described, together with the coordination of 4-tolylphosphonate **(2c)** as bridging ligand. The resulting complex $[Ni_2(^{Pr}EPTG)(C_7H_7PO_3)(H_2O)_2](ClO_4)_2$ **(39)** with the diamagnetic tolylphosphonate is needed to determine the nickel-nickel exchange interaction present in the complex due to the link-

age through the phosphonate ligand, which is the only exchange coupling of the nickel-nickel ions as planned with the co-ligand design in general. Due to the quite similar coordination spheres of the nickel ions in $[Ni_2(^{Pr}EPTG)(C_7H_7PO_3)(H_2O)_2](ClO_4)_2$ **(39)** and in the nickel complex with the paramagnetic bridging ligand pPO_3Na_2-NIT, $[Ni_2(^{Pr}EPTG)(pPO_3\text{-NIT})(H_2O)_2](ClO_4)_2$ **(40)**, as shown in figure 3.20, it is assumed that the determined nickel-nickel exchange interaction in $[Ni_2(^{Pr}EPTG)(C_7H_7PO_3)(H_2O)_2](ClO_4)_2$ is also present in $[Ni_2(^{Pr}EPTG)(pPO_3\text{-NIT})(H_2O)_2](ClO_4)_2$.

In contrast to the already described nickel complexes of the ^{Pr}EPTG co-ligand with the COOH-NIT radical [139], no additional bridge is realised as intended by the design of the co-ligand ^{Pr}EPTG. To complete the octahedral coordination sphere of the two nickel(II) ions, two water molecules are bound which further stabilise the complex by a hydrogen bridge to the third free oxygen atom of the phosphonate residue. For the first time, the new nitronyl-nitroxide radical pPO_3-NIT is crystallised. Typicial features of nitronyl-nitroxide radicals in the solid state are shown in figure 3.21, together with a list of selected bond lengths and torsion angles. Although the radical is delocalised in the nitronyl-nitroxide unit, differences in the N-O bond lengths and C-N bond lengths are found, as explained in the case of the Phenyl-NIT derivative in section 3.1.1. The averaged N-O bond length is with $\approx$ 1.25 Å in the expected range for nitronyl-nitroxide radicals. The same is true for the twisting of the two ring systems, the phenyl ring and the imidazoline ring. Here, the nitronyl-nitroxide unit N-O-C-N-O is not completely flat, explaining the differences in the two C-C-C-N torsion angles.

The measurement of the magnetic susceptibilities of $[Ni_2(^{Pr}EPTG)(C_7H_7PO_3)(H_2O)_2](ClO_4)_2$ and $[Ni_2(^{Pr}EPTG)(pPO_3\text{-NIT})(H_2O)_2](ClO_4)_2$ are presented in figure 3.22 together with a schematic coupling scheme and a correlation diagram of the nickel-nickel exchange coupling J_{12} and the nickel-radical exchange coupling J_{13}. The value of the nickel-nickel exchange coupling J_{12} = -1.53 cm^{-1} (g_{Ni} = 2.16) was determined by a simulation according to the Heisenberg-Dirac-van-Vleck Hamiltonian $\hat{H} = -2\sum_{i,j} J_{ij} S_i S_j$ for $[Ni_2(^{Pr}EPTG)(C_7H_7PO_3)(H_2O)_2](ClO_4)_2$ as can be seen in figure 3.22. For $[Ni_2(^{Pr}EPTG)(pPO_3\text{-NIT})(H_2O)_2](ClO_4)_2$, the influence of the additional spin centre is clearly seen in the measurement of the magnetic susceptibility. Overall the curve is shifted up in χ*T, so that for the high-temperature region a value of χ*T = 2.6 cm^3*K/mol is reached which is sligthly higher than the expected value of twice 1 cm^3*K/mol plus 0,375 cm^3*K/mol for two uncoupled nickel(II) centres and an uncoupled radical spin of 1/2. The differ-

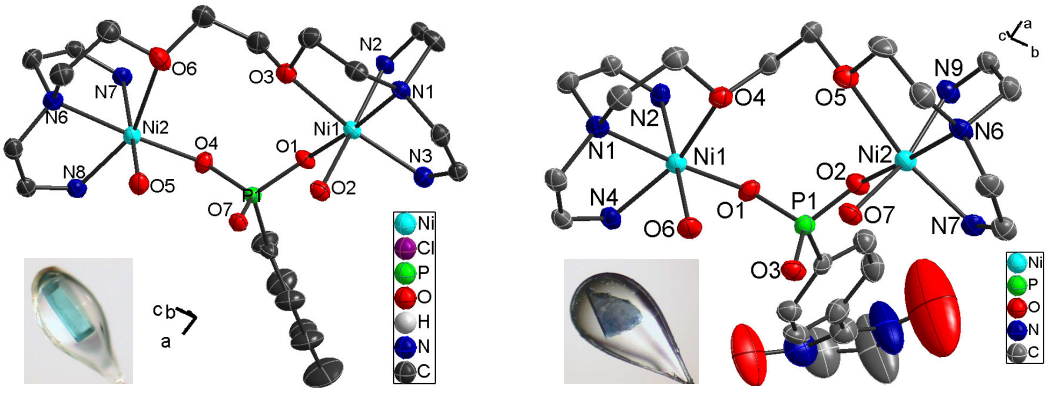

bond lengths	in Å	bond lengths	in Å
Ni1-N1	2.155(2)	Ni1-N1	2.134(4)
Ni1-N2	2.036(2)	Ni1-N2	2.048(4)
Ni1-N3	2.028(2)	Ni1-N4	2.057(4)
Ni1-O1	1.975(2)	Ni1-O1	1.968(3)
Ni1-O2	2.117(2)	Ni1-O6	2.131(3)
Ni1-O3	2.187(2)	Ni1-O4	2.161(3)
Ni2-N6	2.170(2)	Ni2-N6	2.168(4)
Ni2-N7	2.031(2)	Ni2-N9	2.021(4)
Ni2-N8	2.032(2)	Ni2-N7	2.056(4)
Ni2-O4	1.976(2)	Ni2-O2	1.996(3)
Ni2-O5	2.068(2)	Ni2-O7	2.083(3)
Ni2-O6	2.501(2)	Ni2-O5	2.443(3)
Ni1-Ni2	5.408(5)	Ni1-Ni2	5.244(8)
angles	in degree	angles	in degree
O1-Ni1-N1	175.23(7)	O1-Ni1-N1	175.8(1)
O2-Ni1-N2	170.40(7)	O6-Ni1-N2	172.3(1)
O3-Ni1-N3	160.65(7)	O4-Ni1-N4	159.8(1)
O4-Ni2-N6	175.99(7)	O2-Ni2-N6	176.6(1)
O5-Ni2-N7	168.02(8)	O7-Ni2-N9	164.7(1)
O6-Ni2-N8	153.55(7)	O5-Ni2-N7	153.5(1)
		Torsion NIT	27.4(1)/31.4(1)

Figure 3.20: Comparison of the labelled inner cores $[Ni_2(^{Pr}EPTG)(C_7H_7PO_3)(H_2O)_2]^{2+}$ **(39)** (left) and $[Ni_2(^{Pr}EPTG)\ (pPO_3\text{-}NIT)(H_2O)_2]^{2+}$ **(40)** (right); selected bond length and angles are also listed

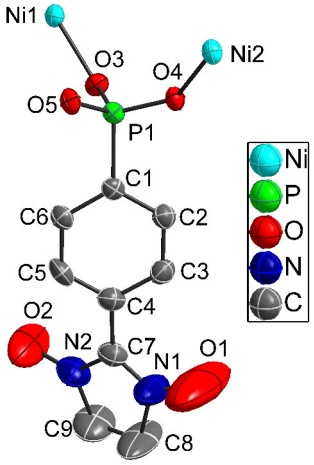

bond length	in Å
P1-O3	1.521(3)
P1-O4	1.519(3)
P1-O5	1.525(3)
P1-C1	1.819(5)
C7-N1	1.252(8)
C7-N2	1.349(7)
C8-N1	1.484(9)
C9-N2	1.507(9)
N1-O1	1.224(10)
N2-O2	1.284(7)
torsion angles	in °
C5-C4-C7-N1	31.4(1)
C3-C4-C7-N2	27.4(1)
N1-C8-C9-N2	14.6(1)

Figure 3.21: Part of the crystal structure of $[Ni_2(^{Pr}EPTG)(pPO_3\text{-}NIT)(H_2O)_2](ClO_4)_2$ **(40)**; H atoms and methyl groups of the nitronyl-nitroxide unit are omitted for clarity; Selected bond lengths and torsion angles are listed

ence arises from the spin-orbit coupling effects of the two nickel metal ions. At low temperatures, a non-zero ground spin state is realised because of the uncompensated spin of the organic radical of 1/2. Overall, the shown coupling scheme with three spin centres and also three coupling constants is appropriate. But the model can be simplified by setting an unique nickel-radical interaction, so J_{13} is identical to J_{23}. Still the two resulting coupling constants are correlated as can be seen at the bottom of figure 3.22, that means that the temperature dependence of the magnetic susceptibility can be reproduced satisfactorily with several sets of parameters. With the parameters obtained from $[Ni_2(^{Pr}EPTG)(C_7H_7PO_3)(H_2O)_2](ClO_4)_2$, a nickel-nickel interaction of J_{12} = -1.53 cm^{-1} and a g-value of nickel of 2.16, it is possible to extract a reasonable value for the nickel-radical coupling constant in the range of J_{13} = [-2, +1] cm^{-1} as indicated by the green line in figure 3.22. Unfortunately, due to the fact that the exchange coupling mediated through the μ_2-bridging phosphonate residue J_{12} is antiferromagnetic in nature and although it is as weak as the expected weak metal-radical interaction J_{13}, the nature of the weak metal-radical interaction J_{13} can not be determined exactly.

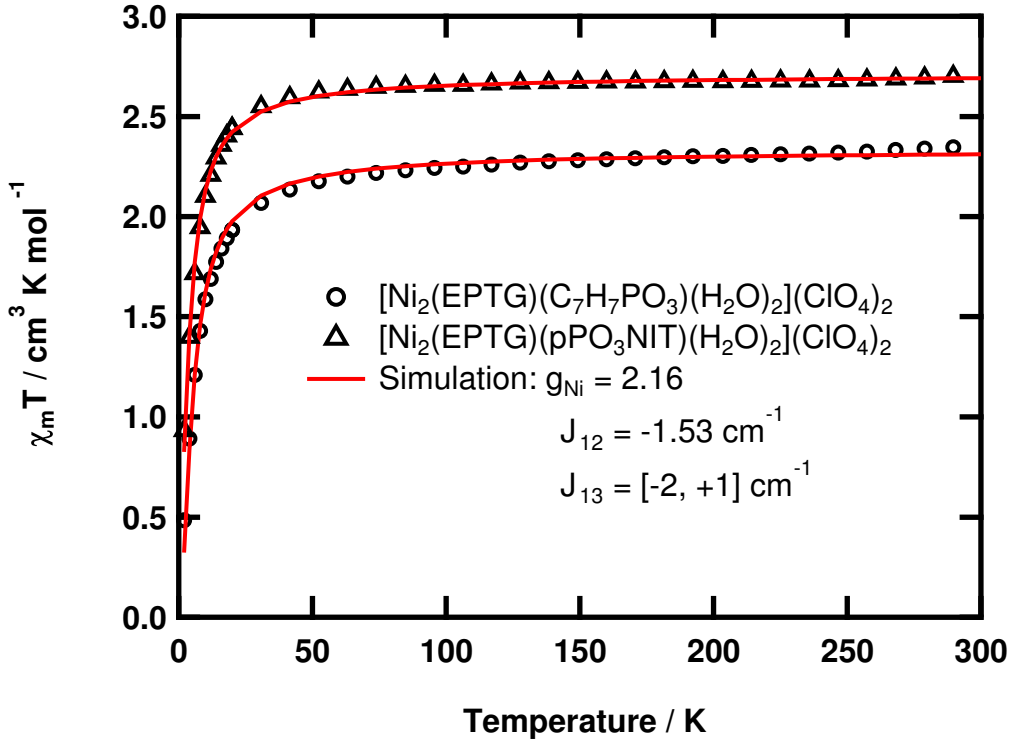

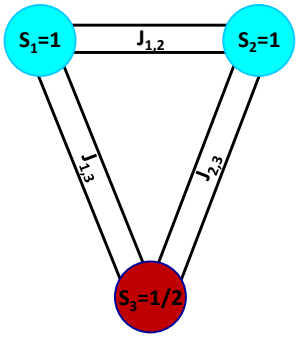

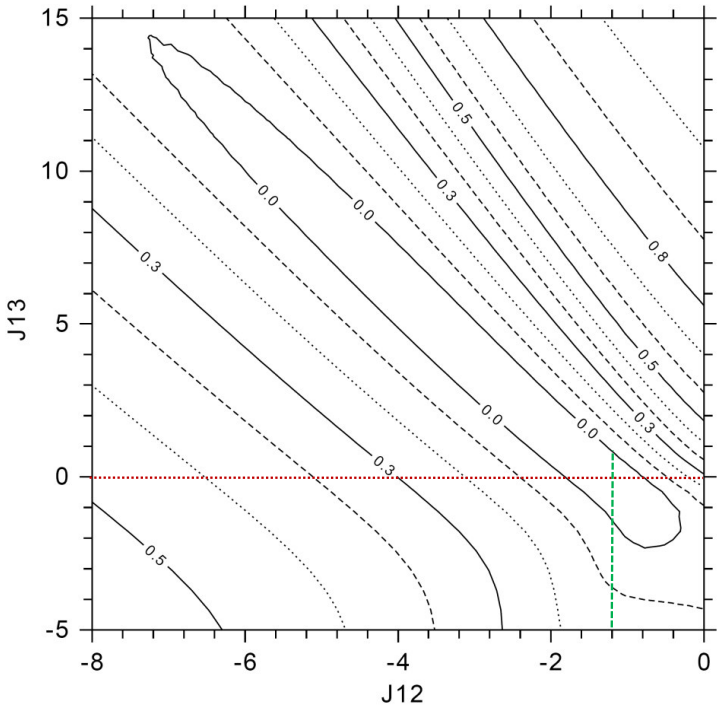

Figure 3.22: Top: measurement of the magnetic susceptibility of $[Ni_2(^{Pr}EPTG)(C_7H_7PO_3)(H_2O)_2](ClO_4)_2$ **(39)** and $[Ni_2(^{Pr}EPTG)(pPO_3NIT)(H_2O)_2](ClO_4)_2$ **(40)** with a field of 1 T, χ*T vs. T plot is shown; bottom: coupling scheme is drawn at the left side, a correlation diagram of J_{12} and J_{13} is shown at the right side

3.3.2 Complex of mPO_3H_2-NIT derivative with ^{Pr}EPTG as Co-Ligand

In case of the new nitronyl-nitroxide radicals pPO_3Na_2-NIT **(28a)** and mPO_3Na_2-NIT **(28b)** , the oxidation with lead dioxide during synthesis, a nitronyl-nitroxide derivative containing some lead impurities is obatined. The ability to bind metal ions via the phosphonate residue is so strong that some lead(II) ions are bound. Usually these impurities do not disturb the following complexation reactions with other divalent metal ions, because a large excess of the transition metal ions is used compared to the small amount of lead impurities. But here, the crystallisation process favours a five nuclear compound, where in principle two dimeric units hold together by the ^{Pr}EPTG co-ligand are further linked by a lead(II) ion. As before in case of the pPO_3H_2-NIT derivative in $[Ni_2(^{Pr}EPTG)(pPO_3\text{-}NIT)(H_2O)_2](ClO_4)_2$ **(40)**, one radical is coordinated per dimeric unit, so in total two mPO_3H_2-NIT derivative are coordinated again in a μ_2-bridging mode as can be seen in figure 3.23. The former free oxygen atom of the phosphonate residue is now coordinated to the lead(II) ion as well as one of the former two coordinated water molecules (which completed the coordination spheres of the nickel(II) ions) which is now a μ_2 hydroxy-bridge to the lead(II) ion. Overall a two-fold rotation axis is found through the lead(II) ion and the chloride ion shown of one of the perchlorate counterions, so that in total only three perchlorate counterions can be found, what further confirms an assumed superposition of one sodium(I) ion with a nickel(II) ion resulting the general formula $[Ni_3Na_1Pb_1(^{Pr}EPTG)_2\ (mPO_3\text{-}NIT)_2(OH)_2](ClO_4)_3$ **(41)**. Selected bond lengths and angles of the compound $[Ni_3Na_1Pb_1(^{Pr}EPTG)_2(mPO_3\text{-}NIT)_2(OH)_2](ClO_4)_3$ can be found in figure 5.81 on page 271 in the appendix. For the first time, the new nitronyl-nitroxide radical mPO_3-NIT is crystallised. Typicial features of nitronyl-nitroxide radicals in the solid state are shown in figure 3.24, together with a list of selected bond lengths and torsion angles. Although the radical is delocalised in the nitronyl-nitroxide unit, differences in the N-O bond lengths and C-N bond lengths are found, as explained in the case of the Phenyl-NIT derivative in section 3.1.1. The averaged N-O bond length is with ≈ 1.31 Å in the expected range for nitronyl-nitroxide radicals. The same is true for the twisting of the two ring systems, the phenyl ring and the imidazoline ring. Here, the nitronyl-nitroxide unit N-O-C-N-O is not completely flat, explaining the differences in the two C-C-C-N torsion angles.

So far only one structure containing a lead ion and a nitronyl-nitroxide derivative is known [123], in the complex $[Pb(NIT2Py)_2(NO_3)_2]$ with NIT2Py = 2-(2'-pyridyl)-4,4,5,5-tetramethylimidazoline-1-oxyl-3-oxide the lead(II) ion is coor-

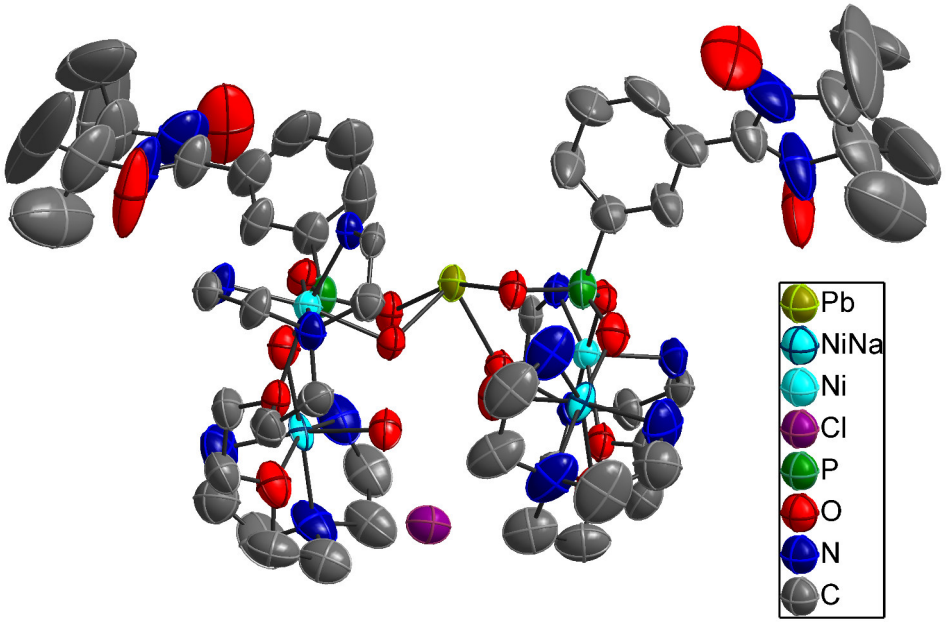

Figure 3.23: Part of the crystal structure of $[Ni_3Na_1Pb_1(^{Pr}EPTG)_2(mPO_3\text{-}NIT)_2(OH)_2](ClO_4)_3$ **(41)**; a superposition of sodium and nickel at one position is needed for charge balance; the ^{Pr}EPTG co-ligands and the perchlorate counterions are not fully shown for clarity, as H atoms omitted for clarity

dianted twice directly by the nitronyl-nitroxide unit of the two radicals and additionally through the pyridyl-nitrogen in the backbone. Futhermore, the coordination sphere of the lead is completed by the two nitrate ions where one is chelating and one is only single-bonded. In this case an effective antiferromagnetic coupling through the diamagnetic lead(II) ion bridge of the two nitronyl-nitroxide radicals is found. In comparison with the complex presented here, such an exchange coupling does not play a significant role due to the fact that the nitronyl-nitroxide unit is not coordinated directly to the lead(II) ion, but only through the second functional group, the posphonate residue.

For the simulation of the magnetic susceptibilitiy of $[Ni_3Na_1Pb_1\ (^{Pr}EPTG)_2\ (mPO_3\text{-}NIT)_2(OH)_2](ClO_4)_3$ **(41)** according to the Heisenberg-Dirac-van-Vleck Hamiltonian $\hat{H} = -2\sum_{i,j} J_{ij} S_i S_j$, the coupling scheme shown in figure 3.25 is used. Due the fact that no exchange coupling through the lead(II) bridge is possible, only two different couplings are considered. The first one is a nickel-nickel coupling labelled $J_{1,2}$ and the second one is a nickel-NIT-coupling labelled $J_{1,3}$, $J_{2,3}$ and $J_{4,5}$. As simplification all nickel-NIT couplings are assumed to be identical, independently

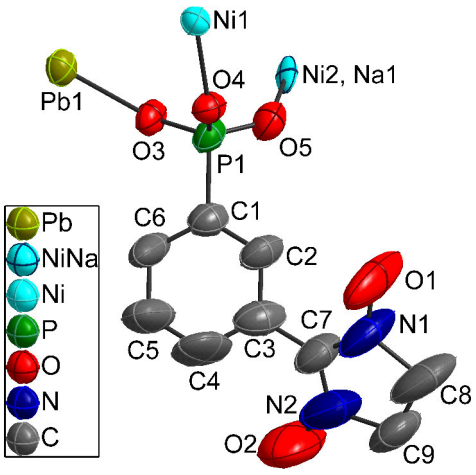

bond length	in Å
P1-O3	1.54(1)
P1-O4	1.49(1)
P1-O5	1.54(1)
P1-C1	1.81(1)
C7-N1	1.32(2)
C7-N2	1.28(2)
C8-N1	1.53(2)
C9-N2	1.52(2)
N1-O1	1.26(2)
N2-O2	1.36(2)
torsion angle	in °
C2-C3-C7-N1	33.9(2)
C4-C3-C7-N2	35.2(2)
N1-C8-C9-N2	9.8(1)

Figure 3.24: Part of the crystal structure of $[Ni_3Na_1Pb_1(^{Pr}EPTG)_2(mPO_3\text{-}NIT)_2(OH)_2](ClO_4)_3$ **(41)**; H atoms and methyl groups of the nitronyl-nitroxide unit are omitted for clarity; Selected bond lengths and torsion angles are listed

in which of the both parts (two nickel ions or one nickel and one sodium ion) the nickel-NIT pair is located. The result of the simulation can be seen in figure 3.25, with g = 2.43 and $J_{1,2}$ = -2.0 cm^{-1} for the nickel-nickel exchange coupling and $J_{1,3} = J_{2,3} = J_{4,5} = 0$ cm^{-1} for the nickel-NIT exchange coupling. Again as discussed for $[Ni_2(^{Pr}EPTG)(pPO_3\text{-}NIT)(H_2O)_2](ClO_4)_2$ **(40)**, the two coupling constants are correlated, so several sets of parameters fit nicely the experimental data. Unfortunately, due to the fact that the exchange coupling mediated through the μ_2-bridging phosphonate residue J_{12} is antiferromagnetic in nature, and although it is as weak as the expected weak metal-radical interaction J_{13}, the nature of the weak metal-radical interaction J_{13} can not be closer determined and therefore it is set to zero in the simulation.

For the first time, two complexes containing the new nitronyl-nitroxide radicals pPO_3Na_2-NIT **(28a)** and mPO_3Na_2-NIT **(28b)** are described. As intended with the choosen co-ligand ^{Pr}EPTG, the superexchange of two metal ions through the co-ligand is not possible anymore. Here, the nickel-nickel interaction (labelled $J_{1,2}$) is defined by the phosphonate bridge of the nitronyl-nitroxide radicals. As expected, this exchange interaction is weak. Due to correlation effects, the nickel-

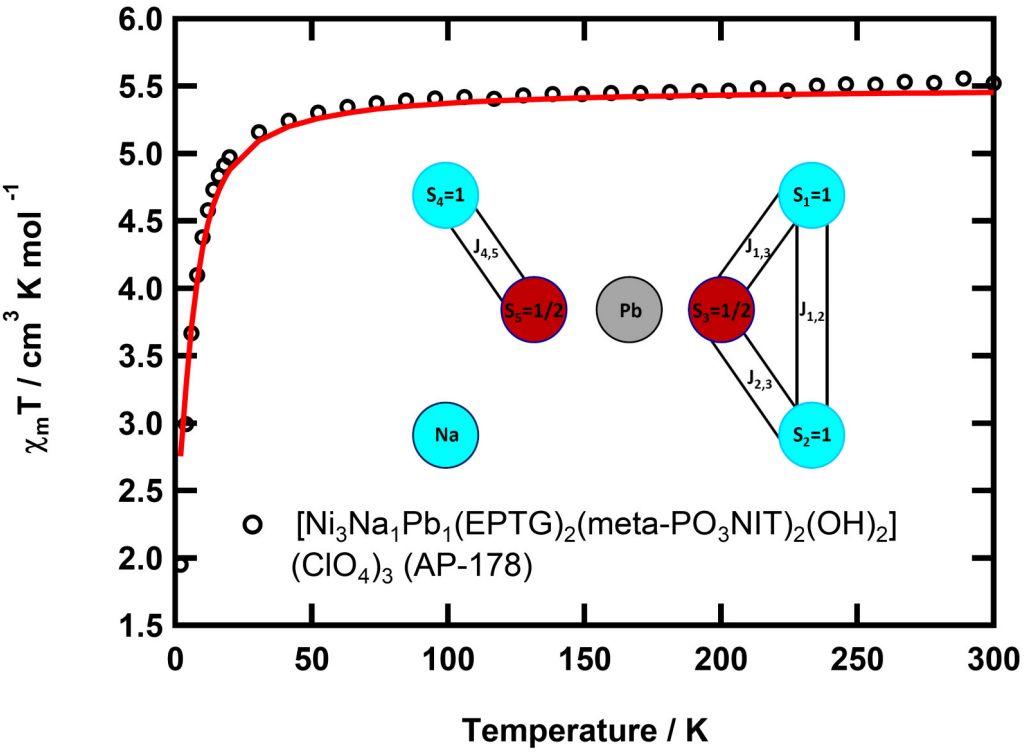

Figure 3.25: Top: measurement of the magnetic susceptibility of [$Ni_3Na_1Pb_1$ (^{Pr}EPTG)$_2$ (mPO_3-NIT)$_2$(OH)$_2$](ClO_4)$_3$ **(41)** with a field of 1 T, χ*T vs. T plot is shown; coupling scheme is drawn as inset; obtained simulation parameters: g = 2.43; $J_{1,2}$ = -2.0 cm^{-1}; $J_{1,3}$ = $J_{2,3}$ = $J_{4,5}$ = 0 cm^{-1}

radical exchange interaction (labelled $J_{1,3}$) could not be determined exactly. In the dimeric COOH-NIT nickel complex with ^{Pr}EPTG as co-ligand, the nickel-radical interaction $J_{1,3}$ = -0.4 cm^{-1} could be exactely determined. Compared to the dimeric nickel complex bridged by COOH-NIT, here in the PO_3-NIT bridged compounds, the nickel-radical interaction is assumed to be stronger, because the phosphonate residue is more electron-withdrawing. A spin shift from the nitronyl-nitroxide unit on the phosphonate residue was already proven in section 3.2.

Nevertheless, the two new complexes [Ni_2(^{Pr}EPTG)(pPO_3-NIT)(H_2O)$_2$](ClO_4)$_2$ **(40)** and [$Ni_3Na_1Pb_1$ (^{Pr}EPTG)$_2$ (mPO_3-NIT)$_2$(OH)$_2$](ClO_4)$_3$ **(41)** are nice examples of compounds, where the nitronyl-nitroxide unit is not bound directly to the metal ions, but through the additional functional group introduced in the phenyl ring.

3.4 PART 2: Summary

The synthesis and fully characterisation by X-ray analysis, UV/Vis spectroscopy, EPR and cyclovoltammetric measurements of three new nitronyl-nitroxide radical derivatives, namely SO_3H-NIT **(33)**, pPO_3H_2-NIT **(27a)** and mPO_3H_2-NIT **(27b)** , were presented. These new nitronyl-nitroxide radicals are particular interesting, because they are, except for the COOH-NIT derivative, the only nitronyl-nitroxide radicals known with a second functional group, that is acidic in nature. The pH-dependence of the nitronyl-nitroxide radical unit was reviewed in general, because intrinsically a protonation of the nitronyl-nitroxide radical unit is possible in the new nitronyl-nitroxide radical derivatives due to the additional acidic functional group.

For the Phenyl-NIT derivative the behaviour in an acidic media was described in a qualitative way by Ullman et al. 1968 [48]. The assumed intermediate protonated nitronyl-nitroxide radical species [Phenyl-NIT**H**]$^+$ could be confirmed for the first time in this work experimentally by UV/Vis spectroscopy and theoretically by DFT calculations. The decay process described for the Phenyl-NIT derivative seems also likely for the meta-phosphonate substituted nitronyl-nitroxide radical derivative mPO_3Na_2-NIT under acidic conditions in solution. With time a decrease of the typical band for a protonated nitronyl-nitroxide radical around 450 nm in the UV/Vis spectra could be observed. The behaviour of the para-phosphonate substituted nitronyl-nitroxide radical derivative is more complicated under acidic conditions in solution, so that further studies are needed to understand the behaviour in general and the difference to the meta-substituted derivative. Nevertheless, for both phosphonate substituted nitronyl-nitroxide radicals it was proven by UV/Vis spectroscopy that the zwitter-ionic species pPO_3H-NIT**H** and mPO_3H-NIT**H** play a significant role under acidic conditions. Furthermore, the continuous wave X-band EPR spectra of the two phosphonate substituted nitronyl-nitroxide radicals were discussed in contrast to the two phosphonic acid substituted nitronyl-nitroxide radicals. The shift of the spin density in the nitronyl-nitroxide unit depending on the degree of protonation of the second functional group was in the focus and a significant spin shift to the nitrogen atoms was found upon deprotonating the second functional group.

Due to the fact that the nuclear spin of the phosphorus present interacts with the unpaired electron, with the two phosphonate substituted nitronyl-nitroxide radicals an ideal probe was obtained for the investigation of the spin density shift

on the second functional group depending on the degree of protonation of the second functional group. DFT calculations were carried out, which predicts that with deprotonating the second functional group the electron spin density on the second functional group should be significantly increased. By pulsed X-band EPR experiments, HYSCORE, the interaction of the electron spin with the ^{1}H, ^{14}N, ^{13}C and ^{31}P nuclei could be visualised. The interaction with the ^{31}P nucleus was further investigated by W-band ENDOR experiments taking advantage of the higher spectral resolution of the g-factor, so that orientation selective measurements were possible. With the result of these measurements not only very good simulations of the X-band HYSCORE spectra were possible, from the paramters the spin densities in the s-type and p-type orbitals located at the phosphorus centres could be calculated, and directly compared with the theoretically obtained Mulliken spin densities by DFT calculations. The Mulliken spin densities are higher than the experimentally determined spin densities, but the expected range is matched.

Finally the new nitronyl-nitroxide derivatives could be successfully incorporated in metal ion complexes, in which the coordination to the metal ions was realised by the phosphonate residue, and not directly by the nitronyl-nitroxide unit. A special designed co-ligand named ^{Pr}EPTG was used to avoid exchange couplings of the metal ions through the co-ligand but only through the phosphonate residue of the nitronyl-nitroxide radical. As a result the strength of the metal-metal exchange coupling is decreased. However, the residual antiferromagnetic character of the exchange interaction through the μ_2-phosphonate bridge prevents the unambiguous determination of the weak metal-radical interaction. In all three new complexes with the ^{Pr}EPTG co-ligand, that were synthesised and completely characterised, no additional direct coordination of the nitronyl-nitroxide radical unit is observed. This promises stronger exchange interactions, so that the building up of coordination polymers (one-dimensional I^0O^1, two-dimensional I^0O^2 or three-dimensional I^0O^3) with the new nitronyl-nitroxide derivatives with acidic second functional groups is still a future goal.

4

Conclusion

Hybrid inorganic-organic framework materials are extremely versatile. Independently of the class of material, extended inorganic hybrid material or coordination polymers, in this work strategies were presented, how to influence the dimensionality of the compound. In case of metal phosphonate compounds, the pH-value was adjusted during the reaction and the degree of protonation of the phosphonate ligand was controlled. Due to the fact that all obtained metal phosphonate compounds were neutral, no additional counterion was incorporated in the structure and the ligand to metal ratio could be predicted. The final composition of the compounds was dependant of a changing amount of water completing the octahedral coordination spheres of the transition metal ions. Several new metal-phosphonate compounds ranging from zero-dimensional (I^0O^0, co-crystallisation of $M(H_2O)_6$ with the deprotonated phosphonate ligand), over one-dimensional (I^1O^0, chain structures) to two-dimensional (I^2O^0, layered structures) were discussed in detail concerning their magnetic behaviour. In general, the exchange interactions expected in inorganic hybrid materials are strong, because often a superexchange through a single oxygen atom is possible. Here, often several competing exchange interactions were present, so that complicated magnetic behaviours were observed.

In coordination polymers, the dimensionality of the compound can be controlled by the geometry of the node or secondary building unit (SBU) combined with the geometry of the linker. Here, in the case of the formiate and the acetate ion, small carboxylates were used as linear linkers. A new class of one-dimensional ladder-like chain compounds based on the windmill motive was presented. Furthermore, new insighths in a known two-dimensional layered structure were gained. In general, the exchange interactions expected in coordination polymers are weak, because often the exchange path through the linker is long, e.g. in 4,4'-bipyridine. But with a careful selection of SBU and linker molecules it is as well possible to obtain interesting molecular magnetic materials.

Three new examples of nitronyl-nitroxide radicals were presented, where an additional acidic functionality was introduced. The consequences of the acidic character of the additionally introduced sulfonic acid or phosphonic acid group on the nitronyl-nitroxide radical unit was investigated in detail for the first time. With the phosphonic acid substituted nitronyl-nitroxide radicals, perfect samples for the investigation of the spin shift in nitronyl-nitroxide radicals by EPR spectroscopy in general are obtained, due to the phosphorus present. Also the protonation state of the additional phosphonic acid group was taken into account.

Furthermore, in this work the first metal complexes of the new acidic substituted nitronyl-nitroxide radicals were presented. The coordination of nickel(II) metal ions to the acidic, second functional group of the nitronyl-nitroxide radical was described. The magnetic exchange interactions of the metal ions and the metal-radical exchange interactions were investigated. So far, no incorporation of the new acidic substituted nitronyl-nitroxide radicals in extended hybrid inorganic-organic framework materials was achieved.

Independently of the used class of hybrid inorganic-organic framework materials, interesting molecular magnetic materials can be designed due to the fact that the dimensionality of the compounds can be controlled. With nitronyl-nitroxide radicals as organic linkers, in future even more spin carriers can be incorporated in the hybrid inorganic-organic framework materials and the magnetic behaviour can be enhanced.

5

Experimental Part

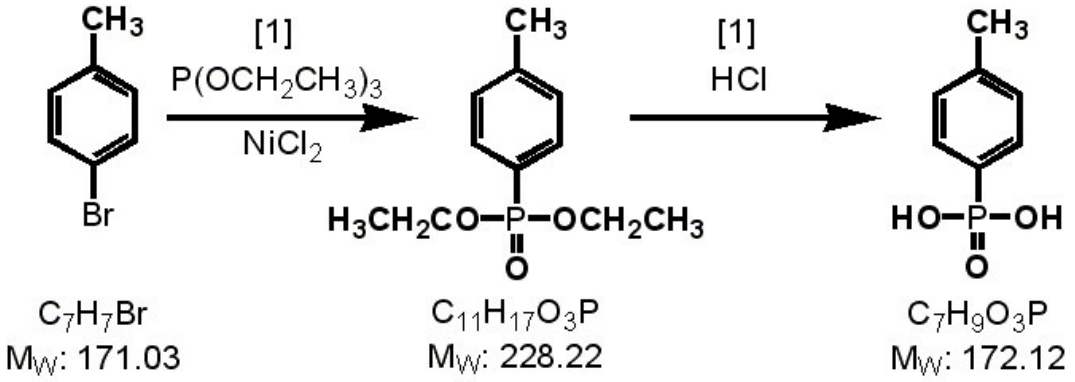

Figure 5.1: Synthesis strategy of the different aromatic phosphonate ligands with a methyl substituent, exemplarily shown on the para substituent, [1] Chem.Ber., 103, 2428-2436 (1970)

5.1 Extended Systems

5.1.1 Aromatic Phosphonate Systems

5.1.1.1 Ligands with a Methyl Substituent

The following general procedure was carried out under an inert atmosphere of argon. The appropiate bromotoluene derivate (M_W = 171.0 g/mol, n = 0.25 mol, m = 42.76 g) was added to a catalytic amount of water free nickel chloride (M_W = 129.7 g/mol, n = 11 mmol, m = 1.5 g). The orange reaction solution was heated up to 180°C, before triethylphosphite (M_W = 166.2 g/mol, n = 0.30 mol, m = 49.85 g) was added carefully with a syringe. The reaction solution turned blue-violet and emerging ethylbromide was distilled off. After the complete addition of triethylphosphite, the reaction mixture still was heated up for 30 minutes. In a fractional distillation the desired phosphonic acid diethyl ester could be obtained in the last fraction (boiling point above 120°C). Saponification of the phosphonic acid diethyl ester with concentrated hydrochlorid acid (V = 150 ml) yielded the free tolyl-phosphonic acid derivate.

2-Tolyl-phosphonic acid diethyl ester (1a)
Research Journal: XE-191
Literature: P. Tavs, Chem.Ber., 103 (8), 2428 (1970) [75]

Yield: M_W = 228.22 g/mol, n = 0.23 mol, m = 51.92 g, 91%
^{1}H-NMR ($CDCl_3$, 400 MHz): Figure 5.7 on page 211

δ (ppm): 1.22 (t, 6H, CH_3, [12,15]), 2.48 (t, 3H, CH_3, [9]), 4.01 (dq, 4H, CH_2, [11,14]), 7.15 (m, 2H, CH, [1,5]), 7.31 (t, 1H, CH, [6]), 7.82 (dd, 1H, CH, [2])

3-Tolyl-phosphonic acid diethyl ester (1b)

Research Journal: XE-189
Literature: P. Tavs, Chem.Ber., 103 (8), 2428 (1970) [75]

Yield: M_W = 228.22 g/mol, n = 0.22 mol, m = 50.21 g, 88%
^{1}**H-NMR ($CDCl_3$, 400 MHz)**: Figure 5.9 on page 212
δ (ppm): 1.21 (t, 6H, CH_3, [12,15]), 2.28 ppm (s, 3H, CH_3, [9]), 3.99 ppm (dq, 4H, CH_2, [11,14]), 7.24 ppm (m, 2H, CH, [1,6]), 7.51 (m, 2H, CH, [2,4])
^{31}**P-NMR ($CDCl_3$, 166 MHz)**: δ = 19.6 ppm

4-Tolyl-phosphonic acid diethyl ester (1c)

Research Journal: XE-186
Literature: P. Tavs, Chem.Ber., 103 (8), 2428 (1970) [75]

Yield: M_W = 228.22 g/mol, n = 0.20 mol, m = 46.21 g, 81%
^{1}**H-NMR ($CDCl_3$, 400 MHz)**: Figure 5.11 on page 213
δ (ppm): 1.26 (t, 6H, CH_3, [12,15]), 2.34 (s, 3H, CH_3, [7]), 4.04 (dq, 4H, CH_2, [11,14]), 7.22 (dd, 2H, CH, [1,5]), 7.65 (dd, 2H, CH, [2,4])

2-Tolyl-phosphonic acid (2a)

Research Journal: XE-191
Literature: P. Tavs, Chem.Ber., 103 (8), 2428 (1970) [75]

Yield: M_W = 172.12 g/mol, n = 0.18 mol, m = 30.48 g, 77%
^{1}**H-NMR (DMSO, 400 MHz)**: Figure 5.8 on page 211
δ (ppm): 2.47 (s, 3H, CH_3, [11]), 7.19 (m, 2H, CH, [1,5]), 7.33 (t, 1H, CH, [6]), 7.69 (dd, 1H, CH, [2])
^{31}**P-NMR (DMSO, 166 MHz)**: δ = 13.4 ppm
IR (KBr): Figure 5.41 on page 228
ν (cm^{-1}) = 2800 (br, ν_s OH phosphonate), 2313 (m, ν_s CH3 methyl), 1599 and 1454 (m, ν_s C=C), 1204 (s, ν_s P=O), 1002 and 982 (s, ν_{as} P-OH) 814 and 761 (m, δ_{oop} 4H ring), 689 (w, δ_{oop} ring)

3-Tolyl-phosphonic acid (2b)
Research Journal: XE-189
Literature: P. Tavs, Chem.Ber., 103 (8), 2428 (1970) [75]

Yield: M_W = 172.12 g/mol, n = 0.20 mol, m = 34.46 g, 91%
^{1}**H-NMR (DMSO, 400 MHz)**: Figure 5.10 on page 212
δ (ppm): 2.27 (s, 3H, CH_3, [11]), 7.27 (m, 2H, CH, [1,6]), 7.42 (m, 2H, CH, [2,4])
^{31}**P-NMR (DMSO, 166 MHz)**: δ = 13.8 ppm
IR (KBr): Figure 5.41 on page 228
ν (cm^{-1}) = 2779 (br, ν_s OH phosphonate), 2335 (m, ν_s CH3 methyl), 1602 and 1453 (m, ν_s C=C), 1229 (s, ν_s P=O), 1048 and 1012 (s, ν_{as} P-OH), 938 (s, δ_{oop} 1H ring), 860 and 786 (m, δ_{oop} 3H ring), 692 (m, δ_{oop} ring)

4-Tolyl-phosphonic acid (2c)
Research Journal: XE-186
Literature: P. Tavs, Chem.Ber., 103 (8), 2428 (1970) [75]

Yield: M_W = 172.12 g/mol, n = 0.18 mol, m = 30.29 g, 88%
^{1}**H-NMR (DMSO, 400 MHz)**: Figure 5.12 on page 213
δ (ppm): 2.28 (s, 3H, CH_3, [7]), 7.21 (dd, 2H, CH, [1,5]), 7.52 (dd, 2H, CH, [2,4])
IR (KBr): Figure 5.41 on page 228
ν (cm^{-1}) = 2923 (br, ν_s OH phosphonate), 2248 (w, ν_s CH3 methyl), 1605 and 1401 (m, ν_s C=C), 1181 (s, ν_s P=O), 1058 and 1010 (s, ν_{as} P-OH), 810 (m, δ_{oop} 2H ring), 650 (m, δ_{oop} ring)

5.1.1.2 Ligands with a Carboxilic Acid Substituent

Literature: Gattermann, Die Praxis des organischen Chemikers, p. 480 [152]

The following general procedure of oxidation was carried out. The appropiate tolyl-phosphonic acid derivate (M_W = 172.12 g/mol, n = 0.10 mol, m = 17.21 g) and three equivalents of potassium hydroxide (M_W = 56.10 g/mol, n = 0.30 mol, m = 16.83 g) were dissolved in 500 ml of water. Before heating up the reaction solution to 130°C, 10 g of potassium permanganate (M_W = 158.04 g/mol, n = 0.25 mol, m = 39.51 g (in total)) was added. The remaining potassium permanganate was added in small parts to the hot reaction solution in one hour.

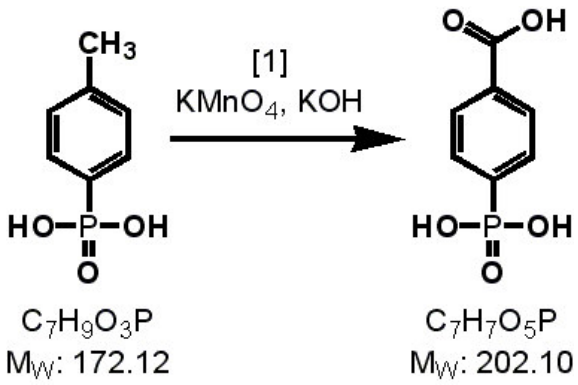

Figure 5.2: Synthesis strategy of the different aromatic phosphonate ligands with a carboxilic acid substituent, exemplarily shown on the para substituent; [1] Gattermann: Die Praxis des organischen Chemikers, 485

The heating was continued for four hours, whereas the solution should lose the violet colour of the potassium permanganate. If the solution was still coloured, the excess of potassium permanganate was destroyed with a sodium sulfite solution. The emerging manganese dioxide was sucked off, while the solution was still hot. The cold solution was acidified with concentrated hydrochloric acid, so that the desired phosphono- benzoic acid could be obtained.

2-Phosphono-benzoic acid (3a)

Research Journal: XE-194

Yield: M_W = 202.10 g/mol, n = 0.06 mol, m = 12.53 g, 62%
^{1}**H-NMR (DMSO, 400 MHz)**: Figure 5.13 on page 214
δ (ppm): 7.46 (m, 2H, CH, [1,6]), 7.79 (m, 2H, CH, [2,5])
^{13}**C-NMR (D_2O, 100 MHz)**: Figure 5.14 on page 214
δ (ppm): 127.7 (d, [2]), 128.2 (d, [5]), 129.2 (d, [6]), 131.5 (d, [4]), 134.4 (d, [3]), 140.0 (d, [1]), 178.3 (d, [11])
^{31}**P-NMR (D_2O, 166 MHz)**: δ = 11.6 ppm
IR (KBr): Figure 5.42 on page 229
ν (cm^{-1}) = 3350 (br, ν_s, COOH bridged), 3053 (w, ν_s CH ring), 2807 (br, ν_s OH phosphonate), 1707 (s, ν_{as} C=O), 1574 (m, ν_s C=C), 1310 (m, ν_s C=O), 1135 (s, ν_s P=O), 967 and 907 (s, ν_{as} P-OH), 809 and 744 (m, δ_{oop} 4H ring), 693 (w, δ_{oop} ring)

3-Phosphono-benzoic acid (3b)

Research Journal: AP-101

Yield: M_W = 202.10 g/mol, n = 0.07 mol, m = 14.35 g, 71%
^{1}H-NMR (D_2O, 400 MHz): Figure 5.15 on page 215
δ (ppm): 7.53 (t, 1H, [1]), 7.94 (dd, 1H, [2]), 8.02 (d, 1H, [6]), 8.25 (d, 1H, [4])
^{13}C-NMR (D_2O, 100 MHz): Figure 5.16 on page 215
δ (ppm): 128.8 (d, [1]), 129.5 (d, [5]), 131.3 (d, [4]), 132.2 (d, [6]), 133.5 (d, [3]), 135.1 (d, [2]), 169.7 (s, [11])
^{31}P-NMR (D_2O, 166 MHz): δ = 14.7 ppm
IR (KBr): Figure 5.42 on page 229
ν (cm^{-1}) = 3585 (br, ν_s, COOH bridged), 3074 (w, ν_s CH ring), 2844 (br, ν_s OH phosphonate), 1702 and 1682 (s, ν_{as} C=O), 1600 and 1583 (m, ν_s C=C), 1320 (s, ν_s C=O), 1174 and 1161 (m, ν_s P=O), 1009 and 960 (s, ν_{as} P-OH), 860 and 745 (m, δ_{oop} 3H ring), 692 (w, δ_{oop} ring)

4-Phosphono-benzoic acid (3c)

Research Journal: XE-151

Yield: M_W = 202.10 g/mol, n = 0.09 mol, m = 17.38 g, 86%
^{1}H-NMR (D_2O, 400 MHz): Figure 5.17 on page 216
δ (ppm): 7.68 (dd, 2H, [2,4]), 7.90 (dd, 2H, [1,5])
^{13}C-NMR (D_2O, 100 MHz): Figure 5.18 on page 216
δ (ppm): 129.2 (d, [2,4]), 130.3 (d, [1,5]), 131.6 (s, [6]), 138.4 (d, [3]), 169.7 (s, [7])
^{31}P-NMR (D_2O, 166 MHz): δ = 13.4 ppm
IR (KBr): Figure 5.42 on page 229
ν (cm^{-1}) = 3489 (br, ν_s, COOH bridged), 2851 (br, ν_s OH phosphonate), 1688 (s, ν_{as} C=O), 1563 and 1430 (m, ν_s C=C), 1320 and 1300 (s, ν_s C=O), 1177 (m, ν_s P=O), 1027 and 1016 (s, ν_{as} P-OH), 949 (m, δ_{oop} COOH), 865 (m, δ_{oop} 2H ring), 698 (w, δ_{oop} ring)

5.1.1.3 Benzimidazole substituted Phosphonate Ligand

1-Carboethoxy-2-chloromethylbenzimidazole (4)

Research Journal: XE-202
Literature: H. Sigel et al., Org. Biomol. Chem., 1, 1819 - 1826 (2003) [73]

The following procedure was carried out under an inert atmosphere of argon. To a suspension of 2-chloromethylbenzimidazole (M_W = 166.61 g/mol, n = 0.04 mol, m = 6.62 g) in dry dioxane (V = 100 mL) ethyl chloroformate (M_W = 108.5

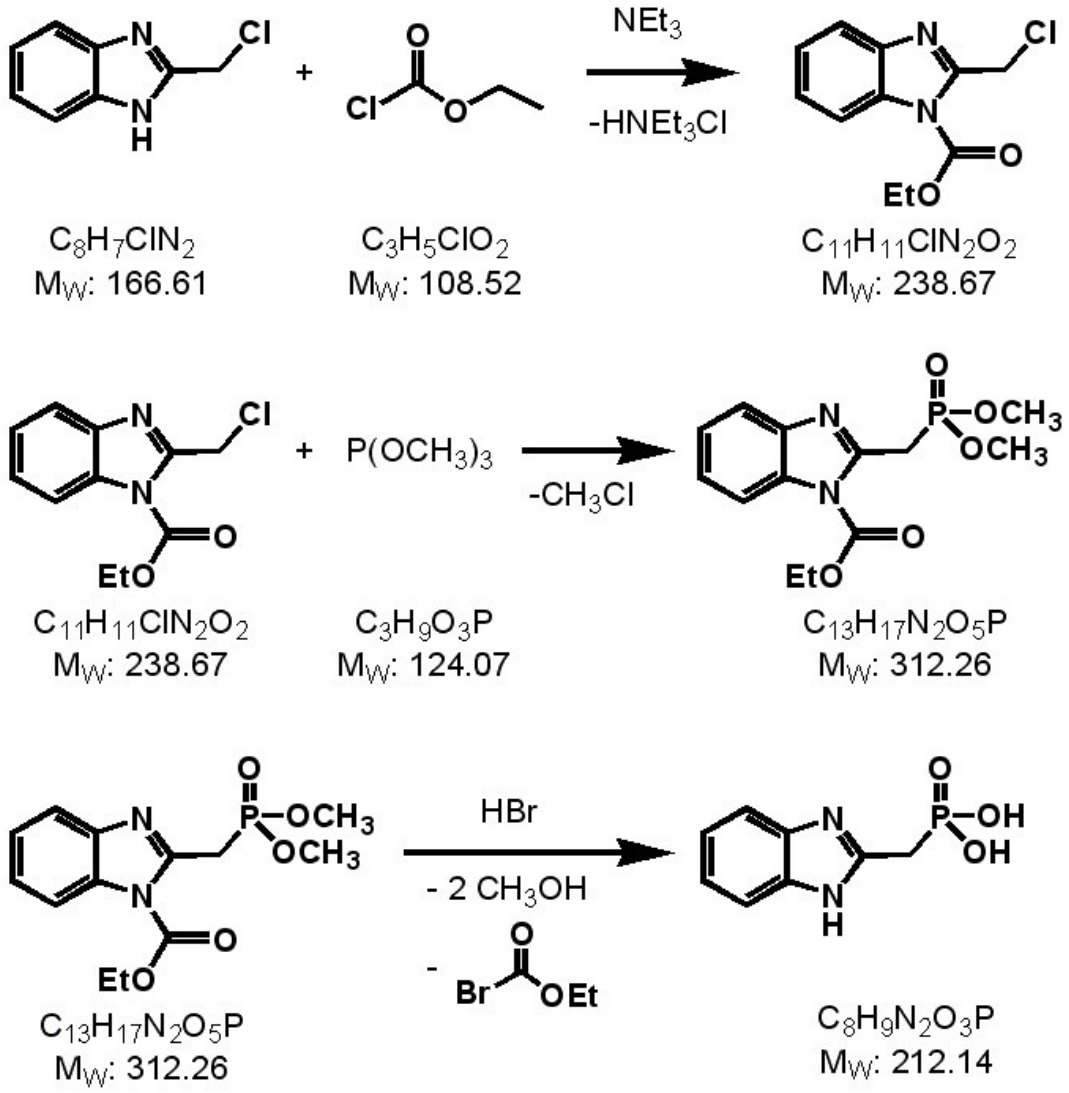

Figure 5.3: The synthesis of (1H-Benzoimidazol-2-ylmethyl-)phosphonic acid **(6)** is schematically shown.

g/mol, n = 0.04 mol, m = 4.33 g, d = 1.140 g/mL, V = 3.8 mL) was added with a syringe. Then, the addition of dry triethylamine (M_W = 101.2 g/mol, n = 0.04 mol, m = 4.09 g, d = 0.730 g/mL, V = 5.6 mL) followed gradually, also with a syringe. The reaction mixture was stirred at room temperature for 1 h, and then refluxed for 3 h. The reaction mixture was filtered while hot and the filtrate was evaporated to oil. Dry diethyl ether (V = 100 mL) was added and the reaction mixture was again evaporated to dryness to obtain the desired compound as an orange solid **(4)**.

Yield: M_W = 238.67 g/mol, calculated with literature yield of 71%
^{1}**H-NMR (CDCl$_3$, 400 MHz)**: Figure 5.19 on page 217
δ (ppm): 1.51 (t, 3H, [16]), 4.56 (q, 2H, [15]), 5.05 (s, 2H, [10]), 7.34 (m, 2H,

[3,6]), 7.72 (t, 1H, [1]), 7.92 (t, 1H, [2])

(1-Carboethoxy-benzimidazol-2-yl-methyl)phosphonic acid dimethyl ester (5)
Research Journal: XE-209
Literature: H. Sigel et al., Org. Biomol. Chem., 1, 1819 - 1826 (2003) [73]

A mixture of (5) (M_W = 238.68 g/mol, n = 28 mmol, m = 6.7 g) and trimethylphosphite (M_W = 124.08 g/mol, n = 0.48 mol, m = 59.43 g, d = 1.052 g/mL, V = 56 mL) was stirred under reflux for 9 h in dry argon atmosphere and then the excess of phosphite was evaporated. The product was separated from impurities by means of column chromatography (silica gel, chloroform : acetone, 4 : 1). After evaporation, the desired compound could be obtained as a yellowish oil **(5)**.

Yield: M_W = 312.26 g/mol, n = 21 mmol, m = 6.4 g, 72%
^{1}H-NMR ($CDCl_3$, 400 MHz): Figure 5.20 on page 217
δ (ppm): 1.49 (t, 3H, [19]), 3.73 (d, 6H, [20,21]), 3.98 (d, 2H, [10]), 4.53 (q, 2H, [18]), 7.28 (m, 2H, [3,6]), 7.65 (t, 1H, [1]), 7.85 (t, 1H, [2])

(1H-Benzimidazol-2-yl-methyl)phosphonic acid (6)
Research Journal: XE-219
Literature: H. Sigel et al., Org. Biomol. Chem., 1, 1819 - 1826 (2003) [73]

The ester (6) (M_W = 312.26 g/mol, n = 21 mmol, m = 6.4 g) in 40% aq. HBr solution (V = 55 mL) was refluxed over night. The solvent was removed under reduced pressure and the residue dissolved in saturated aq. $NaHCO_3$ solution which was filtered off any impurities and acidified with 6 M hydrochloric acid. The resulting precipitate was filtered off, washed with water and dried in vacuo. The desired compound could be obtained as a yellow solid **(6)**.

Yield: M_W = 212.15 g/mol, n = 16 mmol, m = 3.47 g, 80%
^{1}H-NMR (CF_3COOD, 400 MHz): Figure 5.21 on page 218
δ (ppm): 3.86 (d, 2H, [10]), 7.42 (m, 2H, [3,6]), 7.50 (m, 2H, [1,2])
IR (KBr): Figure 5.42 on page 229
ν (cm^{-1}) = 2969 (m, ν_s NH benzimidazole), 2360 (w, ν_s CH2 methylene), 1630 and 1463 (m, ν_s C=C), 1567 (m, δ NH benzimidazole), 1248 (s, ν_s P=O), 1162 (s, ν_s CN benzimidazole), 946 and 912 (m, ν_{as} P-OH), 830 and 745 (m, δ_{oop} 4H ring)

5.1.1.4 Mononuclear Compounds with Aromatic Phosphonate Ligands

$[Ni(H_2O)_6(meta\text{-}HOOCC_6H_4PO_3H)_2]^*(meta\text{-}HOOCC_6H_4PO_3H_2)_2$ (7)
Research Journal: AP-103-40

Nickel chloride salt (M_W = 237.7 g/mol, n = 2.5 mmol, m = 0.594 g) and 3-Phosphono-benzoic acid **(3b)** (M_W = 202 g/mol, n = 5 mmol, m = 1.010 g) were suspended in 20 ml water. The reaction mixture was transferred in a teflon vessel with a volume of 37 ml, which was closed and build in a home-made steel autoclave. The reaction was heated up to 180°C, hold for 24h at that temperature and cooled down with a rate of approximately 2°C/h to room temperature again. All insoluble material was filtered off and the filtrate was left undisturbed for several days. The desired compound could be obtained as green block-like single crystalline material, which was washed several times with water.

Crystal data: Figure 5.57 on page 242

$[M(H_2O)_6(para\text{-}HOOCC_6H_4PO_3H)_2]^*4(H_2O)$, M=Co,Ni

The appropiate metal salt (Ni: $NiCl_2{}^*6H_2O$, M_W = 237.7 g/mol, n = 1 mmol, m = 0.238 g; Co: $Co(NO_3)_2{}^*6H_2O$, M_W = 291.0 g/mol, n = 1 mmol, m = 0.291 g) and 4-Phosphono-benzoic acid **(3c)** (M_W = 202 g/mol, n = 1 mmol, m = 0.202 g) were suspended in 25 ml water. The reaction mixture was transferred in a teflon vessel with a volume of 37 ml, which was closed and build in a home-made steel autoclave. The reaction was heated up to 180°C, hold for 24h at that temperature and cooled down with a rate of approximately 2°C/h to room temperature again. All insoluble material was filtered off and the filtrate was left undisturbed for several days. The desired compound could be obtained as block-like single crystalline material, which was washed several times with water.

$[Co(H_2O)_6(para\text{-}HOOCC_6H_4PO_3H)_2]^*4(H_2O)$ (8a)
Research Journal: XE-154

Crystal data: Figure 5.58 on page 244
IR (KBr): Figure 5.44 on page 231
ν (cm^{-1}) = 3463 (br, ν_s, COOH bridged), 1704 (s, ν_{as} C=O), 1610 and 1564 (m,

ν_s C=C), 1317 and 1297 (s, ν_s C=O), 1148 (m, ν_s P=O), 1105 and 986 (s, ν_{as} P-OH), 936 (m, δ_{oop} COOH), 860 (w, δ_{oop} 2H ring), 696 (w, δ_{oop} ring)

$[Ni(H_2O)_6(para\text{-}HOOCC_6H_4PO_3H)_2]*4(H_2O)$ (8b)
Research Journal: XE-126-30

Crystal data: Figure 5.58 on page 244

5.1.1.5 1D Chain Compounds with Aromatic Phosphonate Ligands

$[Mn(meta\text{-}HOOCC_6H_4PO_3H)_2(H_2O)_2]_n$ (9)
Research Journal: AP-120-40

Manganese chloride salt (M_W = 197.9 g/mol, n = 1 mmol, m = 0.198 g) and 3-Phosphono-benzoic acid **(3b)** (M_W = 202 g/mol, n = 5 mmol, m = 1.010 g) were suspended in 15 ml water. After adjusting the pH-value to 2.4 with 4.3 ml of a 0.1 molar sodium hydroxide solution, the reaction mixture cleared up. It was slowly evaporated at 50°C over night, so that the desired compound could be obtained as colourless needle-like single crystalline material.

Crystal data: Figure 5.59 on page 245
Powder diffractogram: Figure 5.60 on page 246
IR (KBr): Figure 5.43 on page 230
ν (cm^{-1}) = 3499 (br, ν_s, COOH bridged), 2837 (br, ν_s OH phosphonate), 1705 and 1634 (s, ν_{as} C=O), 1600 and 1580 (m, ν_s C=C), 1317 and 1278 (s, ν_s C=O), 1188 and 1159 (s, ν_s P=O, 1. bridging mode), 1132 and 1108 (m, ν_s P=O, 2. bridging mode), 1027 and 998 (s, ν_{as} P-OH, 1. bridging mode), 940 (s, ν_{as} P-OH, 2. bridging mode), 856 and 753 (m, δ_{oop} 3H ring), 685 (m, δ_{oop} ring)
Elemental analysis: found: 33.51% C, 3.17% H;
calculated ($C_{14}H_{16}MnO_{12}P_2*1/2H_2O$): 33.49% C, 3.41% H

$[Co(para\text{-}HOOCC_6H_4PO_3H)_2(H_2O)]_n$ (10)

Solvothermal Method: Research Journal XE-126-10, AP-090, AP-091

Several metal to ligand ratios were tried out, starting from 1:1 (XE-126-10), over 1:2 (AP-090) to 2:3 (AP-091), which was the most suitable one. Also several cobalt salts ($CoCl_2$*$6H_2O$, $CoSO_4$*$7H_2O$ or $Co(NO_3)_2$*$6H_2O$) were tried out, of which the chloride salt was the most suitable one. Cobalte chloride salt (M_W = 237.9 g/mol, n = 2 mmol, m = 0.476 g) and 4-Phosphono-benzoic acid **(3c)** (M_W = 202 g/mol, n = 3 mmol, m = 0.606 g) were suspended in 20 ml water. The reaction mixture was transferred in a teflon vessel with a volume of 37 ml, which was closed and build in a home-made steel autoclave. The reaction was heated up to 180°C, hold for 24h at that temperature and cooled down with a rate of approximately 2°C/h to room temperature again. The desired compound could be obtained as green needle-like single crystalline material, which was washed several times with water. The obtained product was seldom phase pure, often also pink block-like single crystals of $[Co(H_2O)_6(para\text{-}HOOCC_6H_4PO_3H)_2]$*$4(H_2O)$ **(8a)** and pink plate-like single crystals of $[Co(para\text{-}HOOCC_6H_4PO_3)]_n$ **(13)** were found. The crystals were sorted by hand.

Crystal data: Figure 5.61 on page 247
IR (KBr): Figure 5.45 on page 232
ν (cm^{-1}) = 3100 (br, ν_s, OH of COOH), 1695 (s, ν_{as} C=O), 1564 and 1434 (m, ν_s C=C), 1277 (m, ν_s C=O), 1167 (s, ν_s P=O), 985 (s, ν_{as} P-OH), 912 (m, δ_{oop} COOH), 859 (m, δ_{oop} 2H ring), 714 (m, δ_{oop} ring)
Elemental analysis: found: 35.09% C, 2.99% H;
calculated ($C_{14}H_{14}CoO_{11}P_2$): 35.09% C, 2.95% H

Non-Solvothermal Method: Research Journal AP-127

Cobalte chloride salt (M_W = 237.9 g/mol, n = 3 mmol, m = 0.714 g) was dissolved in 5 ml water. 4-Phosphono-benzoic acid **(3c)** (M_W = 202 g/mol, n = 3 mmol, m = 0.606 g) was dissolved separately in 15 ml of a 0.1 molar sodium hydroxide solution with an adjusted pH-value of 2.4. The solutions were mixed and 10 ml of water was added. Ultrasonification resulted a clear pink-coloured solution. The reation mixture was slowly evaporated at 50°C over night, so that the desired compound could be obtained as green needle-like single crystalline material. Again, the crystals had to be separated of all pink solid material and they were washed several times with water. The crystal quality was not as good as in the solvothermal method.

Powder diffractogram: Figure 5.62 on page 248
IR (KBr): Figure 5.45 on page 232

ν (cm^{-1}) = 3095 (br, ν_s, OH of COOH), 1695 (s, ν_{as} C=O), 1564 and 1433 (m, ν_s C=C), 1277 (m, ν_s C=O), 1166 (s, ν_s P=O), 988 (s, ν_{as} P-OH), 908 (m, δ_{oop} COOH), 858 (m, δ_{oop} 2H ring), 713 (m, δ_{oop} ring)
Elemental analysis: found: 34.95% C, 3.04% H;
calculated ($C_{14}H_{14}CoO_{11}P_2$): 35.09% C, 2.95% H

5.1.1.6 2D Layered Compounds with Aromatic Phosphonate Ligands

$[Co(CH_3C_6H_4PO_3)(H_2O)]_n$

Cobalte sulfate salt (M_W = 281.1 g/mol, n = 10 mmol, m = 2.82 g) and the appropiate Tolyl-phosphonic acid **(2c)** or **(2b)** (M_W = 172 g/mol, n = 10 mmol, m = 1.72 g) were suspended in 20 ml water. The reaction mixture was transferred in a teflon vessel with a volume of 37 ml, which was closed and build in a home-made steel autoclave. The reaction was heated up to 180°C, hold for 24h at that temperature and cooled down with a rate of approximately 2°C/h to room temperature again. The desired compound could be obtained as pink plate-like single crystalline material, which was washed several times with water.

$[Co(para\text{-}CH_3C_6H_4PO_3)(H_2O)]_n$ (11a)
Research Journal: XE-193-20

Crystal data: Figure 5.64 on page 250
Elemental analysis: found: 33.99% C, 3.70% H;
calculated ($C_7H_9CoO_4P$): 34.03% C, 3.67% H

$[Co(meta\text{-}CH_3C_6H_4PO_3)(H_2O)]_n$ (11b)
Research Journal: XE-193-40

Crystal data: Figure 5.63 on page 249
IR (KBr): Figure 5.43 on page 230
ν (cm^{-1}) = 3438 (br, ν_s H_2O), 1631 and 1384 (m, ν_s C=C), 1133 (s, ν_s P=O), 1097 and 979 (s, ν_{as} P-OH), 776 and 728 (w, δ_{oop} 3H ring), 687 (m, δ_{oop} ring)

$[M(HOOCC_6H_4PO_3)(H_2O)]_n$, M = Mn,Co,Ni
Research Journal: AP-140

The appropiate metal chloride salt (Mn: M_W = 197.9 g/mol, n = 2 mmol, m = 0.395 g; Co: M_W = 237.9 g/mol, n = 2 mmol, m = 0.476 g; Ni: M_W = 237.7 g/mol, n = 2 mmol, m = 0.475 g) was dissolved in 10 ml water. 3-Phosphonobenzoic acid **(3b)** (M_W = 202 g/mol, n = 2 mmol, m = 0.404 g) was dissolved in 8.6 ml of a 0.1 molar sodium hydroxide solution with an adjusted pH-value of 2.4. The two solutions were mixed. The reaction mixture was transferred in a teflon vessel with a volume of 37 ml, which was closed and build in a home-made steel autoclave. The reaction was heated up to 180°C, hold for 24h at that temperature and cooled down with a rate of approximately 2°C/h to room temperature again. The desired compound could be obtained as phase pure material, which was filtered off and washed several times with water.

$[Mn(HOOCC_6H_4PO_3)(H_2O)]_n$ (12a)
Research Journal: AP-140-30, AP-123-10

Crystal data: Figure 5.65 on page 252
Powder diffractogram: Figure 5.66 on page 253
IR (KBr): Figure 5.43 on page 230
ν (cm^{-1}) = 3446 (br, ν_s, COOH bridged), 1698 (s, ν_{as} C=O), 1598 (m, ν_s C=C), 1310 and 1268 (m, ν_s C=O), 1158 (m, ν_s P=O), 1000 and 983 (s, ν_{as} P-OH), 827 and 748 (w, δ_{oop} 3H ring), 682 (w, δ_{oop} ring)
Elemental analysis: found: 30.63% C, 2.52% H;
calculated ($C_7H_7MnO_6P$): 30.79% C, 2.58% H

$[Co(HOOCC_6H_4PO_3)(H_2O)]_n$ (12b)
Research Journal: AP-140-10, AP-118-40

Crystal data: Figure 5.67 on page 254
Powder diffractogram: Figure 5.68 on page 255
IR (KBr): Figure 5.43 on page 230
ν (cm^{-1}) = 3416 (br, ν_s, COOH bridged), 1697 (s, ν_{as} C=O), 1599 (m, ν_s C=C), 1316 and 1270 (m, ν_s C=O), 1159 (m, ν_s P=O), 974 (s, ν_{as} P-OH), 831 and 749 (w, δ_{oop} 3H ring), 679 (w, δ_{oop} ring)
Elemental analysis: found: 33.98% C, 3.08% H;
calculated ($C_7H_7CoO_6P$*$C_7H_7O_5P$*H_2O): 33.82% C, 3.24% H

$[Ni(HOOCC_6H_4PO_3)(H_2O)]_n$ (12c)
Research Journal: AP-140-20, AP-114

Powder diffractogram: Figure 5.69 on page 256
IR (KBr): Figure 5.44 on page 231
ν (cm^{-1}) = 3412 (br, ν_s, COOH bridged), 1696 (s, ν_{as} C=O), 1600 (m, ν_s C=C), 1320 and 1270 (m, ν_s C=O), 1159 (m, ν_s P=O), 976 (s, ν_{as} P-OH), 835 and 750 (w, δ_{oop} 3H ring), 680 (w, δ_{oop} ring)
Elemental analysis: found: 29.49% C, 2.52% H;
calculated ($C_7H_7NiO_6P$*1/2H_2O): 29.42% C, 2.82% H

$[Co(para\text{-}HOOCC_6H_4PO_3)]_n$ (13)
Research Journal: XE-199-10

Cobalte chloride salt (M_W = 237.9 g/mol, n = 1.4 mmol, m = 0.333 g) was dissolved in 10 ml water. 4-Phosphono-benzoic acid **(3c)** (M_W = 202 g/mol, n = 1 mmol, m = 0.202 g) was dissolved separately in 10 ml of a 0.1 molar sodium hydroxide solution with an adjusted pH-value of 2.4. The solutions were mixed and transferred in a teflon vessel with a volume of 37 ml, which was closed and build in a home-made steel autoclave. The reaction was heated up to 200°C, hold for 24h at that temperature and cooled down with a rate of approximately 2°C/h to room temperature again. The desired compound could be obtained as pink plate-like single crystalline material, which was washed several times with water.

Crystal data: Figure 5.70 on page 257
IR (KBr): Figure 5.45 on page 232
ν (cm^{-1}) = 3088 (br, ν_s, OH of COOH), 1707 and 1686 (s, ν_{as} C=O), 1564 and 1431 (m, ν_s C=C), 1296 and 1281 (m, ν_s C=O), 1148 and 1119 (m, ν_s P=O), 979 (s and broad, ν_{as} P-OH), 863 (m, δ_{oop} 2H ring), 717 (m, δ_{oop} ring)
Elemental analysis: found: 32.56% C, 1.83% H;
calculated ($C_7H_5CoO_5P$): 32.46% C, 1.95% H

$[Cu(para\text{-}HOOCC_6H_4PO_3)]_n$ (14)
Research Journal: XE-204

Copper chloride salt (M_W = 167.0 g/mol, n = 1 mmol, m = 0.167 g) was dissolved in 15 ml water. 4-Phosphono-benzoic acid **(3c)** (M_W = 202 g/mol, n = 1 mmol, m = 0.202 g) was dissolved separately in 10 ml of a 0.1 molar sodium hydroxide solution with an adjusted pH-value of 2.4. The solutions were mixed

and transferred in a teflon vessel with a volume of 37 ml, which was closed and build in a home-made steel autoclave. The reaction was heated up to 200°C, hold for 24h at that temperature and cooled down with a rate of approximately 2°C/h to room temperature again. The desired compound could be obtained as green rhombic shaped single crystalline material, which was washed several times with water.

Crystal data: Figure 5.71 on page 258
IR (KBr): Figure 5.45 on page 232
ν (cm^{-1}) = 3090 (br, ν_s, OH of COOH), 1699 (s, ν_{as} C=O), 1564 and 1432 (m, ν_s C=C), 1296 and 1281 (m, ν_s C=O), 1147 and 1118 (s, ν_s P=O), 1030 and 1010 (s, ν_{as} P-OH), 945 (s, δ_{oop} COOH), 863 (m, δ_{oop} 2H ring), 717 (m, δ_{oop} ring)
Elemental analysis: found: 36.14% C, 2.00% H;
calculated ($C_7H_5CuO_5P$*$C_7H_7O_5P$): 36.26% C, 2.17% H

[Co(ortho-$OOCC_6H_4PO_3H$)(H_2O)]$_n$ (15)
Research Journal: AP-118

Cobalte chloride salt (M_W = 237.9 g/mol, n = 1 mmol, m = 0.238 g) and 2-Phosphono-benzoic acid **(3a)** (M_W = 202 g/mol, n = 1 mmol, m = 0.202 g) were suspended in 15 ml water. The pH-value was adjusted to 2.4 with 4.3 ml of a 0.1 molar sodium hydroxide solution. The reaction mixture was transferred in a teflon vessel with a volume of 37 ml, which was closed and build in a home-made steel autoclave. The reaction was heated up to 180°C, hold for 24h at that temperature and cooled down with a rate of approximately 2°C/h to room temperature again. The desired compound could be obtained as pink plate-like single crystalline material, which was washed several times with water.

Crystal data: Figure 5.72 on page 259
IR (KBr): Figure 5.46 on page 233
ν (cm^{-1}) = 3553 (br, ν_s, H_2O), 3374 and 2850 (br, ν_s OH bridged), 1598 and 1582 (s, ν_{as} C=O), 1560 (m, ν_s C=C), 1388 (s, ν_s C=O), 1141 and 1124 (s, ν_s P=O), 1026 and 906 (m, ν_{as} P-OH), 757 and 741 (m, δ_{oop} 4H ring)
Elemental analysis: found: 30.33% C, 2.57% H;
calculated ($C_7H_7CoO_6P$): 30.35% C, 2.55% H

5.1.1.7 Compound with the Benzimidazole Phosphonate

$[Co_2(H_2O)_6(O_3PCH_2C_7H_5N_2)_2]$*$6H_2O$ (16)
Research Journal: AP-139-10

Cobalte chloride salt (M_W = 237.9 g/mol, n = 1 mmol, m = 0.238 g) was dissolved in 10 ml water. (1H-Benzimidazol-2-yl-methyl)phosphonic acid **(6)** (M_W = 211.9 g/mol, n = 1 mmol, m = 0.212 g) was suspended separately in 10 ml water. Sodium hydroxide (M_W = 40.0 g/mol, n = 3 mmol, m = 0.120 g) was dissolved separately in 5 ml water. All three solutions were mixed and transferred in a teflon vessel with a volume of 37 ml, which was closed and build in a home-made steel autoclave. The reaction was heated up to 180°C, hold for 24h at that temperature and cooled down with a rate of approximately 2°C/h to room temperature again. All insoluble material was filtered off and the filtrate was left undisturbed for several days. The desired compound could be obtained as pink rhombic shaped single crystalline material, which was washed several times with water.

Crystal data: Figure 5.73 on page 261
IR (KBr): Figure 5.46 on page 233
ν (cm^{-1}) = 3100 (br, ν_s OH), 1626 and 1456 (m, ν_s C=C), 1536 (w, δ NH benzimidazole), 1281 (w, ν_s P=O), 1141 (m, ν_s CN benzimidazole), 1041 and 975 (s, ν_{as} P-OH), 777 and 746 (m, δ_{oop} 4H ring)
Elemental analysis: found: 25.44% C, 4.91% H, 7.45% N;
calculated ($C_{16}H_{38}Co_2N_4O_{18}P_2$): 25.48% C, 5.08% H, 7.43% N

5.1.1.8 Approaches: 3D Network Compounds with Aromatic Phosphonate Ligands

$[(HNC_5H_4C_5H_4NH)(HOOCC_6H_4PO_3H)_2]$*$2H_2O$ (17)
Research Journal: AP-139-20

Manganese chloride salt (M_W = 161.9 g/mol, n = 1 mmol, m = 0.162 g), 3-Phosphono-benzoic acid **(3b)** (M_W = 202 g/mol, n = 2 mmol, m = 0.404 g) and 4,4'-Bipyridine (M_W = 156.2 g/mol, n = 1 mmol, m = 0.156 g) were suspended in 25 ml water. Ultrasonification of the reaction mixture resulted a colourless milk-like suspension. The reaction mixture was transferred in a teflon vessel with a volume of 37 ml, which was closed and build in a home-made steel autoclave. The reaction was heated up to 180°C, hold for 24h at that temperature and cooled down with a rate of approximately 2°C/h to room temperature again. All insoluble

material was filtered off and the filtrate was left undisturbed for several days. The desired compound could be obtained as orange block-like crystals.

Crystal data: Figure 5.74 on page 262
IR (KBr): Figure 5.44 on page 231
ν (cm^{-1}) = 3267 (br, ν_s, COOH bridged), 3107 (w, ν_s CH ring, Phos), 3066 (w, ν_s CH ring, Bipy), 2844 (w and br, ν_s OH, Phos), 1921 (w, Bipy), 1703 (s, ν_{as} C=O), 1645 and 1597 (m, ν_s C=C), 1267 (s, ν_s C=O), 1150 and 1133 (s, ν_s P=O), 1048 (s, ν_{as} P-OH), 984 (m, Bipy), 826 and 756 (m, δ_{oop} 3H ring, Phos), 655 (w, δ_{oop} ring, Phos), 609 (w, δ_{oop} 2H ring, Bipy), 594 (m, δ_{oop} ring, Bipy)

$[Pr_2(H_2O)_8(HOOCC_6H_4PO_3H)_6]$ (18)

Research Journal: AP-166

Praseodymium chloride salt (M_W = 247.4 g/mol, n = 1 mmol, m = 0.247 g) was dissolved in 10 ml water. 3-Phosphono-benzoic acid **(3b)** (M_W = 202 g/mol, n = 1 mmol, m = 0.202 g) was dissolved separately in 15 ml water. The two solutions were mixed. The reaction mixture was transferred in a teflon vessel with a volume of 37 ml, which was closed and build in a home-made steel autoclave. The reaction was heated up to 180°C, hold for 24h at that temperature and cooled down with a rate of approximately 2°C/h to room temperature again. The desired compound could be obtained as colourless plate-like crystalline material, which was filtered off and washed several times with water.

Crystal data: Figure 5.75 on page 263
IR (KBr): Figure 5.44 on page 231
ν (cm^{-1}) = 3383 (br, ν_s, COOH bridged), 3086 (w, ν_s CH ring), 1704 and 1679 (s, ν_{as} C=O), 1600 and 1582 (m, ν_s C=C), 1319 (s, ν_s C=O), 1175 and 1162 (m, ν_s P=O, 1. binding mode), 1131 and 1115 (s, ν_s P=O, 2. binding mode), 1082 and 1007 (m, ν_{as} P-OH, 1. binding mode), 1038 and 985 (m, ν_{as} P-OH, 2. binding mode), 846 and 745 (m, δ_{oop} 3H ring), 684 (m, δ_{oop} ring)

5.1.2 Carboxylate Systems

5.1.2.1 Formiate System: $[Fe^{II}_2Fe^{III}_2(HCOO)_{10}(\gamma\text{-}C_6H_7N)_6]_n$

Literature: Rentschler et al., ChemPhysChem, 5 (11), 1755 (2004) [119]
Research Journal: AP-007

Water (V = 3 ml) and formic acid (n = 265.0 mmol, V = 10 ml) were added to 1.0 g of powdered iron (n = 17.9 mmol). Then 25 ml of γ-picoline (n = 256.3 mmol) was added, before the reaction solution was heated for five hours. The colour changed from yellow to green-brown. In an inert atmosphere, the reaction solution was filtered off while still hot. The solution was kept one week undisturbed to obtain blue and sheet-like crystals of $[Fe^{II}_2Fe^{III}_2(HCOO)_{10}(\gamma\text{-}C_6H_7N)_6]_n$ **(19)**, that were suitable for X-ray single crystal analysis.

Crystal data: Figure 5.76 on page 264
IR (KBr): Figure 5.39 on page 227
ν (cm^{-1}) = 3054 (w, ν_s CH ring), 2963 (w, ν_s CH3), 2873 (w, ν_s CH formiate), 1662 (s, ν_s C=N), 1580 und 1558 (s, ν_{as} C=O), 1381(m, δ_s CH formiate), 1337 (s, ν_s C=O), 804 (m, δ_{oop} ring)

Elemental analysis: found: 44.45% C, 4.06% H, 6.82% N;
calculated: 44.83% C, 4.25% H, 6.82%N

5.1.2.2 Acetate System:$[M_2(CH_3COO)_4(C_{10}H_8N_2)_2]_n$

The appropiate metal sulfate salt (MSO_4*$7H_2O$, M = Fe: M_W = 278.0 g/mol, n = 2 mmol, m = 0.556 g; M = Co: M_W = 281.1 g/mol, n = 2 mmol, m = 0.562 g) was suspended in a mixture of 15 ml dimethylformamide and 10 ml acetic acid. 4,4'-Bipyridine (M_W = 156.2 g/mol, n = 2 mmol, m = 0.312 g) was added. The reaction mixture was transferred in a teflon vessel with a volume of 37 ml, which was closed and build in a home-made steel autoclave. The reaction was heated up to 180°C, hold for 24h at that temperature and cooled down with a rate of approximately 2°C/h to room temperature again. The desired compound could be obtained as single crystalline material, which was separeted from unreacted starting materials and washed several times with water.

$[Fe_2(CH_3COO)_4(C_{10}H_8N_2)_2]_n$ (20a)
Research Journal: AP-068-40

IR (KBr): Figure 5.40 on page 227
ν (cm^{-1}) = 3074 (w, ν_s CH ring), 2923 (w, ν_s CH3 acetate), 1601 and 1578 (s, ν_{as} CO), 1486 (m, ν_s C=C), 1437 (s, ν_s CO), 817 (m, δ_{oop} 5H ring), 730 and 670 (w, δ_{oop} ring)

$[Co_2(CH_3COO)_4(C_{10}H_8N_2)_2]_n$ (20b)
Research Journal: AP-068-30, AP-045-30

Crystal data: Figure 5.78 on page 267
IR (KBr): Figure 5.41 on page 228
ν (cm^{-1}) = 3075 (w, ν_s CH ring), 2924 (w, ν_s CH3 acetate), 1603 and 1592 (s, ν_{as} CO), 1487 (s, ν_s C=C), 1441 and 1406 (s, ν_s CO), 818 (m, δ_{oop} 5H ring), 732 and 672 (w, δ_{oop} ring)

5.2 New Stable Radicals of Nitronyl-Nitroxide Family

5.2.1 Phosphonate Substituent

2,3-Dimethyl-2,3-dinitrobutane (21)
Research Journal: XE-298
Literature: R. Sayre, JACS, 77, 6689-6690 (1955) [153]

2-Nitropropane (M_W = 89.1 g/mol, n = 0.98 mol, m = 87.13 g, V = 88 mL) was dissolved in a 6N sodium hydroxide solution (M_W = 40.0 g/mol, n = 1.02 mol, m = 40.61 g; V(H_2O) = 166 mL). The reaction mixture was cooled with an ice-bath before the bromine (M_W = 159.8 g/mol, n = 0.51 mol, m = 81.06 g, V = 26 mL) was added dropwise. After the complete addition, 300 mL of ethanol were added and the yellow reaction mixture was refluxed for three hours. The reaction mixture was spilled on ice, so that the desired compound could be obtained as slightly yellow powder. This was sucked off and dried in vacuo.

Yield: M_W = 176.2 g/mol, n = 0.31 mol, m = 54.1 g, 62%
^{1}H-NMR ($CDCl_3$, 400 MHz): Figure 5.22 on page 218
δ (ppm): 1.72 ppm (s, 12H, [3,4,5,6])
IR (KBr): Figure 5.46 on page 233
ν (cm^{-1}) = 2961 (w, ν_{as}, CH_3), 2871 (w, ν_s, CH_3), 1543 (s, ν_{as} NO_2), 1341 (s, ν_s NO_2), 853 (m, ν_s C-N)

2,3-Bis(hydroxylamine)-2,3-dimethylbutane (22)
Research Journal: AP-193
Literature: S. Shimono et al., JOC, 69, 475-481 (2004) [154]

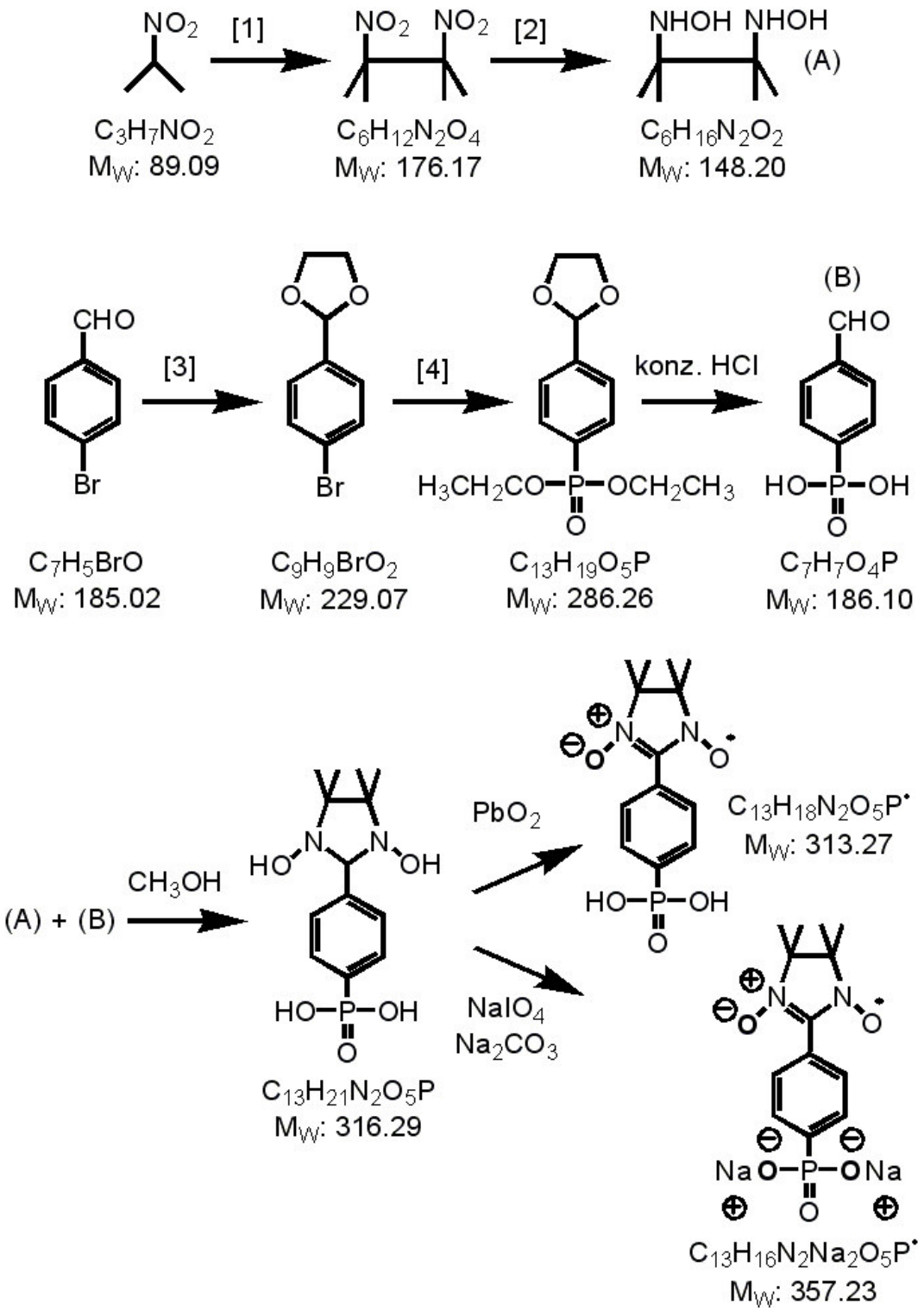

Figure 5.4: The synthesis of the para-phosphonate derivate of a nitronyl-nitroxide radical is schematically shown. [1] JACS,77, 6689-6690 (1955); [2] JOC, 69, 475-481 (2004); [3] JACS, 81, 580-582 (1959); [4] Chem.Ber., 103, 2428-2436 (1970)

Aluminium foil (M_W = 27.0 g/mol, n = 0.66 mol, m = 17.7 g) was cutted in approximately 1 cm^2 pieces. The pieces were washed with a 3% sodium hydroxide solution (M_W = 40.0 g/mol, n = 0.11 mol, m = 4.5 g; V(H_2O) = 150 mL) and cleaned again with destilled water. Next was a 3% mercury chloride solution (M_W = 271.5 g/mol, n = 0.02 mol, m = 4.5 g; V(H_2O) = 150 mL) to produce an aluminium amalgame, that could be identify by small silver coloured drops on the aluminium surface. The pieces were again washed, this time with ethanol (V = 150 ml) and after that with tetrahydrofurane. The reaction mixture was cooled down with the help of an ice-bath to 5°C, before a small amount of water was added (V(H_2O) = 5 mL). 2,3-Dimethyl-2,3-dinitrobutane **(21)** (M_W = 176.2 g/mol, n = 0.06 mol, m =10.0 g) was dissolved separately in 150 mL tetrahydrofurane and slowly added to the reaction mixture, so that the temperature was all the time between 5°C and 15°C. To complete the reaction, it was stirred for three hours and it was allow to heat up to room temperature. The aluminium amalgame was removed by filtration and the filtrate was dried over magnesium sulfate. The solvent was removed, so that the desired compound could be obtained as colourless powder, that was dried in air.

Yield: M_W = 148.2 g/mol, n = 0.03 mol, m = 4.2 g, 47%
^{1}**H-NMR (DMSO, 400 MHz)**: Figure 5.23 on page 219
δ (ppm): 0.96 ppm (s, 12H, [3,4,5,6])
IR (KBr): Figure 5.46 on page 233
ν (cm^{-1}) = 3364 (br, ν_s, OH), 2986 (m, ν_{as}, CH_3), 2942 (w, ν_s, CH_3), 1479 (m, ν_{as} N-O), 1176 (m, ν_s NO_2), 853 (m, ν_s C-N)

2-(Bromo-phenyl)-[1,3]dioxolane

Literature: Hoffmann et al., JACS, 81, 580-582 (1959) [155]

The appropiate bromo-benzaldehyde derivate (M_W = 185.0 g/mol, n = 0.27 mol, m = 50.0 g), ethylene glycole (M_W = 62.1 g/mol, n = 0.28 mol, m = 17.4 g) and p-toluenesulfonic acid (M_W = 190.2 g/mol, n = 1.5 mmol, m = 0.29 g) were dissolved in 100 mL of toluene. The reaction mixture was refluxed over night on a dean-stark apparatus to separate the emerging water. The reaction mixture was cooled and made slightly alkaline with ethanolic potassium hydroxide. The toluene solution then was washed with water, separated, and dried over anhydrous potassium carbonate. The solvent was removed, so that the desired compound could be obtained as yellowish oil.

2-(4-Bromo-phenyl)-[1,3]dioxolane (23a)
Research Journal: AP-075

Yield: M_W = 229.1 g/mol, n = 0.26 mol, m = 58.8 g, 95%
^{1}H-NMR ($CDCl_3$, 400 MHz): Figure 5.24 on page 219
δ (ppm): 4.05 ppm (m, 4H, [10,11]), 5.74 ppm (s, 1H, [7]), 7.33 ppm (d, 2H, [1,5]), 7.49 ppm (d, 2H, [2,4])

2-(3-Bromo-phenyl)-[1,3]dioxolane (23b)
Research Journal: AP-190

Yield: M_W = 229.1 g/mol, n = 0.25 mol, m = 57.0 g, 92%
^{1}H-NMR ($CDCl_3$, 400 MHz): Figure 5.25 on page 220
δ (ppm): 4.05 ppm (m, 4H, [10, 11]), 5.77 ppm (s, 1H, [8]), 7.25 ppm (t, 1H, [1]), 7.39 ppm (d, 1H, [6]), 7.48 ppm (d, 1H, [2]), 7.63 ppm (s, 1H, [4])

([1,3]Dioxolan-2-yl-phenyl)-phosphonic acid diethyl ester
Literature: P. Tavs, Chem.Ber., 103 (8), 2428 (1970) [75]

The following general procedure was carried out under an inert atmosphere of argon. The appropiate bromodioxolane derivate (M_W = 229.1 g/mol, n = 0.22 mol, m = 50.0 g) was added to a catalytic amount of water free nickel chloride (M_W = 129.7 g/mol, n = 15 mmol, m = 2.0 g). The orange reaction solution was heated up to 190°C, before triethylphosphite (M_W = 166.2 g/mol, n = 0.27 mol, m = 45.0 g) was added carefully with a syringe. The reaction solution turned blue-violet and emerging ethylbromide was distilled off. After the complete addition of triethylphosphite, the reaction mixture still was heated up for 30 minutes. In a fractional distillation the desired phosphonic acid diethyl ester could be obtained in the last fraction (boiling point above 120°C). Saponification of the phosphonic acid diethyl ester with concentrated hydrochlorid acid (V = 150 ml) yielded the free formylphenyl-phosphonic acid derivate.

(4-[1,3]Dioxolan-2-yl-phenyl)-phosphonic acid diethyl ester (24a)
Research Journal: AP-083-10

Yield: M_W = 286.3 g/mol, n = 0.18 mol, m = 47.2 g, 80%
^{1}H-NMR ($CDCl_3$, 400 MHz): Figure 5.26 on page 220
δ (ppm): 1.19 ppm (t, 6H, [17,19]), 3.95 ppm (m, 8H, [10,11,16,18]), 5.72 ppm (s, 1H, [7]), 7.47 ppm (dd, 2H, [1,5]), 7.72 ppm (dd, 2H, [2,4])

(3-[1,3]Dioxolan-2-yl-phenyl)-phosphonic acid diethyl ester (24b)
Research Journal: AP-192-10

Yield: M_W = 286.3 g/mol, n = 0.15 mol, m = 43.0 g, 68%
^{1}H-NMR ($CDCl_3$, 400 MHz): Figure 5.27 on page 221
δ (ppm): 1.11 ppm (t, 6H, [12,14]), 3.91 ppm (m, 8H, [11, 13, 17, 18]), 5.62 ppm (s, 1H, [15]), 7.28 ppm (dt, 1H, [1]), 7.46 ppm (d, 1H, [6]), 7.61 ppm (dd, 1H, [2]), 7.74 ppm (d, 1H, [4])

(4-Formyl-phenyl)-phosphonic acid (25a)
Research Journal: AP-083-20

Yield: M_W = 186.1 g/mol, n = 0.15 mol, m = 27.5 g, 82%
^{1}H-NMR (DMSO, 400 MHz): Figure 5.28 on page 221
δ (ppm): 7.83 ppm (dd, 2H, [2,4]), 7.92 ppm (dd, 2H, [1,5]), 10.00 ppm (s, 1H, [9])
IR (KBr): Figure 5.47 on page 234
ν (cm^{-1}) = 2921 (br, ν_s, C-H CHO), 1666 (s, ν_{as} C=O), 1602 and 1562 (s, ν_s C=C), 1392 (m, ν_s C=O), 1213 and 1176 (s, ν_s P=O), 1024 and 1011 (s, ν_{as} P-OH), 925 (m, δ_{oop} CHO), 845 (m, δ_{oop} 2H ring), 704 (w, δ_{oop} ring)

(3-Formyl-phenyl)-phosphonic acid (25b)
Research Journal: AP-192-20

Yield: M_W = 186.1 g/mol, n = 0.11 mol, m = 20.1 g, 72%
^{1}**H-NMR (DMSO, 400 MHz)**: Figure 5.29 on page 222
δ (ppm): 7.66 ppm (dt, 1H, [1]), 7.94 ppm (dd, 1H, [2]), 8.00 ppm (d, 1H, [2]), 8.15 ppm (d, 1H, [4]), 10.03 ppm (s, 1H, [12])
IR (KBr): Figure 5.47 on page 234
ν (cm^{-1}) = 2831 (br, ν_s C-H CHO), 1665 (s, ν_{as} C=O), 1594 (s, ν_s C=C), 1420 (m, ν_s C=O), 1170 and 1114 (s, ν_s P=O), 1012 and 939 (s, ν_{as} P-OH), 863 and 745 (m, δ_{oop} 3H ring), 685 (w, δ_{oop} ring)

[(1,3-Dihydroxy-4,4,5,5-tetramethyl-imidazolidin-2-yl)-phenyl]-phosphonic acid
Literature: C. Hirel et al., Chem. Eur. J., 7, 2007-2014 (2001) [156]

The appropiate Formyl-phenyl-phosphonic acid (M_W = 186.1 g/mol, n = 11 mmol, m = 2.0 g) and 2,3-Bis(hydroxylamine)-2,3-dimethylbutane **(22)** (M_W = 148.2 g/mol, n = 11 mmol, m = 1.6 g) were dissolved separately in as less methanol (for para-derivate) and ethanol (for meta-derivate) as possible. The solutions were mixed and the reaction mixture was stirred over night. The desired compound could be obtained as colourless powder that was filtrated and washed with the appropiate alcohol.

[4-(1,3-Dihydroxy-4,4,5,5-tetramethyl-imidazolidin-2-yl)-phenyl]-phosphonic acid (26a)
Research Journal: AP-194

Yield: M_W = 316.3 g/mol, n = 4 mmol, m = 1.14 g, 33%
^{1}**H-NMR (DMSO, 400 MHz)**: Figure 5.30 on page 222
δ (ppm): 1.04 (s, 6H, [17,18]), 1.08 (s, 6H, [16,19]), 4.55 (s, 1H, [11]), 7.55 (dd, 2H, [1,5]), 7.63 (dd, 2H, [2,4])
^{13}**C-NMR (DMSO, 100 MHz)**: Figure 5.31 on page 223
δ (ppm): 17.49 (s, CH3, [17,18]), 24.58 (s, CH3, [16,19]), 66.46 (s, CN, [13,14]), 90.23 (s, CH, [11]), 128.1 (d, CH, [2,4]), 130.1 (d, CH, [1,5]), 144.5 (s, CC, [6])
^{31}**P-NMR (DMSO, 166 MHz)**: δ = 13.0 ppm
IR (KBr): Figure 5.47 on page 234
ν (cm^{-1}) = 2921 (br, ν_s, C-H), 1666 (s, ν_{as} C-N), 1602 and 1562 (s, ν_s C=C), 1392 (m, ν_s C-N), 1213 and 1176 (s, ν_s P=O), 1024 and 1011 (s, ν_{as} P-OH), 925 (m, δ_{oop} ONCNO), 845 (m, δ_{oop} 2H ring), 704 (w, δ_{oop} ring)

Elemental analysis: found: 46.36% C, 6.91% H, 8.46 % N;
calculated ($C_{13}H_{21}N_2O_5P + H_2O$): 46.71% C, 6.93% H, 8.38 % N

[3-(1,3-Dihydroxy-4,4,5,5-tetramethyl-imidazolidin-2-yl)-phenyl]-phosphonic acid (26b)
Research Journal: AP-196

Yield: M_W = 316.3 g/mol, n = 7 mmol, m = 2.35 g, 67%
^{1}**H-NMR (DMSO, 400 MHz)**: Figure 5.32 on page 223
δ (ppm): 1.06 (s, 6H, [16,19]), 1.08 (s, 6H, [17,18]), 4.51 (s, 1H, [11]), 7.38 (dt, 1H, [1]), 7.57 (m, 2H, [2,6]), 7.83 (d, 1H, [4])
^{13}**C-NMR (DMSO, 100 MHz)**: Figure 5.33 on page 224
δ (ppm): 17.61 (s, [16,17,18,19]), 66.68 (s, [13,14]), 90.88 (s, [11]), 122.0 (d, [2]), 127.7 (d, [1]), 130.1 (d, [4]), 131.4 (d, [6]), 134.5 (d, [3]), 142.1 (d, [5])
^{31}**P-NMR (DMSO, 166 MHz)**: δ = 14.5 ppm
IR (KBr): Figure 5.47 on page 234
ν (cm^{-1}) = 2921 (br, ν_s, C-H), 1666 (s, ν_{as} C-N), 1602 and 1562 (s, ν_s C=C), 1392 (m, ν_s C-N), 1213 and 1176 (s, ν_s P=O), 1024 and 1011 (s, ν_{as} P-OH), 925 (m, δ_{oop} ONCNO), 845 (m, δ_{oop} 2H ring), 704 (w, δ_{oop} ring)
Elemental analysis: found: 48.32% C, 6.84% H, 7.99 % N;
calculated ($C_{13}H_{21}N_2O_5P + CH_3OH$): 48.27% C, 7.23% H, 8.04 % N

[4-(4,4,5,5-tetramethyl-imidazoline-3-oxide-1-oxyl)-phenyl]-phosphonic acid (27a)
Research Journal: AP-203, XE-268

[4-(1,3-Dihydroxy-4,4,5,5-tetramethyl-imidazolidin-2-yl)-phenyl]-phosphonic acid **(26a)** (M_W = 316.3 g/mol, n = 3.2 mmol, m = 1.0 g) was dissolved in 20 mL methanol. Lead dioxide (M_W = 239.1 g/mol, n = 16 mmol, m = 3.8 g) was added and the reaction mixture was stirred over night. All solid remains were filtered off. They were redissolved in 50 mL of dimethylformamide and the solution was left undisturbed for some hours, so that the lead oxide remains could precipitate. The solution was decanted and this procedure was carried out several times to remove most of the lead oxide remains. The filtrate was evaporated to dryness. The desired compound could be obtained as blue powder.

Yield: M_W = 313.3 g/mol, n = 1.3 mmol, m = 0.40 g, 40%

Elemental analysis: found: 32.63% C, 4.39% H, 7.73 % N;
calculated ($C_{13}H_{18}N_2O_5P$ + PbO + 3/2DMF): 32.53% C, 4.45% H, 7.59 % N
Atom absorption spectroscopy: found: 84.2 mg/L;
calculated ($C_{13}H_{18}N_2O_5P$ + PbO + 3/2DMF): 79.3 mg/L

[3-(4,4,5,5-tetramethyl-imidazoline-3-oxide-1-oxyl)-phenyl]-phosphonic acid (27b)

Research Journal: AP-204

[3-(1,3-Dihydroxy-4,4,5,5-tetramethyl-imidazolidin-2-yl)-phenyl]-phosphonic acid **(26b)** (M_W = 316.3 g/mol, n = 3.2 mmol, m = 1.0 g) was dissolved in 20 mL methanol. Lead dioxide (M_W = 239.1 g/mol, n = 16 mmol, m = 3.8 g) was added and the reaction mixture was stirred over night. All solid remains were filtered off and the blue filtrate was left undisturbed for some hours. The solution was decanted and this procedure was carried out several times to remove most of the lead oxide residues. The filtrate was evaporated to dryness. The desired compound could be obtained as blue powder.

Yield: M_W = 313.3 g/mol, n = 0.9 mmol, m = 0.30 g, 30%
IR (KBr): Figure 5.48 on page 235
ν (cm^{-1}) = 3425 (br, ν_s, OH), 2982 (m, ν_{as}, CH_3), 2935 (w, ν_s, CH_3), 1633 (m, ν_{as} C-N), 1551 (w, ν_s C=C), 1384 (m, ν_s C-N), 1356 (m, ν_s N-O), 1217 and 1164 (m, ν_s P=O), 1024 and 1011 (s, ν_{as} P-OH), 963 (m, δ_{oop} ONCNO), 803 (w, δ_{oop} 2H ring), 697 (m, δ_{oop} ring)
Elemental analysis: found: 24.43% C, 1.93% H, 4.05 % N;
calculated ($C_{13}H_{18}N_2O_5P$ + 3/2PbO): 24.09% C, 2.80% H, 4.32 % N **Atom absorption spectroscopy:** found: 111 mg/L;
calculated ($C_{13}H_{18}N_2O_5P$ + 3/2PbO): 79.5 mg/L

[(4,4,5,5-tetramethyl-imidazoline-3-oxide-1-oxyl)-phenyl]-phosphonate sodium salt

Procedure 1: Oxidation with lead dioxide:
The appropiate [(1,3-Dihydroxy-4,4,5,5-tetramethyl-imidazolidin-2-yl)-phenyl]-phosphonic acid derivate **(26a)** or **(26b)** (M_W = 316.3 g/mol, n = 3.2 mmol, m = 1.0 g) was dissolved in 20 mL methanol. Lead dioxide (M_W = 239.1 g/mol, n = 16 mmol, m = 3.8 g) and sodium hydroxide (M_W = 40.0 g/mol, n = 6.4 mmol,

m = 0.25 g) were added and the reaction mixture was stirred over night. All solid remains were filtered off and the blue filtrate was left undisturbed for some hours. The solution was decanted and it was evaporated to dryness. The desired compound could be obtained as blue powder.

Procedure 2: Oxidation with sodium periodate:
The appropiate [(1,3-Dihydroxy-4,4,5,5-tetramethyl-imidazolidin-2-yl)-phenyl]-phosphonic acid derivate **(26a)** or **(26b)** (M_W = 316.3 g/mol, n = 3.2 mmol, m = 1.0 g) was dissolved in 10 mL methanol. Sodium periodate (M_W = 213.9 g/mol, n = 3.2 mmol, m = 0.68 g) was dissolved separately in 10 ml water. Both solutions were united and shaked for 5 minutes. The dark-blue-brown reaction mixture was transferred in a separating funnel filled with 30 ml of chloroform. A red by-product was removed by several extractions with chloroform. Sodium carbonate (M_W = 106.0 g/mol, n = 3.2 mmol, m = 0.34 g) was added slowly, so that the methanol/water phase retained the characteristic blue colour. The methanol/water phase was separated and evaporated to dryness. The desired compound could be obtained as blue powder.

[4-(4,4,5,5-tetramethyl-imidazoline-3-oxide-1-oxyl)-phenyl]-phosphonate sodium salt (28a) **Research Journal**: XE-297 (Procedure 1)
Yield: M_W = 357.2 g/mol, n = 2.5 mmol, m = 0.89 g, 78%
IR (KBr): Figure 5.48 on page 235
ν (cm^{-1}) = 3398 (br, ν_s, OH), 1650 (m, ν_{as} C-N), 1421 (w, ν_s C=C), 1385 (m, ν_s C-N), 1358 (m, ν_s N-O), 1137 (m, ν_s P=O), 1064 (s, ν_{as} P-OH), 972 (m, δ_{oop} ONCNO), 827 (w, δ_{oop} 2H ring), 620 (m, δ_{oop} ring)
Elemental analysis: found: 33.53% C, 5.62% H, 6.31 % N;
calculated ($C_{13}H_{18}N_2O_5P$ + 5 H_2O): 34.91% C, 5.86% H, 6.26 % N
Atom absorption spectroscopy: found: 10.00 mg/L Na, 24.00 mg/L Pb;
calculated ($C_{13}H_{16}N_2Na_2O_5P$ + 5 H_2O): 15.5 mg/L Na, 0 mg/L Pb **ESI mass spectra:** Figure 5.52 on page 239

Research Journal: AP-205 (Procedure 2)
Yield: M_W = 357.2 g/mol, n = 2.4 mmol, m = 0.86 g, 75%
IR (KBr): Figure 5.48 on page 235
ν (cm^{-1}) = 3368 (br, ν_s, OH), 2993 (m, ν_{as}, CH_3), 1697 (m, ν_{as} C-N), 1598 (w, ν_s C=C), 1386 (m, ν_s C-N), 1361 (m, ν_s N-O), 1214 and 1137 (m, ν_s P=O), 1065 (s, ν_{as} P-OH), 978 (s, δ_{oop} ONCNO), 822 (w, δ_{oop} 2H ring), 707 (m, δ_{oop} ring)
Elemental analysis: found: 38.33% C, 3.83% H, 4.99 % N;

calculated ($C_{13}H_{16}N_2Na_2O_5P$ + CH_3OH + 1/2 $NaIO_4$): 33.89% C, 4.06% H, 5.65 % N
Atom absorption spectroscopy: found: 10.42 mg/L Na;
calculated ($C_{13}H_{16}N_2Na_2O_5P$ + CH_3OH + 1/2 $NaIO_4$: 11.6 mg/L Na

[3-(4,4,5,5-tetramethyl-imidazoline-3-oxide-1-oxyl)-phenyl]-phosphonate sodium salt (28b) **Research Journal**: AP-170 (Procedure 1)
Yield: M_W = 357.2 g/mol, n = 2.0 mmol, m = 0.72 g, 63%
IR (KBr): Figure 5.49 on page 236
ν (cm^{-1}) = 3353 (br, ν_s, OH), 2990 (m, ν_{as}, CH_3), 1689 (m, ν_{as} C-N), 1594 (w, ν_s C=C), 1384 (m, ν_s C-N), 1353 (m, ν_s N-O), 1215 and 1163 (m, ν_s P=O), 1074 (s, ν_{as} P-OH), 981 (s, δ_{oop} ONCNO), 810 (w, δ_{oop} 2H ring), 696 (m, δ_{oop} ring)
Elemental analysis: found: 26.65% C, 3.96% H, 4.69 % N;
calculated ($C_{13}H_{16}N_2Na_2O_5P$ + PbO + H_2O): 26.09% C, 3.03% H, 4.68 % N
Atom absorption spectroscopy: found: 7.63 mg/L Na, 46.65 mg/L Pb;
calculated ($C_{13}H_{16}N_2Na_2O_5P$ + PbO + H_2O): 10.2 mg/L Na, 45.9 mg/L Pb **ESI mass spectra:** Figure 5.53 on page 239

Research Journal: AP-206 (Procedure 2)
Yield: M_W = 357.2 g/mol, n = 2.2 mmol, m = 0.78 g, 68%
IR (KBr): Figure 5.49 on page 236
ν (cm^{-1}) = 3353 (br, ν_s, OH), 2990 (m, ν_{as}, CH_3), 1689 (m, ν_{as} C-N), 1594 (w, ν_s C=C), 1384 (m, ν_s C-N), 1353 (m, ν_s N-O), 1215 and 1163 (m, ν_s P=O), 1074 (s, ν_{as} P-OH), 981 (s, δ_{oop} ONCNO), 810 (w, δ_{oop} 2H ring), 696 (m, δ_{oop} ring)
Elemental analysis: found: 37.40% C, 4.75% H, 5.79 % N;
calculated ($C_{13}H_{16}N_2Na_2O_5P$ + CH_3OH + 1/2 $NaIO_4$): 33.89% C, 4.06% H, 5.65 % N
Atom absorption spectroscopy: found: 11.18 mg/L Na;
calculated ($C_{13}H_{16}N_2Na_2O_5P$ + CH_3OH + 1/2 $NaIO_4$: 11.6 mg/L Na

5.2.2 Sulfonate Substituent

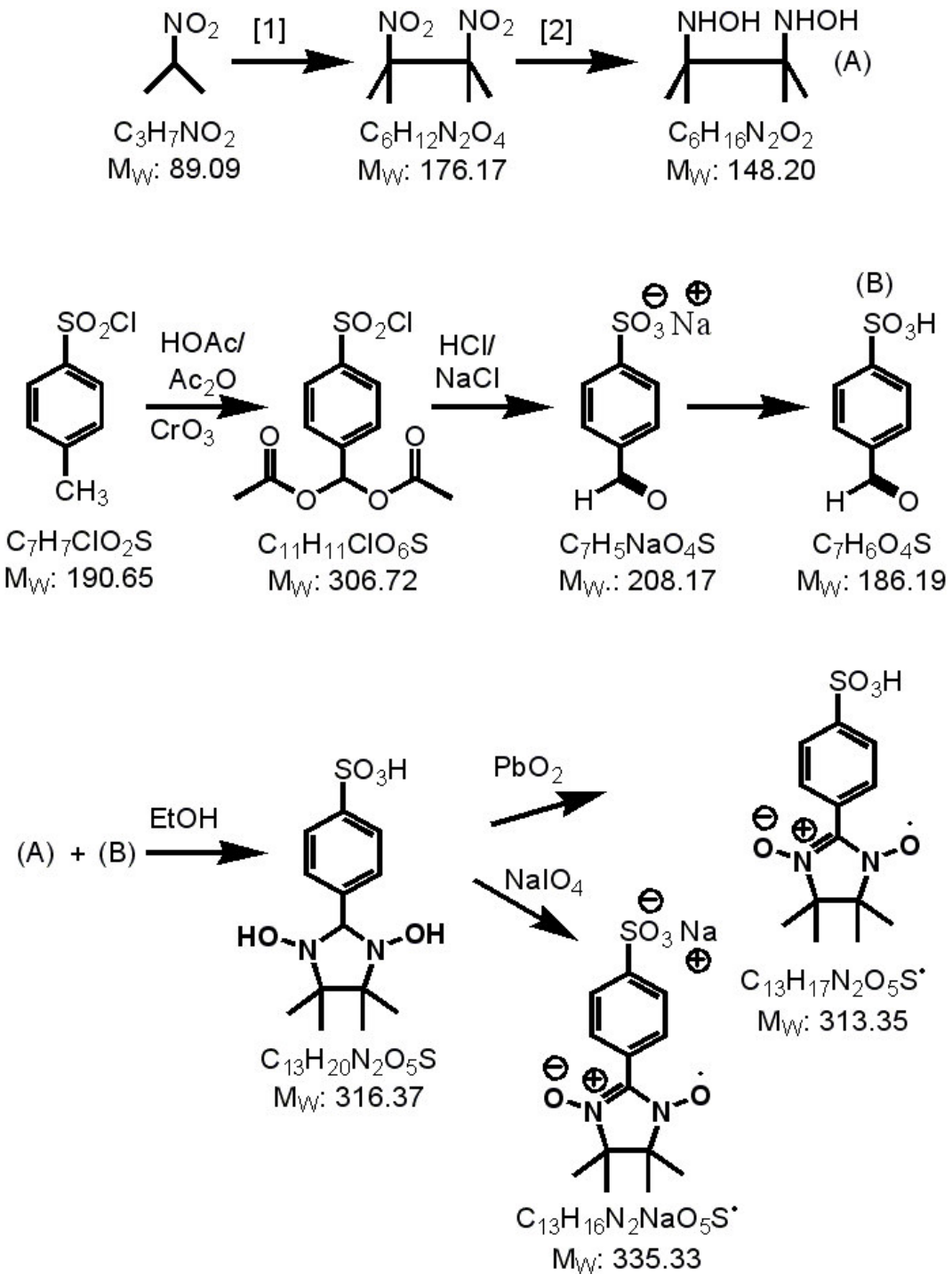

Figure 5.5: The synthesis of the para-sulfonate derivate of a nitronyl-nitroxide radical is schematically shown. [1] JACS,77, 6689-6690 (1955); [2] JOC, 69, 475-481 (2004)

4-(Diacetoxymethyl)benzenesulfonic acid chloride (29)

Research Journal: XE-308

Literature: J. T. Randolph et al., Bioorganic and medicinical chemistry, 14, 4035-4046 (2006) [157]

4-Toluenesulfonic acid chloride (M_W = 190.6 g/mol, n = 0.115 mol, m = 21.9 g) was dissolved in 183 mL concentrated acetic acid and 183 mL acetic acid anhydride. The reaction mixture was cooled with an ice-bath before concentrated sulfuric acid (m = 27.7 g, V = 15 mL) was added dropwise. Then chromium trioxide (M_W = 100.0 g/mol, n = 0.32 mol, m = 32.2 g) pellets were added, so that the temperature of the reaction mixture stayed below 20°C. The reaction mixture was stirrred for 40 h, before it was spilled on ice. The resulting gray solid was filtrated and several times extracted with hot dichlormethane. The dichlormethane extract was dried over sodium sulfate adn the solvent was removed under reduced pressure, so that the desired compound could be obtained as colourless powder.

Yield: M_W = 306.7 g/mol, n = 0.03 mol, m = 10.9 g, 29%
^{1}H-NMR ($CDCl_3$, 400 MHz): Figure 5.34 on page 224
δ (ppm): 2.14 (s, 6H, [12,13]), 7.71 (s, 1H, [7]), 7.76 (d, 2H, [2,4]), 8.07 (d, 2H, [1,5])
IR (KBr): Figure 5.49 on page 236
ν (cm^{-1}) = 3100 (w, ν_s C-H arom), 1763 (s, ν_{as} C-O), 1600 and 1416 (m, ν_s C=C), 1381 (s, ν_s C-O), 1238 and 1191 (s, ν_{as} S-O), 831 (m, δ_{oop} 2H ring), 713 (m, δ_{oop} ring)

4-(Formyl)benzenesulfonate sodium salt (30)

Research Journal: XE-312

4-(Diacetoxymethyl)benzenesulfonic acid chloride **(29)** (M_W = 306.7 g/mol, n = 0.03 mol, m = 10.1 g) was dissolved in 120 mL 3 molar hydrochloric acid and refluxed for 3 h. The reaction mixture was allow to cool, before saturated sodium chloride solution was added to obtain a colourless solid. For completeness the reaction mixture was cooled over night. The desired compound could be obtained as colourless powder that was filtered off and dried in vacuum.

Yield: M_W = 208.2 g/mol, n = 27 mmol, m = 5.7 g, 88%
IR (KBr): Figure 5.49 on page 236

ν (cm^{-1}) = 3486 (br, O-H sulfonate), 3052 (w, ν_s C-H arom), 2871 (m, ν_s C-H aldehyde), 1698 (s, ν_{as} C=O), 1602 and 1410 (m, ν_s C=C), 1386 (s, ν_s C=O), 1210 (s, ν_{as} S-O), 833 (m, δ_{oop} 2H ring), 718 (m, δ_{oop} ring)

4-(Formyl)benzenesulfonic acid (31)

Research Journal: XE-301

4-(Formyl)benzenesulfonate sodium salt **(30)** (M_W = 208.2 g/mol, n = 0.03 mol, m = 6.6 g) was dissolved in methanol. Concentrated hydrochloric acid was added and the resulting sodium chloride was filtrated off. The reaction mixture was evaporated to dryness and the desired compound could be obtained as yellow powder that was further dried in vacuum.

Yield: M_W = 186.2 g/mol, n = 0.03 mmol, m = 5.6 g, 91%
^{1}**H-NMR (DMSO, 400 MHz)**: Figure 5.35 on page 225
δ (ppm): 7.75 (d, 2H, [2,4]), 7.84 (d, 2H, [1,5]), 9.97 (s, 1H, [9])
IR (KBr): Figure 5.50 on page 237
ν (cm^{-1}) = 3484 (br, O-H sulfonate), 3090 and 3051 (w, ν_s C-H arom), 2871 (m, ν_s C-H aldehyde), 1698 (s, ν_{as} C=O), 1600 and 1411 (m, ν_s C=C), 1385 (m, ν_s C=O), 1210 (s, ν_{as} S-O), 831 (m, δ_{oop} 2H ring), 710 (m, δ_{oop} ring)

4-(1,3-Dihydroxy-4,4,5,5-tetramethyl-imidazolidin-2-yl)-benzenesulfonic acid (32)

Research Journal: XE-302

4-(Formyl)benzenesulfonic acid **(31)** (M_W = 186.2 g/mol, n = 15 mmol, m = 2.9 g) and 2,3-Bis(hydroxylamine)-2,3-dimethylbutane **(22)** (M_W = 148.2 g/mol, n = 15 mmol, m = 2.2 g) were dissolved separately in as less ethanol as possible. Both solutions were united and stirred over night. The desired compound could be obtained as colourless powder that was filtrated off and dried in vacuum.

Yield: M_W = 316.4 g/mol, n = 13 mmol, m = 4.5 g, 95%
^{1}**H-NMR (DMSO, 400 MHz)**: Figure 5.36 on page 225
δ (ppm): 0.99 (s, 6H, [14, 15]), 1.03 (s, 6H, [13, 16]), 4.46 (s, 1H, [8]), 7.36 (d, 2H, [2,4]), 7.50 (d, 2H, [1,5])
IR (KBr): Figure 5.50 on page 237

ν (cm^{-1}) = 3432 (br, O-H sulfonate), 2990 (m, ν_{as}, CH_3), 2915 (w, ν_s, CH_3), 1635 (m, ν_{as} C-N), 1461 (m, ν_s C=C), 1378 (m, ν_s C-N), 1218 and 1175 (s, ν_{as} S-O), 804 (m, δ_{oop} 2H ring), 626 (m, δ_{oop} ring)

4-(4,4,5,5-tetramethyl-imidazoline-3-oxide-1-oxyl)-benzenesulfonic acid (33)

Research Journal: AP-211

4-(1,3-Dihydroxy-4,4,5,5-tetramethyl-imidazolidin-2-yl)-benzenesulfonic acid **(32)** (M_W = 316.4 g/mol, n = 3.2 mmol, m = 1.0 g) was dissolved in 20 mL methanol. Lead dioxide (M_W = 239.1 g/mol, n = 16 mmol, m = 3.8 g) was added and the reaction mixture was stirred over night. All solid remains were filtered off and the blue filtrate was left undisturbed for some hours. The solution was decanted and evaporated to dryness. The desired compound could be obtained as blue powder.

Yield: M_W = 313.4 g/mol, n = 1 mmol, m = 0.32 g, 32%
Elemental analysis: found: 37.98% C, 4.21% H, 7.03 % N, 7.80 % S;
calculated ($C_{13}H_{17}N_2O_5S$ + 1/2 PbO): 36.74% C, 4.03% H, 6.95 % N, 7.55 % S

4-(4,4,5,5-tetramethyl-imidazoline-3-oxide-1-oxyl)-benzenesulfonate sodium salt (34)

Research Journal: AP-212

4-(1,3-Dihydroxy-4,4,5,5-tetramethyl-imidazolidin-2-yl)-benzenesulfonic acid **(32)** (M_W = 316.4 g/mol, n = 6.3 mmol, m = 2.0 g) was dissolved in 10 mL methanol. Sodium periodate (M_W = 213.9 g/mol, n = 6.3 mmol, m = 1.4 g) was dissolved separately in 10 ml water. Both solutions were united and shaked for 5 minutes. The dark-blue-brown reaction mixture was transferred in a separating funnel filled with 30 ml of chloroform. A red by-product was removed by several extractions with chloroform. Sodium carbonate (M_W = 106.0 g/mol, n = 3.2 mmol, m = 0.34 g) was added slowly, so that the methanol/water phase retained the characteristic blue colour. The methanol/water phase was separated and evaporated to dryness. The desired compound could be obtained as blue powder.

Yield: M_W = 335.3 g/mol, n = 3.6 mmol, m = 1.2 g, 57%
Elemental analysis: found: 40.55% C, 4.60% H, 7.12 % N, 7.74 % S;

calculated ($C_{13}H_{16}N_2NaO_5S$ + 1/2 Na_2CO_3 + 1/2 H_2O): 40.81% C, 4.31% H, 7.05 % N, 8.07 % S

5.2.3 Chelating Ligands

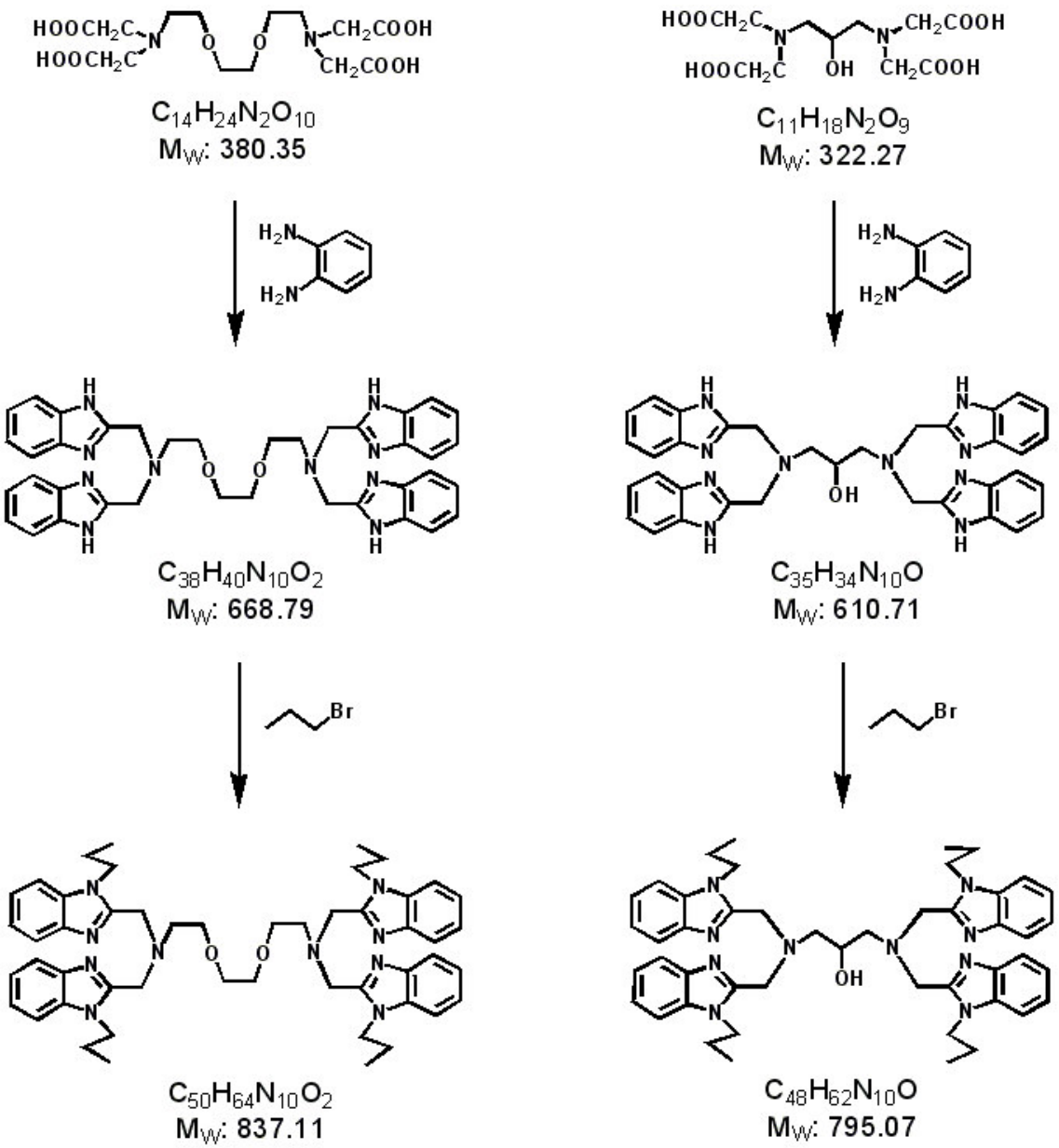

Figure 5.6: The synthesis of the two chelating ligands is shown, left: ^{Pr}EPTG, right: ^{Pr}HPTB

5.2.3.1 ^{Pr}EPTG

N,N,N',N'-tetrakis[(2-benzimidazolyl)methyl]-1,2-di(2-aminoethoxy)ethan (EPTG) (35)

Research Journal: XE-350

Literature: Q. Zhou et al., Inorganica Chimica Acta, 359, 1200-1206 (2006) [158]

1,2-di(2-aminoethoxy)ethan-N,N,N',N'-tetraacetic acid (M_W = 380.4 g/mol, n = 0.07 mol, m = 25.8 g) and o-phenylenediamine (M_W = 108.1 g/mol, n = 0.28 mol, m = 30.6 g) were suspended in 185 ml ethyleneglycole. The reaction mixture was refluxed at 170°C for 5 h. The reaction mixture was allow to cool down, before it was spilled on ice and cooled over night. The water was decanted and a violett solid was obtained, which was recrystallized from hot ethanol. The desired compound could be obtained as a nearly white powder. This was sucked off and dried in vacuo.

Yield: M_W = 668.8 g/mol, n = 0.05 mol, m = 35.0 g, 71%

N,N,N',N'-tetrakis[2-(1-n-propylbenzimidazolyl)methyl]-1,2-di(2-aminoethoxy)ethan (^{Pr}EPTG) (36)

Research Journal: XE-353

Literature: D. Chapman et al., Tetrahedron Letters, 29, 3033-3036 (1988) [159]

EPTG **(35)** (M_W = 668.8 g/mol, n = 0.05 mol, m = 35.0 g) was dissolved in 100 mL DMSO. Potassium hydroxide (M_W = 56.1 g/mol, n = 0.6 mol, m = 33.7 g) was pestled and also suspended in 100 mL DMSO. Both mixtures were united and immediately 1-propyl bromide (M_W = 123.0 g/mol, n = 0.3 mol, m = 36.9 g) was added. The reaction mixture was stirred for 1 h at room temperature, before it was spilled in 200 mL water. The desired compound could be obtained as colourless precipitate, which was sucked off and dried in vacuo.

Yield: M_W = 837.1 g/mol, n = 0.035 mol, m = 29.2 g, 73%

^{1}H-NMR (DMSO, 400 MHz): Figure 5.37 on page 226

δ (ppm): 0.56 (t, 12H, [53,56,59,62]), 1.49 (q, 8H, [52,55,58,61]), 2.54 (m, 4H, [1,8]), 2.78 (t, 4H, [2,7]), 3.43 (t, 4H, [4,5]), 3.99 (m, 16H, [11,12,15,17,51,54, 57,60]), 7.17 (m, 8H, [36,37,40,41,44,45,48,49]), 7.53 (m, 8H, [35,38,39,42,43, 46,47,50])

IR (KBr): Figure 5.51 on page 238

ν (cm^{-1}) = 3049 (w, ν_s, C-H), 2964 (w, ν_{as}, CH_2), 2876 and 2826 (m, ν_s, CH_2), 1615 (m, ν_{as} C-N), 1512 (w, ν_s C=C), 1462 (s, δ_{as} C=N), 1416 (s, δ_s C=N), 1105 (m, ν_s, C-O), 850 and 748 (m, δ_{oop} 4H ring)

5.2.3.2 ^{Pr}HPTB

N,N,N',N',-tetrakis[(2-benzimidazolyl)methyl]-1,3-diaminopropan-2-ol (HPTB) (37)

Research Journal: XE-352
Literature: Q. Zhou et al., Inorganica Chimica Acta, 359, 1200-1206 (2006) [158]

1,3-Diamino-2-hydroxypropane-N,N,N',N'-tetraacetic acid (M_W = 322.3 g/mol, n = 0.08 mol, m = 25.1 g) and o-phenylenediamine (M_W = 108.1 g/mol, n = 0.33 mol, m = 35.6 g) were suspended in 200 ml ethyleneglycole. The reaction mixture was refluxed at 185°C for 5 h. The reaction mixture was allow to cool down, before 100 mL water were added. A colourless precipitate formed. The reaction mixture was decanted and the precipitate was recrystallized from hot acetone. The desired compound could be obtained as a nearly white powder. This was sucked off and dried in vacuo.

Yield: M_W = 610.7 g/mol, n = 0.05 mol, m = 31.5 g, 66%

N,N,N',N',-tetrakis[2-(1-n-propylbenzimidazolyl)methyl]-1,3-diaminopropan-2-ol (^{Pr}HPTB) (38)
Research Journal: XE-354, XE-335
Literature: D. Chapman et al., Tetrahedron Letters, 29, 3033-3036 (1988) [159]

HPTB **(37)** (M_W = 610.7 g/mol, n = 0.05 mol, m = 31.5 g) was dissolved in 100 mL DMSO. Potassium hydroxide (M_W = 56.1 g/mol, n = 0.71 mol, m = 40.0 g) was pestled and also suspended in 100 mL DMSO. Both mixtures were united and immediately 1-propyl bromide (M_W = 123.0 g/mol, n = 0.31 mol, m = 38.1 g) was added. The reaction mixture was stirred for exactely 1 h at room temperature, before it was spilled in 1000 mL water. If the desired product was really pure, it precipitated as white powder. Then it could be sucked off and dried in vacuo. If it was not pure (mainly due to remains of 1-propyl bromide), a brown oil separated at the bottom. The reaction mixture was decanted and extracted two times with

chloroform. The organic phases were united and the solvent was removed under reduced pressure.

Yield: M_W = 795.1 g/mol, n = 0.047 mol, m = 37.6 g, 91%
^{1}H-NMR (DMSO, 400 MHz): Figure 5.38 on page 226
δ (ppm): 0.49 (t, 12H, [49,52,55,58]), 1.38 (q, 8H, [48,51,54,57]), 2.54 (d, 4H, [1,3]), 3.70 (m, 1H, [2]), 3.85 (m, 16H, [7,8,11,13,47,50,53,56]), 7.20 (m, 8H, [32,33,36,37,40,41,44,45]), 7.42 (d, 4H [34,35,42,43]), 7.55 (d, 4H, [31,38,39,46])
IR (KBr): Figure 5.51 on page 238
ν (cm^{-1}) = 3053 (w, ν_s, C-H), 2965 (m, ν_{as}, CH_2), 2933 and 2875 (w, ν_s, CH_2), 1614 (w, ν_{as} C-N), 1511 (m, ν_s C=C), 1462 (s, δ_{as} C=N), 1421 (s, δ_s C=N), 1112 (m, ν_s, C-O), 847 and 748 s, δ_{oop} 4H ring)

5.2.4 Complexes with the new Nitronyl-Nitroxide Radicals

General Procedure:
To a methanolic solution of ^{Pr}EPTG **(36)** (M_W = 837.1 g/mol, n = 0.5 mmol, m = 0.418 g), first a methanolic solution of the appropiate sodium salt of the phosphonate ligand (Sodium salt of 4-Tolyl-phosphonic acid **(2c)** : M_W = 216 g/mol, n = 0.6 mmol, m = 0.130 g; sodium salt of p(m)PO_3H_2-NIT **(28a)** , **(28b)** M_W = 357 g/mol, n = 0.6 mmol, m = 0.214 g) and then also a methanolic solution of the nickel perchlorate salt (M_W = 366 g/mol, n = 1 mmol, m = 0.366 g) is added. All solid remains are filtered off. The reaction solution is heated for a short period of time and then a solid precipitate. The desired complex is filtered off and dried in air. The crystallisation takes place in an acetonitrile solution of the solid when diethylether diffuses slowly in.

$[Ni_2(C_{50}H_{64}N_{10}O_2)(C_7H_7PO_3)(H_2O)_2](ClO_4)_2$ (39)
Research Journal: AP-133

Crystal data: Figure 5.79 on page 268
ESI mass spectra: Figure 5.54 on page 240: m/z = 1224.66 ($C_{57}H_{71}ClN_{10}Ni_2O_9P^+$)

$[Ni_2(C_{50}H_{64}N_{10}O_2)(C_{13}H_{16}N_2PO_5)(H_2O)_2](ClO_4)_2$ (40)
Research Journal: AP-176

Crystal data: Figure 5.80 on page 270
Elemental analysis: found: 47.87% C, 5.64% H, 11.54% N;
calculated ($C_{63}H_{84}Cl_2N_{12}Ni_2O_{17}P_2$*$CH_3CN$*$3H_2O$): 48.92% C, 5.87% H, 11.41% N **ESI mass spectra:** Figure 5.55 on page 240: m/z = 632.15 ($C_{63}H_{80}N_{12}Ni_2O_7P^{\bullet 2+}$, 1265.47), 1364.43 ($C_{63}H_{80}ClN_{12}Ni_2O_11P^{\bullet +}$)

$[Ni_3Na_1Pb_1(C_{50}H_{64}N_{10}O_2)_2\ (C_{13}H_{16}N_2PO_5)_2(OH)_2](ClO_4)_3$ (41)
Research Journal: AP-178

Crystal data: Figure 5.81 on page 271
ESI mass spectra: Figure 5.56 on page 241: m/z = 632.96 ($C_{63}H_{80}N_{12}Ni_2O_7P^{\bullet 2+}$, 1265.47), 1364.22 ($C_{63}H_{80}ClN_{12}Ni_2O_11P^{\bullet +}$)

5.3 Equipment and Methods

Working Techniques
Chemicals were ordered by Acros, Fisher, Scientific, Fluka, Merck, Riedel-de-Haen and Aldrich. If necessary, solvents were dried by standard procedures, cleaned by destillation and stored under inert atmosphere. The synthesis of air and moisture sensitive samples was done by Schlenk techniques with argon 4.6.

Elemental Analysis
Elemental analysis was carried by the microanalytical laboratory of the Johannes Gutenberg University Mainz. Vario EL of the company Heraus was used. The elements carbon, nitrogen and hydrogen were determined.

Electrochemical Experiments
For cyclovoltammetric measurements a three electrode measuring cell with a Princeton Applied Research potentiostat model 263A was used. A graphite electrode was the working electrode. A platin electrode was the counter electrode and the reference electrode was a $Ag/AgNO_3$ electrode. So, the current was measured depending on the applied potential. With time the potential was changed. The mass transport during the reaction was caused by the additional electrolyte solution of tetrabutylammoniumperchlorate. The concentration of the analysed compound was 10^{-4} mol/L, the concentration of the electrolyte was 10^{-2} mol/L. As an internal standard ferrocen was added. The program used was Power Suite of Princeton Applied Research.

NMR Spectra
The NMR spectra were carried out on a Bruker DRX 400 at roomtemperatures (^{1}H at 400.13 MHz, ^{13}C at 100.61 MHz, ^{31}P at 166 MHz). As standards tetramethylsilan and phosphoric acid were used, furthermore the solvent signals were used as internal standard. The spectra were analysed with the program MesReNova.

Mass Spectra
The ESI mass spectra were carried out in the group of Prof. T. H. at the University of Mainz by Dr. L. M.. The instrument was a Finnigan MAT LCQ.

IR Spectra
The IR spectra were measured at a JASCO FT/IR-4200. The samples were comminuted with KBr and measured in the solid-state at room temperature.

Measurement of the magnetic susceptibility
A SQUID Magnetometer MPMS XL was used. The powdered samples were filled

in gelatine capsule and fixed in a plastic straw. The measurement was carried out on a lengths of 4cm, 24 data points were taken. The response function of the volume magnetisation was corrected by the diamagnetic contribution of holder and capsule and with the molecular weight, the molare susceptibility was calculated. Simulation details can be found in the Appendix in section A.

X-ray single crystal structures
Single Crystals were mounted by R. J.-P. on a SMART CCD-Diffrac- tometer equipped with Mo-K_α source. The single crystal structures were solved with the help of Dr. M. P. and Dr. D. S. with the programs SIR 97 and SHELX-2002.

UV/Vis spectra
The UV/Vis spectra were measured on a UV/Vis/NIR-spectrometer V-570 of the company JASCO.

DFT Calculations
DFT Calculations were carried out by Dr. U. S. (Ruhr University, Bochum) on an AMD Opteron QuadCore Linux-Cluster with 32 processor cores. The program ORCA 2.6.35 (by Dr. F. N. and co-worker, University of Bonn) was used. The geometrical optimisation and numerical frequency calculation were determined by the UB3LYP functional with a TZV(P) basis set, as well with the Grid4 option as with TightSCF. The calculation of the spin density and the TDDFT calculations were carried out with the same program, now additional polarisation functions (TZVPP basis set) were taken for the nitrogen, oxygen and phosphorusatoms. The influence of the solvent molecules, methanol, was taken into account by a COSMO model. The graphics were made with gOpenMol.

EPR spectra
EPR spectra were carried out by Dr. Y. A. in the group of Dr. D. H., Max Planck institute of polymer science, Mainz. A Bruker Elexsys 580 cw/pulse EPR spectrometer (X-band 9,7 GHz) was used.

Bibliography

[1] S. R. Batten, S. M. Neville, and D. R. Turner. *Coordination Polymers: Design, Analysis and Application*. RSC Publishing, Thomas Graham House, Science Park, Milton Road, Cambridge CB4 0WF, UK, 2009.

[2] J. Woodward. *Philosophical Transactions*, 33, 1726.

[3] H. J. Buser, D. Schwarzenbach, W. Petter, and A. Ludi. *Inorganic Chemistry*, 16(11):2704–2710, 1977.

[4] O. Kahn. *Molecular Magnetism*. VCH, New York, 1993.

[5] S. Ferlay, T. Mallah, R. Ouhaes, P. Veillet, and M. Verdaguer. *Nature*, 378:701, 1995.

[6] A. K. Cheetham, C. N. R. Rao, and R. K. Feller. *Chemical Communications*, (46):4780–4795, 2006.

[7] R. Lescouëzec, L. M. Toma, J. Vaissermann, M. Verdaguer, F. S. Delgado, C. Ruiz-Pérez, F. Lloret, and M. Julve. *Coordination Chemistry Reviews*, 249(23):2691–2729, 2005.

[8] A. F. Wells. *Three-dimensional Nets and Polyhedra*. Wiley-Interscience, New York, 1977.

[9] B. F. Hoskins and R. Robson. *Journal of the American Chemical Society*, 111(15):5962–5964, 1989.

[10] B. F. Hoskins and R. Robson. *Journal of the American Chemical Society*, 112(4):1546–1554, 1990.

[11] M. O'Keeffe, M. Eddaoudi, H. Li, T. Reineke, and O. M. Yaghi. *Journal of Solid State Chemistry*, 152(1):3–20, 2000.

[12] F. Qianrong, Z. Guangshan, X. Ming, S. Jinyu, W. Yen, Q. Shilun, and

X. Ruren. *Angewandte Chemie International Edition*, 44(25):3845–3848, 2005.

[13] G. Férey, C. Serre, C. Mellot-Draznieks, F. Millange, S. Surblé, J. Dutour, and I. Margiolaki. *Angewandte Chemie International Edition*, 43(46):6296–6301, 2004.

[14] H. Li, M. Eddaoudi, M. O'Keeffe, and O. M. Yaghi. *Nature*, 402:276, 1999.

[15] N.L. Rosi, J. Eddaoudi, M.and Kim, M. O'Keeffe, and O. M. Yaghi. *CrystEngComm*, 4:401, 2002.

[16] C. N. R. Rao, S. Natarajan, and R. Vaidhyanathan. *Angewandte Chemie International Edition*, 43(12):1466–1496, 2004.

[17] P. M. Forster, P. M. Thomas, and A. K. Cheetham. *Chemistry of Materials*, 14(1):17–20, 2001.

[18] W. J. Belcher, C. A. Longstaff, M. R. Neckenig, and J. W. Steed. *Chemical Communications*, (15):1602–1603, 2002.

[19] R. Kiriyama, H. Ibamoto, and K. Matsuo. *Acta Crystallographica*, 7:482–483, 1954.

[20] M. Viertelhaus, H. Henke, C. E. Anson, and A. K. Powell. *European Journal of Inorganic Chemistry*, page 2283, 2003.

[21] M. Viertelhaus, P. Adler, R. Clerac, C. E. Anson, and A. K. Powell. *European Journal of Inorganic Chemistry*, page 692, 2005.

[22] A. Cornia, A. Caneschi, P. Dapporto, A. C. Fabretti, D. Gatteschi, W. Malavasi, C. Sangregorio, and R. Sessoli. *Angewandte Chemie International Edition*, 38(12):1780, 1999.

[23] A. Clearfield. Metal Phosphonate Chemistry. In K. D. Karlin, editor, *Progress in inorganic chemistry*, page 371. Wiley-VCH, 1998.

[24] G. Alberti, U. Costantino, S. Allulli, and N. Tomassini. *Journal of Inorganic and Nuclear Chemistry*, 40(6):1113–1117, 1978.

[25] L. A. Vermeulen and M. E. Thompson. *Nature*, 358:656, 1992.

[26] A. Clearfield and Z. Wang. *Journal of the Chemical Society, Dalton Transactions*, (15):2937–2947, 2002.

[27] D. Cunningham, P. J. D. Hennelly, and T. Deeney. *Inorganica Chimica Acta*, 37:95–102, 1979.

[28] G. E. Fanucci, J. Krzystek, M. W. Meisel, L. Brunel, and D. R. Talham. *Journal of the American Chemical Society*, 120(22):5469–5479, 1998.

[29] C. Bellitto. Transition metal ion phosphonates as hybrid organic-inorganic magnets. In Prof Dr Marc Drillon Prof. Dr. Joel S. Miller, editor, *Magnetism: Molecules to Materials II*, pages 425–456. 2003.

[30] S. Weil and E. Rentschler. *Unpublished Results*.

[31] T. O. Salami, X. Fan, P. Y. Zavalijb, and S. R. J. Oliver. *Dalton Transactions*, pages 1574 – 1578.

[32] S. G. Carling, P. Day, D. Visser, and R. K. Kremer. *Journal of Solid State Chemistry*, 106(1):111–119, 1993.

[33] E. M. Bauer, C. Bellitto, G. Righini, M. Colapietro, G. Portalone, M. Drillon, and P. Rabu. *Inorganic Chemistry*, 47(23):10945–10952, 2008.

[34] C. Bellitto, F. Federici, A. Altomare, R. Rizzi, and S. A. Ibrahim. *Inorganic Chemistry*, 39(8):1803–1808, 2000.

[35] S. Bauer and N. Stock. *Chemie in unserer Zeit*, 42(1):12–19, 2008.

[36] S. Kitagawa, S. Noro, and T. Nakamura. *Chemical Communications*, (7):701–707, 2006.

[37] C. Wu, A. Hu, L. Zhang, and W. Lin. *Journal of the American Chemical Society*, 127(25):8940–8941, 2005.

[38] U. Mueller, M. Schubert, F. Teich, H. Puetter, K. Schierle-Arndt, and J. Pastre. *Journal of Materials Chemistry*, 16(7):626–636, 2006.

[39] L. J. de Jongh and A. R. Miedema. *Advances in Physics*, 23(1):1–260, 1974.

[40] J. G. Bednorz and K. A. Müller. *Zeitschrift für Physik B Condensed Matter*, 64(2):189–193, 1986.

[41] R. J. Glauber. *Journal of Mathematical Physics*, 4(2):294–307, 1963.

[42] A. Caneschi, D. Gatteschi, N. Lalioti, C. Sangregorio, R. Sessoli, G. Venturi, A. Vindigni, A. Rettori, M. Pini, and M. A. Novak. *Angewandte Chemie International Edition*, 40(9):1760–1763, 2001.

[43] R. Clerac, H. Miyasaka, M. Yamashita, and C. Coulon. *Journal of the American Chemical Society*, 124(43):12837–12844, 2002.

[44] T. Liu, D. Fu, S. Gao, Y. Zhang, H. Sun, G. Su, and Y. Liu. *Journal of the American Chemical Society*, 125(46):13976–13977, 2003.

[45] K. Bernot, J. Luzon, R. Sessoli, A. Vindigni, J. Thion, S. Richeter, D. Leclercq, J. Larionova, and A. vanderLee. *Journal of the American Chemical Society*, 130(5):1619–1627, 2008.

[46] C. Rüchardt. *Sitzungsberichte der Heidelberger Akademie der Wissenschaften, Mathematisch-naturwissenschaftliche Klasse*, pages 319–345, 1992.

[47] C. Rüchardt. *Angewandte Chemie International Edition*, 9(11):830–843, 1970.

[48] J. H. Osiecki and E. F. Ullman. *Journal of the American Chemical Society*, 90(4):1078–1079, 1968.

[49] A. Zakrassov, V. Shteiman, Y. Sheynin, M. Botoshansky, M. Kapon, M. Kaftory, R. Del Sesto, and J. Miller. *Helvetica Chimica Acta*, 86(4):1234–1245, 2003.

[50] E. Hernandez, M. Mas, E. Molins, C. Rovira, and J. Veciana. *Angewandte Chemie International Edition*, 32(6):882–884, 1993. 1521-3773.

[51] K. Nakabayashi, M. Kawano, and M. Fujita. *Angewandte Chemie International Edition*, 44(33):5322–5325, 2005.

[52] M. Kinoshita, P. Turek, M. Tamura, K. Nozawa, D. Shiomi, Y. Nakazawa, M. Ishikawa, M. Takahashi, K. Awaga, T. Inabe, and Y. Maruyama. *Chemistry Letters*, 20(7):1225–1228, 1991.

[53] F. Alies, D. Luneau, J. Laugier, and P. Rey. *The Journal of Physical Chemistry*, 97(12):2922–2925, 1993.

[54] L. Zhang, Z. L. Liu, L. H. Weng, D. Z. Liao, Z. H. Jiang, S. P. Yan, P. W. Shen, and M. Baumgarten. *Helvetica Chimica Acta*, 84(4):834–841, 2001.

[55] H. M. McConnell. *The Journal of Chemical Physics*, 39(7):1910–1910, 1963.

[56] M. Deumal, J. Cirujeda, J. Veciana, and J. J. Novoa. *Chemistry - A European Journal*, 5(5):1631–1642, 1999.

[57] R. Chiarelli, M. A. Novak, A. Rassat, and J. L. Tholence. *Nature*, 363:147–149, 1993.

[58] J. S. Miller, A. J. Epstein, and W. M. Reiff. *Science*, 240(4848):40–47, 1988.

[59] S. Nakatsuji and H. Anzai. *Journal of Materials Chemistry*, 7(11):2161–2174, 1997.

[60] A. Caneschi, D. Gatteschi, R. Sessoli, and P. Rey. *Accounts of Chemical Research*, 22(11):392–398, 1989.

[61] J. M. Manriquez, G. T. Yee, R. S. Mclean, A. J. Epstein, and J. S. Miller. . *Science*, 252(5011):1415–1417, 1991.

[62] D. C. Gordon, L. Deakin, A. M. Arif, and J. S. Miller. *Journal of the American Chemical Society*, 122(2):290–299, 1999.

[63] A. Caneschi, D. Gatteschi, N. Lalioti, R. Sessoli, L. Sorace, V. Tangoulis, and A. Vindigni. *Chemistry - A European Journal*, 8(1):286–292, 2002.

[64] A. Caneschi, D. Gatteschi, J. Laugier, P. Rey, and R. Sessoli. *Inorganic Chemistry*, 27(9):1553–1557, 1988.

[65] S. Fokin, V. Ovcharenko, G. Romanenko, and V. Ikorskii. *Inorganic Chemistry*, 43(3):969–977, 2004.

[66] A. Caneschi, D. Gatteschi, P. Rey, and R. Sessoli. *Inorganic Chemistry*, 30(20):3936–3941, 1991.

[67] O. V. Koreneva, G. V. Romanenko, Y. G. Shvedenkov, V. N. Ikorskii, and V. I. Ovcharenko. *Polyhedron*, 22(14-17):2487 – 2497, 2003.

[68] C. Benelli, A. Caneschi, D. Galleschi, J. Laugier, and P. Rey. *Angewandte Chemie International Edition*, 26(9):913–915, 1987. 1521-3773.

[69] M. Tanaka, K. Matsuda, T. Itoh, and H. Iwamura. *Angewandte Chemie International Edition*, 37(6):810–812, 1998.

[70] U. Schatzschneider, T. Weyhermüller, and E. Rentschler. *European Journal of Inorganic Chemistry*, 2001(10):2569–2586, 2001.

[71] M. Jung, D. Sharma, A.and Hinderberger, S. Braun, U. Schatzschneider, and E. Rentschler. *Inorganic Chemistry*, 48(15):7244–7250, 2009.

[72] M. Jung, A. Sharma, D. Hinderberger, S. Braun, U. Schatzschneider, and E. Rentschler. *European Journal of Inorganic Chemistry*, 2009(11):1495–1502, 2009.

[73] M. J. Sanchez-Moreno, R. B. Gomez-Coca, A. Fernandez-Botello, J. Ochocki,

A. Kotynski, R. Griesser, and H. Sigel. *Organic and Biomolecular Chemistry*, 1(10):1819–1826, 2003.

[74] H. H. Jaffe, Leon D. Freedman, and G. O. Doak. *Journal of the American Chemical Society*, 75(9):2209–2211, 1953.

[75] P. Tavs. *Chemische Berichte*, 103(8):2428–2436, 1970.

[76] K. Latham, A. M. Coyle, C. J. Rix, A. Fowless, and J. M. White. *Polyhedron*, 26(2):222–236, 2007.

[77] J. Rueff, V. Caignaert, S. Chausson, A. Leclaire, C. Simon, O. Perez, L. L. Pluart, and P. Jaffrès. *European Journal of Inorganic Chemistry*, 2008(26):4117–4125, 2008.

[78] R. Clarke, K. Latham, C. Rix, M. Hobday, and J. White. *CrystEngComm*, 7(3):28–36, 2005.

[79] S. Natarajan, S. Manual, P. Mahata, V. Rao, P. Ramaswamy, A.k Banerjee, A. Paul, and K. Ramya. *Journal of Chemical Sciences*, 118(6):525–536, 2006.

[80] E. Yang, X. Wang, and Y. Qin. *Chinese Journal of Structural Chemistry*, 25:1365, 2006.

[81] R. L. Carlin. *Magnetochemistry*. Springer-Verlag, New York, Heidelberg, Berlin, Tokyo, 1986.

[82] J. J. Borras-Almenar, E. Coronado, J. Curely, R. Georges, and J. C. Gianduzzo. *Inorganic Chemistry*, 33(23):5171–5175, 1994.

[83] D. Cao, J. Xiao, J. Tong, Y. Li, and L. Zheng. *Inorganic Chemistry*, 46(2):428–436, 2007.

[84] A. Caneschi, D. Gatteschi, J. Laugier, and P. Rey. *Journal of the American Chemical Society*, 109(7):2191–2192, 1987.

[85] J. W. Hall, W. E. Marsh, R. R. Weller, and W. E. Hatfield. *Inorganic Chemistry*, 20(4):1033–1037, 1981.

[86] H. Yoshikawa, C. Kazama, K. Awaga, M. Satoh, and J. Wada. *Chemical Communications*, (30):3169–3170, 2007.

[87] D. Gatteschi, R. Sessoli, and J. Villain. *Molecular Nanomagnets*, volume 5. Oxford, University Press, Oxford, 2006.

[88] A. V. Palii, S. M. Ostrovsky, S. I. Klokishner, O. S. Reu, Z.-M. Sun, A. V. Prosvirin, H.-H. Zhao, J.-G. Mao, and K. R. Dunbar. *Journal of Physical Chemistry A*, 110(51):14003–14012, 2006.

[89] H. Lueken. *Magnetochemie*. B.G. Teubner, Stuttgart, Leipzig, 1999.

[90] M. E. Lines. *Journal of Physics and Chemistry of Solids*, 31(1):101–116, 1970.

[91] F. Lloret, M. Julve, J. Cano, R. Ruiz-Garcia, and E. Pardo. *Inorganica Chimica Acta*, 361(12-13):3432–3445, 2008.

[92] J. Le Bideau, D. Papoutsakis, J. E. Jackson, and D. G. Nocera. *Journal of the American Chemical Society*, 119(6):1313–1316, 1997.

[93] I. Dzyaloshinsky. *Journal of Physics and Chemistry of Solids*, 4(4):241–255, 1958.

[94] T. Moriya. *Physical Review*, 120(1):91–98, 1960.

[95] J. Souletie, P. Rabu, and M. Drillon. *Physical Review B*, 72(21):214427, 2005.

[96] P. Rabu, J. M. Rueff, Z. L. Huang, S. Angelov, J. Souletie, and M. Drillon. *Polyhedron*, 20(11-14):1677–1685, 2001.

[97] C. Günther, H. Görls, and Dörte Stachel. *Acta Crystallographica Section E*, 65(12):i85, 2009.

[98] R. Hammond and J. Barbier. *Acta Crystallographica Section B*, 52(3):440–449, 1996.

[99] M. Ulutagay-Kartin, K. M. S. G. Etheredge, G. L. Schimek, and S. Hwu. *Journal of Alloys and Compounds*, 338(1-2):80 – 86, 2002.

[100] Y. Zhang and A. Clearfield. *Inorganic Chemistry*, 31(13):2821–2826, 1992.

[101] J. Le Bideau, C. Payen, P. Palvadeau, and B. Bujoli. *Inorganic Chemistry*, 33(22):4885–4890, 1994.

[102] S. Raghu, X. Qi, C. Honerkamp, and S. Zhang. *Physical Review Letters*, 100(15):156401, 2008.

[103] L. Fu and C. L. Kane. *Physical Review B*, 76(4):045302, 2007.

[104] S. Kitagawa and K. Uemura. *Chemical Society Reviews*, 34(2):109–119, 2005.

[105] J. Curély, F. Lloret, and M. Julve. *Physical Review B*, 58(17):11465–11483, 1998.

[106] J. H. Derek. The structural and magnetic properties of first-row transition-metal dimers containing hydroxo, substituted hydroxo, and halogen bridges. In J. L. Stephen, editor, *Progress in Inorganic Chemistry*, pages 173–241. 2007.

[107] K. T. McGregor, N. T. Watkins, D. L. Lewis, R. F. Drake, D. J. Hodgson, and W. E. Hatfield. *Inorganic and Nuclear Chemistry Letters*, 9(4):423 – 428, 1973.

[108] E. Stryjewski and N. Giordano. *Advances in Physics*, 26(5):487–650, 1977.

[109] T. D. Li, J.and Keene, D. Cao, S. Decurtins, and L. Zheng. *CrystEngComm*, 11(7):1255–1260, 2009.

[110] J. Rueff, N. Masciocchi, P. Rabu, A. Sironi, and A. Skoulios. *European Journal of Inorganic Chemistry*, 2001(11):2843–2848, 2001.

[111] L. Ma, L. Wang, Y. Wang, S. R. Batten, and J. Wang. *Inorganic Chemistry*, 48(3):915–924, 2009.

[112] J. Rueff, N. Barrier, S. Boudin, V. Dorcet, V. Caignaert, P. Boullay, G. B. Hix, and P.-A. Jaffres. *Dalton Transactions*, (47):10614–10620, 2009.

[113] J.-M. Rueff, A. Leclaire, and P.-A. Jaffrès. *Solid State Sciences*, 11(4):812–817, 2009.

[114] R. Gheorghe, V. Kravtsov, Y. A. Simonov, J.-P. Costes, Y. Journaux, and M. Andruh. *Inorganica Chimica Acta*, 357(5):1613–1618, 2004.

[115] J. Overgaard, E. Rentschler, G. A. Timco, N. V. Gerbeleu, V. Arion, A. Bousseksou, J. P. Tuchagues, and F. K. Larsen. *Journal of the Chemical Society, Dalton Transactions*, (15):2981–2986, 2002.

[116] E. Albert, C. Beatriz, S. Xavier, F. Mercé, and C. Teresa. *European Journal of Inorganic Chemistry*, (32):5082–5087, 2008.

[117] J. L. C. Rowsell and O. M. Yaghi. *Microporous and Mesoporous Materials*, 73(1-2):3–14, 2004.

[118] P. J. Hagrman, D. Hagrman, and J. Zubieta. *Angewandte Chemie International Edition*, 38(18):2638–2684, 1999.

[119] J. Overgaard, E. Rentschler, G. A. Timco, and F. K. Larsen. *ChemPhysChem*, 5(11):1755–1761, 2004.

[120] M. Drillon, P. Panissod, P. Rabu, J. Souletie, V. Ksenofontov, and P. Gütlich. *Physical Review B*, 65(10):104404, 2002.

[121] Melvin B. Robin and Peter Day. Mixed valence chemistry-a survey and classification. volume 10 of *Advances in Inorganic Chemistry*, pages 247–422. Academic Press, 1968.

[122] M. M. Matsushita and T. Sugawara. *Journal of the American Chemical Society*, 127(36):12450–12451, 2005.

[123] G. Wang, Z. Li, J. Xu, and N. Hu. *Acta Crystallographica Section E*, 63(1):m289–m291, 2007.

[124] B. Conerney, P. Jensen, P. E. Kruger, B. Moubaraki, and K. S. Murray. *CrystEngComm*, 5(80):454–458, 2003.

[125] P. S. Mukherjee, K. S. Min, A. M. Arif, and P. J. Stang. *Inorganic Chemistry*, 43(20):6345–6350, 2004.

[126] M. Maarten, A. K. Daniel, H. S. Matthew, L. B. Jessica, M. Jens, and J. L. Stephen. *Angewandte Chemie International Edition*, 40(15):2782–2807, 2001.

[127] E. Reisner, T. C. Abikoff, and S. J. Lippard. *Inorganic Chemistry*, 46(24):10229–10240, 2007.

[128] E. Y. Choi and Y. Kwon. *Inorganic Chemistry Communications*, 7(8):942–945, 2004.

[129] C. J. Connor. Magnetochemistry-Advances in theory and experimentation. In S. J. Lippard, editor, *Progress in inorganic chemistry*, page 203. Wiley-VCH, 1982.

[130] R. Georges, J. J. Borrás-Almenar, E. Coronado, J. Curély, and M. Drillon. One-dimensional magnetism: An overview of the models. In Prof Dr Marc Drillon Prof. Dr. Joel S. Miller, editor, *Magnetism: Molecules to Materials I*, pages 1–47. 2003.

[131] A. Zheludev, V. Barone, M. Bonnet, B. Delley, A. Grand, E. Ressouche, P. Rey, R. Subra, and J. Schweizer. *Journal of the American Chemical Society*, 116(5):2019–2027, 1994.

[132] A. Caneschi, J. Laugier, and P. Rey. *Journal of the Chemical Society, Perkin Transactions 1*, pages 1077–1079, 1987.

[133] D. Bordeaux, J. Lajzerowicz-Bonneteau, R. Briere, H. Lemaire, and A. Rassat. *Organic Magnetic Resonance*, 5(1):47–52, 1973.

[134] M. Minguet, D. B. Amabilino, K. Wurst, and J. Veciana. *Journal of the Chemical Society, Perkin Transactions 2*, (5):670–676, 2001.

[135] M. F. Semmelhack, C. S. Chou, and D. A. Cortes. *Journal of the American Chemical Society*, 105(13):4492–4494, 1983.

[136] C. Bätz, P. Amann, H. J. Deiseroth, and L. Dulog. *Liebigs Annalen der Chemie*, 1994(7):739–740, 1994.

[137] K. Inoue and H. Iwamura. *Chemical Physics Letters*, 207(4-6):551–554, 1993.

[138] C. Elpelt. *Modellkomplexe zur Untersuchung der Radikal-Metall-Wechselwirkung innerhalb des wasseroxidierenden Zentrums im Photosystem II*. PhD thesis, Johannes Gutenberg - Universität Mainz.

[139] M. Jung. *Magnetische Wechselwirkung Spin-Austauschgekoppelter Systeme mit Nitroxid und Nitronyl-Nitroxid Radikalen*. PhD thesis, Johannes Gutenberg - Universität Mainz.

[140] G. A. A. Saracino, A. Tedeschi, G. D'Errico, R. Improta, L. Franco, M. Ruzzi, C. Corvaia, and V. Barone. *The Journal of Physical Chemistry A*, 106(44):10700–10706, 2002.

[141] E. Ruiz, J. Cirera, and S. Alvarez. S. *Coordination Chemistry Reviews*, 249(23):2649–2660, 2005.

[142] Y. Pontillon, A. Caneschi, D. Gatteschi, A. Grand, E. Ressouche, R. Sessoli, and J. Schweizer. *Chemistry - A European Journal*, 5(12):3616–3624, 1999.

[143] M. Kaupp and F. H. Köhler. *Coordination Chemistry Reviews*, 253(19-20):2376–2386, 2009.

[144] J. Cirujeda, J. Vidal-Gancedo, O. Jürgens, F. Mota, J. J. Novoa, C. Rovira, and J. Veciana. *Journal of the American Chemical Society*, 122(46):11393–11405, 2000.

[145] A. G. Maryasov and M. K. Bowman. *Journal of Magnetic Resonance*, 179(1):120–135, 2006.

[146] C. Rancurel, D. B. Leznoff, J.-P. Sutter, S. Golhen, L. Ouahab, J. Kliava, and O. Kahn. *Inorganic Chemistry*, 38(21):4753–4758, 1999.

[147] H. Kurreck, B. Kirste, and W. Lubitz. *Angewandte Chemie International Edition*, 23(3):173–194, 1984.

[148] D. Hinderberger, R. P. Piskorski, M. Goenrich, R. K. Thauer, A. Schweiger, J. Harmer, and B. Jaun. *Angewandte Chemie International Edition*, 45(22):3602–3607, 2006.

[149] L. Angeloni, A. Caneschi, L. David, A. Fabretti, F. Ferraro, D. Gatteschi, A. le Lirzin, and R. Sessoli. *Journal of Materials Chemistry*, 4(7):1047–1053, 1994.

[150] J. S. Seo, N. Sung, R. C. Hynes, and J. Chin. *Inorganic Chemistry*, 35(26):7472–7473, 1996.

[151] F. B. Johansson, A. D. Bond, U. G. Nielsen, B. Moubaraki, K. S. Murray, K. J. Berry, J. A. Larrabee, and C. J. McKenzie. *Inorganic Chemistry*, 47(12):5079–5092, 2008.

[152] L. Gattermann, H. Wieland, T. Wieland, and W. Sucrow. *Die Praxis des organischen Chemikers*. W. de Gruyter, Berlin, New York, 1982.

[153] R. Sayre. *Journal of the American Chemical Society*, 77(24):6689–6690, 1955.

[154] S. Shimono, R. Tamura, N. Ikuma, T. Takimoto, N. Kawame, O. Tamada, N. Sakai, H. Matsuura, and J. Yamauchi. *The Journal of Organic Chemistry*, 69(2):475–481, 2003.

[155] A. K. Hoffmann and W. M. Thomas. *Journal of the American Chemical Society*, 81(3):580–582, 1959.

[156] C. Hirel, K. E. Vostrikova, J. Pécaut, V. I. Ovcharenko, and P. Rey. *Chemistry*, 7(9):2007–2014, 2001.

[157] J. T. Randolph, P. P. Huang, W. J. Flosi, D. DeGoey, L. L. Klein, C. M. Yeung, C. Flentge, M. Sun, C. Zhao, T. Dekhtyar, H. Mo, L. Colletti, W. Kati, K. C. Marsh, A. Molla, and D. J. Kempf. *Bioorganic and Medicinal Chemistry*, 14(12):4035–4046, 2006.

[158] Q. Zhou and P. Yang. *Inorganica Chimica Acta*, 359(4):1200–1206, 2006.

[159] D. R. Chapman and C. A. Reed. *Tetrahedron Letters*, 29(25):3033–3036, 1988.

Acknowledgement

I am heartily thankful to my supervisor, Prof. Dr. E. R., whose encouragement and support from the initial to the final level enabled me to develop an understanding of molecular magnetic materials. I really liked her trustful management of the working group in general, what promoted strongly my personal developement.

Further I would like to thank my second supervisor, Prof. Dr. H. J. E., for opening my views on research and for the transmission of theoretical knowledge.

I am grateful to Prof. K. A., who allowed me to spent three months in his research lab in Nagoya, Japan. Aside from the new measurement techniques, I also learned personally a lot of his open-minded manner.

I am indebted to my collaboration partners, Dr. Y. A. and Dr. D. H. from the Max-Planck Institute of Polmer Science, Mainz for the EPR measurements, Dr. U. S. from the Ruhr University, Bochum for the DFT calculations and finally T. G. and Dr. V. K., University of Mainz, for the pressure dependent studies.

It is a pleasure to thank all people working with me in the lab, especially Dr. P. A. (for his attitude), Dr. M. J. and Dr. C. E. (for their inspiring work on nitronyl-nitroxide radicals), F. R. (for spending his whole "university life" with me), M. J. (not only for the time in Japan) and Dr. L. C. (for all scientific and non-scientific discussions). Thanks to the alumni of the group (F. B., T. M. and S. W.) as well as the actual members of the group (Dr. M. S., Dr. D. D., C. D., J. K., J. O., P. H., C. P., D. H., I. A. and N. S.), the working atmosphere was all the time good.

I would like to show my gratitude to R. J.-P., Dr. D. S. and Dr. M. P. for the help with the X-ray crystal structures as well as Dr. L. M. for measuring ESI spectra. Dr. F. F. is acknowledged for his LaTEXnical support and the layout of this thesis. Thanks to T. D. and his physics colleagues for the help with the MATHEMATICA program.

Furthermore, I would like to thank the Graduate School of Excellence "Material Science in Mainz (MAINZ)" for the financial support of this thesis and for the possibilities offered by the program. It was a pleasure to be a part of the MATCOR class with all the amazing members. A special thank to the MAINZ office in person of S. J. and Dr. M. B..

Thanks to my friends, who remind me sometimes that research is important, but not everything.

This thesis would not have been possible unless the support, trust and love of my family.

Last, but not least I want to thank my boyfriend F. D. for his manifold support, his patience and his love.

Appendix

A Simulation of the Magnetic Susceptibility

A.1 JulX

The program julX written by E. Bill was used for the simulation and analysis of magnetic susceptibiltiy data[1]. JulX is designed as an easy-to use and self-contained spin-Hamiltonian program for the visualization and simulation of magnetic susceptibility data from powder samples or frozen solutions of small molecular systems with up to four coupled spins with local multiplicities up to $S_i = 5/2$. JulX is based on a full matrix diagonalisation and energies are calaculated using following Hamiltonian $\hat{H}$ with $\hat{H}_{ex}$ (exchange operator), $\hat{H}_{ZFS}$ (zero-field splitting operator) and $\hat{H}_{Zee}$ (Zeeman operator):

$$\hat{H} = \hat{H}_{ex} + \hat{H}_{ZFS} + \hat{H}_{Zee} \tag{5.1}$$

$$\hat{H}_{ex} = -2\sum_{i,j} J_{i,j}\vec{S}_i\vec{S}_j \tag{5.2}$$

$$\hat{H}_{ZFS} = \sum_i D_i \left[S_{z,i}^2 - \frac{1}{3}S_i(S_i+1) + \frac{E_i}{D_i}(S_{x,i}^2 - S_{y,i}^2) \right] \tag{5.3}$$

$$\hat{H}_{Zee} = \sum_i g\beta\vec{S}_i \cdot \vec{B} \tag{5.4}$$

Due to the full matrix diagonalisation realised in JulX, the calculating time is long and only four spin centres with a maximum spin of 5/2 can be taken into account.

A.2 Routines based on MATHEMATICA

For the simulation of high-spin cobalt(II) compounds, routines based on MATHEMATICA 6 developed by Lloret et al.[2] are used. In the limit of weak magnetic coupling compared to spin-orbit coupling it is possible to describe the magnetic properties of six-coordinated high-spin cobalt(II) compounds with an empirical expression. An axial distortion is taken into account, so that the variable parameters are Δ (axial distortion parameter: 0-1000 cm^{-1}), α (orbital reduction factor: 0.75-1.5) and λ (spin-orbit coupling: 90-180 cm^{-1}). Furthermore the magnetic coupling J is incorporated by a perturbational approach, so that the magnetic susceptibility in the whole temperature range can be described as a function of J,

[1] http://ewww.mpi-muelheim.mpg.de/bac/logins/bill/julX en.php
[2] Inorganica Chimica Acta, 361, 12-13, 3432-3445, 2008

Δ, α and λ. The calculation of the magnetic susceptibility of a polynuclear compound requires the treatment of each cobalt(II) ion as a spin doublet S=1/2 with a value of the Lande factor g described by an empirical expression G(T,J). For many compounds like dimers, high-nucearity complexes, one-dimensional chains or two-dimensional layered sytems analytical expressions are known in case of local spin doublets. Then the Lande factor g has to be replaced by the G(T,J) function and the spin value by an effective spin of 1/2, so that these expressions can also be applied on cobalt(II) compounds.

Dimer

$$\chi_m[T] = \frac{N_A\beta^2}{3kT}(G[T])^2 F_{dim}[T] \tag{5.5}$$

$$G[T] = g[T] + \frac{\delta g P_0[T]}{2} \tag{5.6}$$

$$g[T] = \frac{\sum_{k=0}^{4}(\prod_{j=1}^{3}(\sum_{i=0}^{2} A_{i,j,k}x_j^i))T^k}{\sum_{k=0}^{4}(\prod_{j=1}^{3}(\sum_{i=0}^{2} B_{i,j,k}x_j^i))T^k} \tag{5.7}$$

$$\delta g = \frac{-100J}{81\alpha\lambda} + (\alpha+2) \tag{5.8}$$

$$P_0[T] = \frac{exp(\frac{-4\alpha\lambda}{k_1 T})}{3+2exp(\frac{-5\alpha\lambda}{2k_1 T} + exp\frac{-4\alpha\lambda}{k_1 T})} \tag{5.9}$$

$$F_{dim}[T] = \frac{6}{3+exp(\frac{-25J}{9k-1T})} \tag{5.10}$$

with N_A = 6.02213*10^{23}, β = 9.27402*10^{-21}
k = 1.38066*10^{-16}, k_1 = 0.6950387 cm^{-1}
$x_1 = \alpha$, $x_2 = \Delta$, $x_3 = \lambda$

2D Heisenberg Lattice

$$\chi_m[T] = \frac{9Q}{25J}(G[T])^2 F_{dim}[T] \tag{5.11}$$

$$G[T] = g[T] + \frac{\delta g P_0[T]}{2} \tag{5.12}$$

$$g[T] = \frac{\sum_{k=0}^{4}(\prod_{j=1}^{3}(\sum_{i=0}^{2} A_{i,j,k}x_j^i))T^k}{\sum_{k=0}^{4}(\prod_{j=1}^{3}(\sum_{i=0}^{2} B_{i,j,k}x_j^i))T^k} \tag{5.13}$$

$$\tag{5.14}$$

$$\delta g = \frac{-100J}{81\alpha\lambda} + (\alpha + 2) \tag{5.15}$$

$$P_0[T] = \frac{exp(\frac{-4\alpha\lambda}{k_1 T})}{3 + 2exp(\frac{-5\alpha\lambda}{2k_1 T} + exp\frac{-4\alpha\lambda}{k_1 T})} \tag{5.16}$$

$$F_{dim}[T] = (3\Theta[T] + \sum_{n=1}^{6} \frac{C_n}{\Theta[T]^{n-1}})^{-1} \tag{5.17}$$

$$\Theta[T] = \frac{12k_1 T}{25J} \tag{5.18}$$

with Q = 0.260741683, k_1 = 0.6950387 cm^{-1}

$x_1 = \alpha$, $x_2 = \Delta$, $x_3 = \lambda$

$C_1 = 4$, $C_2 = 2.667$, $C_3 = 1.185$

$C_4 = 0.149$, $C_5 = -0.191$, $C_6 = 0.001$

B NMR spectra

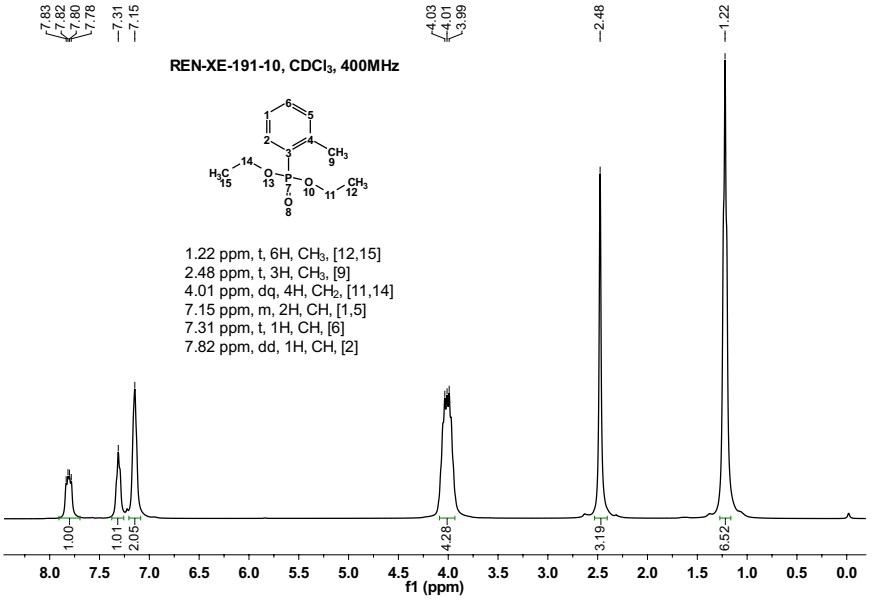

Figure 5.7: ^{1}H-NMR spectra of 2-Tolyl-phosphonic acid diethyl ester **(1a)**

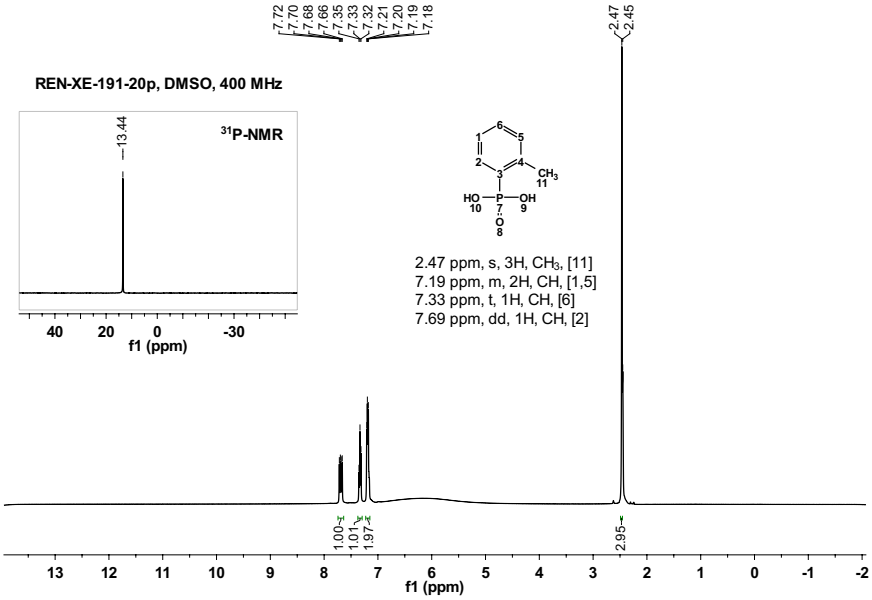

Figure 5.8: ^{1}H-NMR spectra and ^{31}P-NMR of 2-Tolyl-phosphonic acid **(2a)**

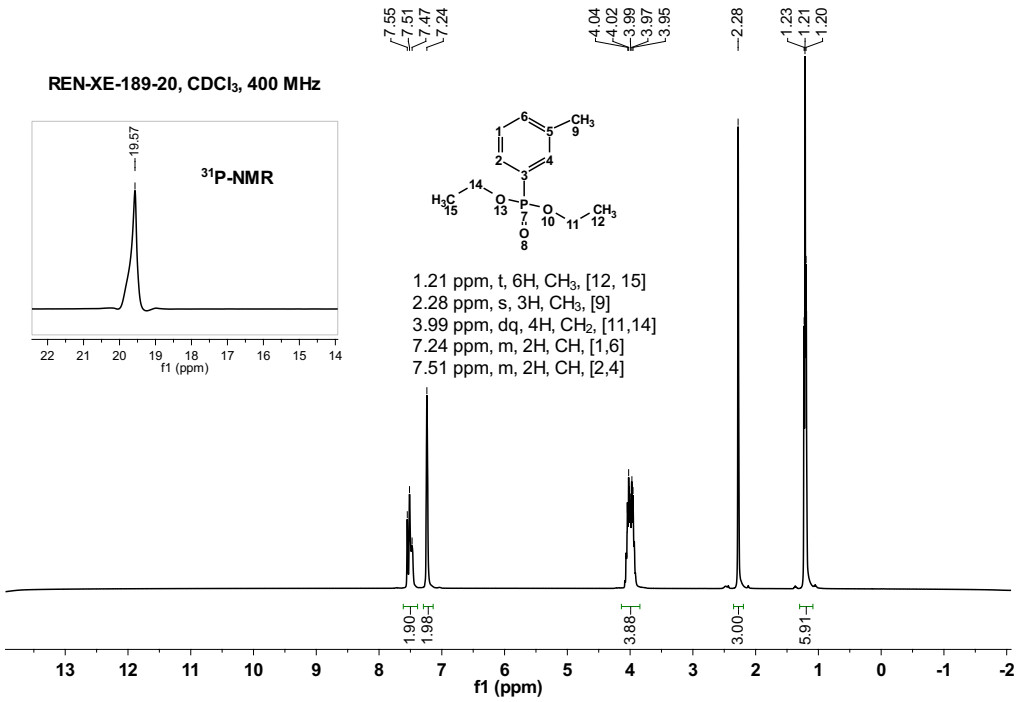

Figure 5.9: ^{1}H-NMR and ^{31}P-NMR spectra of 3-Tolyl-phosphonic acid diethyl ester **(1b)**

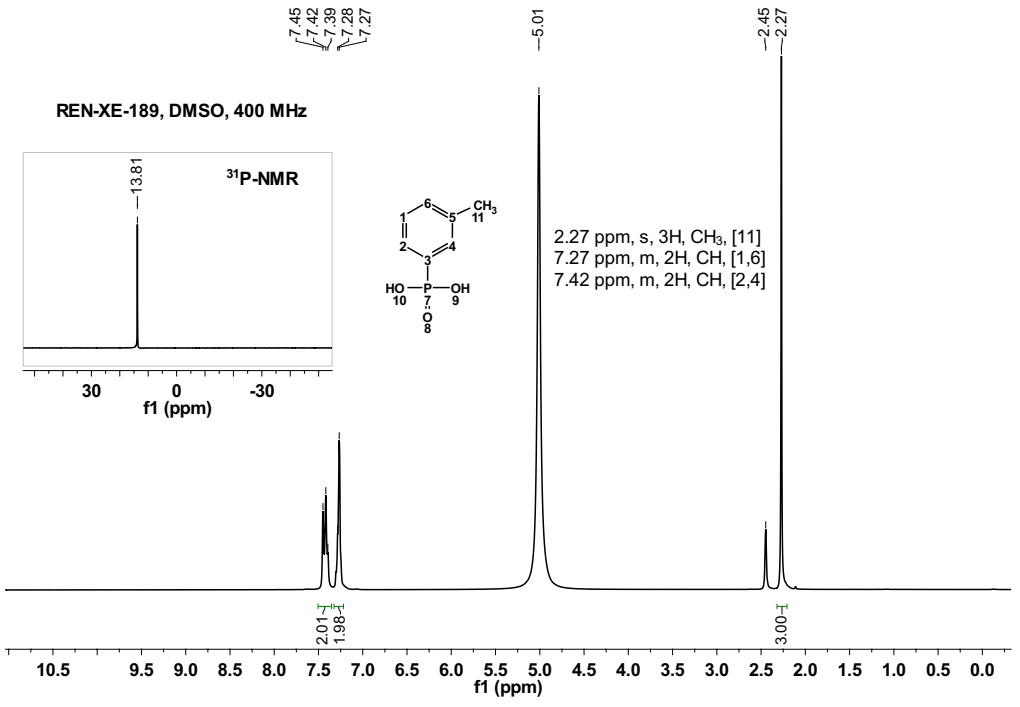

Figure 5.10: ^{1}H-NMR and ^{31}P-NMR spectra of 3-Tolyl-phosphonic acid **(2b)**

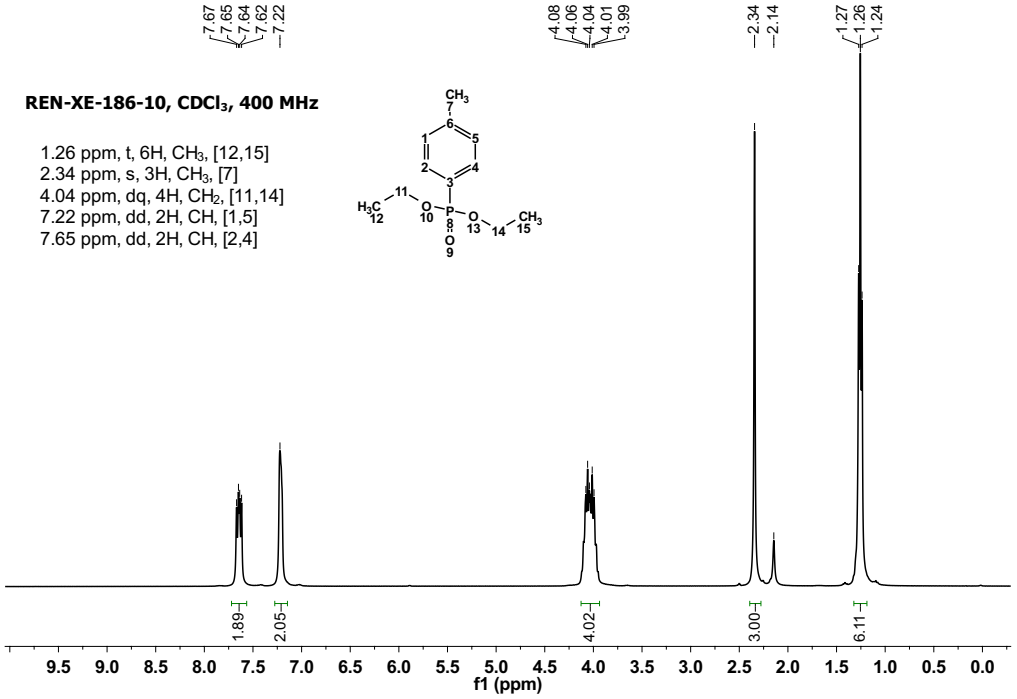

Figure 5.11: [1]H-NMR spectra of 4-Tolyl-phosphonic acid diethyl ester **(1c)**

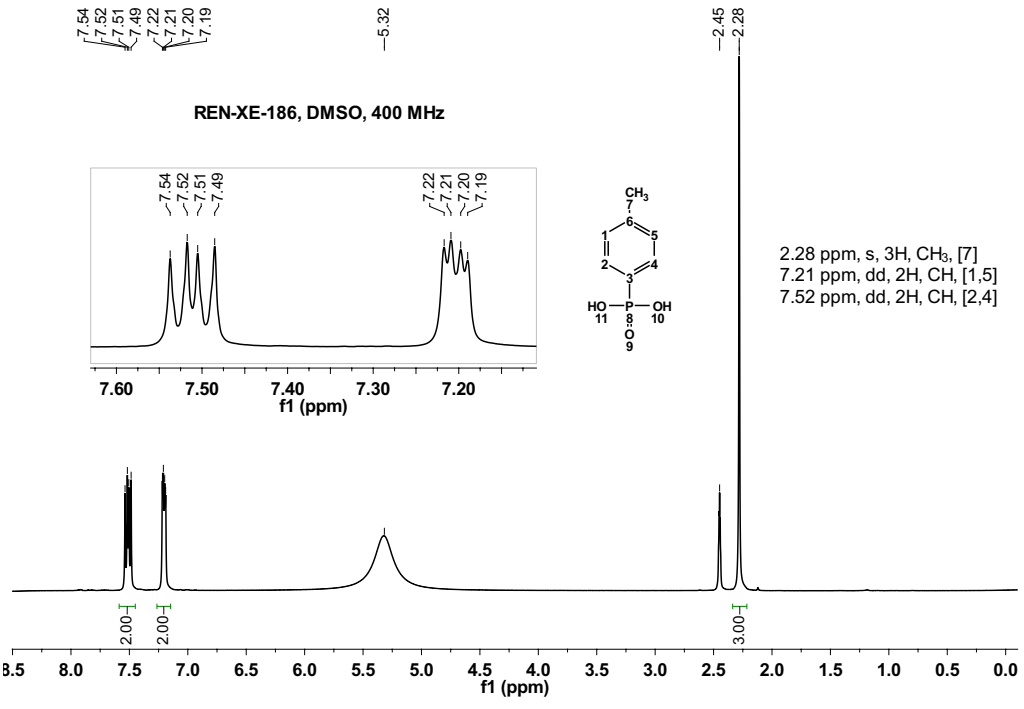

Figure 5.12: [1]H-NMR spectra of 4-Tolyl-phosphonic acid **(2c)**

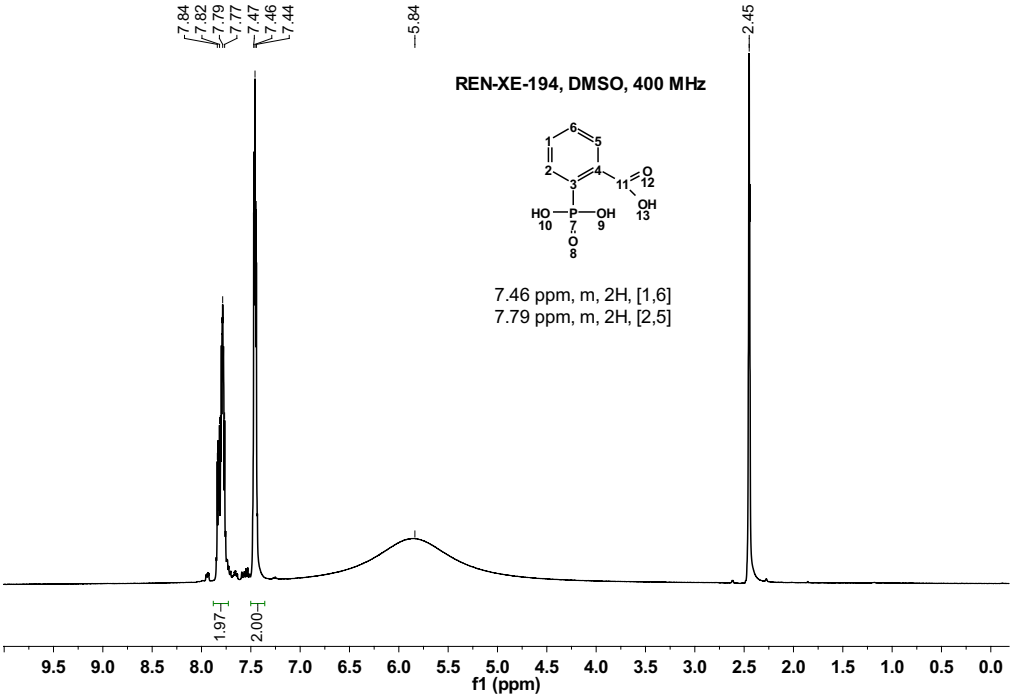

Figure 5.13: ^{1}H-NMR spectra of 2-Phosphono benzoic acid **(3a)**

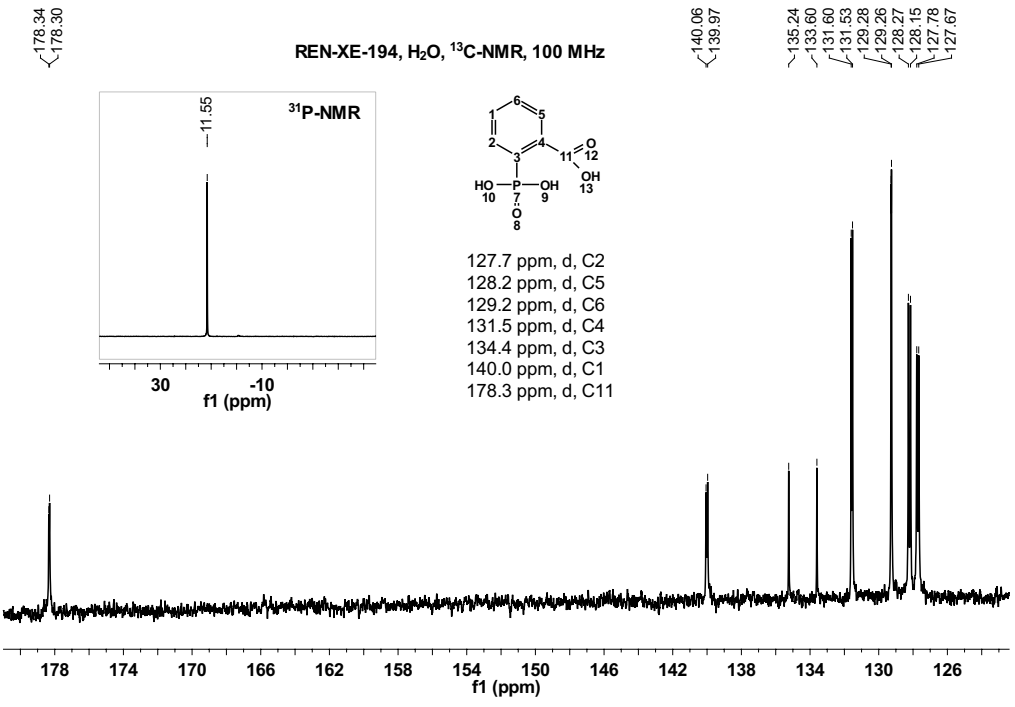

Figure 5.14: ^{13}C-NMR and ^{31}P-NMR spectra of 2-Phosphono benzoic acid **(3a)**

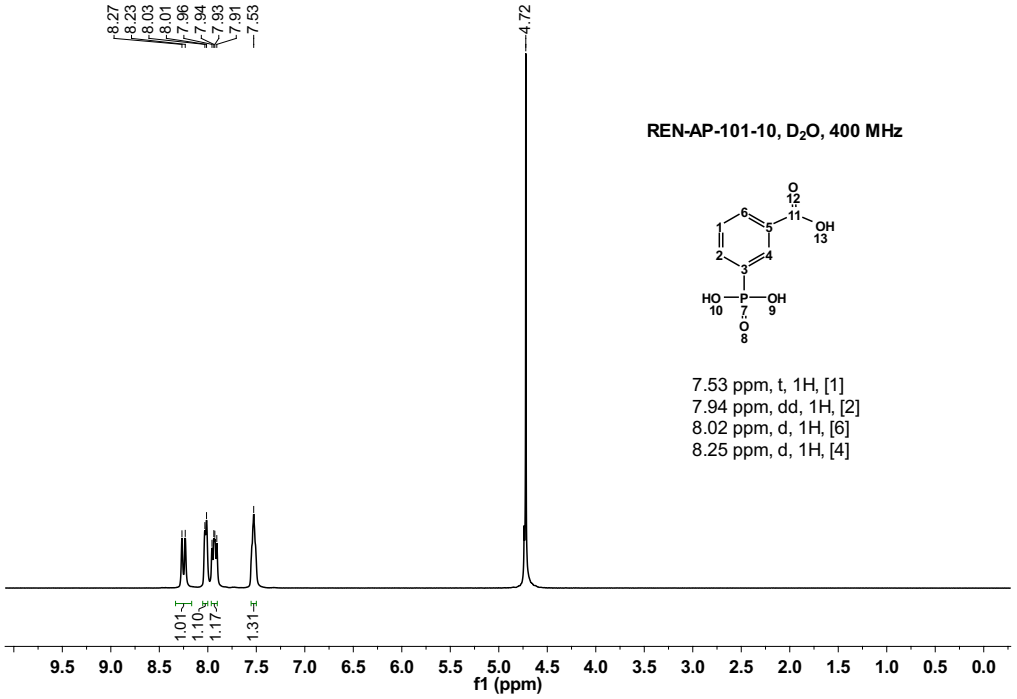

Figure 5.15: ^{1}H-NMR spectra of 3-Phosphono benzoic acid **(3b)**

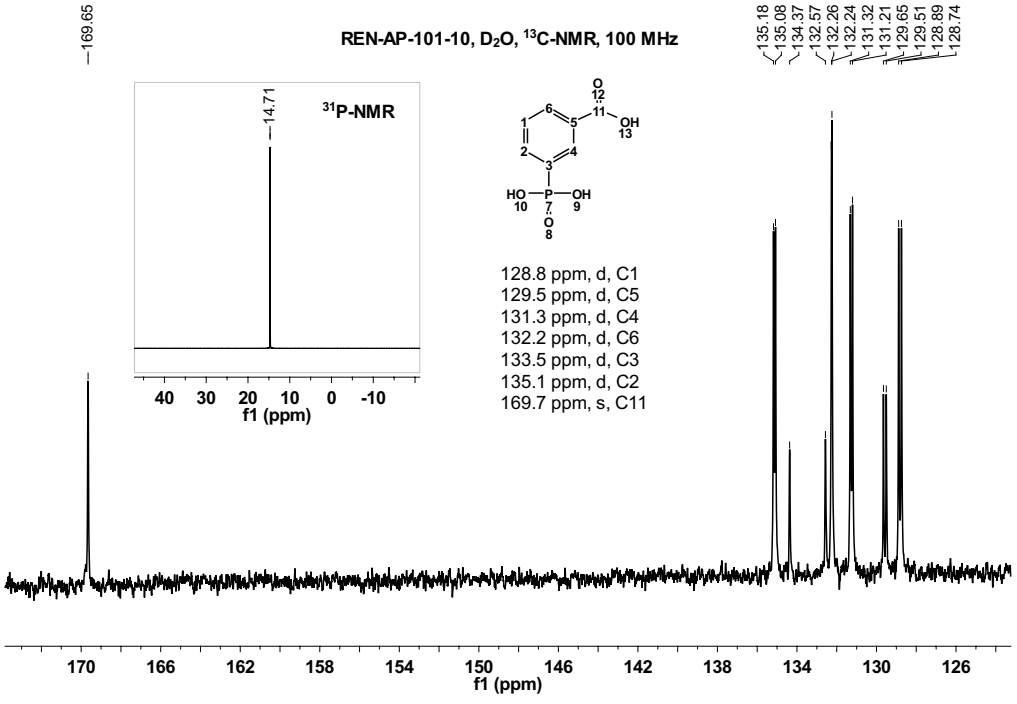

Figure 5.16: ^{13}C-NMR and ^{31}P-NMR spectra of 3-Phosphono benzoic acid **(3b)**

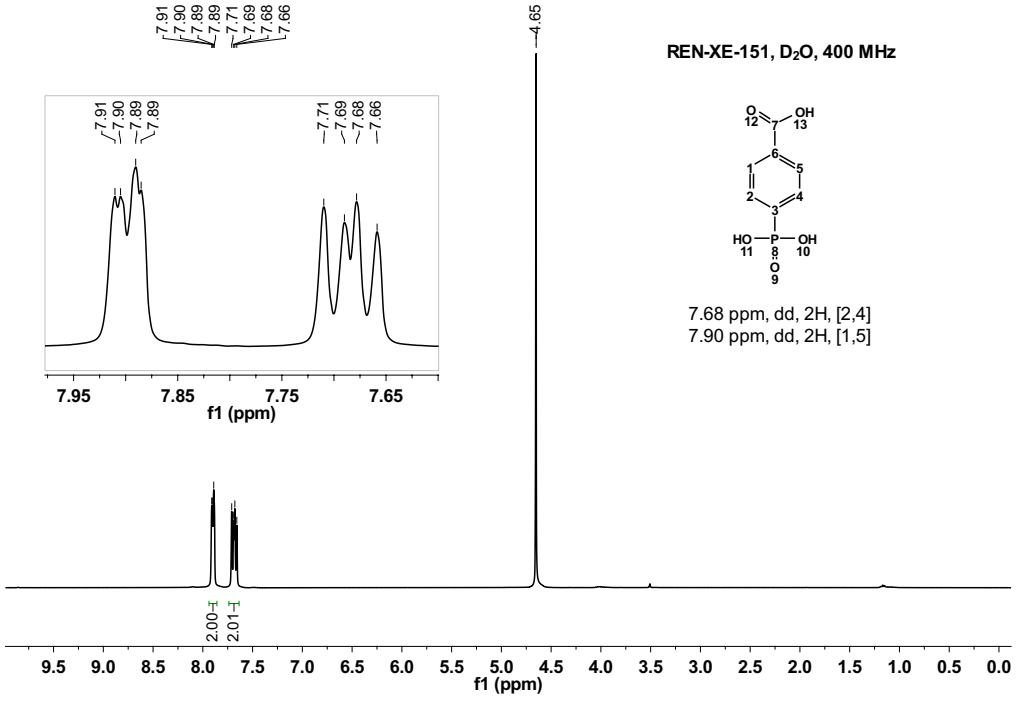

Figure 5.17: ^{1}H-NMR spectra of 4-Phosphono benzoic acid **(3c)**

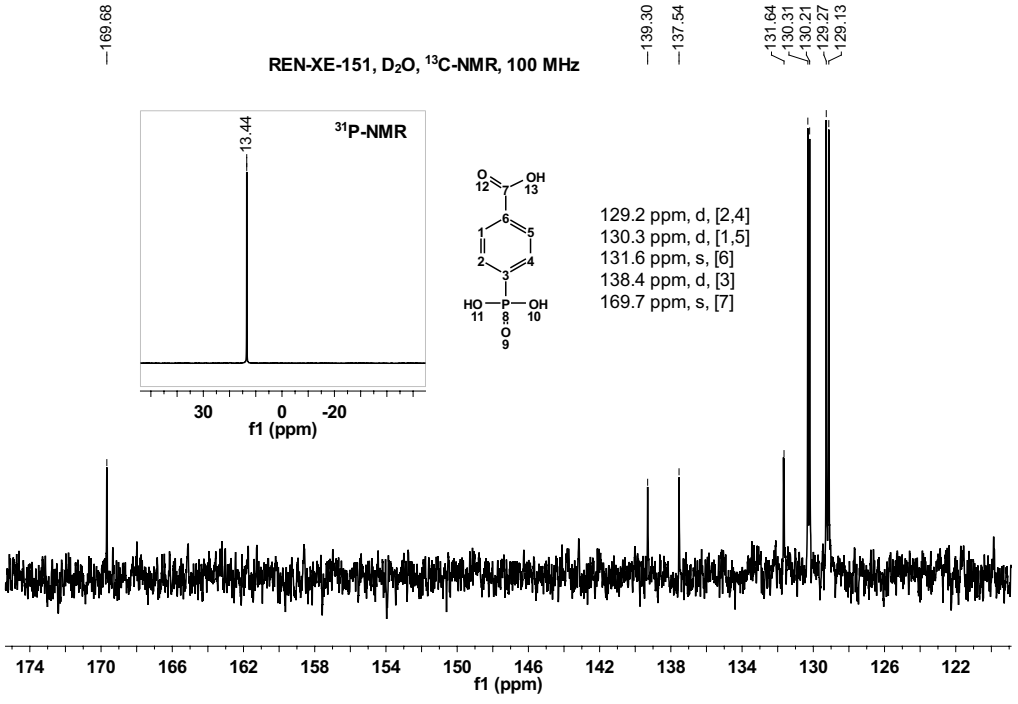

Figure 5.18: ^{13}C-NMR and ^{31}P-NMR spectra of 4-Phosphono benzoic acid **(3c)**

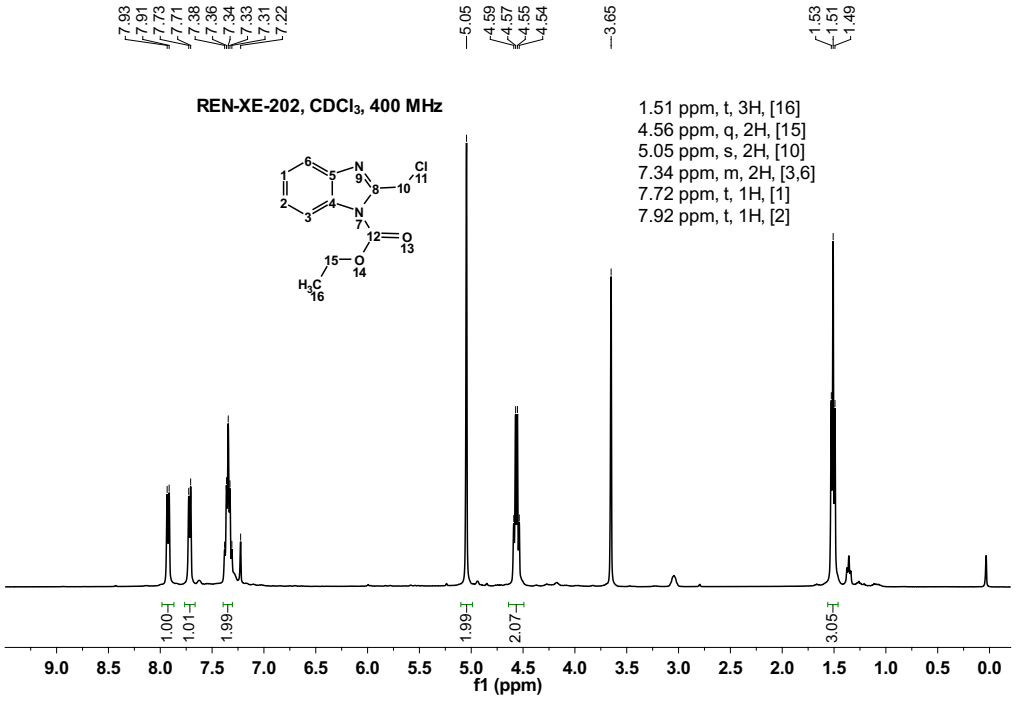

Figure 5.19: [1]H-NMR spectra of 1-Carboethoxy-2-chloromethylbenzimidazole **(4)**

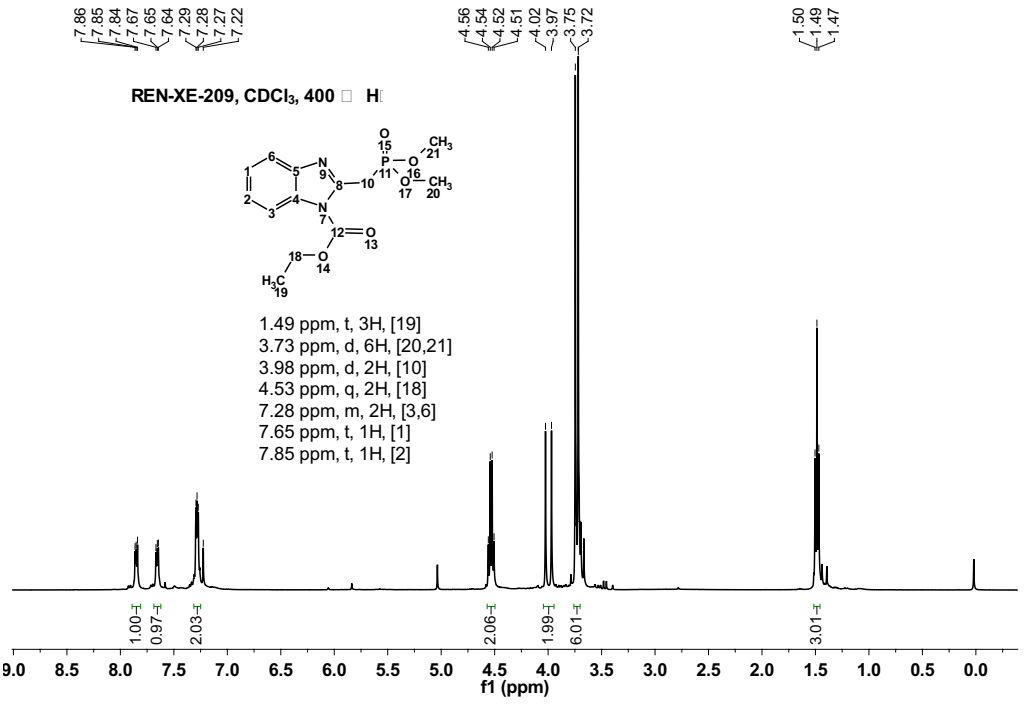

Figure 5.20: [1]H-NMR spectra of 1-Carboethoxy-benzimidazol-2-yl-methyl)phosphonic acid dimethyl ester **(5)**

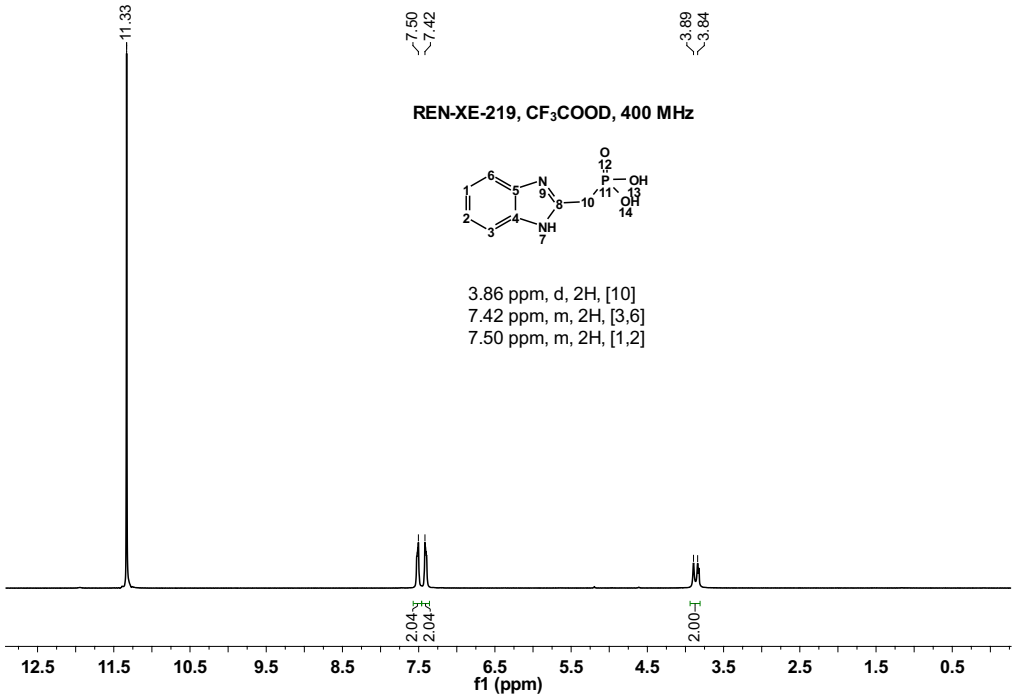

Figure 5.21: ^{1}H-NMR spectra of 1H-Benzimidazol-2-yl-methyl)phosphonic acid **(6)**

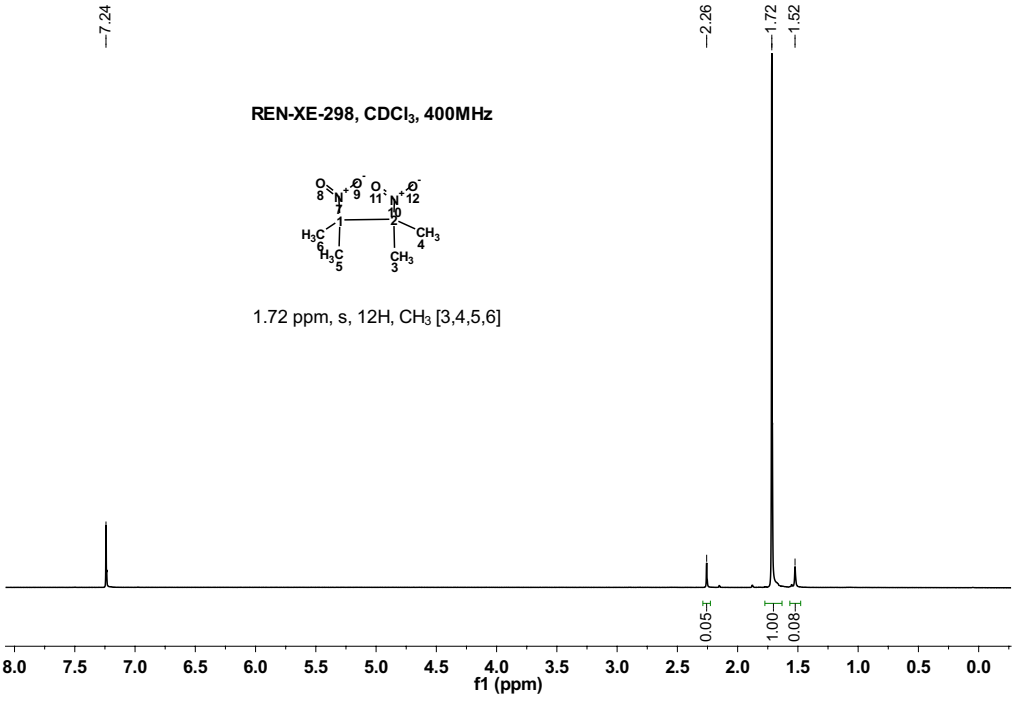

Figure 5.22: ^{1}H-NMR spectra of 2,3-Dimethyl-2,3-dinitrobutane **(21)**

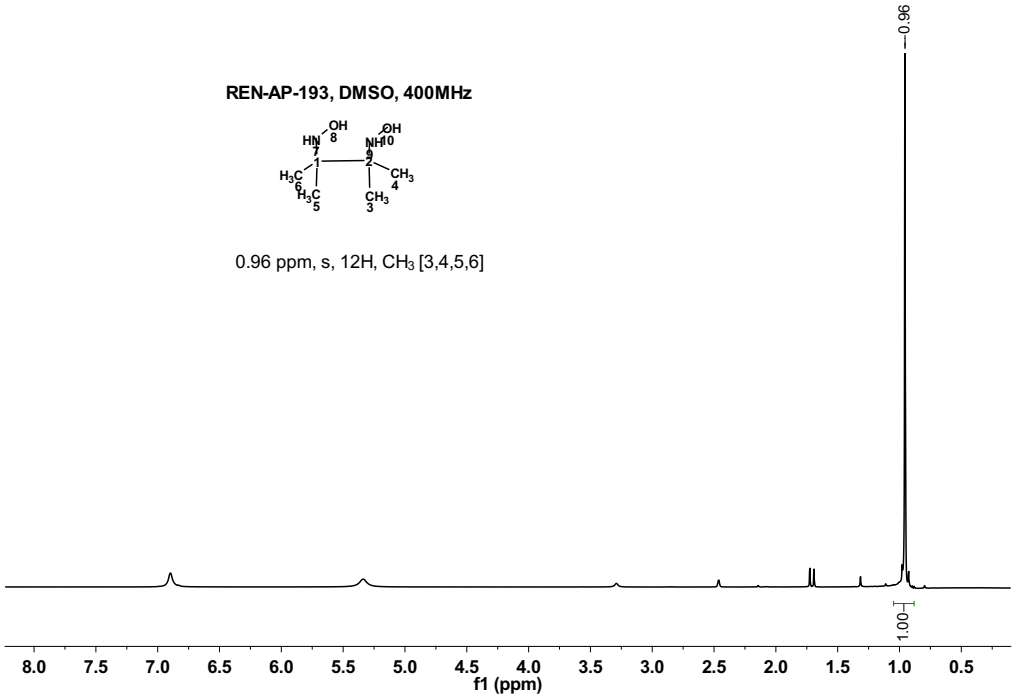

Figure 5.23: ^{1}H-NMR spectra of 2,3-Bis(hydroxylamine)-2,3-dimethylbutane **(22)**

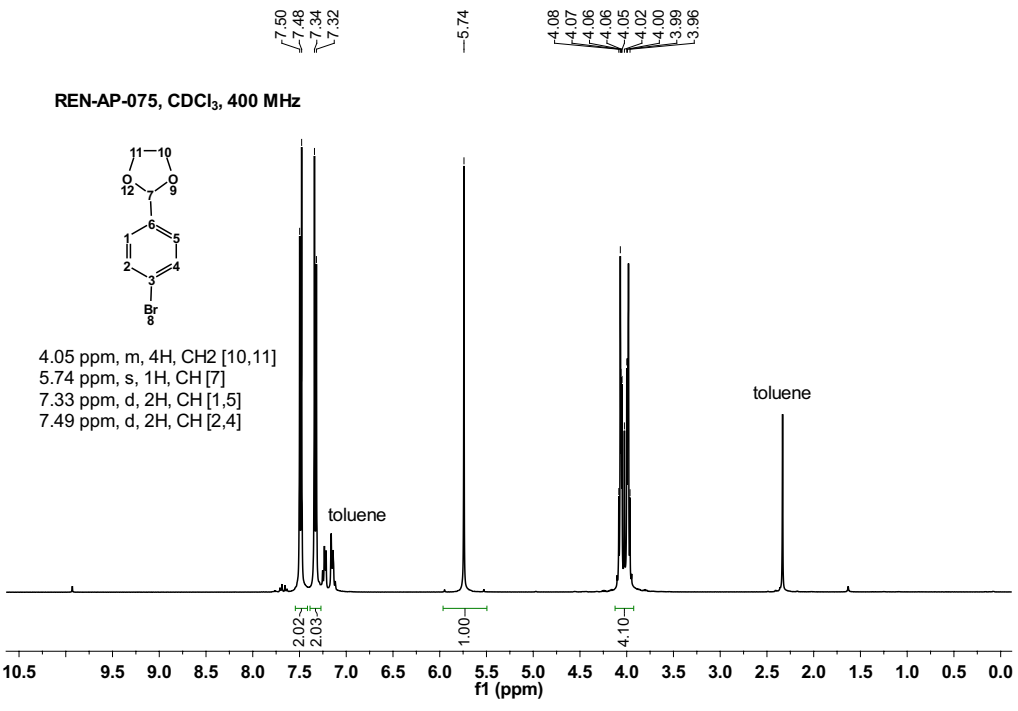

Figure 5.24: ^{1}H-NMR spectra of 2-(4-Bromo-phenyl)-[1,3]dioxolane **(23a)**

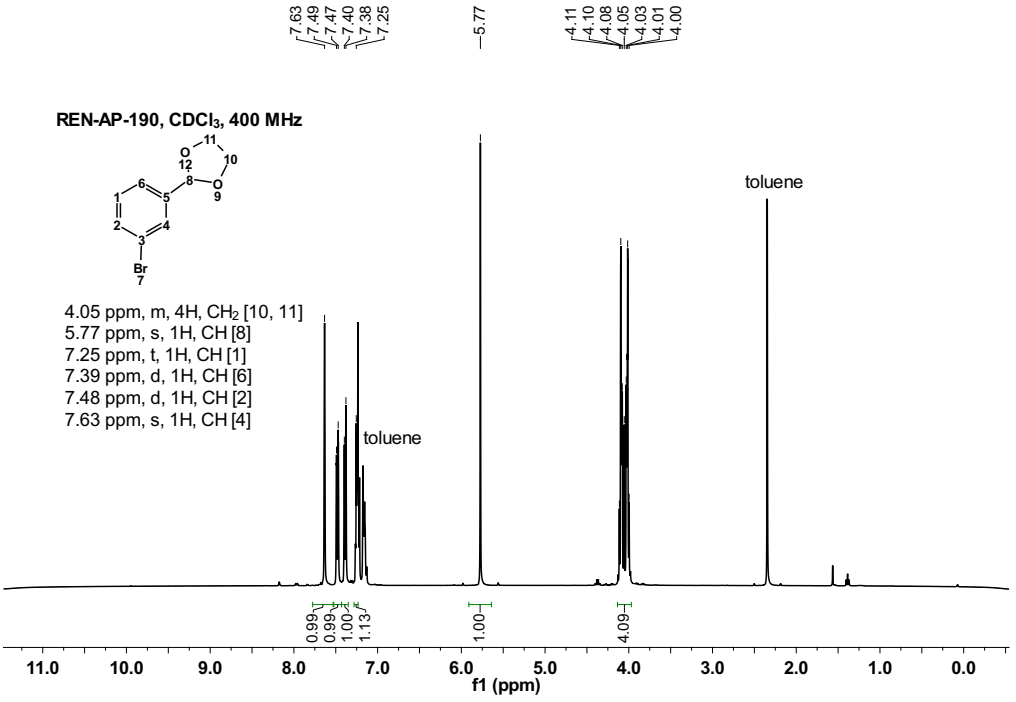

Figure 5.25: ^{1}H-NMR spectra of 2-(3-Bromo-phenyl)-[1,3]dioxolane **(23b)**

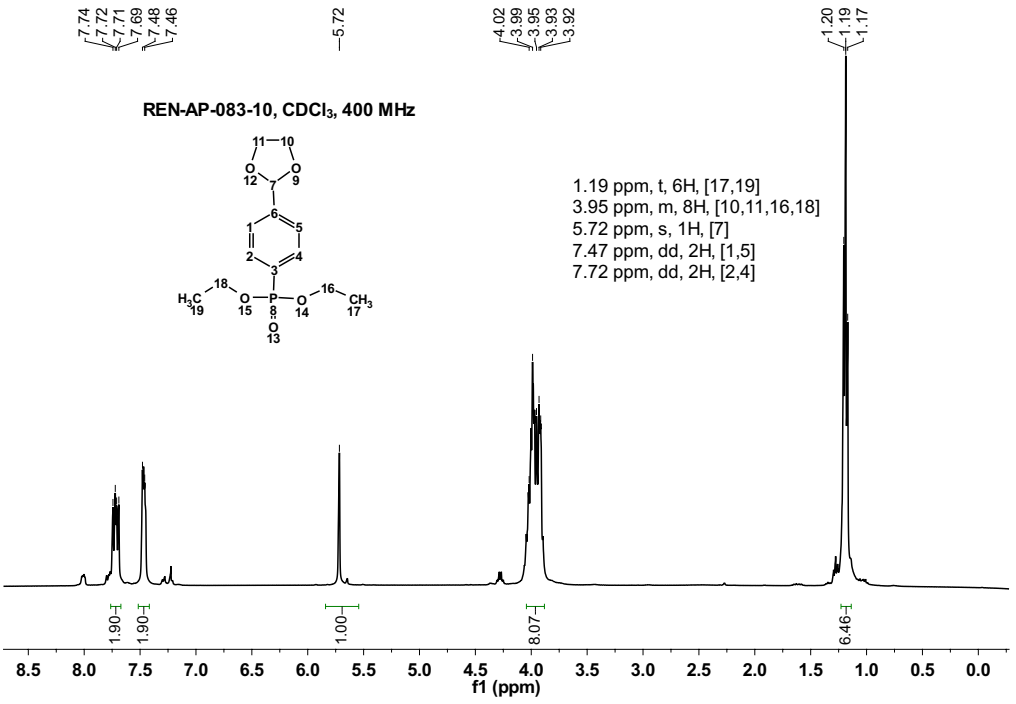

Figure 5.26: ^{1}H-NMR spectra of (4-[1,3]Dioxolan-2-yl-phenyl)-phosphonic acid diethyl ester **(24a)**

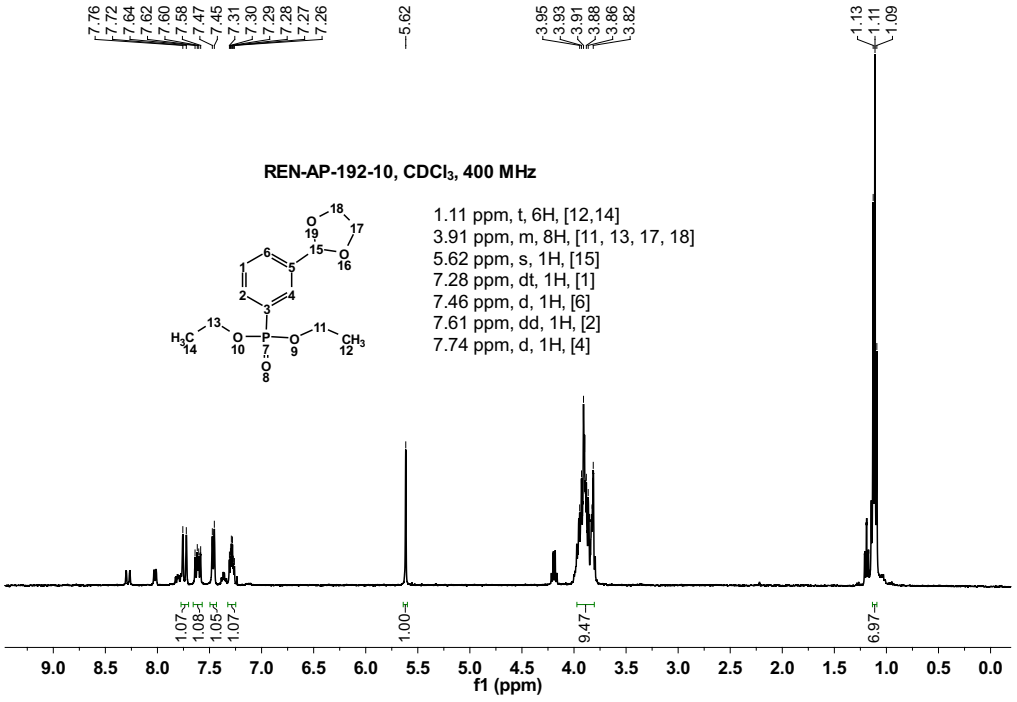

Figure 5.27: ^{1}H-NMR spectra of (3-[1,3]Dioxolan-2-yl-phenyl)-phosphonic acid diethyl ester **(24b)**

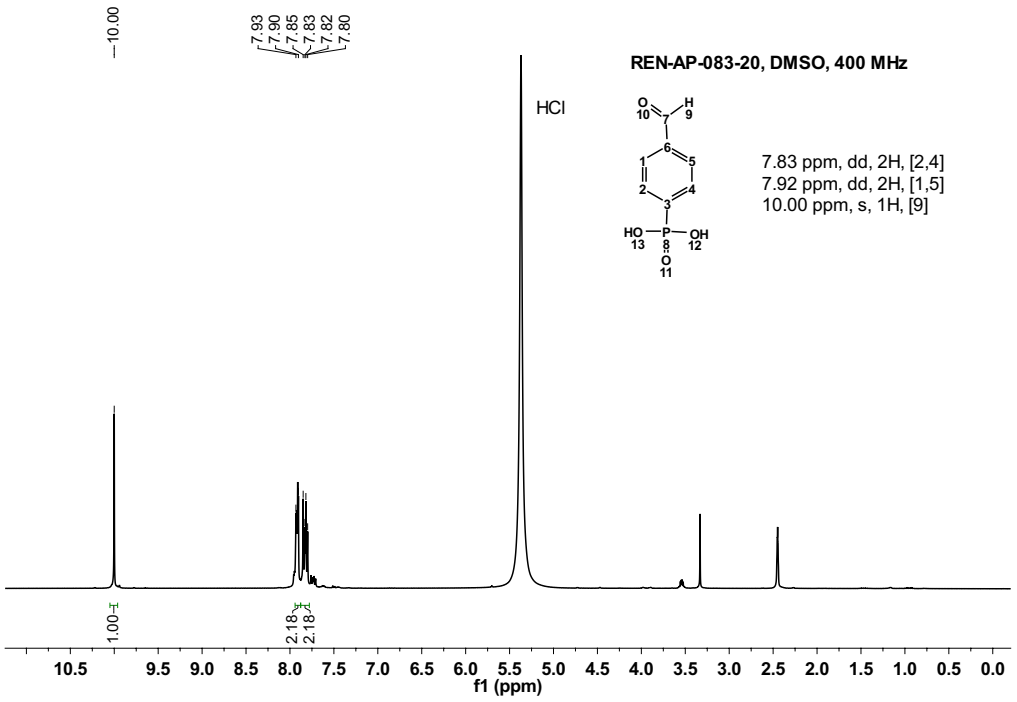

Figure 5.28: ^{1}H-NMR spectra of (4-Formyl-phenyl)-phosphonic acid **(25a)**

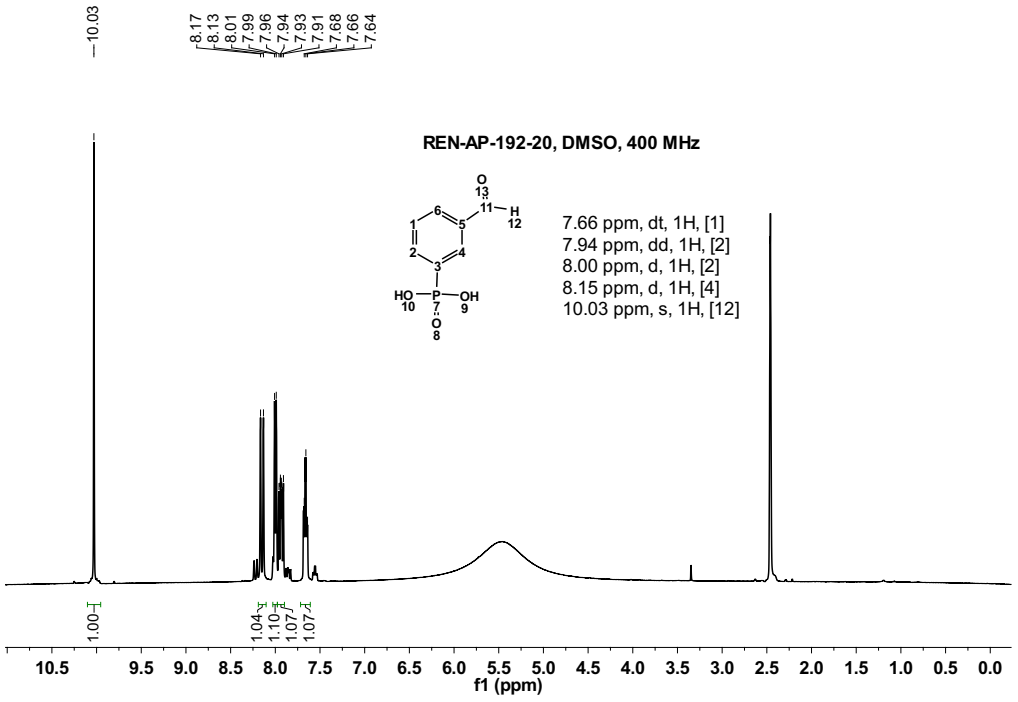

Figure 5.29: ^{1}H-NMR spectra of (3-Formyl-phenyl)-phosphonic acid **(25b)**

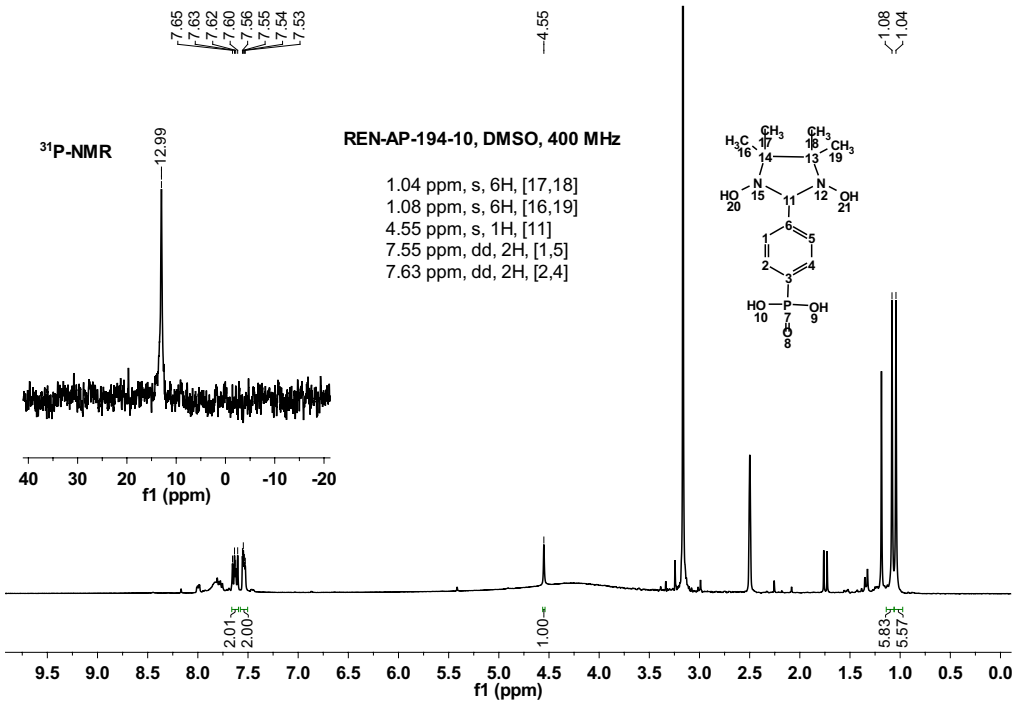

Figure 5.30: ^{1}H-NMR and ^{31}P-NMR spectra of [4-(1,3-Dihydroxy-4,4,5,5-tetramethyl-imidazolidin-2-yl)-phenyl]-phosphonic acid **(26a)**

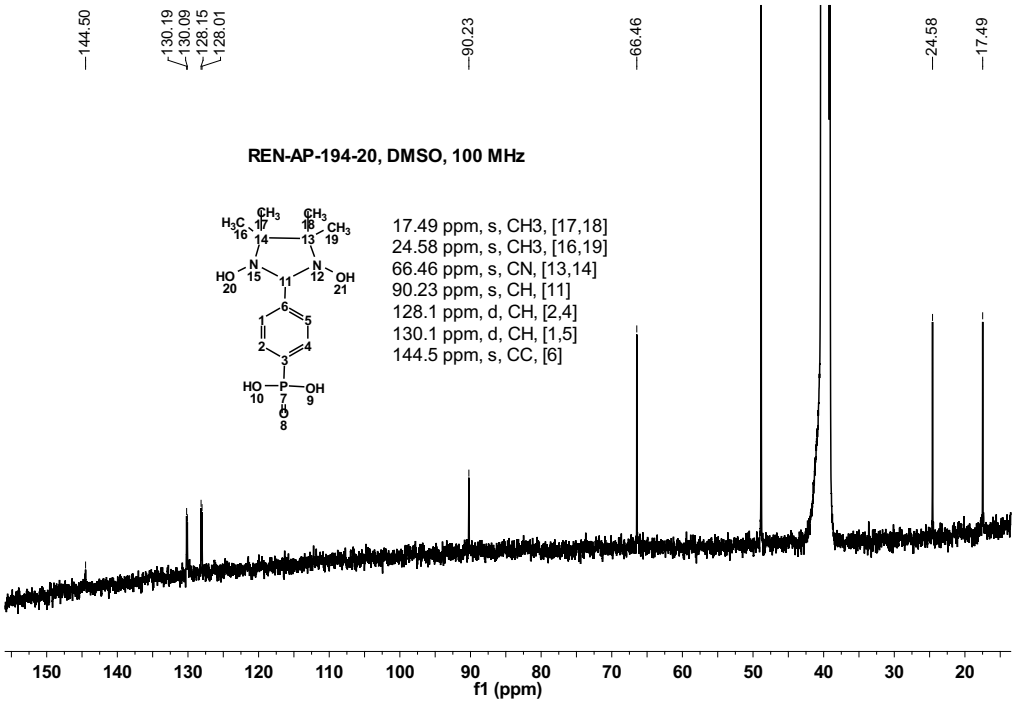

Figure 5.31: ^{13}C-NMR spectra of [4-(1,3-Dihydroxy-4,4,5,5-tetramethyl-imidazolidin-2-yl)-phenyl]-phosphonic acid **(26a)**

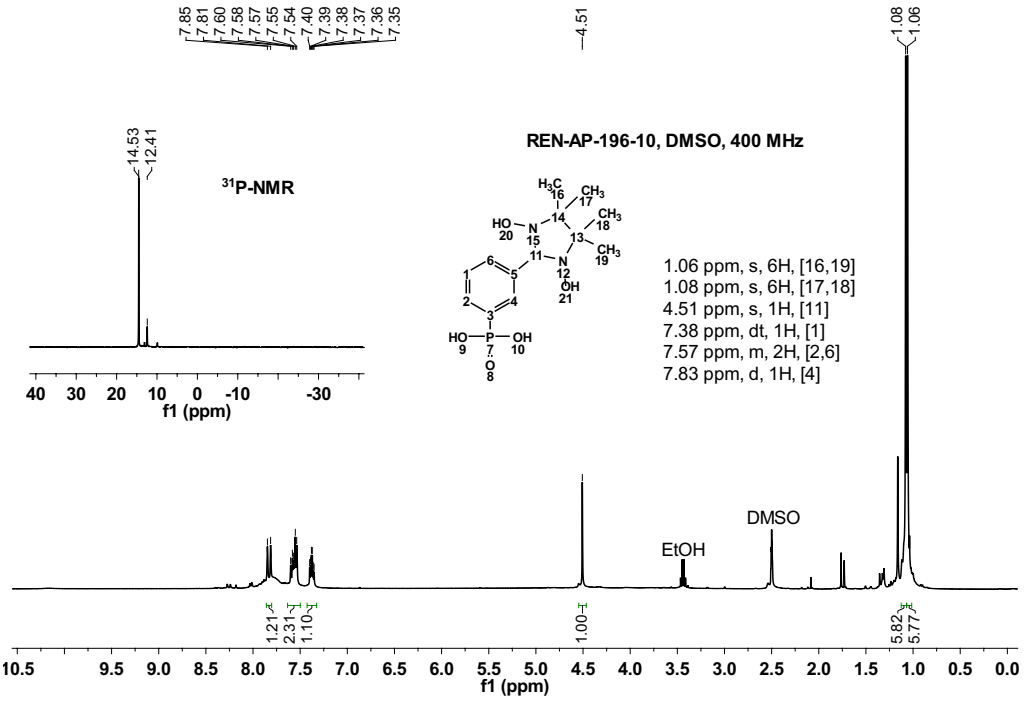

Figure 5.32: ^{1}H-NMR and ^{31}P-NMR spectra of [3-(1,3-Dihydroxy-4,4,5,5-tetramethyl-imidazolidin-2-yl)-phenyl]-phosphonic acid **(26b)**

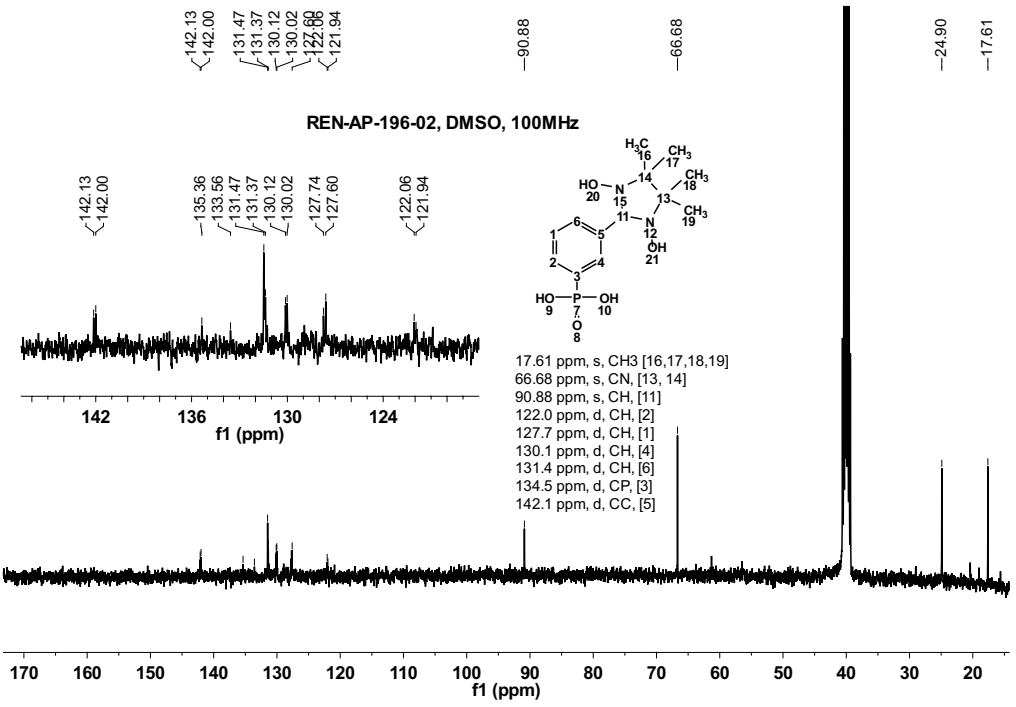

Figure 5.33: ^{13}C-NMR spectra of [3-(1,3-Dihydroxy-4,4,5,5-tetramethyl-imidazolidin-2-yl)-phenyl]-phosphonic acid **(26b)**

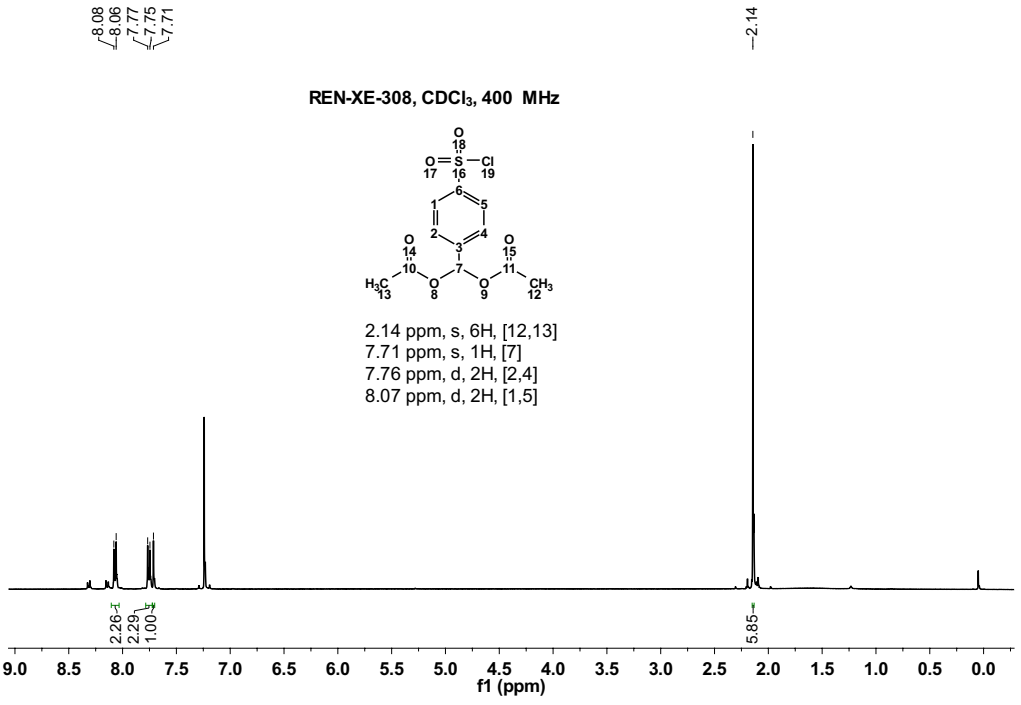

Figure 5.34: ^{1}H-NMR spectra of 4-(Diacetoxymethyl)benzenesulfonic acid chloride **(29)**

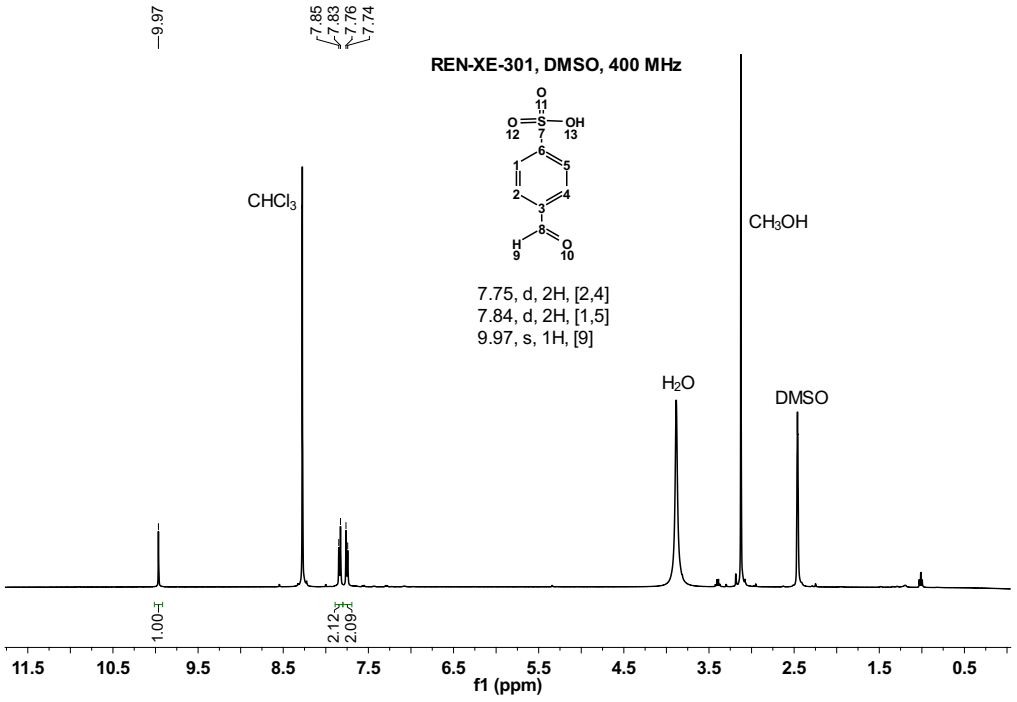

Figure 5.35: [1]H-NMR spectra of 4-(Formyl)benzenesulfonic acid **(31)**

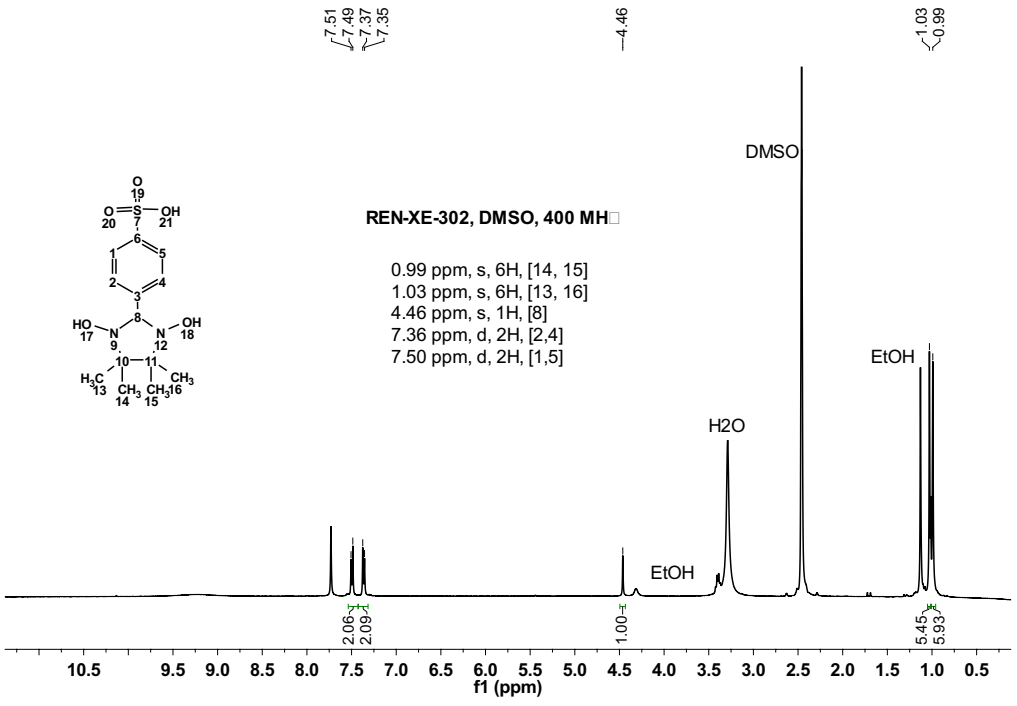

Figure 5.36: [1]H-NMR spectra of 4-(1,3-Dihydroxy-4,4,5,5-tetramethyl-imidazolidin-2-yl)-benzenesulfonic acid **(32)**

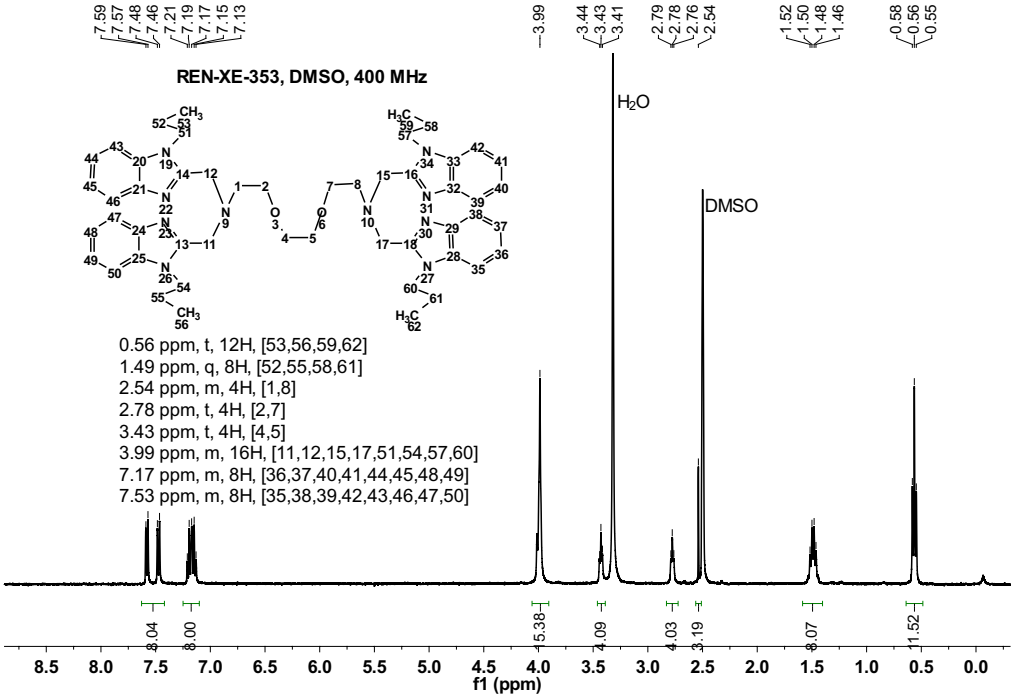

Figure 5.37: ^{1}H-NMR spectra of ^{Pr}EPTG **(36)**

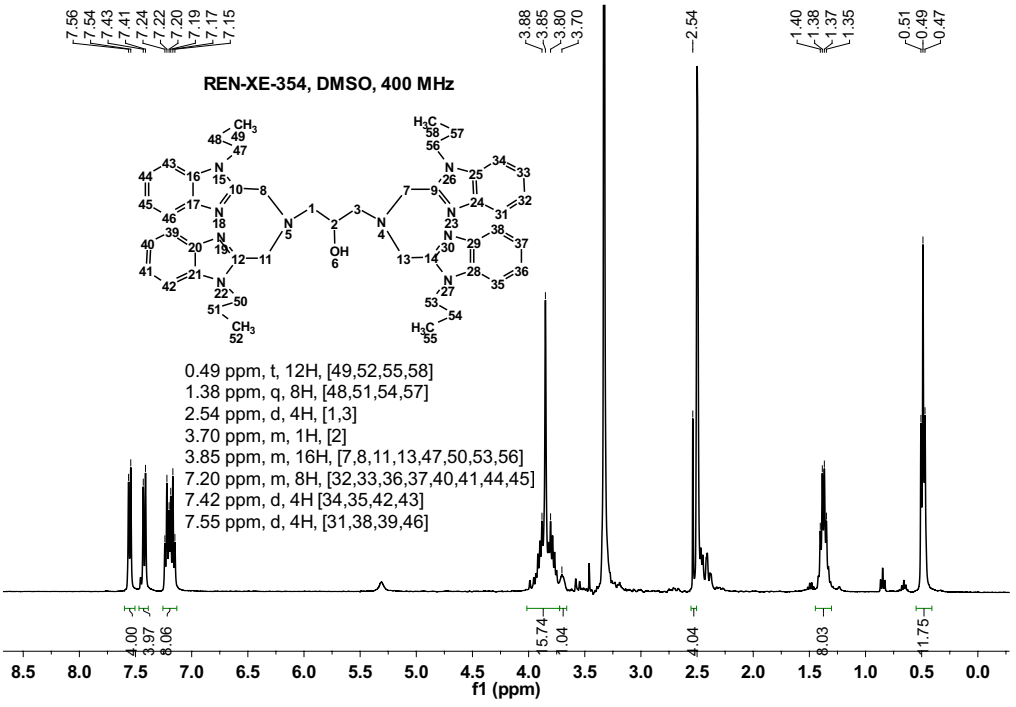

Figure 5.38: ^{1}H-NMR spectra of ^{Pr}HPTB **(38)**

C Infrared spectra

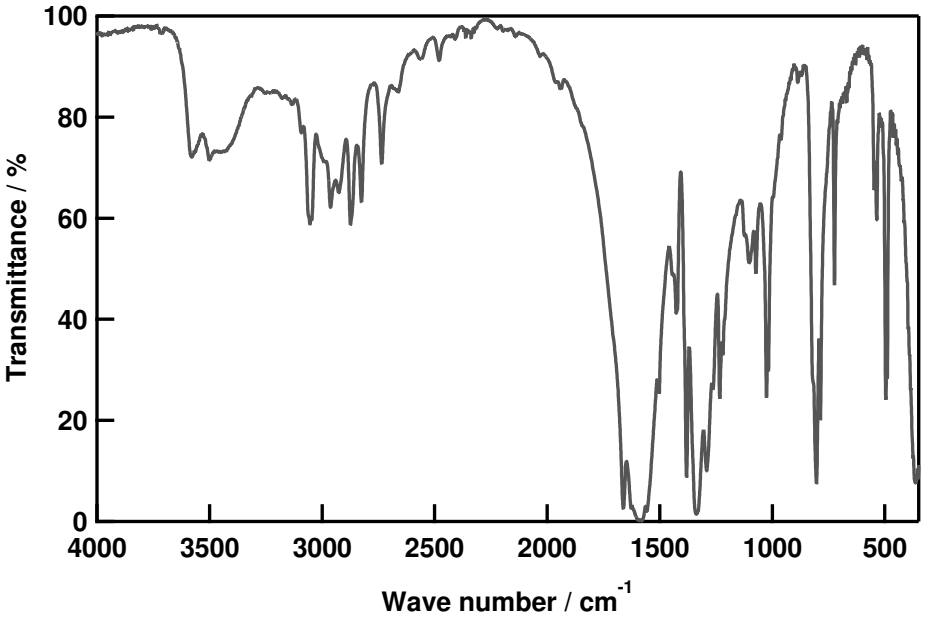

Figure 5.39: Infrared spectra of $[Fe^{II}_2Fe^{III}_2(HCOO)_{10}(\gamma\text{-}C_6H_7N)_6]_n$ **(19)** (AP007)

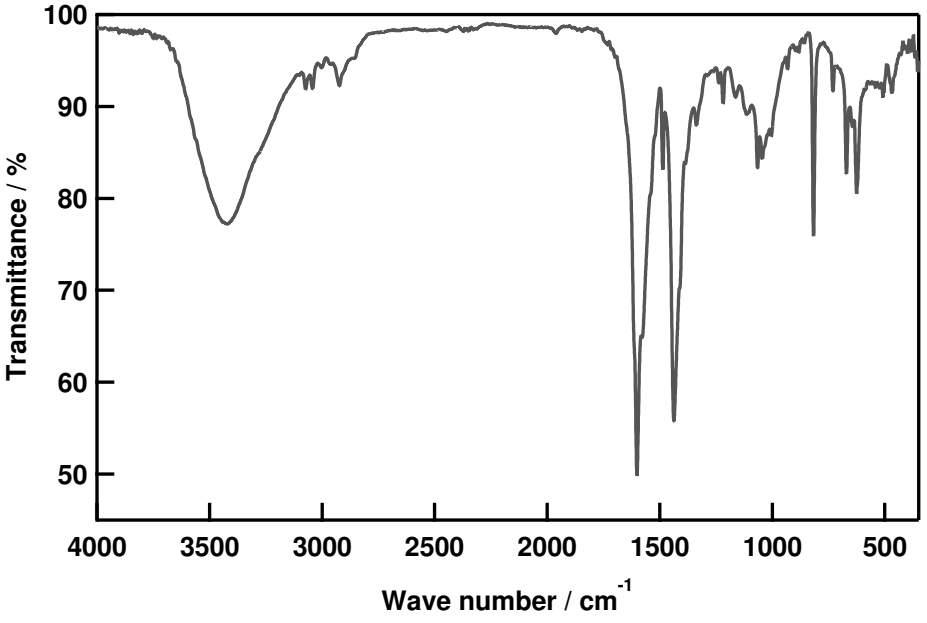

Figure 5.40: Infrared spectra of $[Fe_2(CH_3COO)_4(C_{10}H_8N_2)_2]_n$ **(20a)** (AP06840)

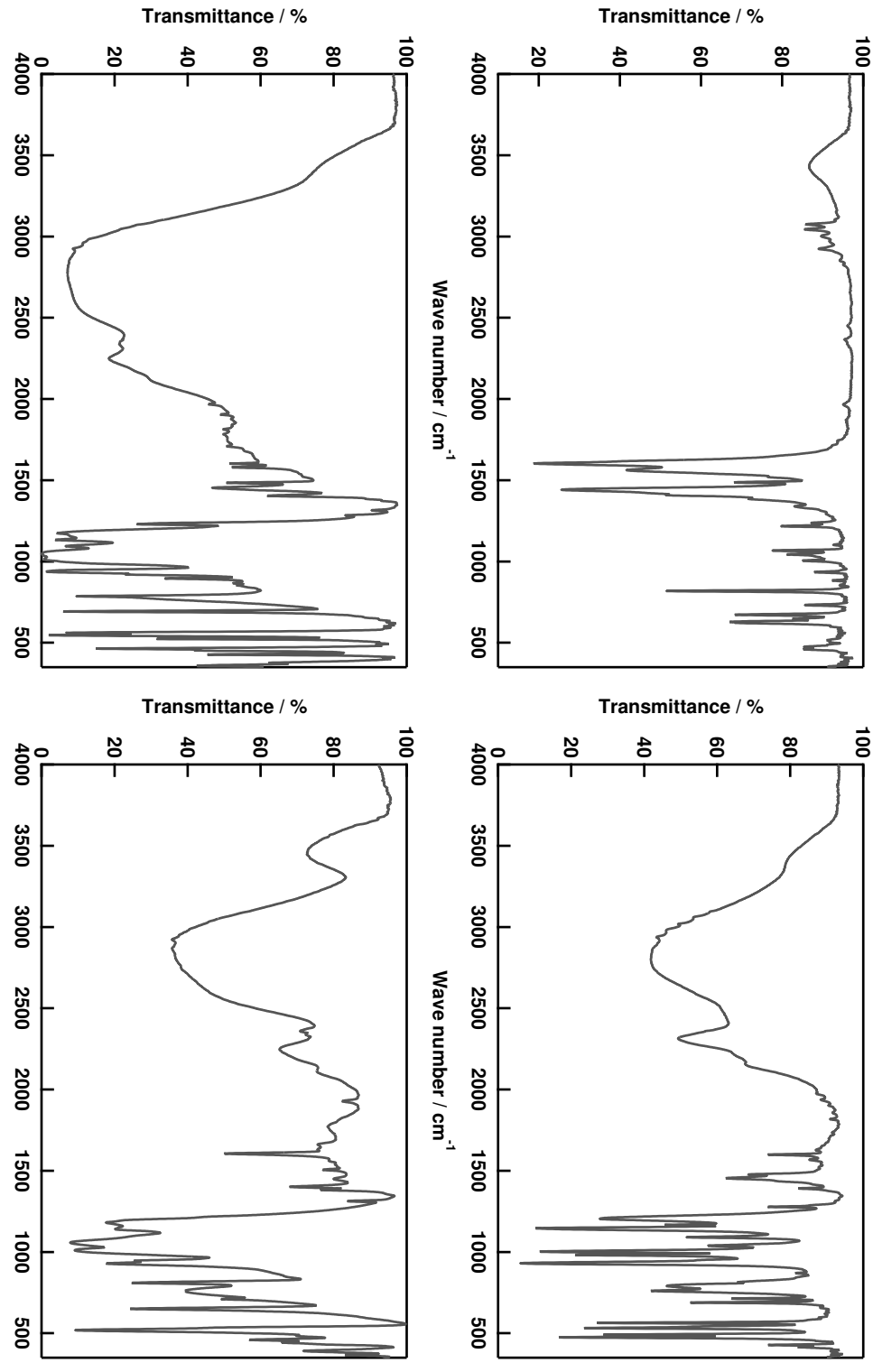

Figure 5.41: Infrared spectra of $[Co_2(CH_3COO)_4(C_{10}H_8N_2)2]_n$ **(20b)** (top left), 2-Tolyl-phosphonic acid **(2a)** (top right), 3-Tolyl-phosphonic acid **(2b)** (bottom left), 4-Tolyl-phosphonic acid **(2c)** (bottom right)

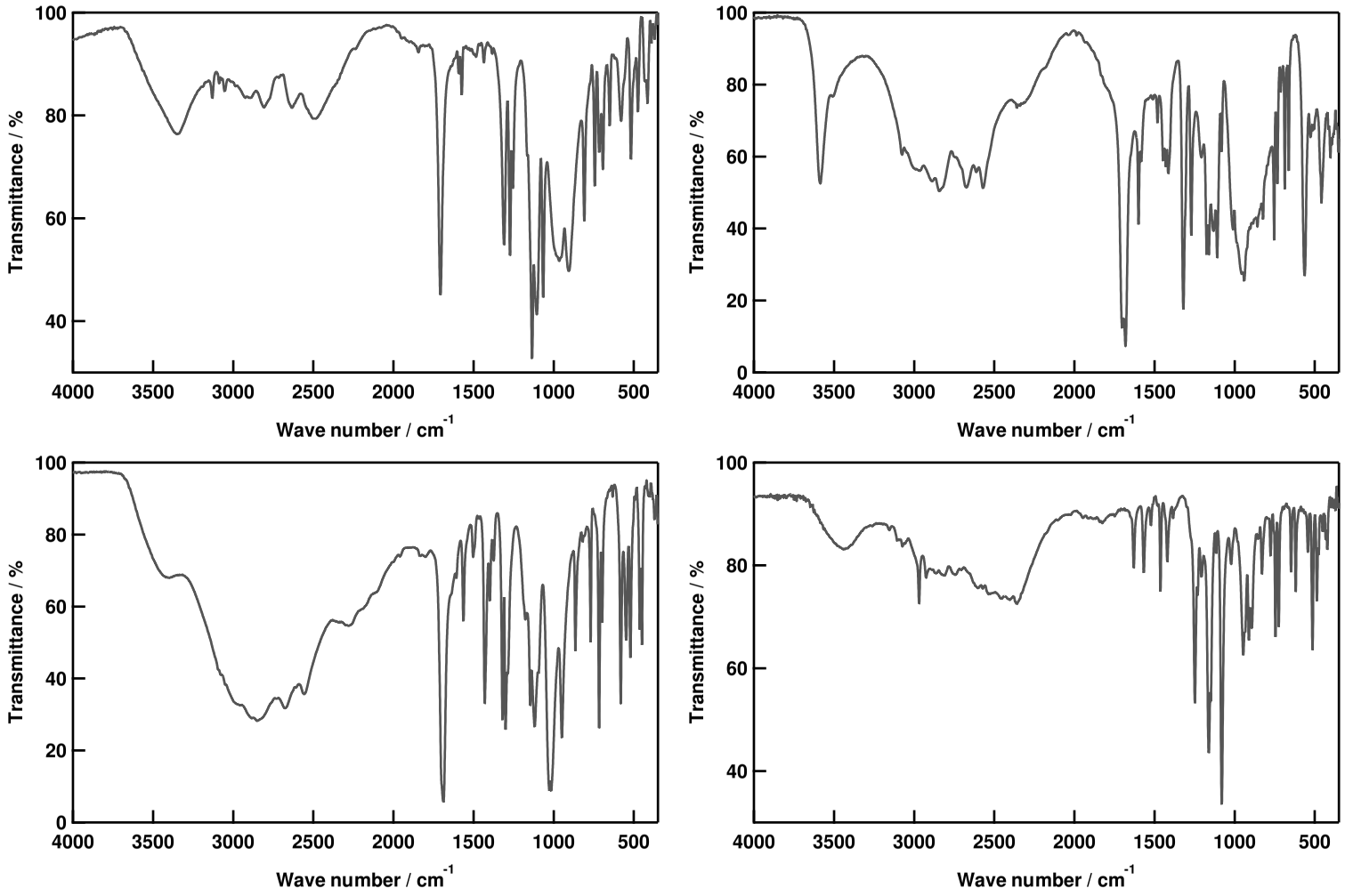

Figure 5.42: Infrared spectra of 2-Phosphono benzoic acid **(3a)** (top left), 3-Phosphono benzoic acid **(3b)** (top right), 4-Phosphono benzoic acid **(3c)** (bottom left), 1H-Benzimidazol-2-yl-methyl)phosphonic acid **(6)** (bottom right)

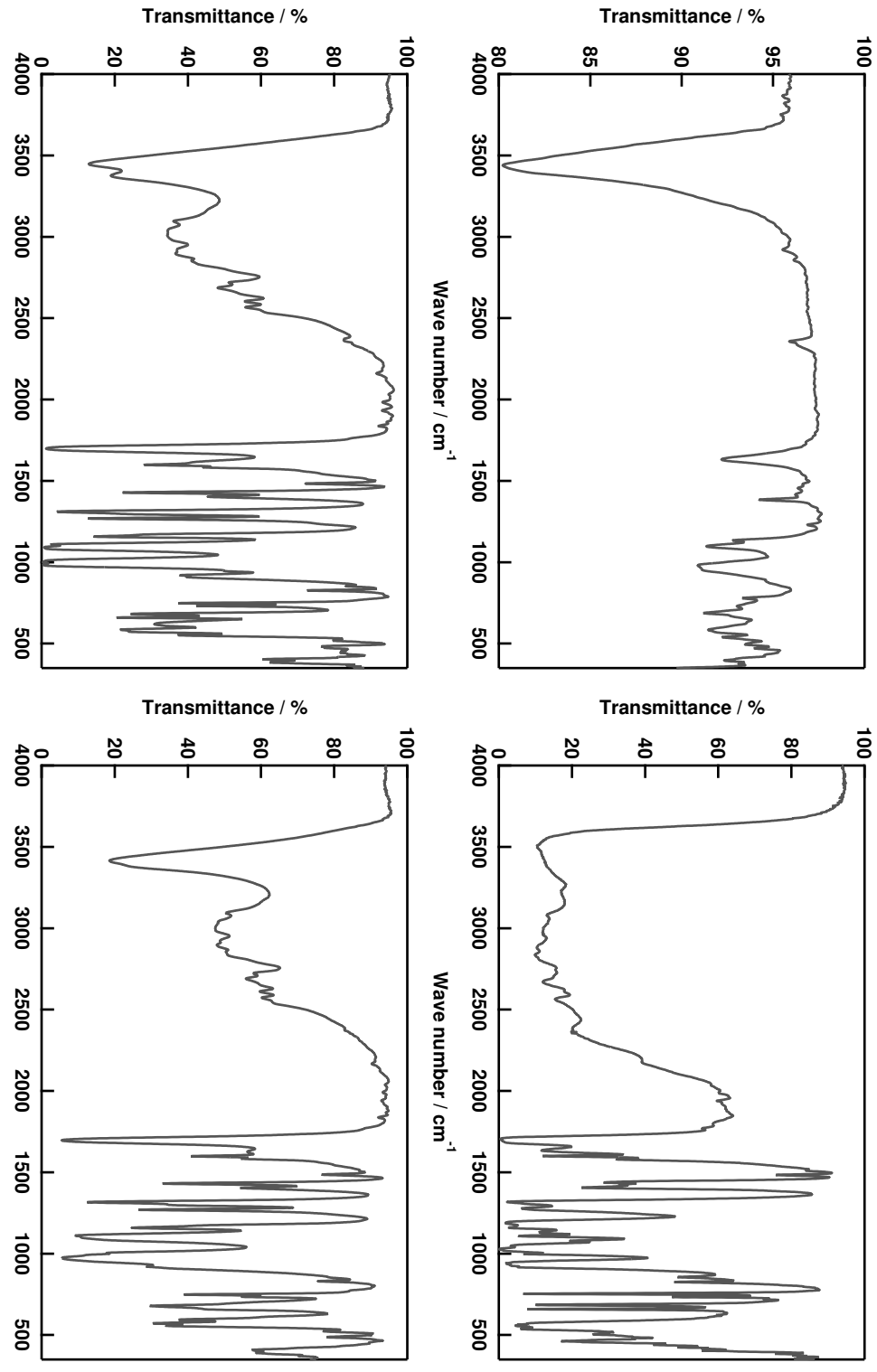

Figure 5.43: Infrared spectra of $[Co(meta\text{-}CH_3C_6H_4PO_3)(H_2O)]_n$ **(11b)** (top left), $[Mn(meta\text{-}HOOCC_6H_4PO_3H)_2(H_2O)_2]_n$ **(9)** (top right), $[Mn(HOOCC_6H_4PO_3)(H_2O)]_n$ **(12a)** (bottom left), $[Co(HOOCC_6H_4PO_3)(H_2O)]_n$ **(12b)** (bottom right)

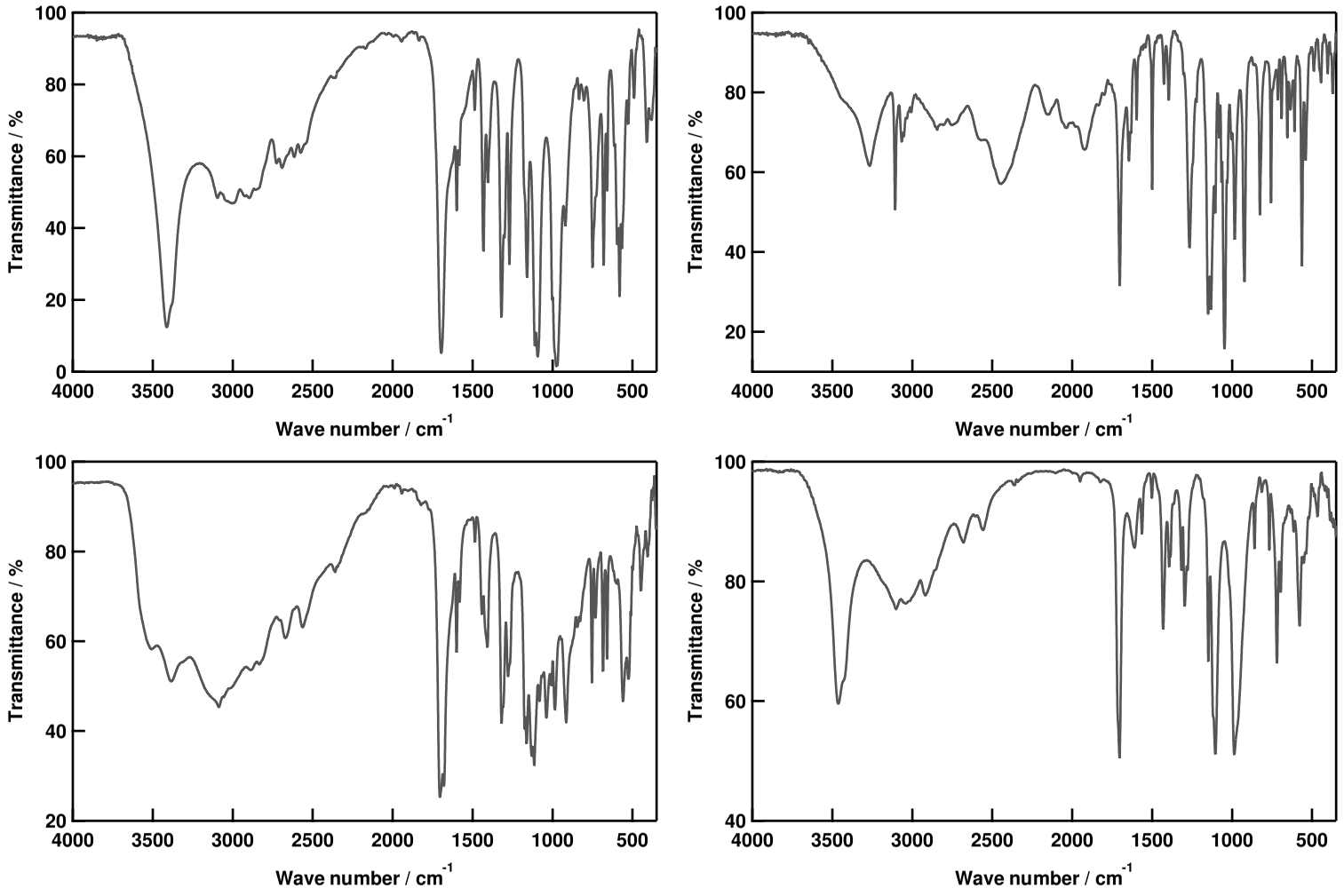

Figure 5.44: Infrared spectra of $[Ni(HOOCC_6H_4PO_3)(H_2O)]_n$ **(12c)** (top left), $[(HNC_5H_4C_5H_4NH)(HOOCC_6H_4PO_3H)_2]*2H_2O$ **(17)** (top right), $[Pr_2(H_2O)_8(HOOCC_6H_4PO_3H)_6]$ **(18)** (bottom left), $[Co(H_2O)_6(para\text{-}HOOCC_6H_4PO_3H)_2]*4(H_2O)$ **(8a)** (bottom right)

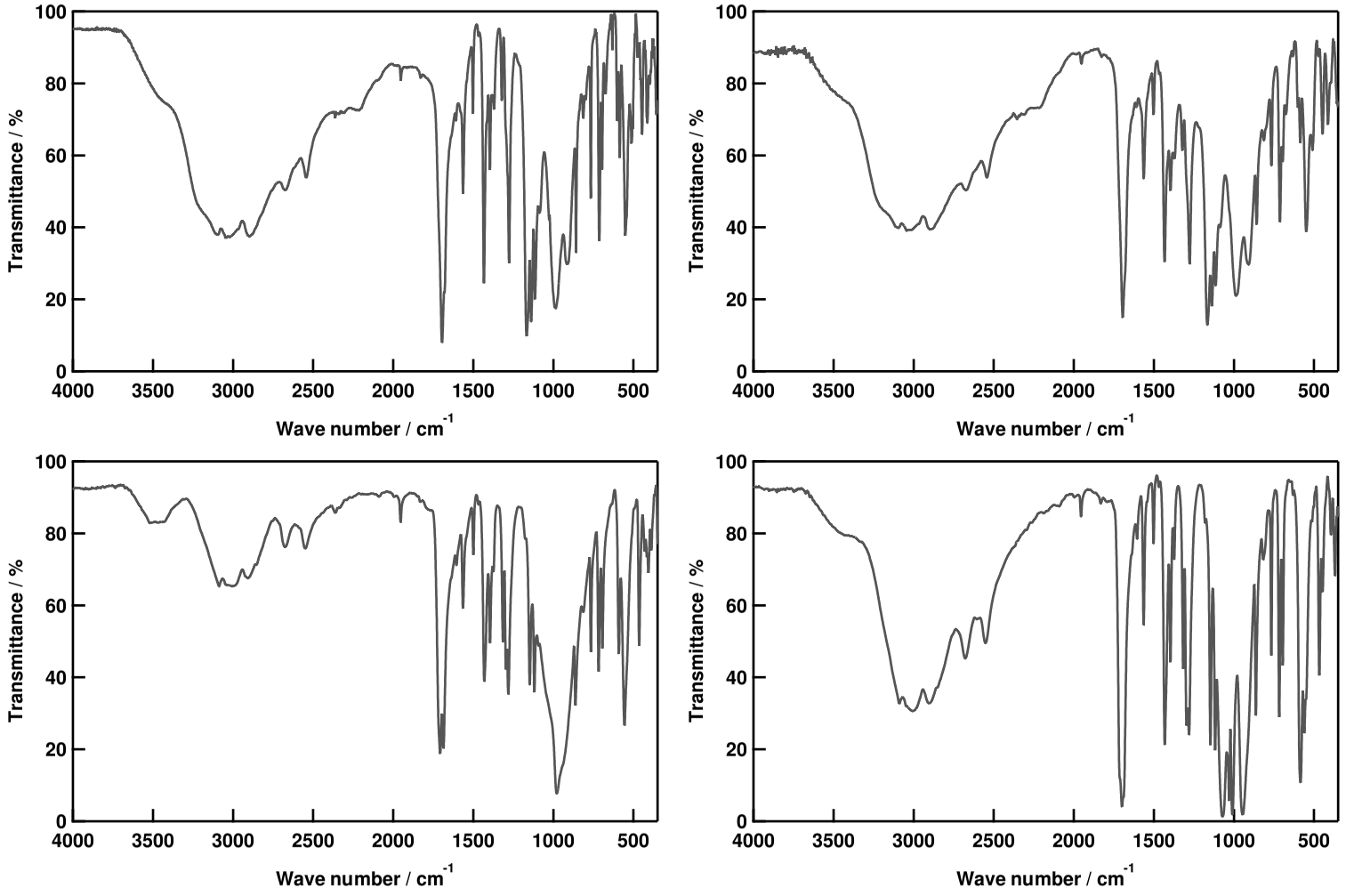

Figure 5.45: Infrared spectra of $[Co(para\text{-}HOOCC_6H_4PO_3H)_2(H_2O)]_n$ **(10)**, Solvothermal Method (top left), $[Co(para\text{-}HOOCC_6H_4PO_3H)_2(H_2O)]_n$ **(10)**, Non-Solvothermal Method (top right), $[Co(para\text{-}HOOCC_6H_4PO_3)]_n$ **(13)** (bottom left), $[Cu(para\text{-}HOOCC_6H_4PO_3)]_n$ **(14)** (bottom right)

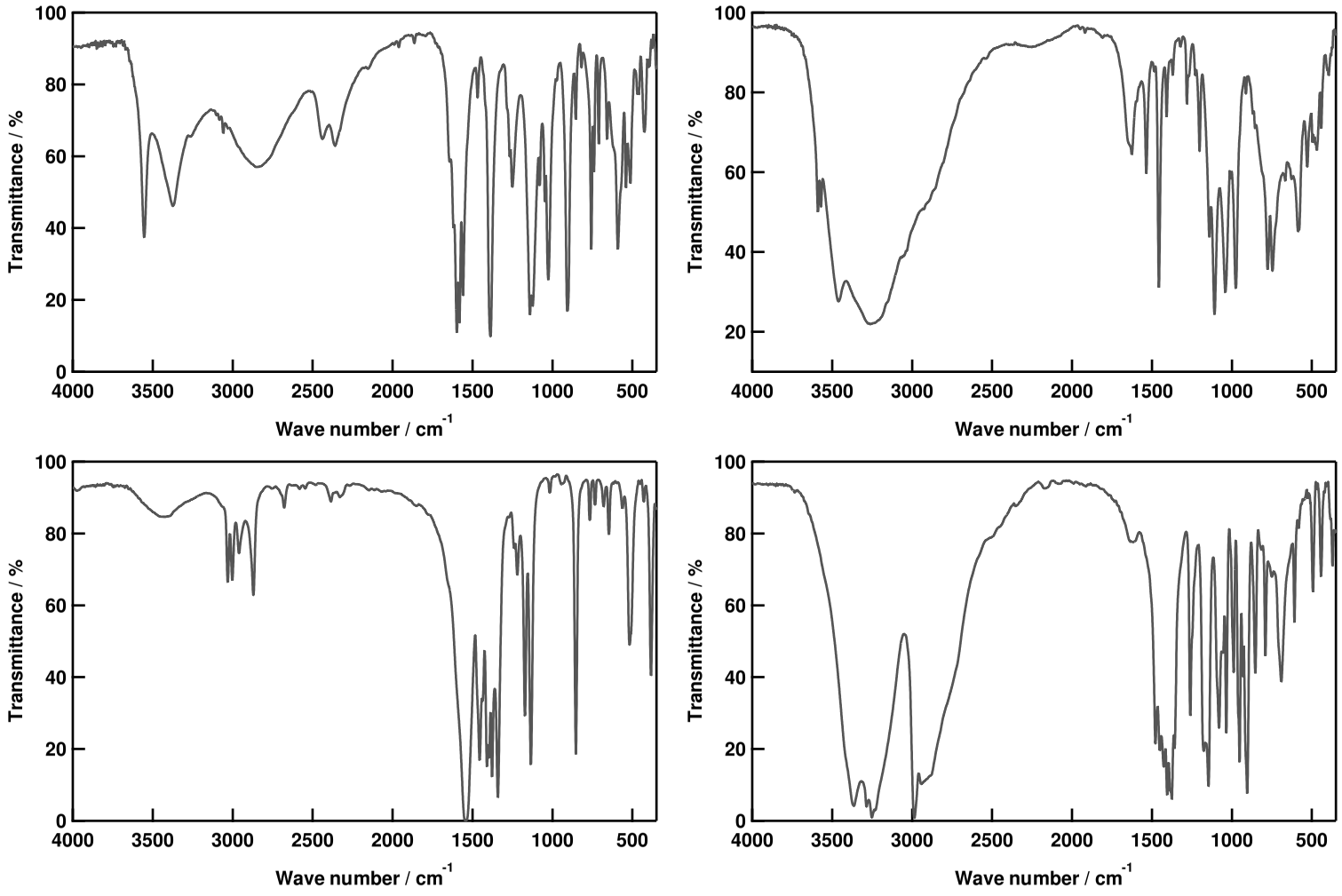

Figure 5.46: Infrared spectra of $[Co(ortho\text{-}OOCC_6H_4PO_3H)(H_2O)]_n$ **(15)** (top left), $[Co_2(H_2O)_6(O_3PCH_2C_7H_5N_2)_2]*6H_2O$ **(16)** (top right), 2,3-Dimethyl-2,3-dinitrobutane **(21)** (bottom left), 2,3-Bis(hydroxylamine)-2,3-dimethylbutane **(22)** (bottom right)

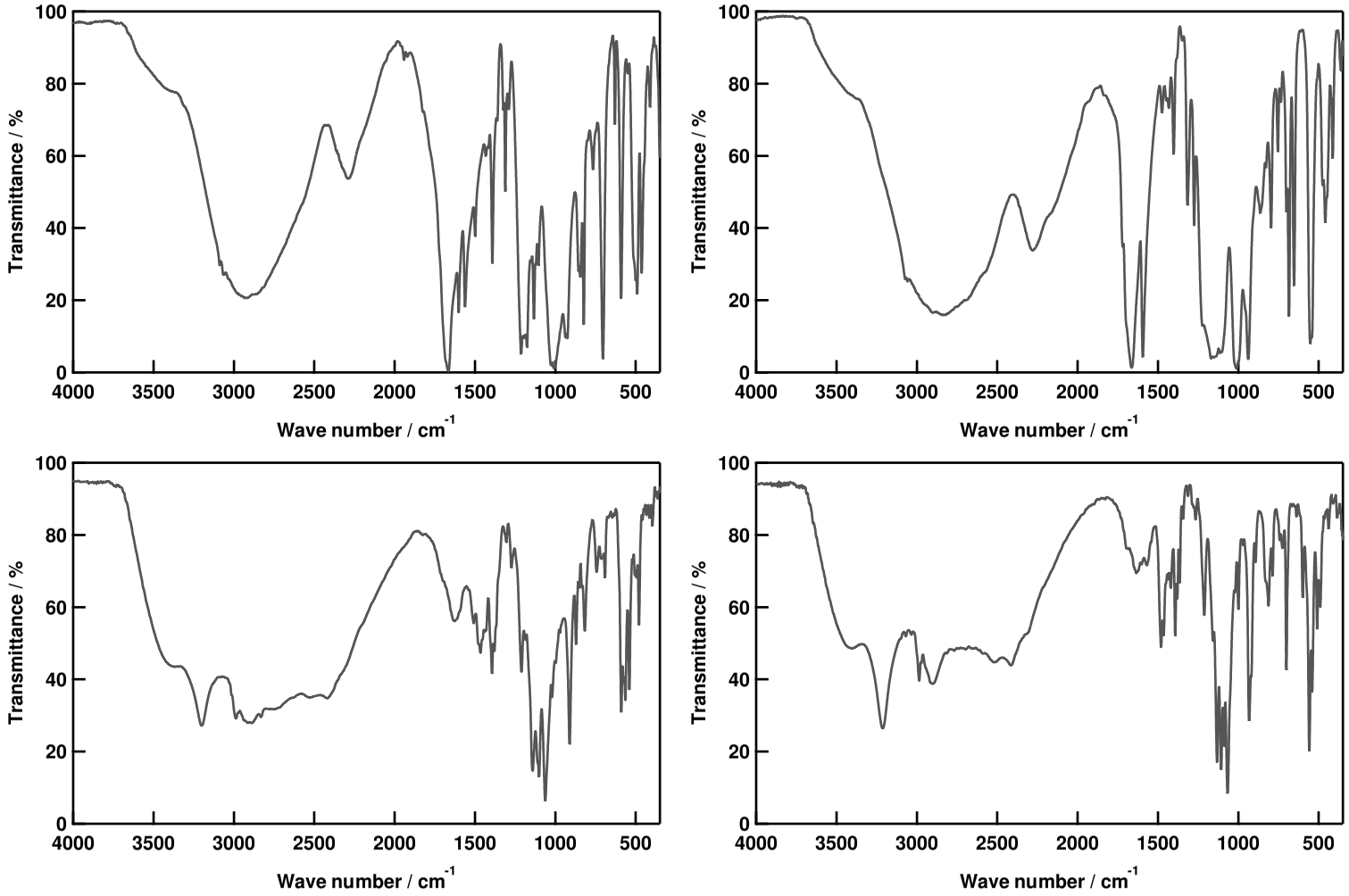

Figure 5.47: Infrared spectra of (4-Formyl-phenyl)-phosphonic acid **(25a)** (top left), (3-Formyl-phenyl)-phosphonic acid **(25b)** (top right), [4-(1,3-Dihydroxy-4,4,5,5-tetramethyl-imidazolidin-2-yl)-phenyl]-phosphonic acid **(26a)** (bottom left), [3-(1,3-Dihydroxy-4,4,5,5-tetramethyl-imidazolidin-2-yl)-phenyl]-phosphonic acid **(26b)** (bottom right)

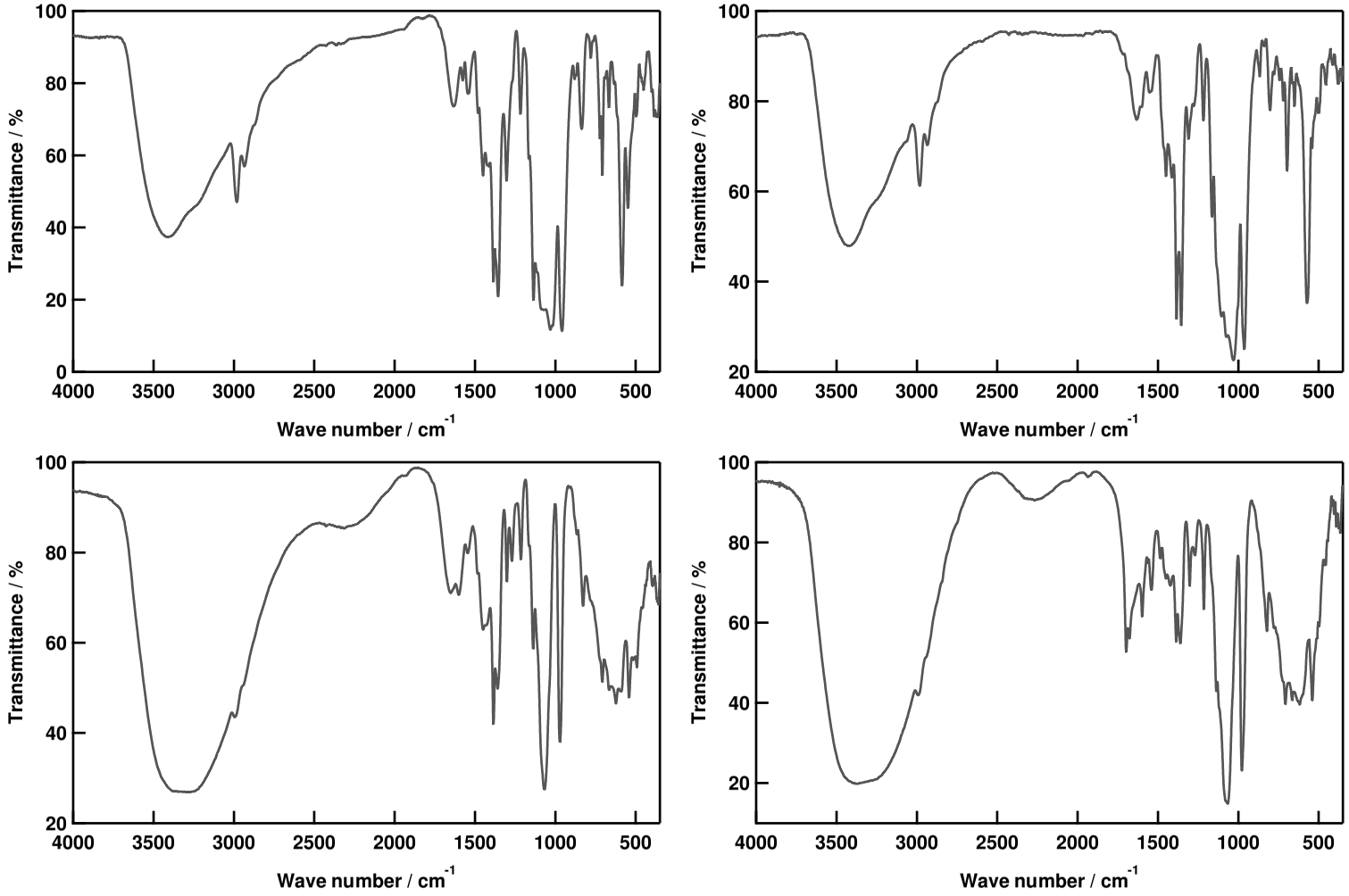

Figure 5.48: Infrared spectra of [4-(4,4,5,5-tetramethyl-imidazoline-3-oxide-1-oxyl)-phenyl]-phosphonic acid **(27a)** (top left), [3-(4,4,5,5-tetramethyl-imidazoline-3-oxide-1-oxyl)-phenyl]-phosphonic acid **(27b)** (top right), [4-(4,4,5,5-tetramethyl-imidazoline-3-oxide-1-oxyl)-phenyl]-phosphonate sodium salt **(28a)** , procedure 1: oxidation with lead dioxide (bottom left), [4-(4,4,5,5-tetramethyl-imidazoline-3-oxide-1-oxyl)-phenyl]-phosphonate sodium salt **(28a)** , procedure 2: oxidation with sodium periodate (bottom right)

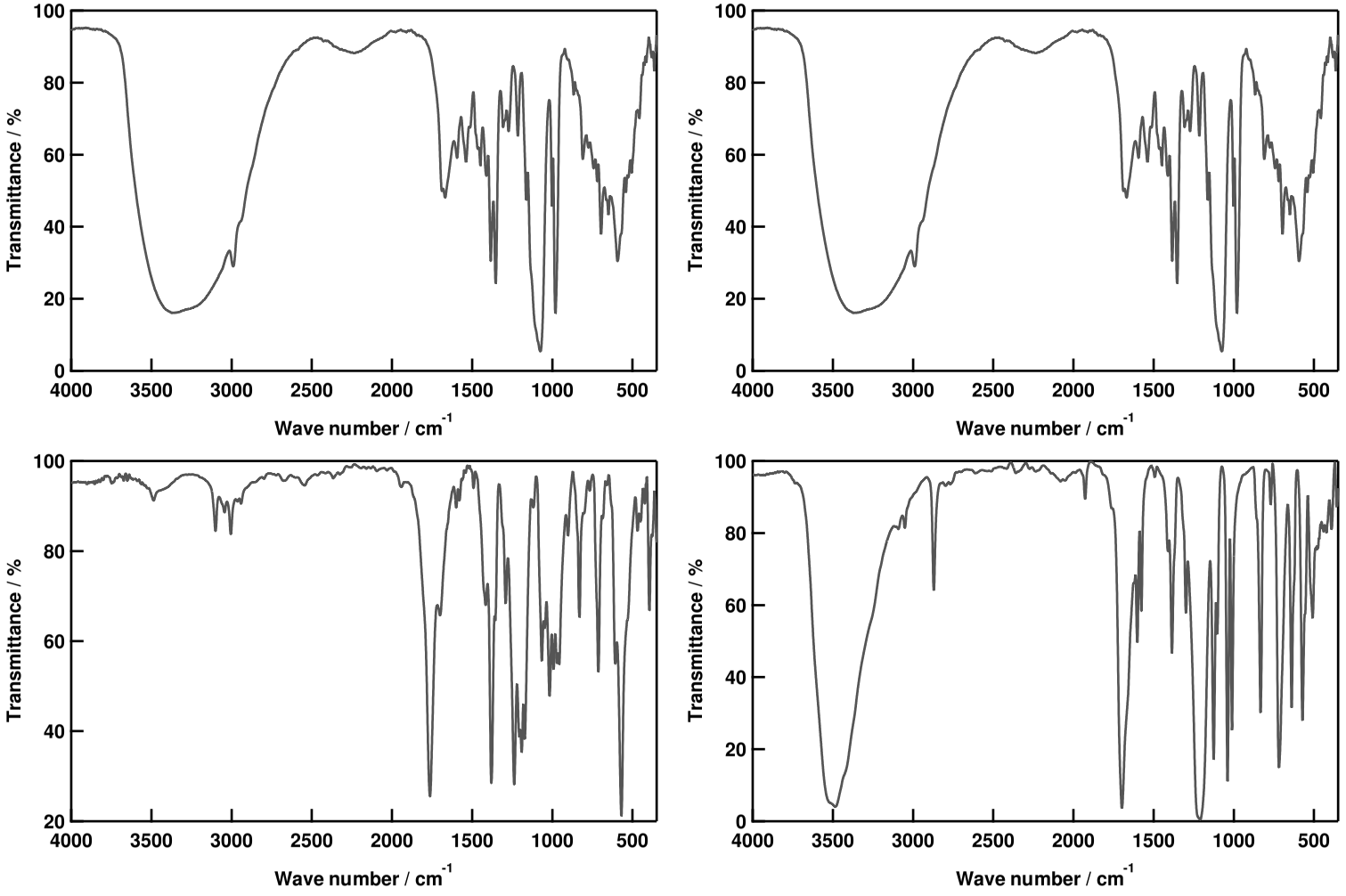

Figure 5.49: Infrared spectra of [3-(4,4,5,5-tetramethyl-imidazoline-3-oxide-1-oxyl)-phenyl]-phosphonate sodium salt **(28b)** , procedure 1: oxidation with lead dioxide (top left), [3-(4,4,5,5-tetramethyl-imidazoline-3-oxide-1-oxyl)-phenyl]-phosphonate sodium salt **(28b)** , procedure 2: oxidation with sodium periodate (top right), 4-(Diacetoxymethyl)benzenesulfonic acid chloride **(29)** (bottom left), 4-(Formyl)benzenesulfonate sodium salt **(30)** (bottom right)

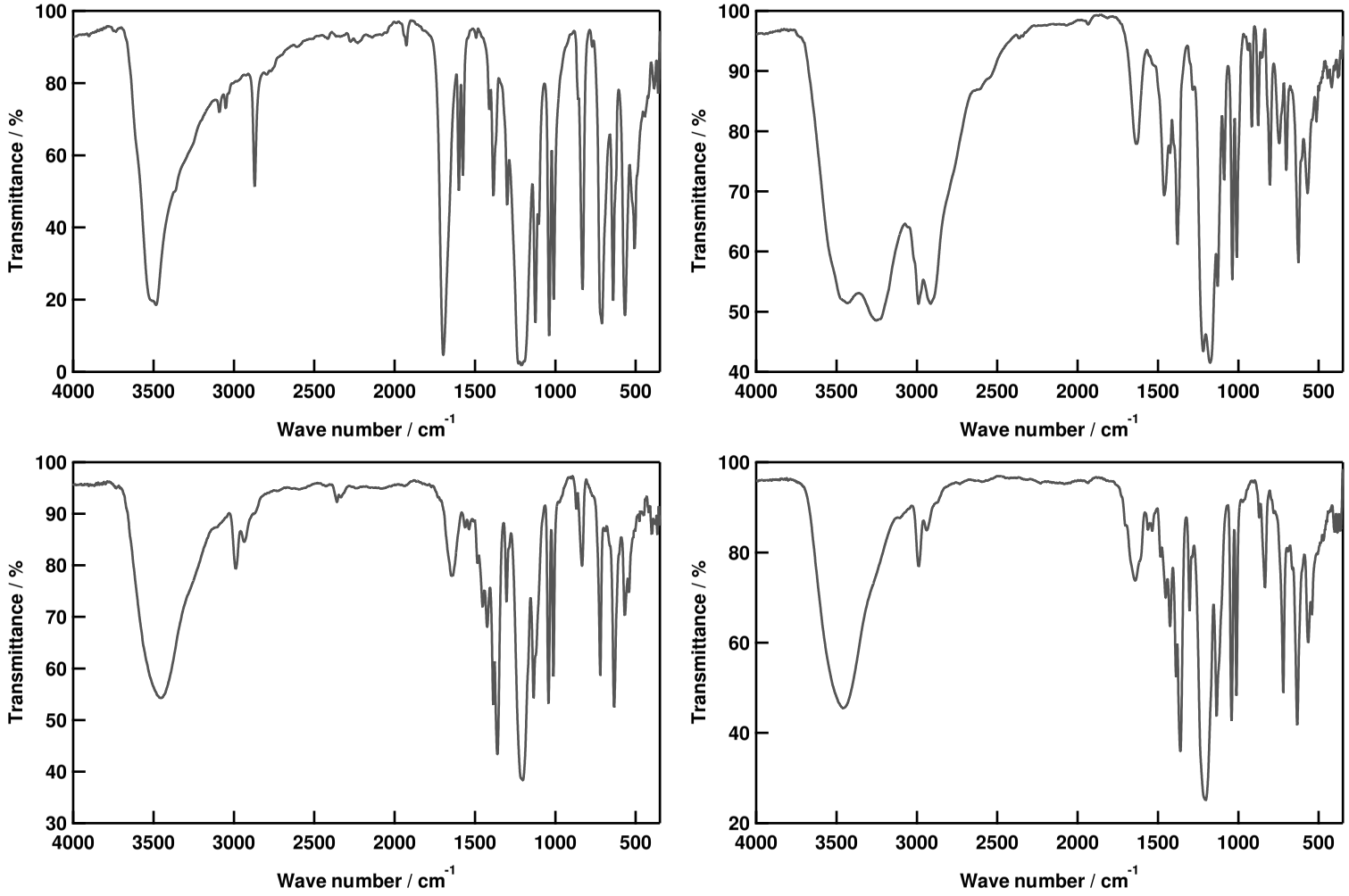

Figure 5.50: Infrared spectra of 4-(Formyl)benzenesulfonic acid **(31)** (top left), 4-(1,3-Dihydroxy-4,4,5,5-tetramethyl-imidazolidin-2-yl)-benzenesulfonic acid **(32)** (top right), 4-(4,4,5,5-tetramethyl-imidazoline-3-oxide-1-oxyl)-benzenesulfonic acid **(33)** (bottom left), 4-(4,4,5,5-tetramethyl-imidazoline-3-oxide-1-oxyl)-benzenesulfonate sodium salt **(34)** (bottom right)

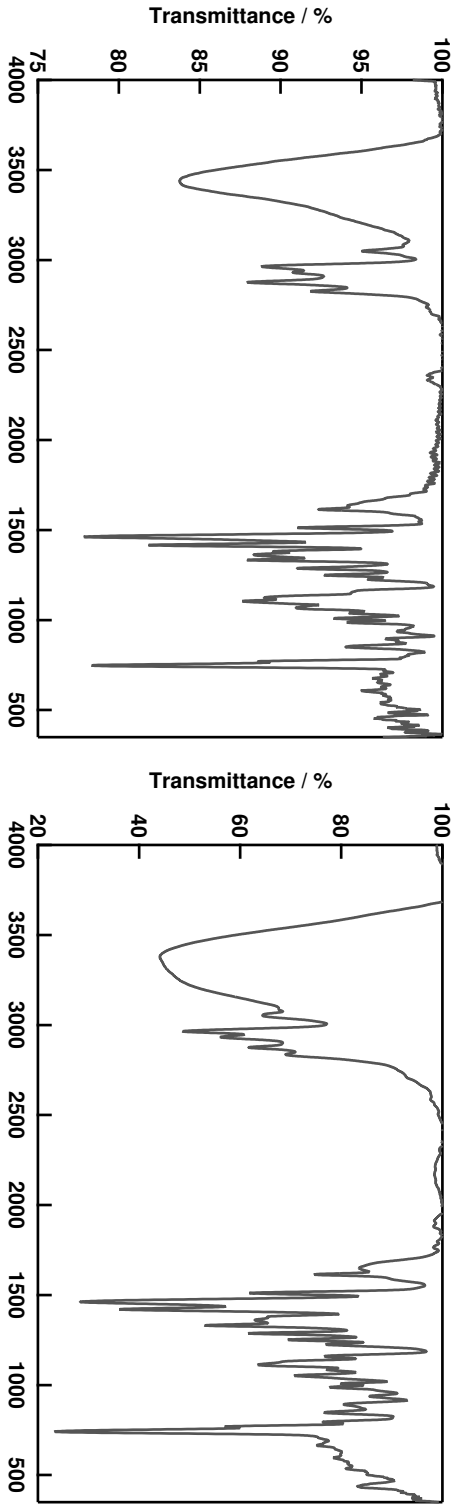

Figure 5.51: Infrared spectra of ^{Pr}EPTG **(36)** (top left), ^{Pr}HPTB **(38)** (top right)

D ESI Mass Spectra

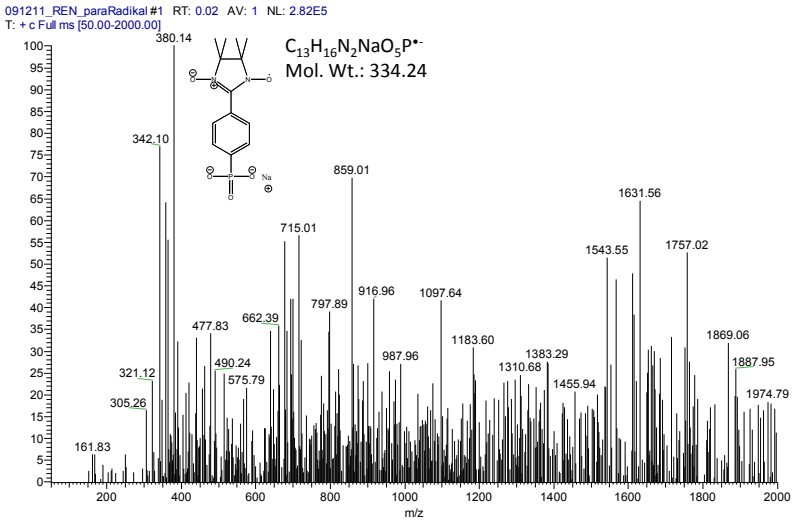

Figure 5.52: Mass spectra of [4-(4,4,5,5-tetramethyl-imidazoline-3-oxide-1-oxyl)-phenyl]-phosphonate sodium salt **(28a)**

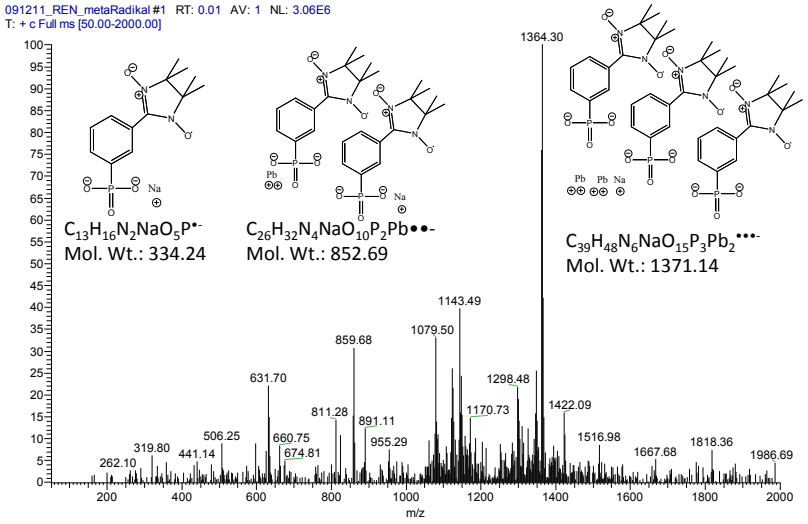

Figure 5.53: Mass spectra of [3-(4,4,5,5-tetramethyl-imidazoline-3-oxide-1-oxyl)-phenyl]-phosphonate sodium salt **(28b)**

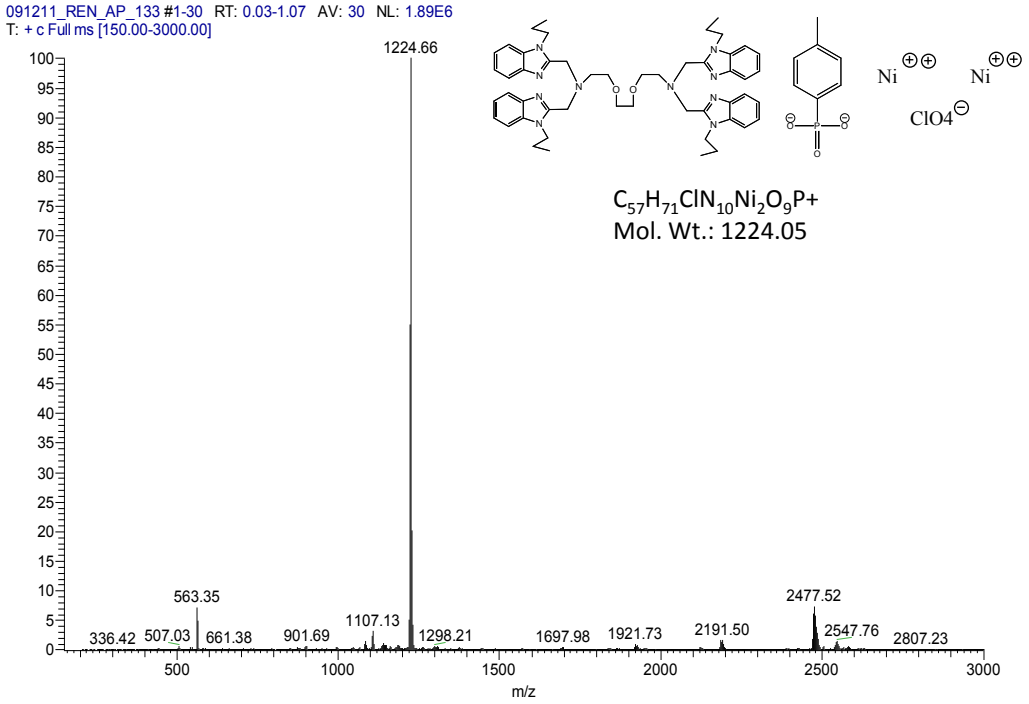

Figure 5.54: Mass spectra of $[Ni_2(C_{50}H_{64}N_{10}O_2)(C_7H_7PO_3)(H_2O)_2](ClO_4)_2$ **(39)**

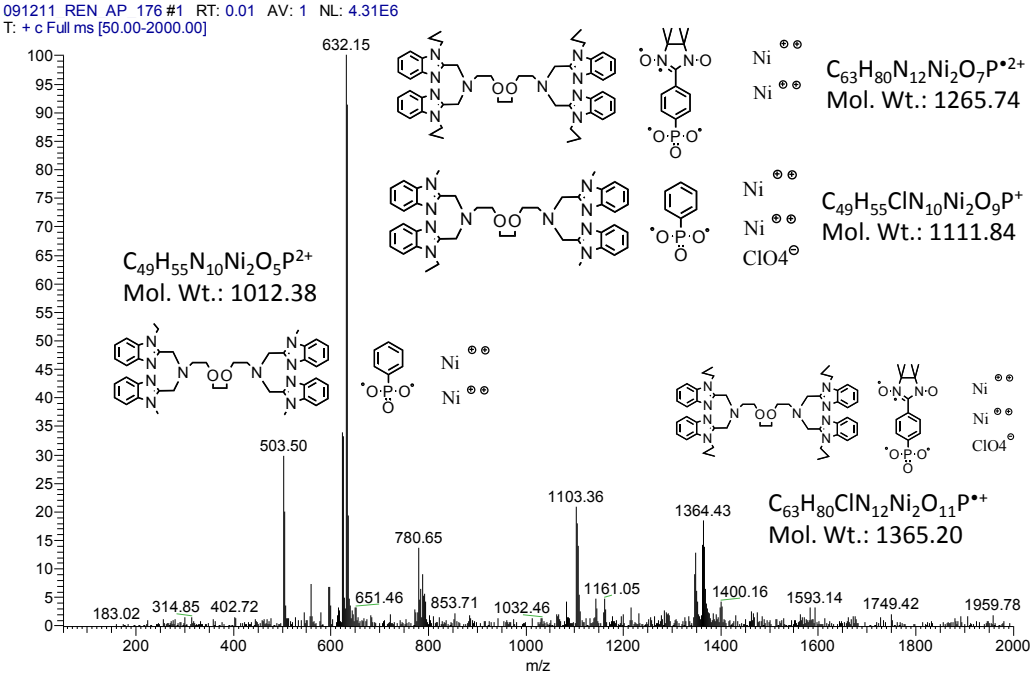

Figure 5.55: Mass spectra of $[Ni_2(C_{50}H_{64}N_{10}O_2)(C_7H_7PO_3)(H_2O)_2](ClO_4)_2$ **(39)**

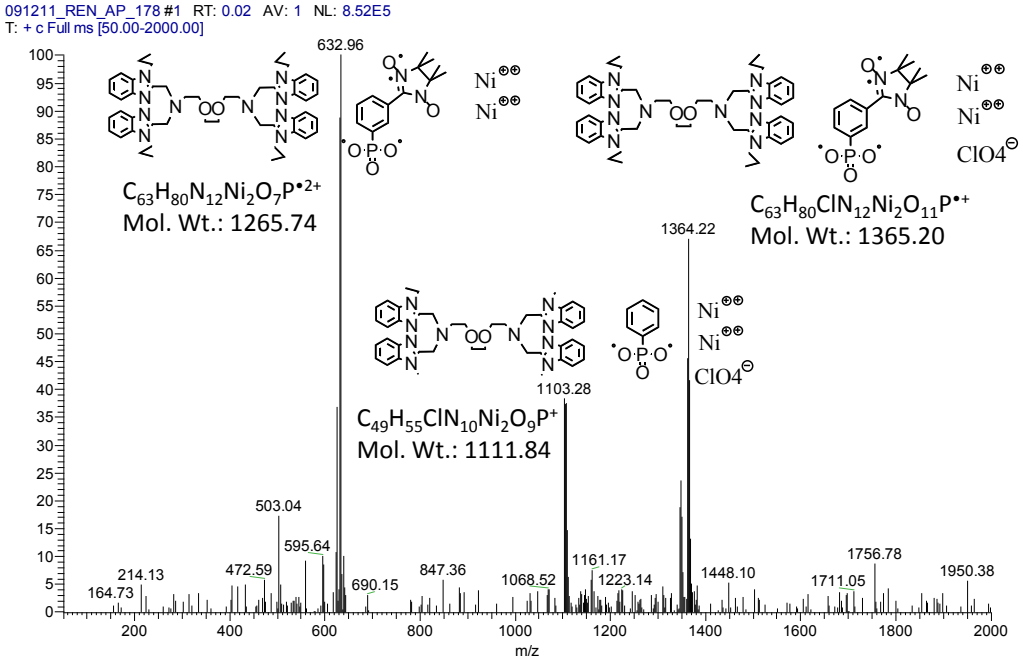

Figure 5.56: Mass spectra of $[Ni_2(C_{50}H_{64}N_{10}O_2)(C_7H_7PO_3)(H_2O)_2](ClO_4)_2$ **(39)**

E Diffraction data

E.1 $[Ni(H_2O)_6(HOOCC_6H_4PO_3H)_2]^*(HOOCC_6H_4PO_3H_2)_2$ (7)

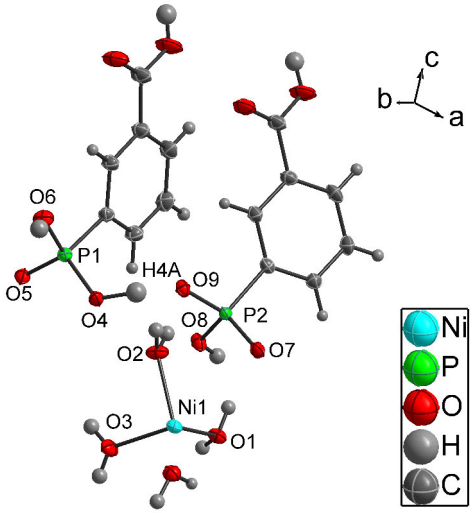

Figure 5.57: Asymmetric unit of $[Ni(H_2O)_6(meta\text{-}HOOCC_6H_4PO_3H)_2]^*(meta\text{-}HOOCC_6H_4PO_3H_2)_2$ (AP10340)

atoms	bond length / Å	atoms	bond length / Å
Ni1-O1	2.076(1)	P1-O4	1.544(1)
Ni1-O2	2.041(1)	P1-O5	1.507(1)
Ni1-O3	2.059(1)	P1-O6	1.546(1)
O4-H4A	1.108(1)	P2-O7	1.517(1)
O9-H4A	1.329(1)	P2-O8	1.560(1)
		P2-O9	1.527(1)
atoms	angle /°	atoms	angle /°
O1-Ni1-O2	92.94(4)	O4-P1-O5	109.38(6)
O1-Ni1-O3	90.18(5)	O4-P1-O6	111.73(7)
O2-Ni1-O3	88.38(5)	O5-P1-O6	110.88(6)
O4-H4A-O9		O7-P2-O8	110.67(6)
		O7-P2-O9	112.99(7)
		O8-P2-O9	105.82(6)

Table 5.1: Selected bond lengths and angles of $[Ni(H_2O)_6(meta\text{-}HOOCC_6H_4PO_3H)_2]^*(meta\text{-}HOOCC_6H_4PO_3H_2)_2$, numbering according to figure 5.57

Compound Formula sum	**(7)** $C_{28}\ H_{42}\ Ni\ O_{28}\ P_4$	**(8a)** $C_{14}\ H_{32}\ Co\ O_{20}\ P_2$	**(8b)** $C_{14}\ H_{32}\ Ni\ O_{20}\ P_2$	**(9)** $C_{14}\ H_{16}\ Mn\ O_{12}\ P_2$	**(10)** $C_{14}\ H_{14}\ Co\ O_{11}\ P_2$
Formula weight / g/mol	1009.2	640.8	641.0	493.15	479.2
Crystal colour	green	pink	green	colourless	green
Crystal lattice	monoclinic	monoclinic	monoclinic	triclinic	monoclinic
Space group	P 21/a	C 2/c	C 2/c	P -1	P c
a / Å	13.3704(7)	31.934(1)	31.649(3)	7.6092(6)	19.437(2)
b / Å	7.1708(3)	6.8209(2)	6.8375(6)	7.7529(6)	5.9809(7)
c / Å	21.6384(10)	12.5290(4)	12.484(1)	17.2521(14)	7.5244(9)
α / °	90	90	90	78.046(2)	90
β / °	99.419(2)	103.513(2)	103.224(2)	84.969(2)	93.200(2)
γ /°	90	90	90	67.323(2)	90
Cell volume / $Å^3$	2046.65(27)	2653.52(13)	2629.90(64)	918.66(22)	873.36(20)
Calculated density / g/cm^3	1.64	1.60	1.62	1.78	1.82
No. measured reflections	27 488	18 180	6 865	9 917	13 124
No. unique reflections	4 843	5 771	2 965	4 302	6 161
No. observed reflections	4 250	4 500	2 493	3 425	5 813
No. parameters	290	196	164	266	256
GOOF	1.125	1.063	1.018	1.054	1.052
R_{all}	0.032	0.049	0.051	0.054	0.034
$R_{observed}$	0.025	0.036	0.043	0.038	0.032

E.2 $[M(H_2O)_6(para\text{-}HOOCC_6H_4PO_3H)_2]^*4(H_2O)$ (8a) , (8b)

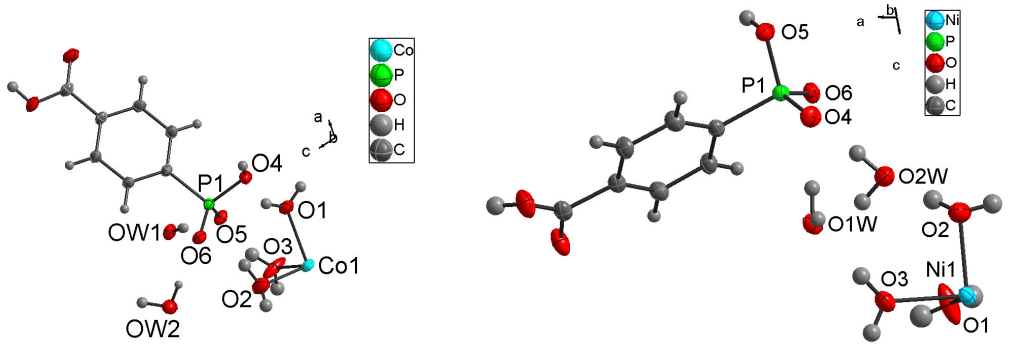

Figure 5.58: Asymmetric unit of $[Co(H_2O)_6(para\text{-}HOOCC_6H_4PO_3H)_2]^*4(H_2O)$ (XE154) (left) and of $[Ni(H_2O)_6(para\text{-}HOOCC_6H_4PO_3H)_2]^*4(H_2O)$ (XE12630) (right)

atoms	bond length / Å	atoms	angle /°
Co1-O1	2.111(1)	O1-Co1-O2	88.74(4)
Co1-O2	2.067(1)	O1-Co1-O3	87.06(4)
Co1-O3	2.059(1)	O2-Co1-O3	91.08(5)
P1-O4	1.590(1)	O4-P1-O5	105.84(5)
P1-O5	1.506(1)	O4-P1-O6	110.53(5)
P1-O6	1.508(1)	O5-P1-O6	115.71(5)
Ni1-O1	2.040(2)	O1-Ni1-O2	89.52(9)
Ni1-O2	2.044(2)	O1-Ni1-O3	87.31(8)
Ni1-O3	2.036(2)	O2-Ni1-O3	89.77(7)
P1-O4	1.505(2)	O4-P1-O5	105.81(9)
P1-O5	1.586(2)	O4-P1-O6	115.92(9)
P1-O6	1.504(2)	O5-P1-O6	110.20(9)

Table 5.2: Selected bond lengths and angles of $[M(H_2O)_6(para\text{-}HOOCC_6H_4PO_3H)_2]^*4(H_2O)$, numbering according to figure 5.58; further crystal data can be found in table E.1 on page 243

E.3 [Mn(meta-HOOCC$_6$H$_4$PO$_3$H)$_2$(H$_2$O)$_2$]$_n$ (9)

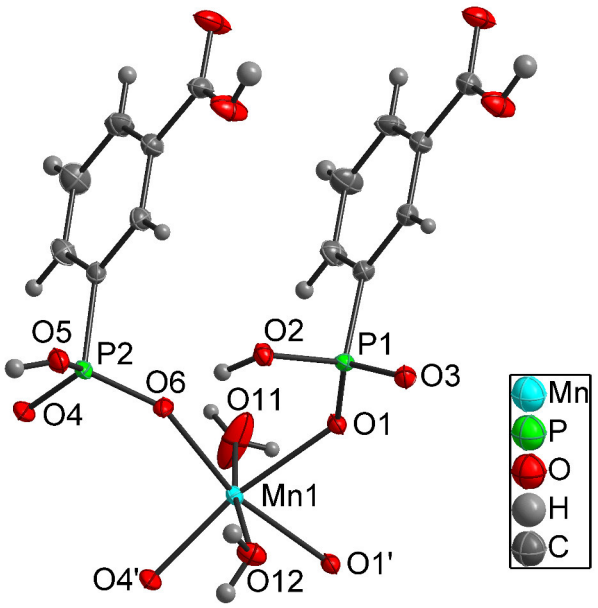

Figure 5.59: Asymmetric unit of [Mn(meta-HOOCC$_6$H$_4$PO$_3$H)$_2$(H$_2$O)$_2$]$_n$ (AP12040)

atoms	bond length / Å	atoms	bond length / Å
Mn1-O1	2.250(2)	P1-O1	1.522(2)
Mn1-O1'	2.199(2)	P1-O2	1.581(2)
Mn1-O4'	2.077(2)	P1-O3	1.505(2)
Mn1-O6	2.120(2)	P2-O4	1.498(2)
Mn1-O11	2.161(3)	P2-O5	1.571(2)
Mn1-O12	2.273(2)	P2-O6	1.523(2)
atoms	angle /°	atoms	angle /°
O1-Mn1-O4'	166.93(8)	O1-P1-O2	107.81(10)
O1'-Mn1-O6	165.59(7)	O1-P1-O3	116.21(11)
O11-Mn1-O12	172.15(9)	O2-P1-O3	108.19(11)
O1-Mn1-O1'	79.27(7)	O4-P2-O5	112.07(12)
O1-Mn1-O6	87.10(7)	O4-P2-O6	116.09(11)
O1-Mn1-O11	91.13(11)	O5-P2-O6	104.67(11)
O1-Mn1-O12	83.18(7)		

Table 5.3: Selected bond lengths and angles of [Mn(meta-HOOCC$_6$H$_4$PO$_3$H)$_2$(H$_2$O)$_2$]$_n$, numbering according to figure 5.59; further crystal data can be found in table E.1 on page 243

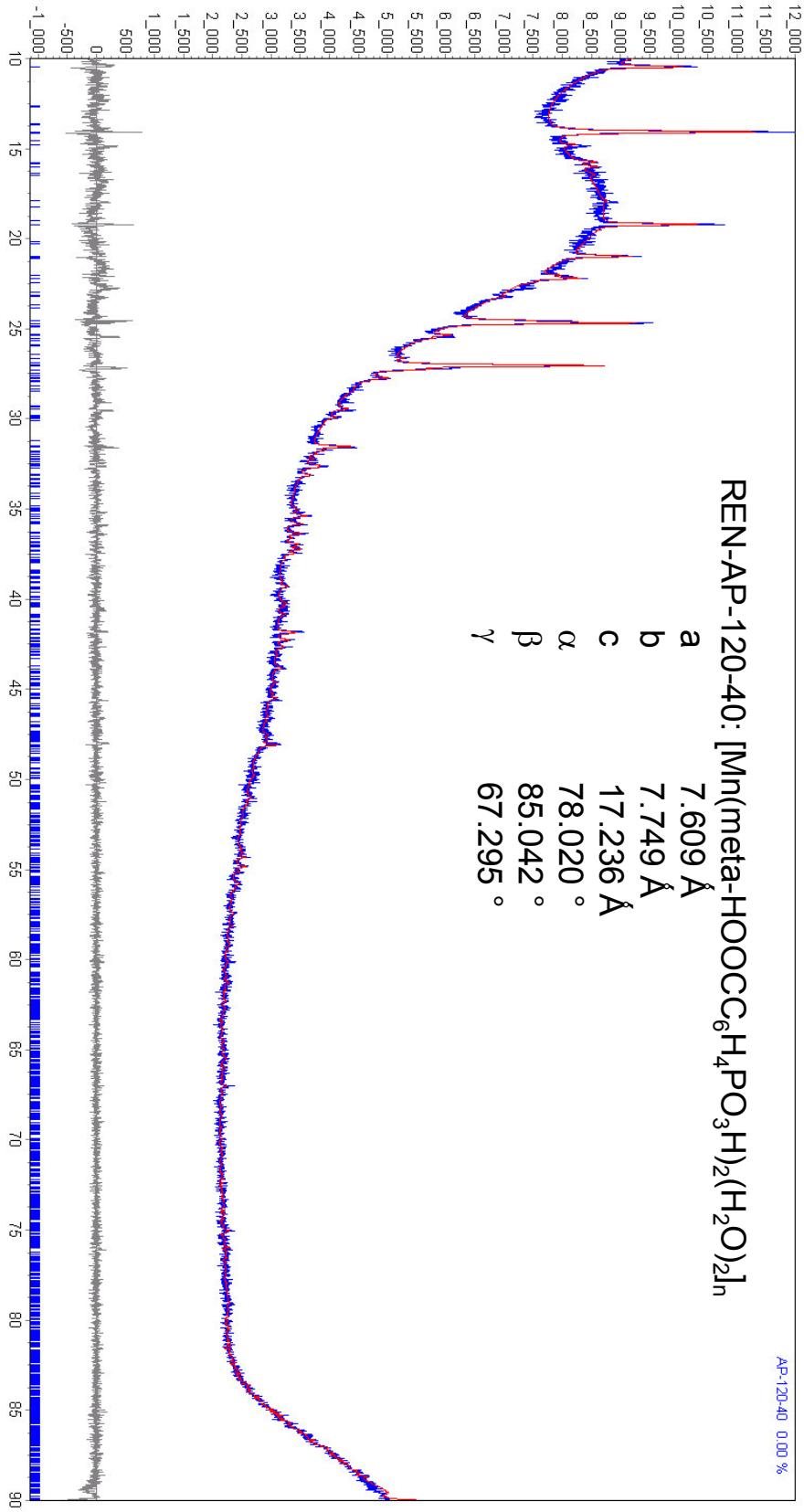

Figure 5.60: Powder diffractogram of $[Mn(HOOCC_6H_4PO_3H)_2(H_2O)_2]_n$, simulation according to cell parameters of the single crystal measurement (LeBay-Fit); material is phase-pure, preparation in tape causes amorphous signals

E.4 [Co(para-HOOCC$_6$H$_4$PO$_3$H)$_2$(H$_2$O)]$_n$ (10)

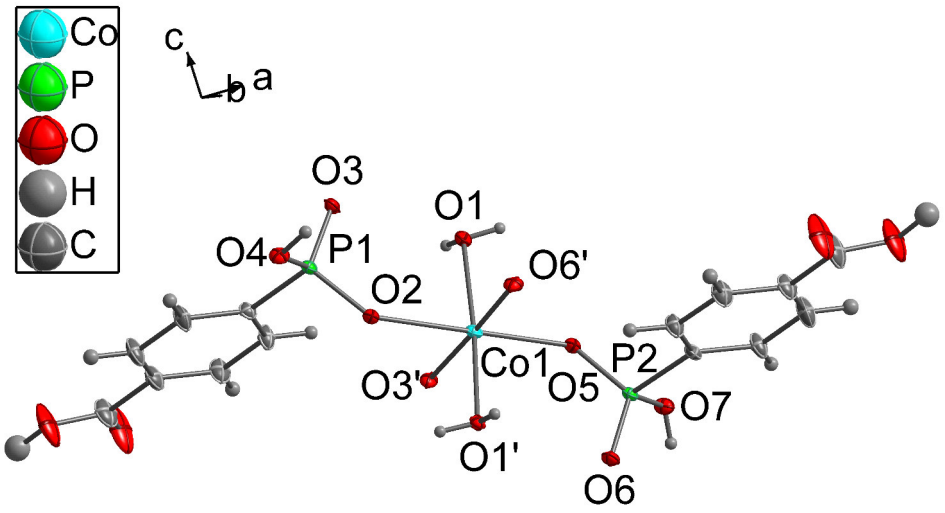

Figure 5.61: Asymmetric unit of [Co(para-HOOCC$_6$H$_4$PO$_3$H)$_2$(H$_2$O)]$_n$ (XE12610)

atoms	bond length / Å	atoms	bond length / Å
Co1-O1	2.143(2)	P1-O2	1.584(2)
Co1-O1'	2.150(2)	P1-O3	1.498(2)
Co1-O2	2.264(2)	P1-O4	1.515(2)
Co1-O3'	1.977(2)	P2-O5	1.526(2)
Co1-O5	2.145(2)	P2-O6	1.500(2)
Co1-O6'	1.993(2)	P2-O7	1.572(2)
atoms	angle /°	atoms	angle /°
O1-Co1-O1'	175.36(7)	O2-P1-O3	107.99(9)
O2-Co1-O5	179.35(7)	O2-P1-O4	109.09(9)
O3'-Co1-O6'	175.40(8)	O3-P1-O4	115.82(10)
O1-Co1-O2	89.00(6)	O5-P2-O6	114.50(9)
O1-Co1-O3'	90.76(7)	O5-P2-O7	107.40(9)
O1-Co1-O5	91.23(6)	O6-P2-O7	111.56(9)
O1-Co1-O6'	91.21(7)		

Table 5.4: Selected bond lengths and angles of [Co(para-HOOCC$_6$H$_4$PO$_3$H)$_2$(H$_2$O)]$_n$, numbering according to figure 5.61; further crystal data can be found in table E.1 on page 243

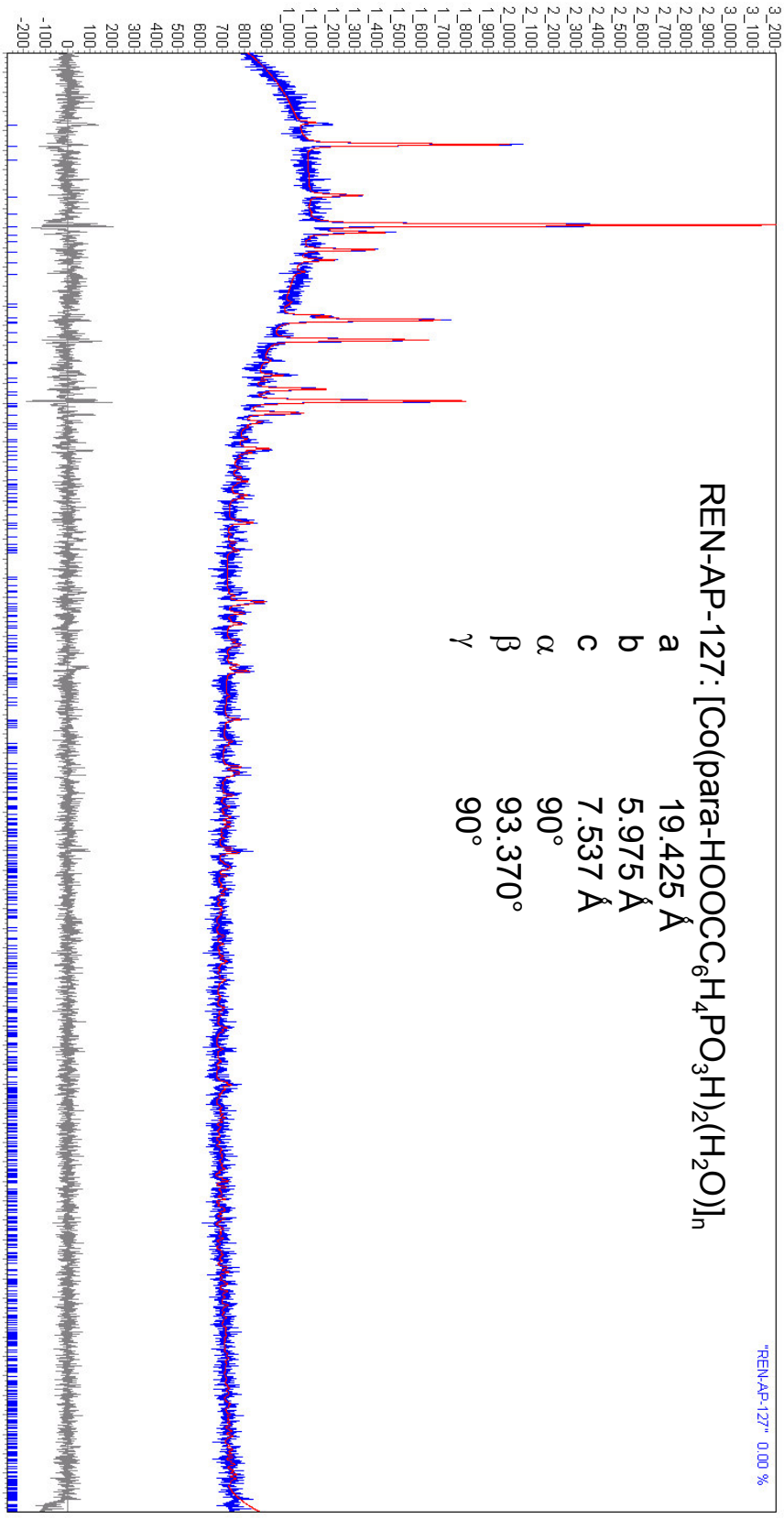

Figure 5.62: Powder diffractogram of $[Co(para\text{-}HOOCC_6H_4PO_3H)_2(H_2O)]_n$, simulation according to cell parameters of the single crystal measurement (LeBay-Fit); material is phase-pure, preparation in tape causes amorphous signals

E.5 [Co(meta-$CH_3C_6H_4PO_3$)(H_2O)]$_n$ (11b)

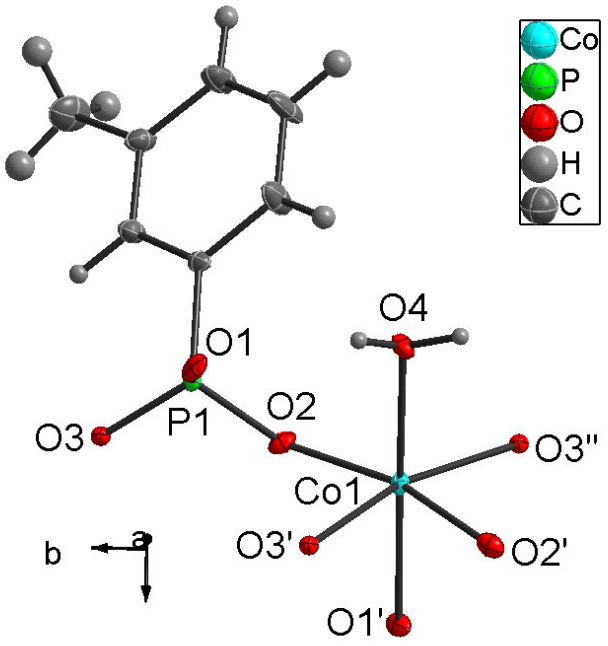

Figure 5.63: Asymmetric unit of [Co(meta-$CH_3C_6H_4PO_3$)(H_2O)]$_n$ (XE19340)

atoms	bond length / Å	atoms	bond length / Å
Co1-O1'	2.061(3)	P1-O1	1.510(3)
Co1-O2	2.060(3)	P1-O2	1.568(3)
Co1-O2'	2.218(3)	P1-O3	1.541(3)
Co1-O3'	2.234(3)		
Co1-O3"	2.092(3)		
Co1-O4	2.108(3)		
atoms	angle /°	atoms	angle /°
O1'-Co1-O4	173.1(1)	O1-P1-O2	111.9(2)
O2-Co1-O2'	162.9(1)	O1-P1-O3	114.1(2)
O3'-Co1-O3"	162.7(1)	O2-P1-O3	104.7(2)
O1'-Co1-O2	91.8(1)		
O1'-Co1-O2'	85.6(1)		
O1'-Co1-O3'	85.2(1)		
O1'-Co1-O3"	91.8(1)		

Table 5.5: Selected bond lengths and angles of [Co(meta-$CH_3C_6H_4PO_3$)(H_2O)]$_n$, numbering according to figure 5.63; further crystal data can be found in table E.5 on page 251

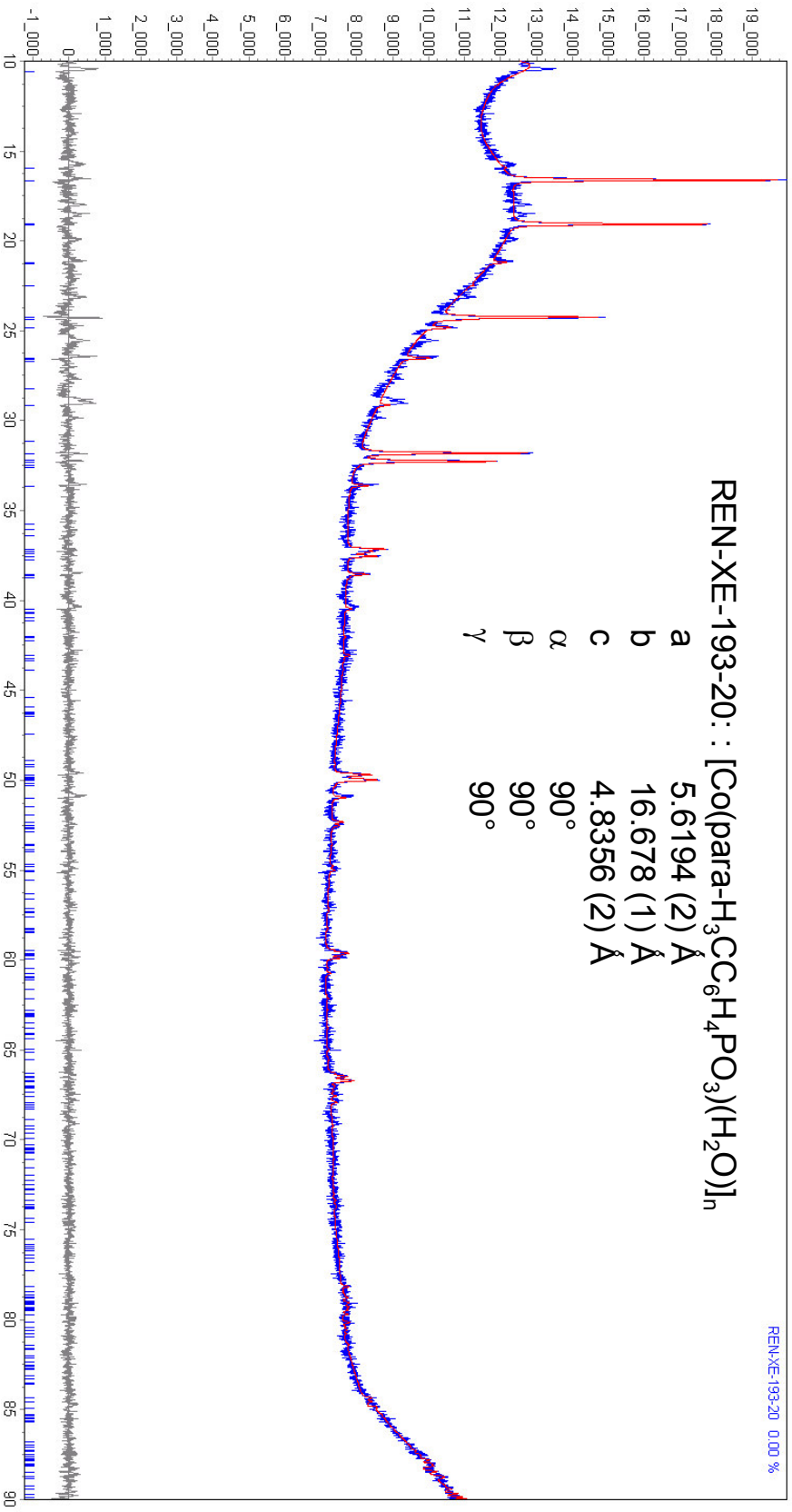

Figure 5.64: Powder diffractogram of $[Co(para\text{-}CH_3C_6H_4PO_3)(H_2O)]_n$, simulation starting with the cell parameters of the single crystal measurement of $[Co(C_6H_5PO_3)(H_2O)]_n$ from reference [30] (LeBay-Fit), due to the quality of the data the obtained cell parameters are only a hint for a possible structure; preparation in tape causes amorphous signals

Compound	**(11b)**	**(12a)**	**(12b)**	**(13)**	**(14)**
Formula sum	C_7 H_9 Co O_4 P	C_7 H_7 Mn O_6 P	C_7 H_7 Co O_6 P	C_{14} H_{10} Co_2 O_{10} P_2	C_7 H_5 Cu O_5 P
Formula weight / g/mol	247.1	273.0	277.0	518.0	263.6
Crystal colour	pink	colourless	pink	pink	green
Crystal lattice	orthorhombic	monoclinic	monoclinic	monoclinic	monoclinic
Space group	P 21 c n	P 21/n	P 21/n	C 2	C 2/m
a / Å	4.8020(4)	4.9628(5)	4.8556(1)	4.9127(5)	5.203(2)
b / Å	5.6702(4)	31.943(4)	31.8632(9)	8.4621(9)	8.122(3)
c / Å	30.803(2)	5.7787(6)	5.6722(2)	19.276(2)	19.378(6)
α / °	90	90	90	90	90
β / °	90	94.771(5)	94.012(2)	90.488(3)	100.604(9)
γ /°	90	90	90	90	90
Cell volume / Å^3	838.71(16)	912.92(24)	875.416(44)	801.30(23)	804.96(75)
Calculated density / g/cm^3	1.96	1.99	2.10	2.15	2.18
No. measured reflections	6 403	10 815	13 035	9 076	7 310
No. unique reflections	1 865	2 108	2 661	1 877	1 054
No. observed reflections	1 641	1 446	2 338	1 832	825
No. parameters	113	136	138	165	99
GOOF	1.128	0.905	1.056	1.075	1.128
R_{all}	0.045	0.069	0.040	0.047	0.068
$R_{observed}$	0.039	0.035	0.035	0.047	0.045

E.6 $[Mn(HOOCC_6H_4PO_3)(H_2O)]_n$ (12a)

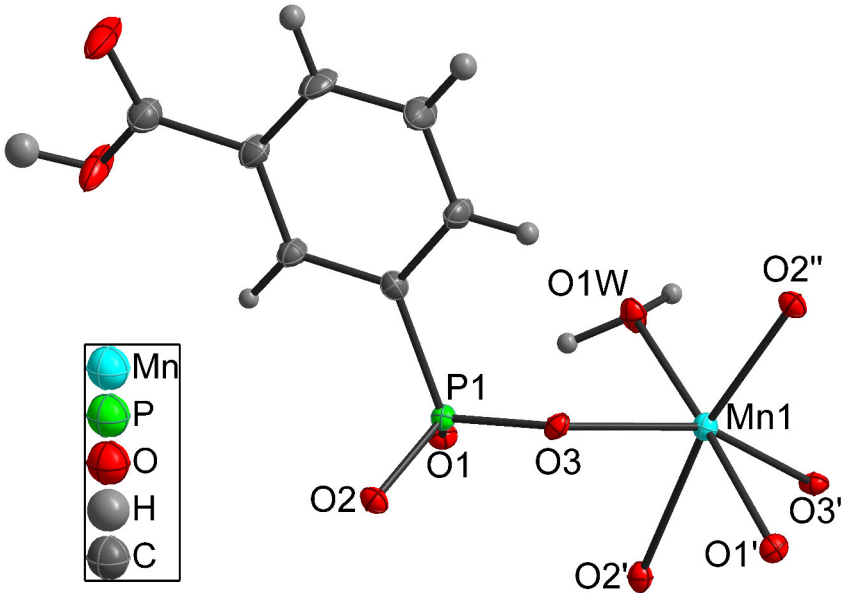

Figure 5.65: Asymmetric unit of $[Mn(HOOCC_6H_4PO_3)(H_2O)]_n$ (AP12310)

atoms	bond length / Å	atoms	bond length / Å
Mn1-O1'	2.129(2)	P1-O1	1.516(2)
Mn1-O2'	2.503(2)	P1-O2	1.543(2)
Mn1-O2"	2.124(2)	P1-O3	1.547(2)
Mn1-O3	2.115(2)		
Mn1-O3'	2.207(2)		
Mn1-O1W	2.207(2)		
atoms	angle /°	atoms	angle /°
O1'-Mn1-O1W	173.10(8)	O1-P1-O2	112.24(12)
O2'-Mn1-O2"	167.52(8)	O1-P1-O3	112.39(11)
O3-Mn1-O3'	152.25(10)	O2-P1-O3	106.18(11)
O1'-Mn1-O2'	85.85(7)		
O1'-Mn1-O2"	92.01(8)		
O1'-Mn1-O3	94.62(8)		
O1'-Mn1-O3'	86.25(7)		

Table 5.6: Selected bond lengths and angles of $[Mn(HOOCC_6H_4PO_3)(H_2O)]_n$, numbering according to figure 5.65; further crystal data can be found in table E.5 on page 251

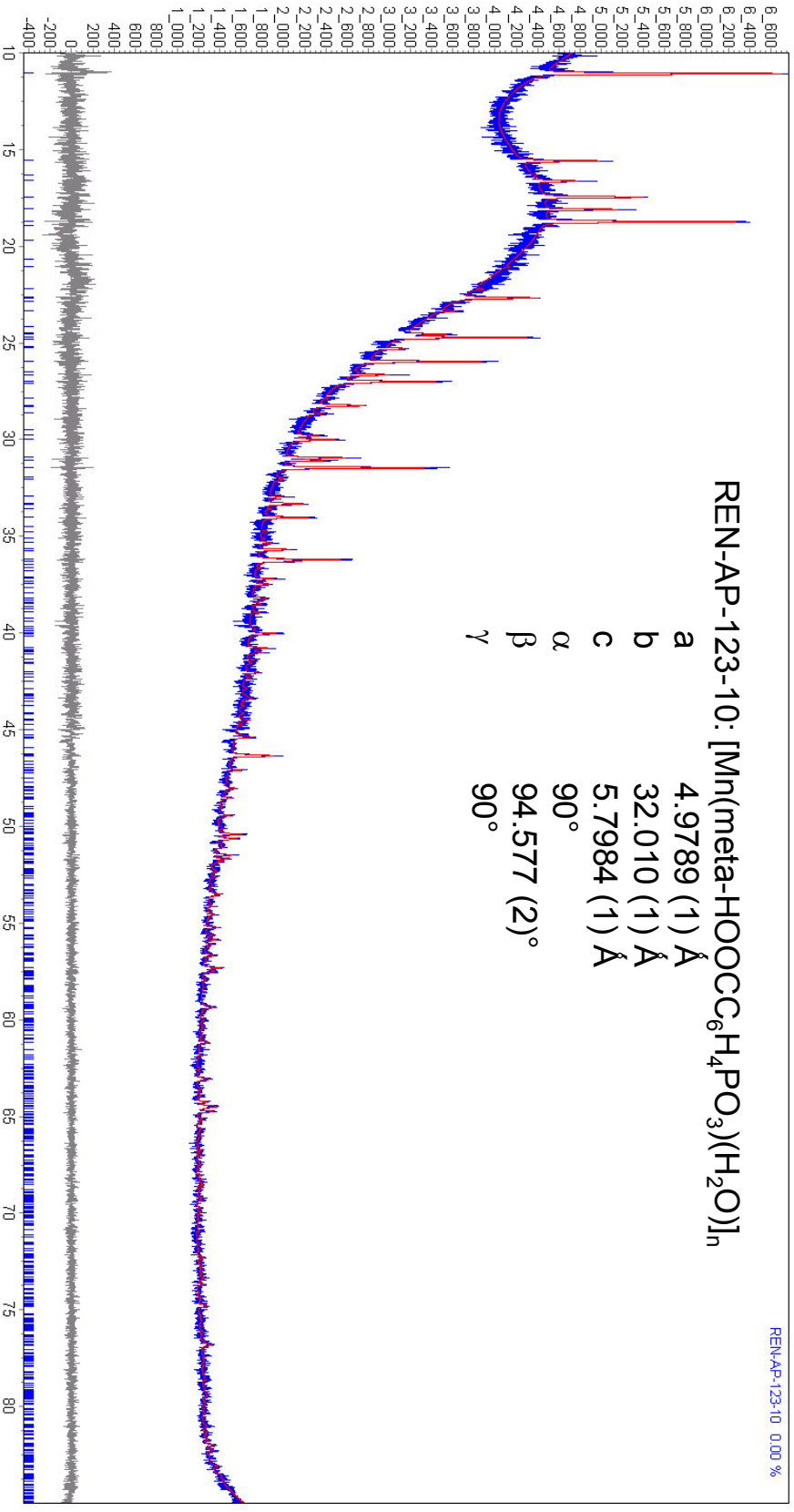

Figure 5.66: Powder diffractogram of [Mn(HOOCC$_6$H$_4$PO$_3$)(H$_2$O)]$_n$, simulation according to cell parameters of the single crystal measurement (LeBay-Fit); material is phase-pure, preparation in tape causes amorphous signals

E.7 $[Co(HOOCC_6H_4PO_3)(H_2O)]_n$ (12b)

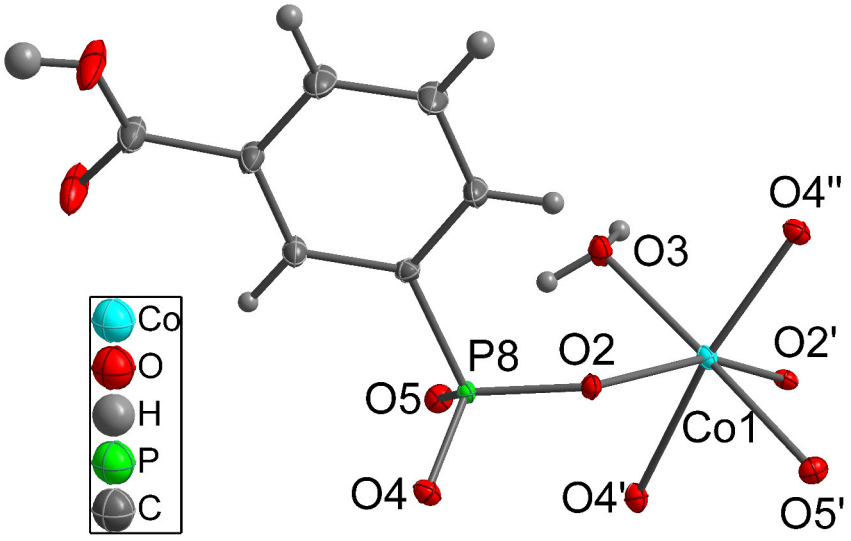

Figure 5.67: Asymmetric unit of $[Co(HOOCC_6H_4PO_3)(H_2O)]_n$ (AP10330)

atoms	bond length / Å	atoms	bond length / Å
Co1-O2	2.046(1)	P8-O2	1.553(2)
Co1-O2'	2.132(1)	P8-O4	1.544(1)
Co1-O3	2.111(1)	P8-O5	1.514(1)
Co1-O4'	2.372(2)		
Co1-O4"	2.075(1)		
Co1-O5'	2.061(1)		
atoms	angle /°	atoms	angle /°
O2-Co1-O2'	155.59(7)	O2-P8-O4	104.79(8)
O3-Co1-O5'	174.94(6)	O2-P8-O5	112.99(8)
O4'-Co1-O4"	167.15(7)	O4-P8-O5	113.11(8)
O5'-Co1-O2	93.82(2)		
O5'-Co1-O2'	86.60(5)		
O5'-Co1-O4'	86.91(5)		
O5'-Co1-O4"	90.83(6)		

Table 5.7: Selected bond lengths and angles of $[Co(HOOCC_6H_4PO_3)(H_2O)]_n$, numbering according to figure 5.67; further crystal data can be found in table E.5 on page 251

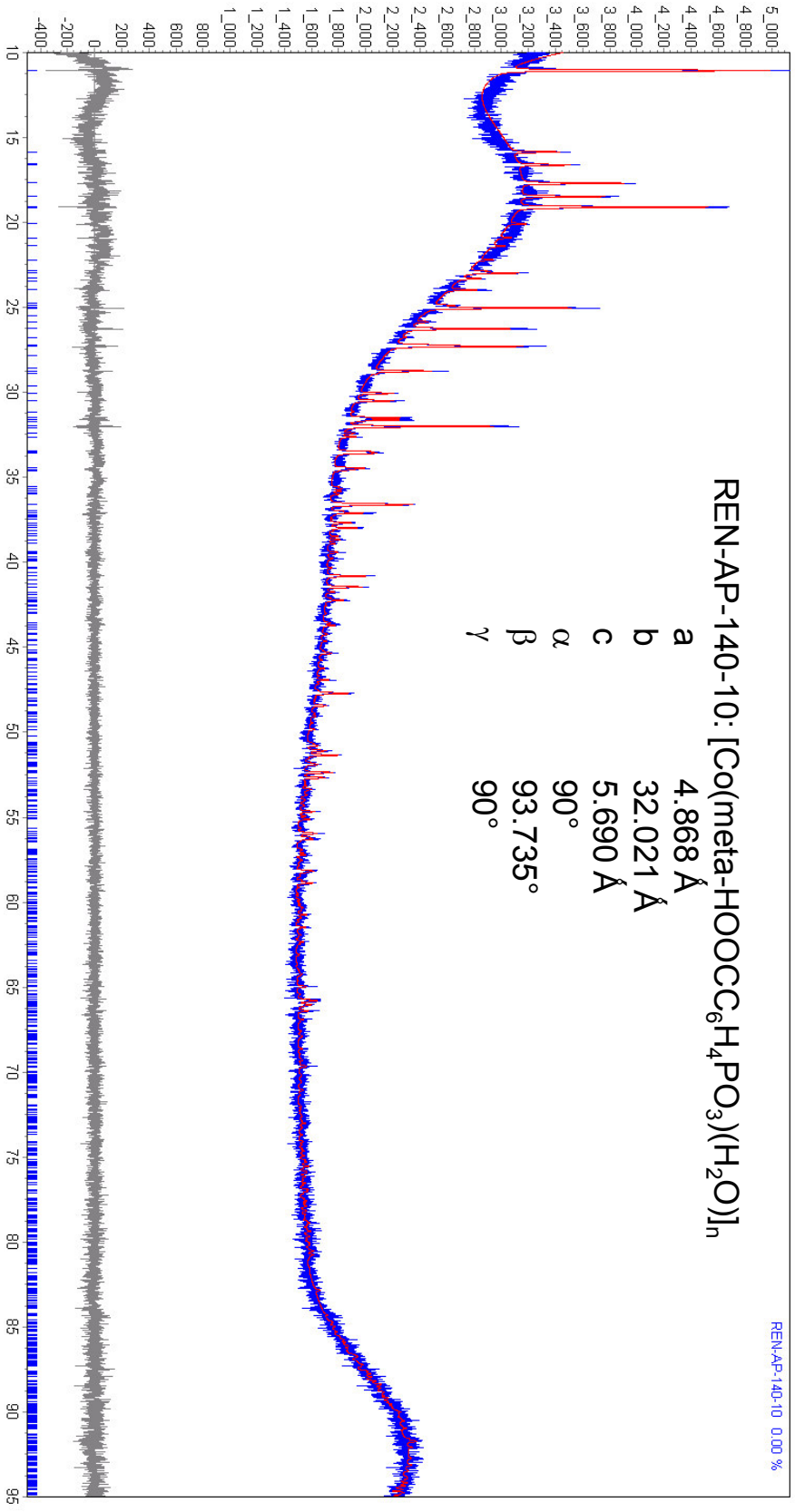

Figure 5.68: Powder diffractogram of $[Co(HOOCC_6H_4PO_3)(H_2O)]_n$, simulation according to cell parameters of the single crystal measurement (LeBay-Fit); material is phase-pure, preparation in tape causes amorphous signals

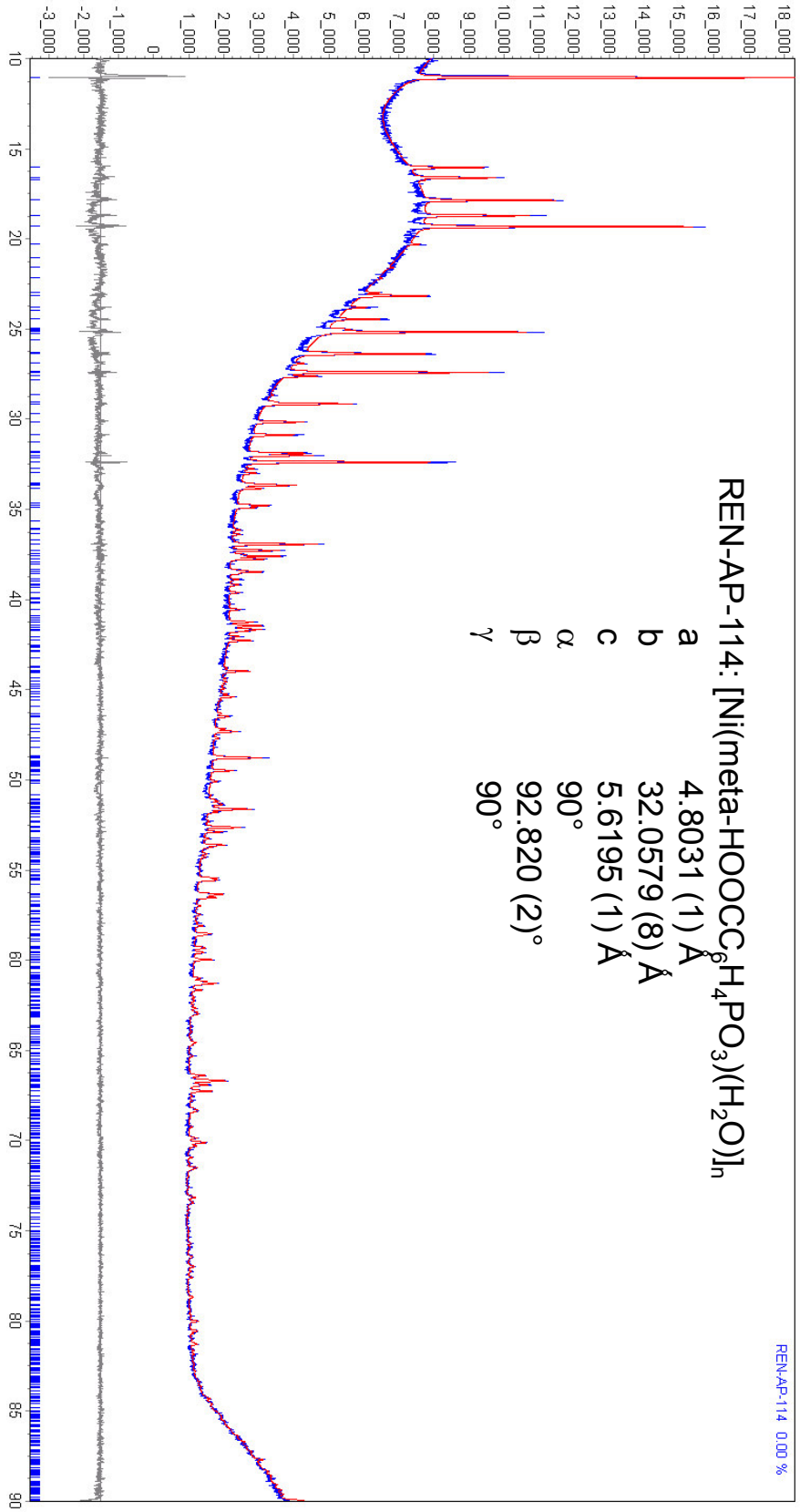

Figure 5.69: Powder diffractogram of $[Ni(HOOCC_6H_4PO_3H)_2(H_2O)_2]_n$, simulation according to cell parameters of the single crystal measurement of $[Co(HOOCC_6H_4PO_3)(H_2O)]_n$ (LeBay-Fit); material is phase-pure, preparation in tape causes amorphous signals

E.8 [Co(para-HOOCC$_6$H$_4$PO$_3$)]$_n$ (13)

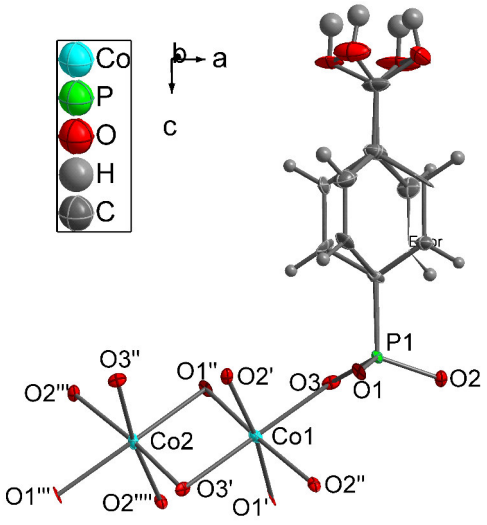

Figure 5.70: Asymmetric unit of [Co(para-HOOCC$_6$H$_4$PO$_3$)]$_n$ (XE19910)

atoms	bond length / Å	atoms	bond length / Å
Co1-O1’	2.106(4)	Co2-O1”	2.104(3)
Co1-O2’	2.061(4)	Co2-O2”’	2.133(4)
Co1-O3	2.106(3)	Co2-O3’	2.084(4)
Co1-Co2	2.8320(4)	P1-O1	1.520(4)
		P1-O2	1.546 (2)
		P1-O3	1.562(5)
atoms	angle /°	atoms	angle /°
O1’-Co1-O2’	171.31(1)	O1”-Co2-O1”’	171.7(2)
O1”-Co1-O2”	171.31(1)	O2”’-Co2-O3’	173.10(1)
O3-Co1-O3’	173.3(2)	O2””-Co2-O3”	173.10(1)
O3-Co1-O1’	94.9(2)	O1”-Co2-O2”’	90.3(1)
O3-Co1-O1”	90.1(1)	O1”-Co2-O2””	84.0(1)
O3-Co1-O2’	91.1(1)	O1”-Co2-O3’	95.6(1)
O3-Co1-O2”	84.5(1)	O1”-Co2-O3”	90.5(1)
Co1-O1”-Co2	84.5(1)	O1-P1-O2	114.0(3)
Co1-O3’-Co2	85.0(1)	O1-P1-O3	111.5(1)
		O2-P1-O3	109.0(3)

Table 5.8: Selected bond lengths and angles of [Co(para-HOOCC$_6$H$_4$PO$_3$)]$_n$, numbering according to figure 5.70; further crystal data can be found in table E.5 on page 251

E.9 [Cu(para-HOOCC$_6$H$_4$PO$_3$)]$_n$ (14)

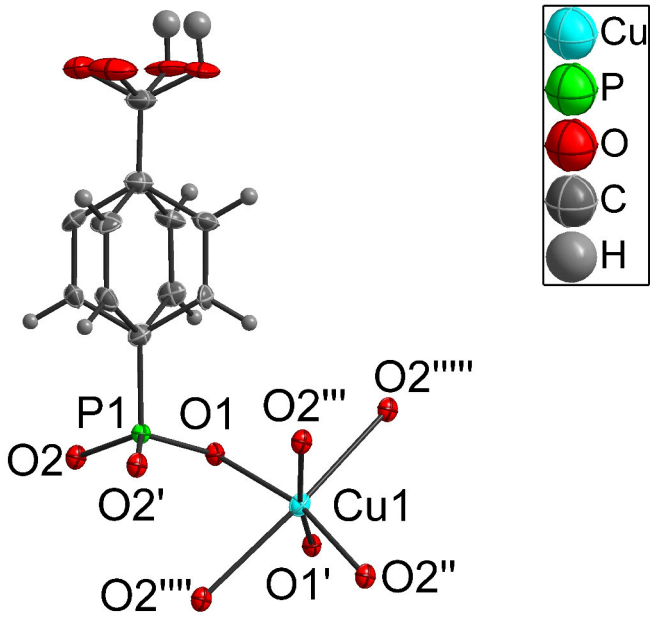

Figure 5.71: Asymmetric unit of [Cu(para-HOOCC$_6$H$_4$PO$_3$)]$_n$ (XE204)

atoms	bond length / Å	atoms	bond length / Å
Cu1-O1	1.970(3)	P1-O1	1.571(5)
Cu1-O1’	1.970(3)	P1-O2	1.528(3)
Cu1-O2”	1.935(3)	P1-O2’	1.528(3)
Cu1-O2”’	1.935(3)		
Cu1-O2””	2.549(4)	Cu1-Cu1	2.84/2.92
Cu1-O2””’	2.549(4)		
atoms	angle /°	atoms	angle /°
O1-Cu1-O2”	164.7(2)	O1-P1-O2	111.1(2)
O1’-Cu1-O2”’	164.7(1)	O1-P1-O2’	111.1(2)
O2””-Cu1-O2””’	171.2(1)	O2-P1-O2’	111.8(3)
O2””-Cu1-O1	81.5(1)		
O2””-Cu1-O1’	91.9(1)	Cu1-O1-Cu1	95.7(1)
O2””-Cu1-O2”	83.4(1)	Cu1-O2-Cu1	77.3(1)
O2””-Cu1-O2”’	102.7(1)		

Table 5.9: Selected bond lengths and angles of [Cu(para-HOOCC$_6$H$_4$PO$_3$)]$_n$, numbering according to figure 5.71; further crystal data can be found in table E.5 on page 251

E.10 [Co(ortho-OOCC$_6$H$_4$PO$_3$H)(H$_2$O)]$_n$ (15)

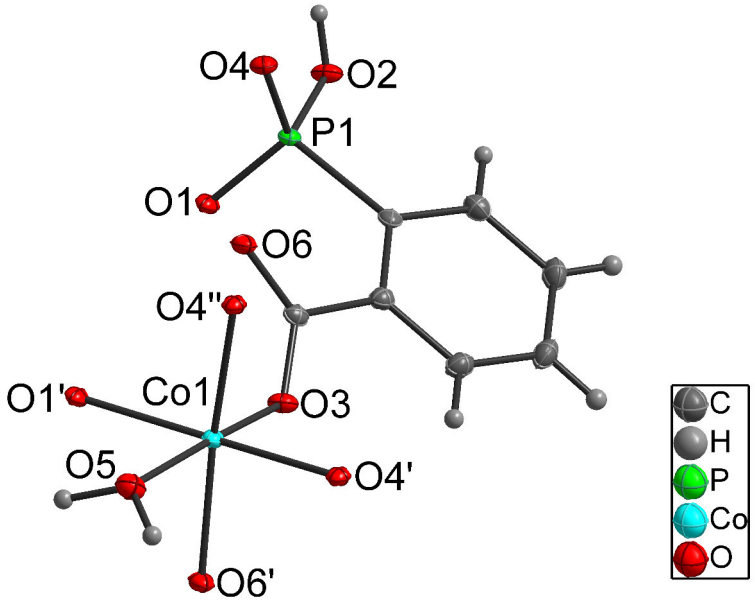

Figure 5.72: Asymmetric unit of [Co(ortho-OOCC$_6$H$_4$PO$_3$H)(H$_2$O)]$_n$ **(15)** (AP118)

atoms	bond length / Å	atoms	bond length / Å
Co1-O1'	2.057(1)	P1-O1	1.517(1)
Co1-O3	2.072(1)	P1-O2	1.587(1)
Co1-O4'	2.053(1)	P1-O4	1.520(1)
Co1-O4''	2.136(1)		
Co1-O5	2.196(1)		
Co1-O6'	2.047(1)		
atoms	angle /°	atoms	angle /°
O1'-Co1-O4'	169.66(5)	O1-P1-O2	108.26(7)
O3-Co1-O5	174.45(5)	O1-P1-O4	116.52(7)
O4''-Co1-O6'	166.51(5)	O2-P1-O4	106.91(7)
O1'-Co1-O3	93.46(5)		
O1'-Co1-O4''	93.16(5)		
O1'-Co1-O5	83.84(5)		
O1'-Co1-O6'	95.20(5)		

Table 5.10: Selected bond lengths and angles of [Co(ortho-OOCC$_6$H$_4$PO$_3$H)(H$_2$O)]$_n$ **(15)**, numbering according to figure 5.72; further crystal data can be found in table E.10 on page 260

Compound	**(15)**	**(16)**	**(17)**	**(18)**
Formula sum	$C_7 H_7 Co O_6 P$	$C_{16} H_{38} Co_2 N_4 O_{18} P_2$	$C_{12} H_{13} N O_6 P$	$C_{21} H_{26} O_{19} P_6 Pr$
Formula weight / g/mol	277.03	754.3	298.2	816.3
Crystal colour	pink	pink	orange	colourless
Crystal lattice	orthorhombic	triclinic	monoclinic	monoclinic
Space group	P c a b	P -1	P 21/c	C 2/c
a / Å	8.6393(3)	7.405(5)	9.5537(4)	42.294(7)
b / Å	9.0003(3)	8.920(5)	7.1308(3)	7.390(1)
c / Å	22.5570(9)	12.637(5)	19.0564(9)	20.098(3)
α / °	90	105.078(5)	90	90
β / °	90	101.794(5)	97.885(1)	117.891(4)
γ /°	90	104.101(5)	90	90
Cell volume / Å^3	1753.95(14)	749.05(24)	1285.95(2)	5552.0(1)
Calculated density / g/cm^3	2.10	1.67	1.54	1.95
No. measured reflections	13 374	16 538	14 402	33 967
No. unique reflections	2 105	3 626	3 129	6 688
No. observed reflections	1 973	3 410	2 775	3 905
No. parameters	136	190	182	397
GOOF	1.102	1.065	1.068	0.959
R_{all}	0.029	0.023	0.041	0.128
$R_{observed}$	0.028	0.021	0.036	0.056

E.11 $[Co_2(H_2O)_6(O_3PCH_2C_7H_5N_2)_2]$*$6H_2O$ (16)

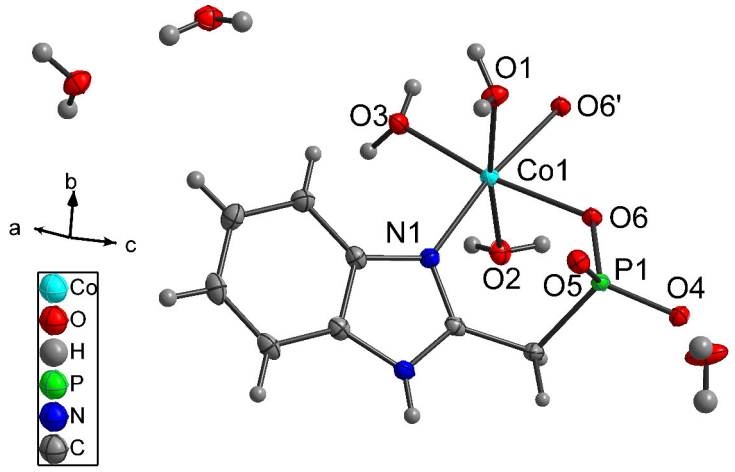

Figure 5.73: Asymmetric unit of $[Co_2(H_2O)_6(O_3PCH_2C_7H_5N_2)_2]$*$6H_2O$ **(16)** (AP13910)

atoms	bond length / Å	atoms	bond length / Å
Co1-O1	2.157(1)	P1-O4	1.531(1)
Co1-O2	2.153(1)	P1-O5	1.514(1)
Co1-O3	2.067(2)	P1-O6	1.539(1)
Co1-O6	2.080(1)		
Co1-O6'	2.119(1)		
Co1-N1	2.098(1)		
atoms	angle /°	atoms	angle /°
O1-Co1-O2	171.92(4)	O4-P1-O5	112.78(7)
O3-Co1-O6	170.80(4)	O4-P1-O6	110.52(6)
N1-Co1-O6'	172.51(4)	O5-P1-O6	113.27(6)
O1-Co1-N1	96.50(5)		
O1-Co1-O3	90.04(5)		
O1-Co1-O6	87.98(5)		
O1-Co1-O6'	86.83(5)		
O6-Co1-O6'	80.56(5)		

Table 5.11: Selected bond lengths and angles of $[Co_2(H_2O)_6(O_3PCH_2C_7H_5N_2)_2]$*$6H_2O$ **(16)**, numbering according to figure 5.73; further crystal data can be found in table E.10 on page 260

E.12 $[(HNC_5H_4C_5H_4NH)(HOOCC_6H_4PO_3H)_2]*2H_2O$ (17)

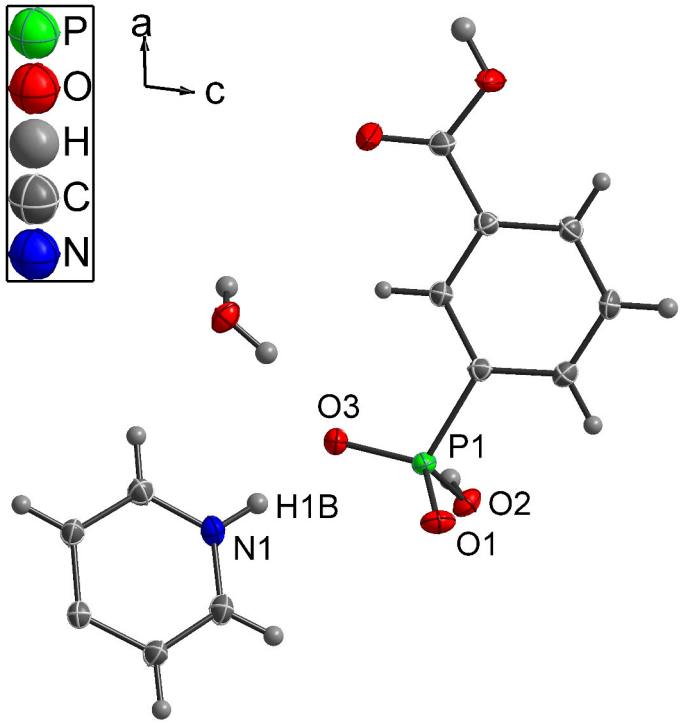

Figure 5.74: Asymmetric unit of $[(HNC_5H_4C_5H_4NH)(HOOCC_6H_4PO_3H)_2]*2H_2O$ **(17)** (AP13920)

atoms	bond length / Å	atoms	angle /°
P1-O1	1.507(1)	O1-P1-O2	106.70(6)
P1-O2	1.576(1)	O1-P1-O3	115.99(6)
P1-O3	1.507(1)	O2-P1-O3	111.27(5)
N1-H1B	0.923(1)	N1-H1B-O3	172.03(8)
O3-H1B	1.706(1)		

Table 5.12: Selected bond lengths and angles of $[(HNC_5H_4C_5H_4NH)(HOOCC_6H_4PO_3H)_2]*2H_2O$ **(17)**, numbering according to figure 5.74; further crystal data can be found in table E.10 on page 260

E.13 $[Pr_2(H_2O)_8(HOOCC_6H_4PO_3H)_6]$ (18)

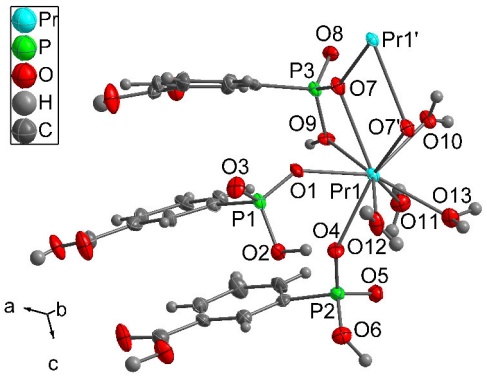

Figure 5.75: Asymmetric unit of $[Pr_2(H_2O)_8(HOOCC_6H_4PO_3H)_6]$ **(18)** (AP166)

atoms	bond length / Å	atoms	bond length / Å
Pr1-O1	2.490(4)	P1-O1	1.495(4)
Pr1-O4	2.478(4)	P1-O2	1.581(4)
Pr1-O7	2.772(4)	P1-O3	1.509(5)
Pr1-O7'	2.422(4)	P2-O4	1.517(4)
Pr1-O9	2.492(4)	P2-O5	1.504(5)
Pr1-O10	2.469(4)	P2-O6	1.580(5)
Pr1-O11	2.526(5)	P3-O7	1.512(5)
Pr1-O12	2.576(4)	P3-O8	1.516(5)
Pr1-O13	2.588(4)	P3-O9	1.564(4)
Pr1-Pr1'	4.327(1)		
atoms	angle /°	atoms	angle /°
O1-Pr1-O4	73.2(1)	O1-P1-O2	109.6(3)
O1-Pr1-O7	67.3(1)	O1-P1-O3	115.8(3)
O1-Pr1-O7'	91.3(2)	O2-P1-O3	108.4(3)
O1-Pr1-O9	79.2(1)	O4-P2-O5	113.5(3)
O7-Pr1-O9	54.8(1)	O4-P2-O6	107.1(3)
O10-Pr1-O11	70.1(1)	O5-P2-O6	111.0(3)
O10-Pr1-O12	131.5(1)	O7-P3-O8	114.3(3)
O10-Pr1-O13	76.82(1)	O7-P3-O9	104.7(2)
Pr1-O7-Pr1'	112.7(2)	O8-P3-O9	110.6(3)

Table 5.13: Selected bond lengths and angles of $[Pr_2(H_2O)_8(HOOCC_6H_4PO_3H)_6]$ **(18)**, numbering according to figure 5.75; further crystal data can be found in table E.10 on page 260

E.14 $[Fe^{II}_2Fe^{III}_2(HCOO)_{10}(\gamma\text{-}C_6H_7N)_6]_n$ (19)

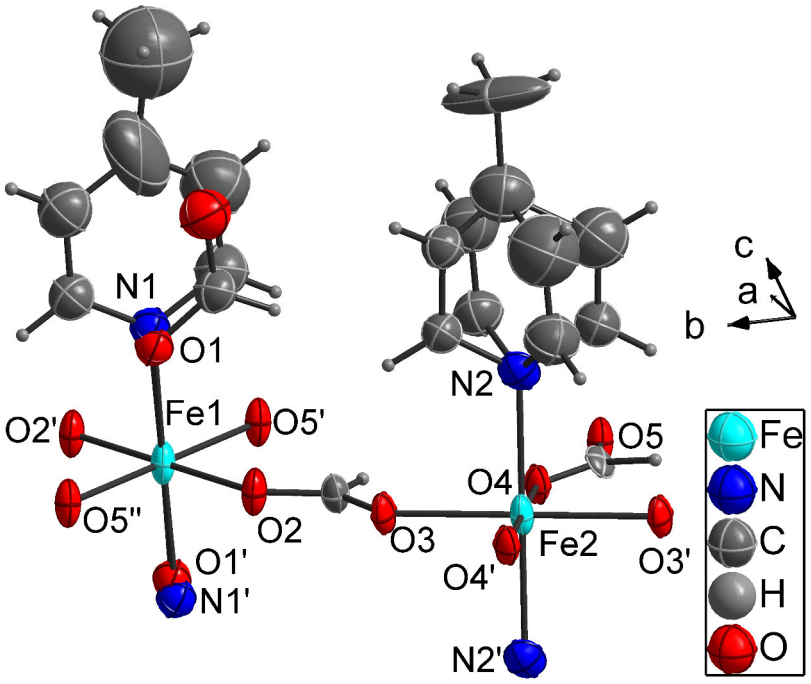

Figure 5.76: Asymmetric unit of $[Fe^{II}_2Fe^{III}_2(HCOO)_{10}(\gamma\text{-}C_6H_7N)_6]_n$ **(19)** (AP007)

atoms	bond length / Å	atoms	bond length / Å
FE1-O1	1.9545(1)	FE2-N2	2.2387(1)
FE1-N1	2.1966(1)		
FE1-O2	2.0012(1)	FE2-O3	2.1102(1)
FE1-O5'	1.9984(1)	FE2-O4	2.1159(1)
atoms	angle /°	atoms	angle /°
O1-FE1-O2	87.590(3)		
N1-FE1-O2	91.900(2)	N2-FE2-O3	89.489(2)
O1-FE1-O5'	91.861(3)		
N1-FE1-O5'	89.469(2)	N2-FE2-O4	89.987(2)
O2-FE1-O5'	89.635(3)	O3-FE2-O4	90.524(3)

Table 5.14: Selected bond lengths and angles of $[Fe^{II}_2Fe^{III}_2(HCOO)_{10}(\gamma\text{-}C_6H_7N)_6]_n$ **(19)**, numbering according to figure 5.76; further crystal data can be found in table E.14 on page 265

Compound	**(19)**	**(20a)**	**(20b)**
Formula sum	$Fe_2\ N_3\ C_{23}\ H_{26}\ O_{10}$	$C_{28}\ H_{28}\ Fe_2\ N_4\ O_8$	$C_{28}\ H_{28}\ Co_2\ N_4\ O_8$
Formula weight / g/mol	1571.01	660.2	666.4
Crystal colour	blue	brown	pink
Crystal lattice	triclinic	triclinic	triclinic
Space group	P -1	P -1	P -1
a / Å	8.5415(4)	7.9615(5)	7.971(5)
b / Å	8.5607(4)	9.1678(5)	9.094(5)
c / Å	10.1757(6)	10.6236(5)	10.668(5)
α / °	65.860(4)	108.999(5)	109.591(5)
β / °	88.713(4)	99.926(5)	99.894(5)
γ /°	89.979(4)	100.941(5)	100.941(5)
Cell volume / $Å^3$	678.79(12)	696.57(23)	601.73(23)
Calculated density / g/cm^3	3.84	1.57	1.60
No. measured reflections		4 402	7 653
No. unique reflections		4 402	2 738
No. observed reflections		3 321	1 423
No. parameters		193	192
GOOF		0.983	0.916
R_{all}		0.083	0.147
$R_{observed}$		0.060	0.075

E.15 $[Fe_2(CH_3COO)_4(C_{10}H_8N_2)_2]_n$ (20a)

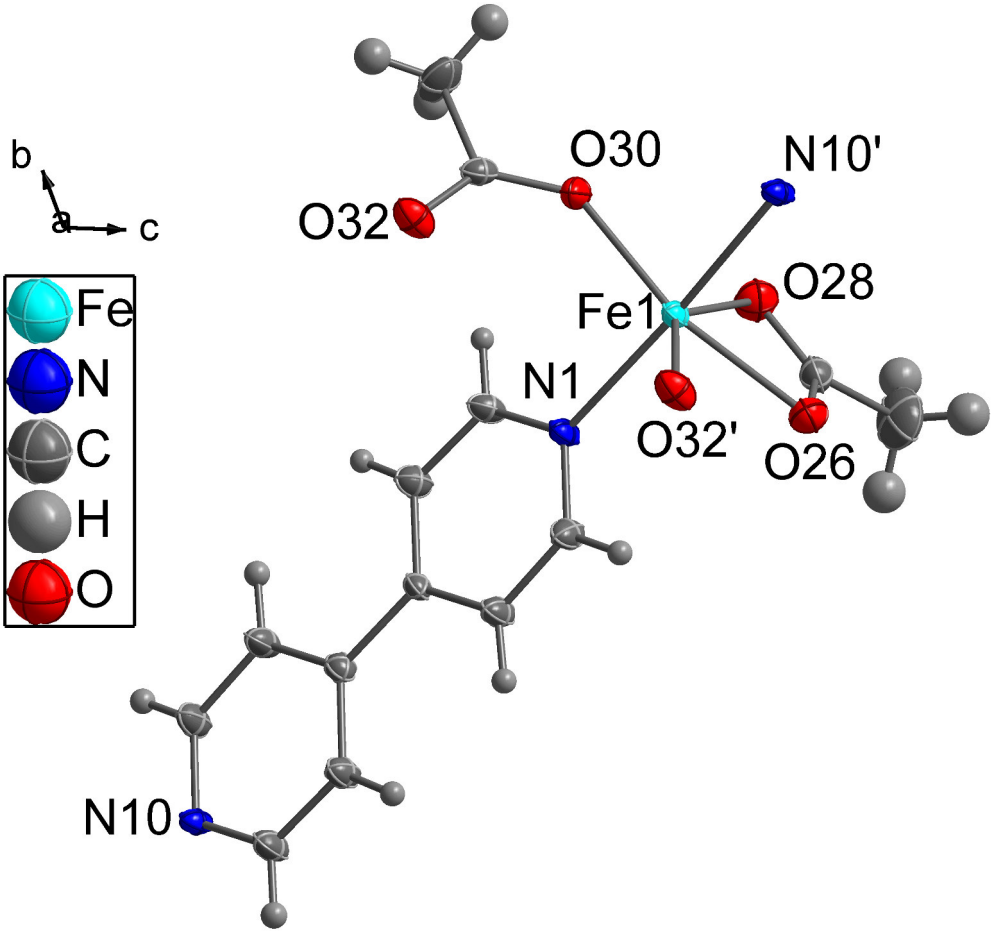

Figure 5.77: Asymmetric unit of $[Fe_2(CH_3COO)_4(C_{10}H_8N_2)_2]_n$ **(20a)** (AP068)

atoms	bond length / Å	atoms	angle /°
Fe1-O26	2.171(3)	O26-Fe1-O30	148.9(1)
Fe1-O28	2.273(3)	O28-Fe1-O32'	145.5(2)
Fe1-O30	2.038(3)	N1-Fe1-N10'	176.6(1)
Fe1-O32'	2.054(3)	O26-Fe1-O28	58.86(9)
Fe1-N1	2.206(2)	O30-Fe1-O32'	124.3(1)
Fe1-N10'	2.201(2)		

Table 5.15: Selected bond lengths and angles of $[Fe_2(CH_3COO)_4(C_{10}H_8N_2)_2]_n$ **(20a)** numbering according to figure 5.77; further crystal data can be found in table E.14 on page 265

E.16 $[Co_2(CH_3COO)_4(C_{10}H_8N_2)_2]_n$ (20b)

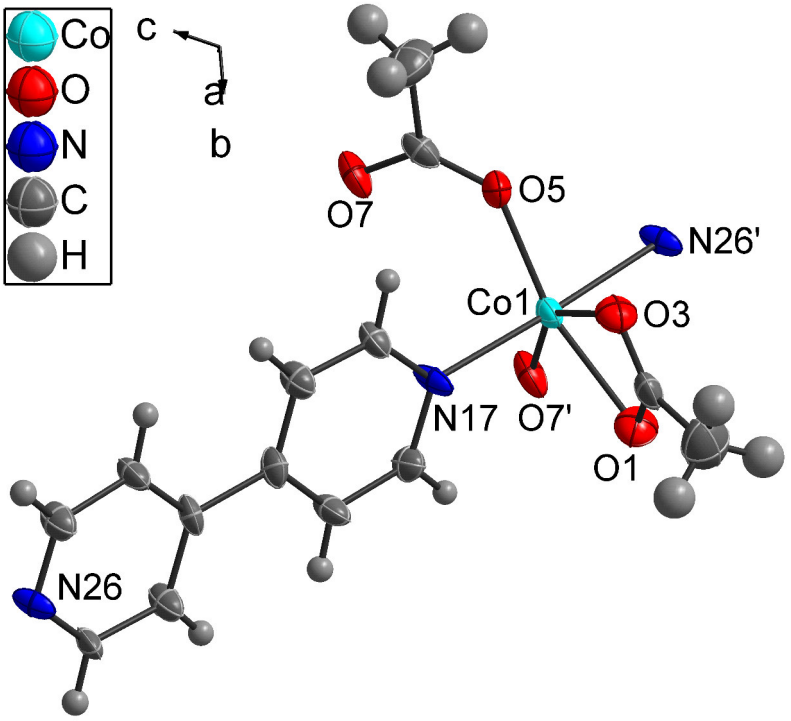

Figure 5.78: Asymmetric unit of $[Co_2(CH_3COO)_4(C_{10}H_8N_2)_2]_n$ **(20b)** (AP04530)

atoms	bond length / Å	atoms	angle /°
Co1-O1	2.184(6)	O1-Co1-O5	150.7(2)
Co1-O3	2.208(6)	O3-Co1-O7'	147.9(2)
Co1-O5	2.006(5)	N17-Co1-N26'	177.0(3)
Co1-O7'	2.018(6)	O1-Co1-O3	59.6(2)
Co1-N17	2.158(6)	O5-Co1-O7'	120.7(2)
Co1-N26'	2.162(6)		

Table 5.16: Selected bond lengths and angles of $[Co_2(CH_3COO)_4(C_{10}H_8N_2)_2]_n$ **(20b)** numbering according to figure 5.78; further crystal data can be found in table E.14 on page 265

E.17 $[Ni_2(C_{50}H_{64}N_{10}O_2)(C_7H_7PO_3)(H_2O)_2](ClO_4)_2$ (39)

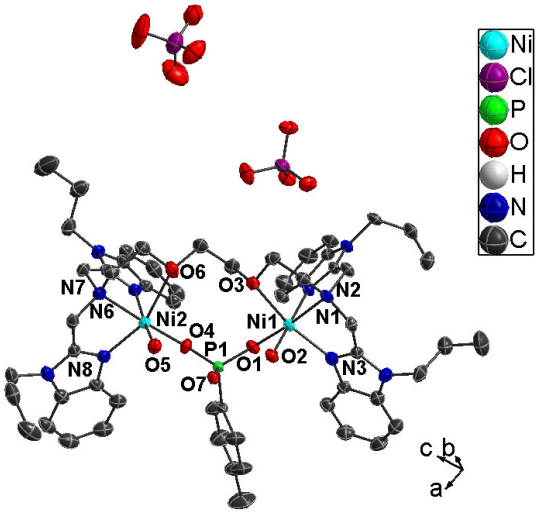

Figure 5.79: Asymmetric unit of $[Ni_2(C_{50}H_{64}N_{10}O_2)(C_7H_7PO_3)(H_2O)_2](ClO_4)_2$ **(39)** (AP133), H atoms omitted for clarity

atoms	bond length / Å	atoms	bond length / Å
Ni1-N1	2.155(2)	Ni2-N6	2.170(2)
Ni1-N2	2.036(2)	Ni2-N7	2.031(2)
Ni1-N3	2.028(2)	Ni2-N8	2.032(2)
Ni1-O1	1.975(2)	Ni2-O4	1.976(2)
Ni1-O2	2.117(2)	Ni2-O5	2.068(2)
Ni1-O3	2.187(2)	Ni2-O6	2.501(2)
Ni1-Ni2	5.408(5)	P1-O4	1.523(2)
P1-O1	1.519(2)	P1-O7	1.534(2)
atoms	angle /°	atoms	angle /°
O1-Ni1-N1	175.23(7)	O4-Ni2-N6	175.99(7)
O2-Ni1-N2	170.40(7)	O5-Ni2-N7	168.02(8)
O3-Ni1-N3	160.65(7)	O6-Ni2-N8	153.55(7)
O1-Ni1-O2	92.45(7)	O4-Ni2-O5	93.30(7)
N1-Ni1-N2	81.20(7)	N6-Ni2-N7	81.88(8)
O1-P1-O4	111.71(9)	O4-P1-O7	111.86 (9)
O1-P1-O7	112.29(9)		

Table 5.17: Selected bond lengths and angles of $[Ni_2(C_{50}H_{64}N_{10}O_2)(C_7H_7PO_3)(H_2O)_2](ClO_4)_2$ **(39)**, numbering according to figure 5.79; further crystal data can be found in table E.17 on page 269

Compound	**(39)**	**(40)**	**(41)**
Formula sum	$C_{64}\ H_{87}\ Cl_2\ N_{13}\ Ni_2\ O_{16}\ P$	$C_{68.5}\ H_{80}\ Cl_2\ N_{15}\ Ni_2\ O_{17}\ P$	$C_{126}\ H_{162}\ Cl_3\ N_{24}\ Na_1\ Ni_3\ O_{28}\ P_2\ Pb_1$
Formula weight / g/mol	1513.76	1604.7	3032.8
Crystal colour	green	blue	blue
Crystal lattice	triclinic	triclinic	monoclinic
Space group	P -1	P -1	C 2/c
a / Å	11.650(1)	12.1891(4)	31.486(2)
b / Å	17.312(1)	17.8176(6)	29.178(2)
c / Å	19.225(2)	19.1372(6)	27.748(2)
α / °	69.478(2)	82.417(2)	90
β / °	80.437(2)	71.828(2)	119.680(2)
γ /°	78.878(2)	77.208(2)	90
Cell volume / $Å^3$	3 542.38(85)	3 842.05(24)	22 147(5)
Calculated density / g/cm^3	1.39	1.39	1.35
No. measured reflections	82 999	71 416	149 605
No. unique reflections	17 123	17 451	22 471
No. observed reflections	11 542	8 020	10 992
No. parameters	887	900	836
GOOF	0.974	0.865	1.152
R_{all}	0.069	0.152	0.204
$R_{observed}$	0.041	0.065	0.112

E.18 $[Ni_2(C_{50}H_{64}N_{10}O_2)(C_{13}H_{16}N_2PO_5)(H_2O)_2](ClO_4)_2$ (40)

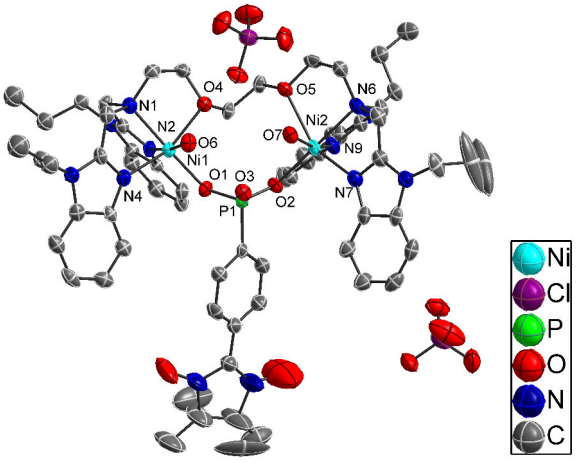

Figure 5.80: Asymmetric unit of $[Ni_2(C_{50}H_{64}N_{10}O_2)(C_{13}H_{16}N_2PO_5)(H_2O)_2](ClO_4)_2$ **(40)** (AP176), H atoms omitted for clarity

atoms	bond length / Å	atoms	bond length / Å
Ni1-N1	2.134(4)	Ni2-N6	2.168(4)
Ni1-N2	2.048(4)	Ni2-N9	2.021(4)
Ni1-N4	2.057(4)	Ni2-N7	2.056(4)
Ni1-O1	1.968(3)	Ni2-O2	1.996(3)
Ni1-O6	2.131(3)	Ni2-O7	2.083(3)
Ni1-O4	2.161(3)	Ni2-O5	2.443(3)
Ni1-Ni2	5.244(8)	P1-O2	1.519(3)
P1-O1	1.521(3)	P1-O3	1.525(3)
atoms	angle /°	atoms	angle /°
O1-Ni1-N1	175.8(1)	O2-Ni2-N6	176.6(1)
O6-Ni1-N2	172.3(1)	O7-Ni2-N9	164.7(1)
O4-Ni1-N4	159.8(1)	O5-Ni2-N7	153.5(1)
O1-Ni1-O6	91.2(1)	O2-Ni2-O7	91.6(1)
N1-Ni1-N2	81.9(1)	N6-Ni2-N9	82.2(1)
Torsion NIT	27.4(1)/31.4(1)	O1-P1-O2	112.2(2)
O1-P1-O3	112.7(2)	O2-P1-O3	112.9(2)

Table 5.18: Selected bond lengths and angles of $[Ni_2(C_{50}H_{64}N_{10}O_2)(C_{13}H_{16}N_2PO_5)(H_2O)_2](ClO_4)_2$ **(40)**, numbering according to figure 5.80; further crystal data can be found in table E.17 on page 269

E.19 $[Ni_3Na_1Pb_1(C_{50}H_{64}N_{10}O_2)_2\ (C_{13}H_{16}N_2PO_5)_2(OH)_2](ClO_4)_3$ (41)

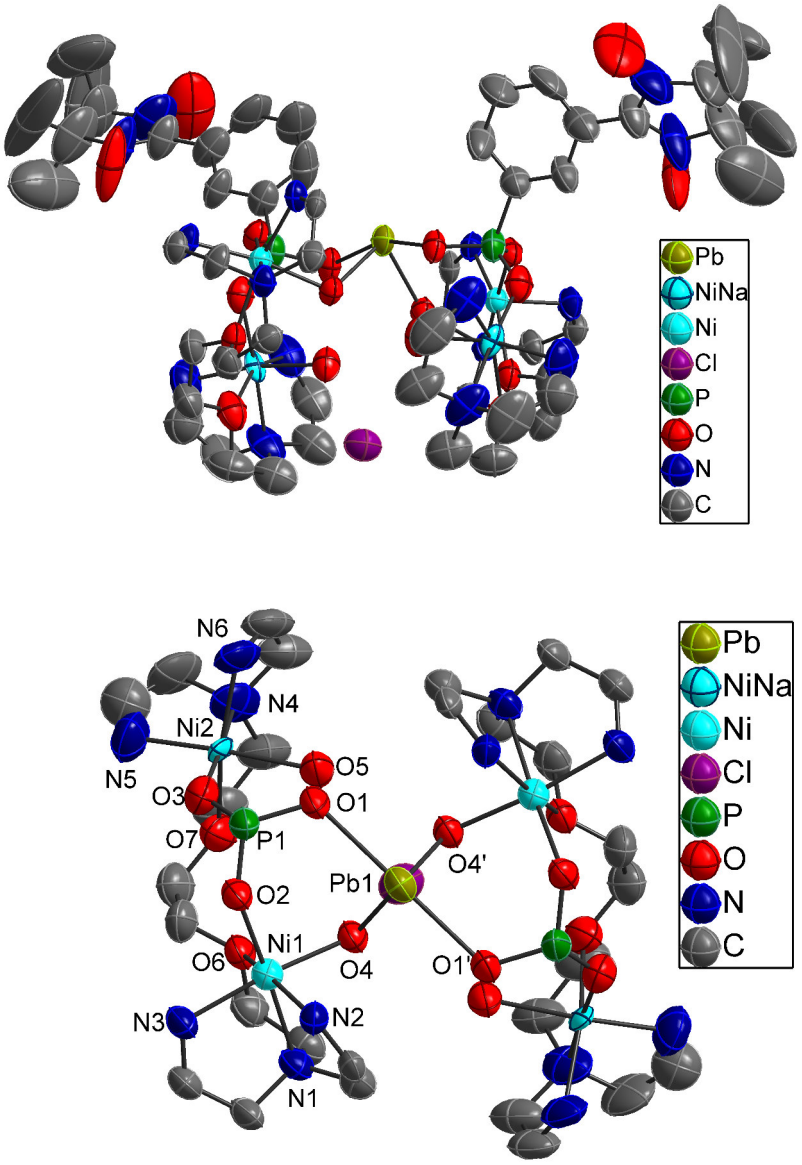

Figure 5.81: Asymmetric unit of $[Ni_3Na_1Pb_1(C_{50}H_{64}N_{10}O_2)_2(C_{13}H_{16}N_2PO_5)_2(OH)_2](ClO_4)_3$ **(41)** (AP178), H atoms omitted for clarity; a superposition of sodium and nickel at one position is needed for charge balance, the ^{Pr}EPTG co-ligand is not fully shown for clarity; inner core is only labelled

atoms	bond length / Å	atoms	bond length / Å
Ni1-N1	2.179(9)	Ni2-N4	2.18(1)
Ni1-N2	2.060(9)	Ni2-N5	1.99(1)
Ni1-N3	2.044(9)	Ni2-N6	2.09(1)
Ni1-O2	2.023(7)	Ni2-O3	2.000(9)
Ni1-O4	2.015(7)	Ni2-O5	2.072(8)
Ni1-O6	2.189(8)	Ni2-O7	2.329(9)
Ni1-Ni2	5.192(3)	P1-O2	1.487(8)
P1-O1	1.539(7)	P1-O3	1.538(9)
Pb1-O1	2.493(7)	Pb1-O4	2.193(7)
atoms	angle /°	atoms	angle /°
O2-Ni1-N1	175.1(3)	O3-Ni2-N4	176.6(4)
O6-Ni1-N2	159.6(3)	O5-Ni2-N5	168.3(5)
O4-Ni1-N3	168.6(3)	O7-Ni2-N6	156.2(5)
O2-Ni1-O6	101.8(3)	O3-Ni2-O7	101.7(3)
N1-Ni1-N2	79.3(3)	N3-Ni2-N4	81.2(6)
Torsion NIT	33.8(3)/35.2(3)	O1-P1-O2	112.9(4)
O1-P1-O3	111.1(5)	O2-P1-O3	112.8(5)
O1-Pb1-O1'	160.7(4)	O4-Pb1-O4'	84.9(3)

Table 5.19: Selected bond lengths and angles of $[Ni_3Na_1Pb_1(C_{50}H_{64}N_{10}O_2)_2(C_{13}H_{16}N_2PO_5)_2(OH)_2](ClO_4)_3$ **(41)**, numbering according to figure 5.81; further crystal data can be found in table E.17 on page 269